CONTENTS

CONTENTS

AERODYNAMICS, AERONAUTICS, AND FLIGHT MECHANICS

ONE
INTRODUCTION

Aeronautics is defined as "the science that treats of the operation of aircraft; also, the art or science of operating aircraft." Basically, with aeronautics, one is concerned with predicting and controlling the forces and moments on an aircraft that is traveling through the atmosphere.

A BRIEF HISTORY

Thursday, December 17, 1903

"When we got up a wind of between 20 and 25 miles was blowing from the north. We got the machine out early and put out the signal for the men at the station. Before we were quite ready, John T. Daniels, W. S. Dough, A. D. Etheridge, W. C. Brinkly of Manteo, and Johnny Moore of Nags Head arrived. After running the engine and propellers a few minutes to get them in working order, I got on the machine at 10:35 for the first trial. The wind, according to our anemometers at this time, was blowing a little over 20 miles (corrected) 27 miles according to the government anemometer at Kitty Hawk. On slipping the rope the machine started off increasing in speed to probably 7 or 8 miles. The machine lifted from the truck just as it was entering the fourth rail. Mr. Daniels took a picture just as it left the tracks. I found the control of the front rudder quite difficult on account of its being balanced too near the center and thus had a tendency to turn itself when started so that the rudder was turned too far on one side and then too far on the other. As a result the machine would rise suddenly to about 10 ft. and then as suddenly, on turning the rudder, dart for the ground. A sudden dart when out about 100 feet from the end of the tracks ended the flight. Time about 12 seconds (not known exactly as watch was not promptly stopped). The level for throwing off the engine was broken, and the skid under the rudder cracked. After repairs, at 20 min. after 11 o'clock Will made the second trial."

The above, taken from Orville Wright's diary, as reported in Reference 1.1, describes mankind's first sustained, controlled, powered flight in a

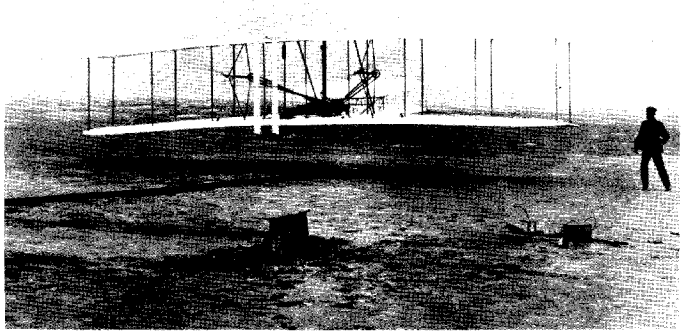

Figure 1.1 The first flight, December 17, 1903. (Courtesy of the National Air and Space Museum, Smithsonian Institution.)

heavier-than-air machine. The photograph, mentioned by Orville Wright, is shown here as Figure 1.1. Three more flights were made that morning. The last one, by Wilbur Wright, began just at 12 o'clock and covered 260 m in 59 s. Shortly after this flight, a strong gust of wind struck the airplane, turning it over and over. Although the machine was severely damaged and never flew again, the Wright Brothers achieved their goal, begun approximately 4 yr earlier.

Their success was no stroke of luck. The Wright Brothers were painstaking in their research and confident of their own results. They built their own wind tunnel and tested, in a methodical manner, hundreds of different airfoil and wing planform shapes. They were anything but a "couple of bicycle mechanics." Their letters to Octave Chanute, a respected civil engineer and aviation enthusiast of the day, reveal the Wright Brothers to have been learned men well versed in basic concepts such as work, energy, statics, and dynamics. A three-view drawing of their first airplane is presented in Figure 1.2.

On September 18, 1901, Wilbur Wright was invited to deliver a lecture before the Western Society of Engineers at a meeting in Chicago, Illinois. Among the conclusions reached by him in that paper were:

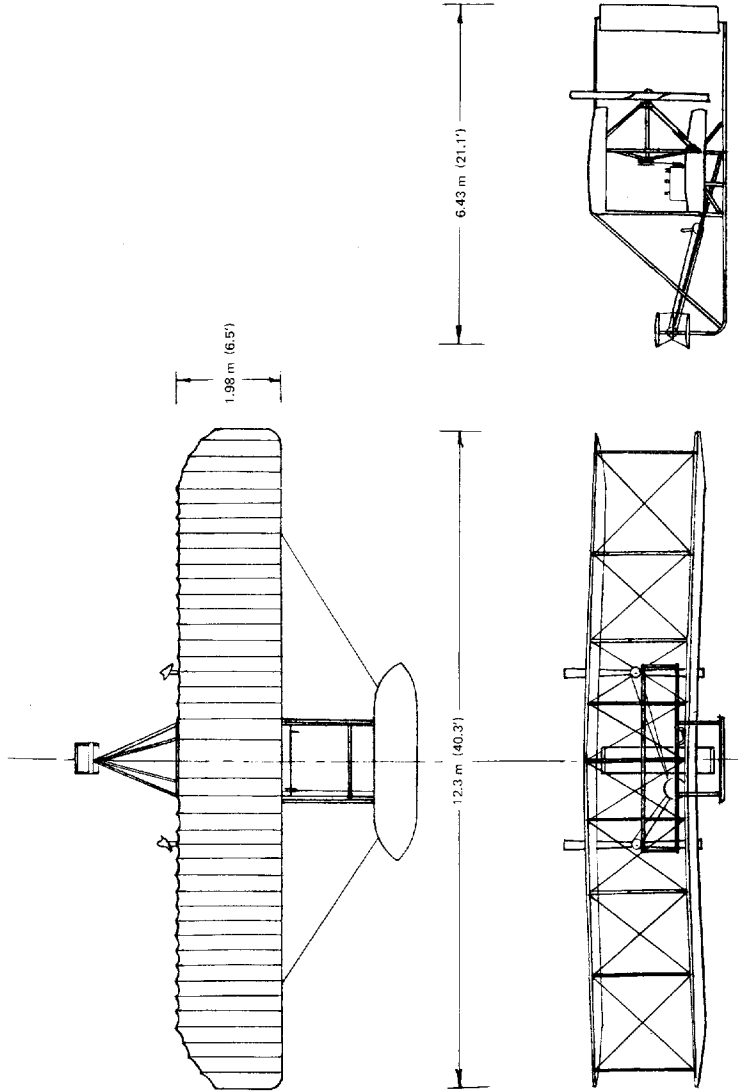

Figure 1.2 Three views of the Wright Brothers' flyer.

1. *"That the ratio of drift to lift in well-shaped surfaces is less at angles of incidence of five degrees to 12 degrees than at an angle of three degrees." ("Drift" is what we now call "drag.")*
2. *"That in arched surfaces the center of pressure at 90 degrees is near the center of the surface, but moves slowly forward as the angle becomes less, till a critical angle varying with the shape and depth of the curve is reached, after which it moves rapidly toward the rear till the angle of no lift is found."*
3. *"That a pair of superposed, or tandem surfaces, has less lift in proportion to drift than either surface separately, even after making allowance for weight and head resistance of the connections."*

These statements and other remarks (see Ref. 1.1) show that the Wright Brothers had a good understanding of wing and airfoil behavior well beyond that of other experimenters of the time.

Following their first successful flights at Kitty Hawk, North Carolina, in 1903, the Wright Brothers returned to their home in Dayton, Ohio. Two years later they were making flights there, almost routinely, in excess of 30 km and 30 min while others were still trying to get off the ground.

Most of the success of the Wright Brothers must be attributed to their own research, which utilized their wind tunnel and numerous experiments with controlled kites and gliders. However, their work was built, to some degree, on the gliding experiments of Otto Lilienthal and Octave Chanute. Beginning in 1891, Lilienthal, working near Berlin, Germany, made approximately 2000 gliding flights over a 5-yr period. Based on measurements obtained from these experiments, he published tables of lift and drag measurements on which the Wright Brothers based their early designs. Unfortunately, Lilienthal had no means of providing direct aerodynamic control to his gliders and relied instead on kinesthetic control, whereby he shifted his weight fore and aft and side to side. On August 9, 1896, as the result of a gust, Otto Lilienthal lost control and crashed from an altitude of approximately 15 m. He died the next day. During 1896 and 1897, Octave Chanute, inspired by Lilienthal's work, designed and built several gliders that were flown by others near Miller, Indiana. Chanute recognized Lilienthal's control problems and was attempting to achieve an "automatic" stability in his designs. Chanute's principal contribution was the addition of both vertical and horizontal stabilizing tail surfaces. In addition, he went to the "box," or biplane, configuration for added strength. Unfortunately, he also relied on kinesthetic control.

When the Wright Brothers began their gliding experiments in the fall of 1900, they realized that adequate control about all three axes was one of the major prerequisites to successful flight. To provide pitch control (i.e., nose up or down), they resorted to an all-movable horizontal tail mounted in front of

the wing. Yaw control (i.e., turning to the left or right) was accomplished by means of an all-movable vertical tail mounted behind the wing. Their method of roll control (i.e., lowering one side of the wing and raising the other) was not as obvious from photographs as the controls about the other two axes. Here, the Wright Brothers devised a means of warping their "box" wing so that the angle of incidence was increased on one side and decreased on the other. The vertical tail, or rudder, was connected to the wing-warping wires so as to produce what pilots refer to today as a coordinated turn.

The Wright Brothers were well ahead of all other aviation enthusiasts of their era. In fact, it was not until 3 yr after their first flight that a similar capability was demonstrated, this by Charles and Gabriel Voisin in Paris, France (Ref. 1.2). On March 30, 1907, Charles Voisin made a controlled flight of approximately 100 m in an airplane similar in appearance to the Wright flyer. A second machine built by the Voisin Brothers for Henri Farman, a bicycle and automobile racer, was flown by Farman later that year on flights that exceeded 2000 m. By the end of that year at least five others succeeded in following the Wright Brothers' lead, and aviation was on its way.

Today we are able to explain the results of the early experimenters in a very rational way by applying well-established aerodynamic principles that have evolved over the years from both analysis and experimentation. These developments have their beginnings with Sir Isaac Newton, who has been called the first real fluid mechanician (Ref. 1.3). In 1687 Newton, who is probably best known for his work in solid mechanics, reasoned that the resistance of a body moving through a fluid is proportional to the fluid density, the velocity squared, and the area of the body.

Newton also postulated the shear force in a viscous fluid to be proportional to the velocity gradient. Today, any fluid obeying this relationship is referred to as a Newtonian fluid.

In 1738, Daniel Bernoulli, a Swiss mathematician, published his treatise, "Hydrodynamics," which was followed in 1743 by a similar work produced by his father, John Bernoulli. The Bernoullis made important contributions to understanding the behavior of fluids. In particular, John introduced the concept of internal pressure, and he was probably the first to apply momentum principles to infinitesimal fluid elements.

Leonhard Euler, another Swiss mathematician, first put the science of hydrodynamics on a firm mathematical base. Around 1755, Euler properly formulated the equations of motion based on Newtonian mechanics and the works of John and Daniel Bernoulli. It was he who first derived along a streamline the relationship that we refer to today as "Bernoulli's equation."

The aerodynamic theories of the 1800s and early 1900s developed from the early works of these mathematicians. In 1894 the English engineer, Frederick William Lanchester, developed a theory to predict the aerodynamic behavior of wings. Unfortunately, this work was not made generally known

Table 1.1 Largest Aircraft Examples Starting with the Wright Brothers

Designer or Manufacturer a. Model Number b. Model Name	First Flight Date	Span, ft	Length, ft	Wing Area, ft^2	Gross Weight, 1000 lb	Empty Weight, 1000 lb	Useful Load, 1000 lb	Power Plant, no. × hp/eng.	Loadings: Wing lb/ft^2	Loadings: Power, lb/hp or lb	Number[a] Flown	Passenger Capacity	Range, ST.M.	Comment
Wright b. Flyer	12/03	40.3	21.1	510	0.75	0.6	0.15[b]	1 × 12 hp	1.47	62.50	1	0	...	Canard biplane and single engines driving two pusher propellers.
Sikorsky/RBVZ b. Ilya Mourometz	4/13	113	67.2	1,615	10.58	7.28	3.3	4 × 100 hp	6.55	26.45	80	16	300	Biplane with tractor engines on lower wing; used effectively as a bomber in W.W.I.
Zeppelin-Staaken a. VGO.1	4/15	138.5	78.7	3,572	20.99	14.38	6.61	3 × 240 hp	5.9	29.2	44	...	...	Biplane with one nose mounted engine and two wing-mounted pushers.
Handley Page a. H.P. 15(V/1500)	4/18	126	64	3,000	30	15	15	4 × 275 hp	10.00	27.27	10	40	1,300	Built to bomb Berlin in W.W.I; biplane with 2 × 2 tractor/pusher arrangement.
Caproni a. Ca 60 b. Transaero	1921[c]	98.4	76.9	7,696	55.12	30.86	24.26	8 × 400 hp	7.16	19.69	0[c]	100	410	Flying boat: triple triplane.
Junkers a. G-38	11/29	144.3	76.1	3,229	44.09	28.66	15.33	2 × 400 hp 2 × 800 hp	13.63	18.33	8[j]	30	746	Engines wing-buried; DLH line service from 1932 to 1944.
Dornier a. Do X	7/29	157.5	131.4	4,736	105.8	72.2	33.6	12 × 500 hp	22.34	17.63	3	100[d]	850	Flying boat.

Table 1.1 (continued)

Designer or Manufacturer a. Model Number b. Model Name	First Flight Date	Span, ft	Length, ft	Wing Area, ft^2	Gross Weight, 1000 lb	Empty Weight, 1000 lb	Useful Load, 1000 lb	Power Plant, no. × hp/eng.	Loadings: Wing lb/ft^2	Loadings: Power, lb/hp or lb	Number[a] Flown	Passenger Capacity	Range, ST.M.	Comment
Kalinin a. K-7	8/33	173.9	91.9	4,887	83.78	53.79	29.99	7 × 750 hp	17.14	15.96	1	...	620	Bomber; projected 120-passenger transport version not built.
Tupolev a. ANT-20 b. Maxim Gorki	5/34	206.7	106.5	5,233	116.84	92.58	24.26	8 × 875 hp	22.33	16.69	2[e]	64[e]	1,240	Equipped with printing press and propaganda aerial loudspeaker system.
Douglas a. XB-19	6/41	212	132.3	4,285	162	75	65	4 × 2,000 hp	32.67	17.50	1	...	7,700	Bomber.
Lockheed a. 89 b. Constitution	11/46	189.1	156.1	3,610	184	114	70	4 × 3,000 hp	50.97	15.33	2	168	4,700	Full double-deck accommodations.
Hughes a. H-4(HK-1)	11/47	320.5	218.5	11,450	400	248	152	8 × 3,000 hp	34.93	16.67	1[k]	700	5,900	Flying boat; all wood.
Convair a. XC-99	11/47	230	182.5	4,772	265	140	125	6 × 3,000 hp	55.53	14.72	1	400	...	6 wing-buried engines with pusher propellers; full double-deck accommodations.
Bristol a. 167 b. Brabazon 1	9/49	230	177	5,317	290	145	145	8 × 2,500 hp	54.54	14.50	1	100	5,500	8 wing-buried engines coupled in pairs to 4 tractor propellers.

Table 1.1 (continued)

Designer or Manufacturer a. Model Number b. Model Name	First Flight Date	Span, ft	Length, ft	Wing Area, ft^2	Gross Weight, 1000 lb	Empty Weight, 1000 lb	Useful Load, 1000 lb	Power Plant, no. × hp/eng.	Loadings: Wing lb/ft^2	Loadings: Power, lb/hp or lb	Number[a] Flown	Passenger Capacity	Range, ST.M.	Comment
Boeing a. YB-52 b. Stratofortress	4/52	185	153	4,000	390	166	224	8 × 10,000 lb	97.50	3.00[c]	744	...	7,000	Bomber.
Boeing a. B-52G b. Stratofortress	3/61	185	157.6	4,000	488	...	...	8 × 13,750 lb	122.00	2.85[d]		...	10,000	Bomber.
Antonov a. An-22 b. Antheus	2/65	211.3	189.6	3,713	551.2	251.4	299.8	4 × 15,000 hp	148.45	9.19	SP[g]	350[h]	6,800	High-wing, tail-loading cargo transport; contra-rotating propellers.
Lockheed a. C-5A b. Galaxy	6/68	222.7	247.7	6,200	764.5	320	444.5	4 × 41,000 lb	123.31	4.78[f]	SP[g]	1,000[i]	7,500	High-wing, nose and tail-loading cargo transport; T-tail.

Source. From F. A. Cleveland, "Size Effects in Conventional Aircraft," *J. of Aircraft*, 7(6), November–December 1970 (33rd Wright Brothers Lecture). Reproduced with permission.

[a] Counting original(s), subsequent series production, and derivatives—if any.
[b] Counting pilot (Orville Wright) and 5 lb of fuel.
[c] Destroyed in taxi-test which resulted in unintended liftoff.
[d] Set world record 21 Oct. 1929 with 169 onboard.
[e] One ANT-20 is built with six 1100-hp engines.
[f] Turbine energy expressed in terms of gas-hp with 0.8 efficiency.
[g] SP = in series production.
[h] Used mainly as freighter: 724-seat stretched version projected.
[i] Triple deck version.
[j] Two in Germany; six in Japan.
[k] Flew only once on high-speed taxi test.

until 1907 in a book published by Lanchester. By then the Wright Brothers had been flying for 3 yr. Much of the knowledge that they had laboriously deduced from experiment could have been reasoned from Lanchester's theory. In 1894, Lanchester completed an analysis of airplane stability that could also have been of value to the Wrights. Again, this work was not published until 1908.

Lanchester's wing theory was somewhat intuitive in its development. In 1918 Ludwig Prandtl, a German professor of mechanics, presented a mathematical formulation of three-dimensional wing theory; today both men are credited with this accomplishment. Prandtl also made another important contribution to the science with his formalized boundary layer concept.

Around 1917 Nikolai Ergorovich Joukowski (the spelling has been anglicized), a Russian professor of rational mechanics and aerodynamics in Moscow, published a series of lectures on hydrodynamics in which the behavior of a family of airfoils was investigated analytically.

The work of these early hydro- and aerodynamicists contributed little, if any, to the progress and ultimate success of those struggling to fly. However, it was the analytical base laid by Euler and those who followed him on which the rapid progress in aviation was built.

After 1908, the list of aviators, engineers, and scientists contributing to the development of aviation grew rapidly. Quantum improvements were accomplished with the use of flaps, retractable gear, the cantilevered wing, all-metal construction, and the turbojet engine. This impressive growth is documented in Table 1.1. Note that in less than 10 yr from the Wright Brothers' first flight, the useful load increased from 667 N (150 lb) to more than 13,300 N (3000 lb). In the next 10 yr, the useful load increased by a factor of 10 and today is more than 1.78×10^6 N (400,000 lb) for the Lockheed C-5A.

Our state of knowledge is now such that one can predict with some certainty the performance of an airplane before it is ever flown. Where analytical or numerical techniques are insufficient, sophisticated experimental facilities are utilized to investigate areas such as high-lift devices, complicated three-dimensional flows in turbomachinery, and aerothermodynamics.

A BRIEF INTRODUCTION TO THE TECHNOLOGY OF AERONAUTICS

Consider the airplane in steady, climbing flight shown in Figure 1.3. The term *steady* means that the airplane is not accelerating; hence, all forces and moments on the aircraft must be in balance. To be more precise, one states that the vector sum of all forces and moments on the airplane must be zero. To depict the angles more clearly, all forces are shown acting through the center of gravity (cg). Although the resultant of all the forces must pass

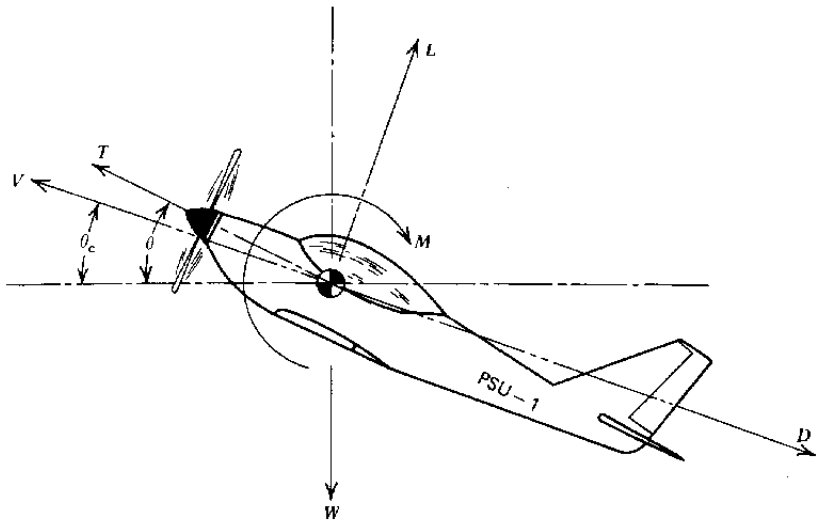

Figure 1.3 Forces and moments on an airplane in a steady climb.

through the center of gravity, it is not generally true that any one of the forces, with the exception of W, must satisfy this condition.

In this figure V represents the velocity vector of the airplane's center of gravity. This vector is shown inclined upward from the horizontal through the angle of climb, θ_c. The angle between the horizontal and the thrust line is denoted as θ. If this line is taken to be the reference line of the airplane, then one states that the airplane is pitched up through this angle. The angle between the reference line and the velocity vector, $\theta - \theta_c$, is referred to as the angle of attack of the airplane. Later we will use other angles of attack referenced to the wing geometry; thus, one must be careful in interpreting lift and drag data presented as a function of the angle of attack.

The thrust, T, is the propelling force that balances mainly the aerodynamic drag on the airplane. T can be produced by a propeller, a turbojet, or a rocket engine.

The lift, L, is defined as the component of all aerodynamic forces generated by the aircraft in the direction normal to the velocity vector, V. In level flight this means principally the upward vertical force produced by the wing. Generally, however, it includes the tail and fuselage forces. For example, in landing many aircraft require a downward force on the horizontal tail in order to trim out the nose-down pitching moment produced by the wing flaps. This trimming force can be significant, requiring a wing lift noticeably in excess of the airplane's weight.

Similar to the lift, the drag, D, is defined as the component of all aerodynamic forces generated by the airplane in the direction opposite to the

velocity vector, V. This force is composed of two principal parts, the parasite drag and the induced drag. The induced drag is generated as a result of producing lift; the parasite drag is the drag of the fuselage, landing gear, struts, and other surfaces exposed to the air. There is a fine point concerning the drag of the wing to be mentioned here that will be elaborated on later. Part of the wing drag contributes to the parasite drag and is sometimes referred to as profile drag. The profile drag is closely equal to the drag of the wing at zero lift; however, it does increase with increasing lift. This increase is therefore usually included as part of the induced drag. In a strict sense this is incorrect, as will become clearer later on.

W is the gross weight of the airplane and, by definition, acts at the center of gravity of the airplane and is directed vertically downward. It is composed of the empty weight of the airplane and its useful load. This latter weight includes the payload (passengers and cargo) and the fuel weight.

The pitching moment, M, is defined as positive in the nose-up direction (clockwise in Figure 1.3) and results from the distribution of aerodynamic forces on the wing, tail, fuselage, engine nacelles, and other surfaces exposed to the flow. Obviously, if the airplane is in trim, the sum of these moments about the center of gravity must be zero.

We know today that the aerodynamic forces on an airplane are the same whether we move the airplane through still air or fix the airplane and move the air past it. In other words, it is the relative motion between the air and airplane and not the absolute motion of either that determines the aerodynamic forces. This statement was not always so obvious. When he learned of the Wright Brothers' wind tunnel tests, Octave Chanute wrote to them on October 12, 1901 (Ref. 1.1) and referred to "natural wind." Chanute conjectured in his letter:

"It seems to me that there may be a difference in the result whether the air is impinged upon by a moving body or whether the wind impinges upon the same body at rest. In the latter case each molecule, being driven from behind, tends to transfer more of its energy to the body than in the former case when the body meets each molecule successively before it has time to react on its neighbors."

Fortunately, Wilbur and Orville Wright chose to believe their own wind tunnel results.

Returning to Figure 1.3, we may equate the vector sum of all forces to zero, since the airplane is in equilibrium. Hence, in the direction of flight,

$$T \cos(\theta - \theta_c) - D - W \sin \theta_c = 0 \tag{1.1}$$

Normal to this direction,

$$W \cos \theta_c - L - T \sin(\theta - \theta_c) = 0 \tag{1.2}$$

These equations can be solved for the angle of climb to give

$$\theta_c = \tan^{-1} \frac{T \cos(\theta - \theta_c) - D}{L + T \sin(\theta - \theta_c)} \tag{1.3}$$

In this form, θ_c appears on both sides of the equation. However, let us assume *a priori* that θ_c and $(\theta - \theta_c)$ are small angles. Also, except for very high performance and V/STOL (vertical or short takeoff and landing) airplanes, the thrust for most airplanes is only a fraction of the weight. Thus, Equation 1.3 becomes

$$\theta_c \simeq \frac{T - D}{W} \tag{1.4}$$

For airplanes propelled by turbojets or rockets, Equation 1.4 is in the form that one would normally use for calculating the angle of climb. However, in the case of airplanes with shaft engines, this equation is modified so that we can deal with power instead of thrust.

First, consider a thrusting propeller that moves a distance S in time t at a constant velocity, V. The work that the propeller performs during this time is, obviously,

$$\text{work} = TS$$

Power is the rate at which work is performed; hence,

$$\text{power} = T \frac{S}{t}$$

But S/t is equal to the velocity of advance of the propeller. Hence the power available from the propeller is given by

$$P_{\text{avail}} = TV \tag{1.5}$$

Similarly, the power required by a body traveling through the air with a velocity of V and having a drag of D will be

$$P_{\text{req'd}} = DV$$

Thus, returning to Equation 1.4, by multiplying through by WV, we get

$$W(V\theta_c) = P_{\text{avail}} - P_{\text{req'd}} \tag{1.6}$$

The quantity $V\theta_c$ is the vertical rate of climb, V_c. The difference between the power that is required and that available is referred to as the excess power, P_{XS}. Thus Equation 1.6 shows that the vertical rate of climb can be obtained by equating the excess power to the power required to lift the airplane's weight at the rate V_c. In operating an airplane this means the following. A pilot is flying at a given speed in steady, level flight with the engine throttle only partially open. If the pilot advances the throttle while maintaining a constant airspeed, the power from the engine will then be in excess of that required for level flight, and the airplane will climb.

Suppose, instead of keeping it constant, the pilot, while opening the throttle, allows the airspeed to increase in such a manner as to maintain a constant altitude. When a wide open throttle (WOT) condition is reached the maximum power available is equal to the power required. This is the condition for maximum airspeed, "straight and level."

From this brief introduction into airplane performance, it is obvious that we must be able to estimate the aerodynamic forces on the airplane before we can predict its performance. Also, a knowledge of the characteristics of its power plant-propulsor combination is essential.

In addition to performance, the area of "flying qualities" is very important to the acceptance of an airplane by the customer. Flying qualities refers primarily to stability and control, but it also encompasses airplane response to atmospheric disturbances.

Let us briefly consider the pitching moment M, shown in Figure 1.3. This moment, which must be zero for steady, trimmed flight, results mainly from the lift on the wing and tail. In addition, contributions arise from the fuselage, nacelles, propulsor, and distribution of pressure over the wing. Suppose now that the airplane is trimmed in steady, level flight when it is suddenly disturbed (possibly by a gust or an input from the pilot) such that it pitches up by some amount. Before it can respond, the airplane's path is still essentially horizontal, so that the angle between the velocity vector and the plane's axis is momentarily increased. It will be shown later that, at a given airspeed, the moment, M, is dependent on this angle, defined previously as the angle of attack. Since the moment was initially zero before the airplane was disturbed, it follows that, in general, it will have some value other than zero due to the increase in angle of attack. Suppose this increment in M is positive. In this case the tendency would then be for the angle of attack to increase even further. This is an unstable situation where the airplane, when disturbed, tends to move even further from its steady-state condition. Thus, for the airplane to exhibit a more favorable, stable response, we desire that the increment in M caused by an angle of attack change be negative.

This is about as far as we can go without considering in detail the generation of aerodynamic forces and moments on an airplane and its components. The preceding discussion has shown the importance of being able to predict these quantities from both performance and flying qualities viewpoints. The following chapters will present detailed analytical and experimental material sufficient to determine the performance and stability and control characteristics of an airplane.

As you study the material to follow, keep in mind that it took the early aviation pioneers a lifetime to accumulate only a fraction of the knowledge that is yours to gain with a few months of study.

The primary system of units to be used in this text is the SI (Systems Internationale) system. Since this system is just now being adopted in the United States, a comparison to the English system is presented in Appendix A.1. Also, to assure familiarity with both systems, a limited number of exercises are given in the English system. For a more complete explanation of the SI system, see Reference 1.4.

PROBLEMS

1.1 Calculate the rate of climb of an airplane having a thrust-to-weight ratio of 0.25 and a lift-to-drag ratio of 15.0 at a forward velocity of 70 m/s (230 fps). Express V_c in meters per second. Current practice is to express rate of climb in feet per minute. What would be your answer in these units?

1.2 Which of the systems (ball and track) pictured below are in equilibrium? Which are stable?

1.3 An aircraft weighs 45,000 N (10,117 lb) and requires 597 kW (800 hp) to fly straight and level at a speed of 80 m/s (179 mph). If the available power is 895 kW (1200 hp), how fast will the airplane climb when the throttle is advanced to the wide open position?

1.4 For an aircraft with a high thrust-to-weight ratio, the angle of climb is not necessarily small. In addition, for certain V/STOL aircraft, the thrust vector can be inclined upward significantly with respect to the direction of flight. If this angle is denoted as θ_T, show that

$$\theta_c = \tan^{-1} \frac{T \cos \theta_T - D}{L + T \sin \theta_T}$$

1.5 A student pushes against the side of a building with a force of 6 N for a period of 4 hr. How much work was done?

1.6 An aircraft has a lift-to-drag ratio of 15. It is at an altitude of 1500 m (4921 ft) when the engine fails. An airport is 16 km (9.94 miles) ahead. Will the pilot be able to reach it?

REFERENCES

1.1 McFarland, Marvin W., editor, *The Papers of Wilbur and Orville Wright, Including the Chanute-Wright Letters*, McGraw-Hill, New York, 1953.

1.2 Harris, Sherwood, *The First to Fly, Aviation's Pioneer Days*, Simon and Schuster, New York, 1970.

1.3 Robertson, James M., *Hydrodynamics in Theory and Application*, Prentice-Hall, Englewood Cliffs, N.J., 1965.

1.4 Mechtly, E. A., *The International System of Units, Physical Constants and Conversion Factors*, NASA SP-7012, U.S. Government Printing Office, Washington, D.C., 1969.

1.5 Cleveland, F. A., "Size Effects in Conventional Aircraft Design," *J. of Aircraft*, 7(6), November–December 1970 (33rd Wright Brothers Lecture).

TWO
FLUID MECHANICS

This chapter will stress the principles in fluid mechanics that are especially important to the study of aerodynamics. For the reader whose preparation does not include fluid mechanics, the material in this chapter should be sufficient to understand the developments in succeeding chapters. For a more complete treatment, see any of the many available texts on fluid mechanics (e.g., Refs. 2.1 and 2.2).

Unlike solid mechanics, one normally deals with a continuous medium in the study of fluid mechanics. An airplane in flight does not experience a sudden change in the properties of the air surrounding it. The stream of water from a firehose exerts a steady force on the side of a burning building, unlike the impulse on a swinging bat as it connects with the discrete mass of the baseball.

In solid mechanics, one is concerned with the behavior of a given, finite system of solid masses under the influence of force and moment vectors acting on the system. In fluid mechanics one generally deals not with a finite system, but with the flow of a continuous fluid mass under the influence of distributed pressures and shear stresses.

The term *fluid* should not be confused with the term *liquid*, since the former includes not only the latter, but gases as well. Generally a fluid is defined as any substance that will readily deform under the influence of shearing forces. Thus a fluid is the antonym of a solid. Since both liquids and gases satisfy this definition, they are both known as fluids. A liquid is distinguished from a gas by the fact that the former is nearly incompressible. Unlike a gas, the volume of a given mass of liquid remains nearly constant, independent of the pressure imposed on the mass.

FLUID STATICS AND THE ATMOSPHERE

Before treating the more difficult case of a fluid in motion, let us consider a fluid at rest in static equilibrium. The mass per unit volume of a fluid is defined as the mass density, usually denoted by ρ. The mass density is a

constant for liquids, but it is a function of temperature, T, and pressure, p, for gases. Indeed, for a gas, p, ρ, and T are related by the equation of state

$$p = \rho RT \tag{2.1}$$

R is referred to as the gas constant and has a value of 287.3 $m^2/°K\text{-}sec^2$ for air at normal temperatures. In Equation 2.1, T is the thermodynamic or absolute temperature in degrees Kelvin. T and the Celsius temperature, t, are related by

$$T = t + 273.15 \tag{2.2}$$

A container filled with a liquid is pictured in Figure 2.1*a*. A free-body diagram of a small slug of the fluid is shown in Figure 2.1*b*. This slug has a

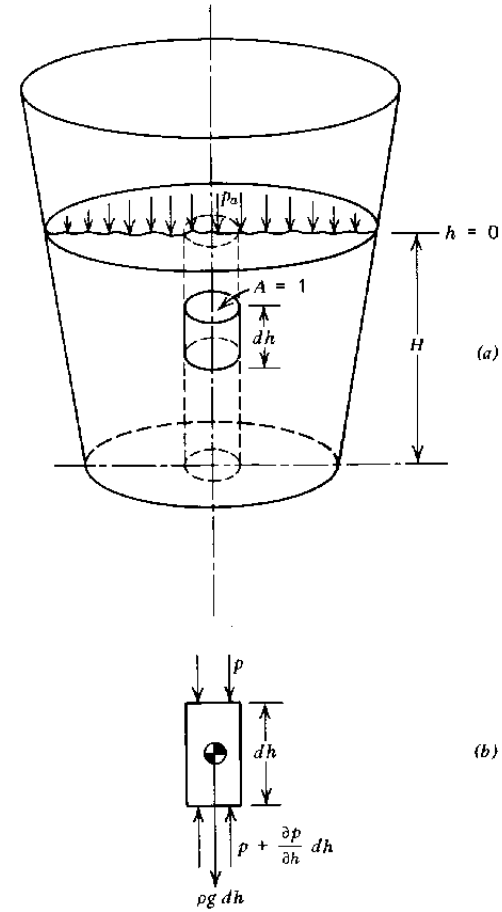

Figure 2.1 The variation of pressure with depth in a liquid.

unit cross-sectional area and a differential length of dh. Acting downward over the upper surface is the static pressure, p, while acting upward over the lower face is this same pressure plus the rate of increase of p with depth multiplied by the change in depth, dh. The static pressure also acts inward around the sides of the element, but this contributes nothing to the balance of forces in the vertical direction. In addition to the pressure forces, the weight of the fluid element, $\rho g\, dh$, acts vertically downward; g is the gravitational constant.

Summing forces on the element in the vertical direction leads to

$$\frac{dp}{dh} = \rho g \tag{2.3}$$

Integrating Equation 2.3 from $h = 0$ at the surface to any depth, h, results in the static pressure as a function of the depth.

$$p = p_a + \rho g h \tag{2.4}$$

where p_a is the atmospheric pressure at the free surface.

A manometer is a device frequently used to measure pressures. It is based on Equation 2.4. Consider the experimental setup pictured in Figure 2.2. Here, a device known as a pitot-static tube is immersed in and aligned with a gas flow. The impact of the gas being brought to rest at the nose of the tube produces a pressure higher than that along the sides of the tube. This pressure, known as the total pressure, is transmitted through a tube to one side of a U-shaped glass tube partially filled with a liquid. Some distance back from the nose of the pitot-static tube the pressure is sampled through a small opening that is flush with the sides of the tube. This opening, if it is far enough back from the nose, does not disturb the flow so that the pressure sampled by it is the same as the static pressure of the undisturbed flow. This static pressure is transmitted to the right side of the glass U-tube manometer. The total pressure, being higher than the static pressure, causes the liquid in the left side of the U-tube to drop while the level on the right side rises.

If we denote p as the static pressure and $p + \Delta p$ as the total pressure, the pressure at the bottom of the U-tube can be calculated by Equation 2.4 using either the right or left side of the tube. Equating the results from the two sides gives

$$p + \Delta p + \rho g h_0 = p + \rho g(\Delta h + h_0)$$

or

$$\Delta p = \rho g\, \Delta h \tag{2.5}$$

Hence, the difference of the liquid levels in the two sides of the manometer is a direct measure of the pressure difference applied across the manometer. In this case we could then determine the difference between the total pressure

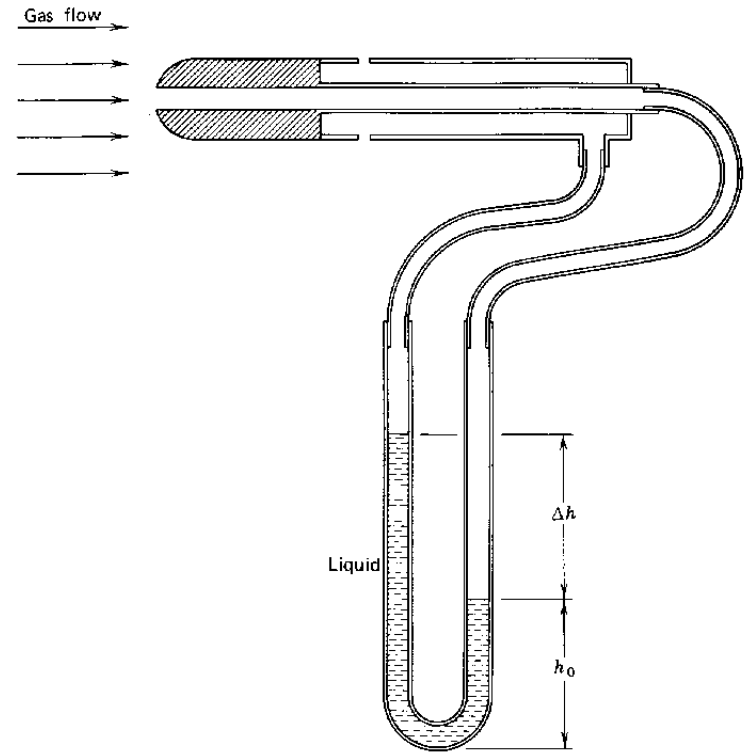

Figure 2.2 Pitot-static tube connected to a U-tube liquid manometer.

and static pressure in the gas flow from which, as we will see later, the velocity of the gas can be calculated.

Now consider the variation of static pressure through the atmosphere. Again the forces acting on a differential mass of gas will be treated in a manner similar to the development of Equation 2.3 for a liquid. However, h will be taken to be the altitude above the ground and, since the gravitational attraction is now opposite to the direction of increasing h, the sign of Equation 2.3 changes. For the atmosphere,

$$\frac{dp}{dh} = -\rho g \tag{2.6}$$

The mass density, ρ, is not a constant in this case, so that Equation 2.6 cannot be integrated immediately. In order to perform the integration the equation of state, Equation 2.1, is substituted for ρ, which leads to

$$\frac{dp}{p} = -\frac{g\, dh}{RT} \tag{2.7}$$

From experimental observation, the variation of temperature with altitude is known or, at least, a standard variation has been agreed on. Up to an altitude of 11 km, the temperature is taken to decrease linearly with altitude at a rate, known as the lapse rate, of 6.51 °C/km. Thus, Equation 2.7 becomes

$$\frac{dp}{p} = -\frac{dT}{T}\frac{1}{R(dT/dh)}$$

or

$$\delta = \theta^{5.2561} \tag{2.8}$$

where δ is the ratio of the static pressure at altitude to the pressure at sea level and θ is the corresponding absolute temperature ratio.

Using the equation of state, the corresponding density ratio, σ, is obtained immediately from Equation 2.8.

$$\sigma = \frac{\delta}{\theta}$$

or

$$\sigma = \theta^{4.2561} \tag{2.9}$$

Using the standard lapse rate and a sea level temperature of 288.15 °K, θ as a function of altitude is given by

$$\theta = 1 - 0.02256\,h \tag{2.10}$$

where h is the altitude in kilometers.

The lower region of the atmosphere up to an altitude for which Equations 2.8 to 2.10 hold is referred to as the troposphere. This is the region in which most of today's flying is done. Above 11 km and up to an altitude of approximately 23 km, the temperature is nearly constant. This region forms the lower part of the stratosphere. Through the remainder of the stratosphere, the temperature increases, reaching approximately 270 °K at an altitude of around 50 km.

Figure 2.3 presents graphs (taken from Ref. 2.3) of the various properties of the standard atmosphere as a function of altitude. Each property is presented as a ratio to its standard sea level value denoted by the subscript "0." In addition to p, ρ, and T, the acoustic velocity and kinematic viscosity are presented. These two properties will be defined later.

One normally thinks of altitude as the vertical distance of an airplane above the earth's surface. However, the operation of an airplane depends on the properties of the air through which it is flying, not on the geometric height. Thus the altitude is frequently specified in terms of the *standard atmosphere.* Specifically, one refers to the *pressure altitude* or the *density altitude* as the height in the standard atmosphere corresponding to the pressure or density, respectively, of the atmosphere in which the airplane is operating. An airplane's altimeter is simply an absolute pressure gage calibrated according to

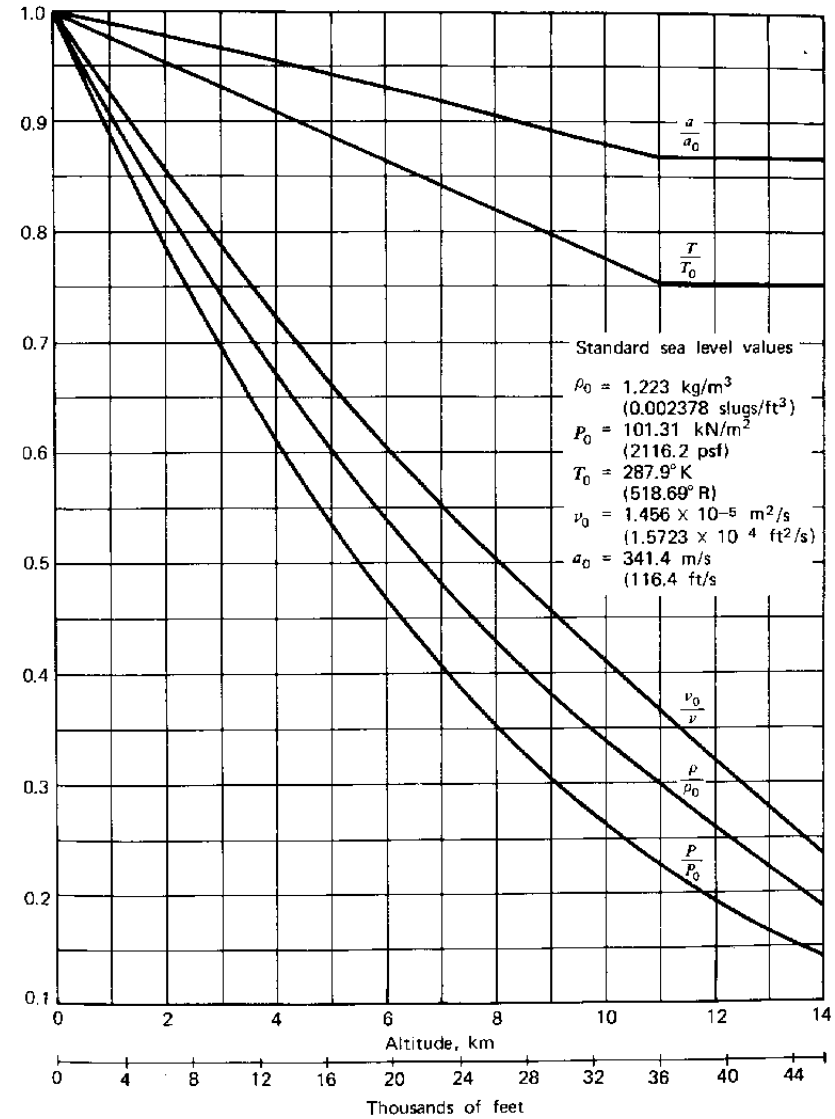

Figure 2.3 The standard atmosphere.

the standard atmosphere. It has a manual adjustment to allow for variations in sea level barometric pressure. When set to standard sea level pressure (760 mm Hg, 29.92 in. Hg), assuming the instrument and static pressure source to be free of errors, the altimeter will read the pressure altitude. When set to the local sea level barometric pressure (which the pilot can obtain over the

radio while in flight), the altimeter will read closely the true altitude above sea level. A pilot must refer to a chart prescribing the ground elevation above sea level in order to determine the height above the ground.

FLUID DYNAMICS

We will now treat a fluid that is moving so that, in addition to gravitational forces, inertial and shearing forces must be considered.

A typical flow around a streamlined shape is pictured in Figure 2.4. Note that this figure is labled "two-dimensional flow"; this means simply that the flow field is a function only of two coordinates (x and y, in the case of Figure 2.4) and does not depend on the third coordinate. For example, the flow of wind around a tall, cylindrical smokestack is essentially two-dimensional except near the top. Here the wind goes over as well as around the stack, and the flow is three-dimensional. As another example, Figure 2.4 might represent the flow around a long, streamlined strut such as the one that supports the wing of a high-wing airplane. The three-dimensional counterpart of this shape might be the blimp.

Several features of flow around a body in general are noted in Figure 2.4. First, observe that the flow is illustrated by means of streamlines. A streamline is an imaginary line characterizing the flow such that, at every point along the line, the velocity vector is tangent to the line. Thus, in two-dimensional

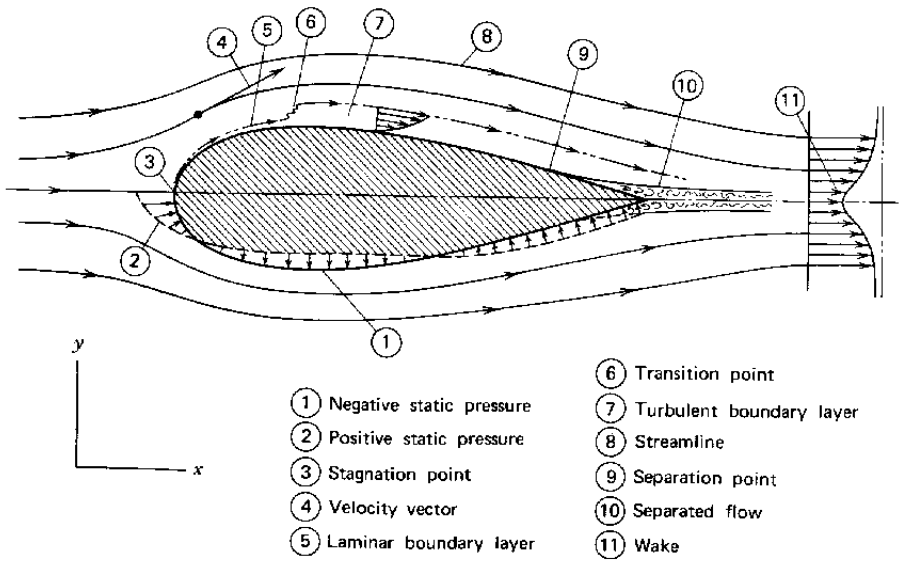

Figure 2.4 Two-dimensional flow around a streamlined shape.

flow, if $y(x)$ defines the position of a streamline, $y(x)$ is related to the x and y components of the velocity, $u(x)$ and $v(x)$, by

$$\frac{dy}{dx} = \frac{v(x)}{u(x)} \tag{2.11}$$

Note that the body surface itself is a streamline.

In three-dimensional flow a surface swept by streamlines is known as a stream surface. If such a surface is closed, it is known as a stream tube.

The mass flow accelerates around the body as the result of a continuous distribution of pressure exerted on the fluid by the body. An equal and opposite reaction must occur on the body. This static pressure distribution, acting everywhere normal to the body's surface, is pictured on the lower half of the body in Figure 2.4. The small arrows represent the local static pressure, p, relative to the static pressure, p_0, in the fluid far removed from the body. Near the nose p is greater than p_0; further aft the pressure becomes negative relative to p_0. If this static pressure distribution, acting normal to the surface, is known, forces on the body can be determined by integrating this pressure over its surface.

In addition to the local static pressure, shearing stresses resulting from the fluid's viscosity also give rise to body forces. As fluid passes over a solid surface, the fluid particles immediately in contact with the surface are brought to rest. Moving away from the surface, successive layers of fluid are slowed by the shearing stresses produced by the inner layers. (The term "layers" is used only as a convenience in describing the fluid behavior. The fluid shears in a continuous manner and not in discrete layers.) The result is a thin layer of slower moving fluid, known as the boundary layer, adjacent to the surface. Near the front of the body this layer is very thin, and the flow within it is smooth without any random or turbulent fluctuations. Here the fluid particles might be described as moving along in the layer on parallel planes, or laminae; hence the flow is referred to as laminar.

At some distance back from the nose of the body, disturbances to the flow (e.g., from surface roughnesses) are no longer damped out. These disturbances suddenly amplify, and the laminar boundary layer undergoes transition to a turbulent boundary layer. This layer is considerably thicker than the laminar one and is characterized by a mean velocity profile on which small, randomly fluctuating velocity components are superimposed. These flow regions are shown in Figure 2.4. The boundary layers are pictured considerably thicker than they actually are for purposes of illustration. For example, on the wing of an airplane flying at 100 m/s at low altitude, the turbulent boundary 1.0 m back from the leading edge would be only approximately 1.6 cm thick. If the layer were still laminar at this point, its thickness would be approximately 0.2 cm.

Returning to Figure 2.4, the turbulent boundary layer continues to thicken toward the rear of the body. Over this portion of the surface the fluid

is moving into a region of increasing static pressure that is tending to oppose the flow. The slower moving fluid in the boundary layer may be unable to overcome this adverse pressure gradient, so that at some point the flow actually separates from the body surface. Downstream of this separation point, reverse flow will be found along the surface with the static pressure nearly constant and equal to that at the point of separation.

At some distance downstream of the body the separated flow closes, and a wake is formed. Here, a velocity deficiency representing a momentum loss by the fluid is found near the center of the wake. This decrement of momentum (more precisely, momentum flux) is a direct measure of the body drag (i.e., the force on the body in the direction of the free-stream velocity).

The general flow pattern described thus far can vary, depending on the size and shape of the body, the magnitude of the free-stream velocity, and the properties of the fluid. Variations in these parameters can eliminate transition or separation or both.

One might reasonably assume that the forces on a body moving through a fluid depend in some way on the mass density of the fluid, ρ, the size of the body, l, and the body's velocity, V. If we assume that any one force, F, is proportional to the product of these parameters each raised to an unknown power, then

$$F \propto \rho^a V^b l^c$$

In order for the basic units of mass, length, and time to be consistent, it follows that

$$\frac{ML}{T^2} = \left(\frac{M}{L^3}\right)^a \left(\frac{L}{T}\right)^b L^c$$

Considering M, L, and T in order leads to three equations for the unknown exponents a, b, and c from which it is found that $a = 1$, $b = 2$, and $c = 2$. Hence,

$$F \propto \rho V^2 l^2 \tag{2.12}$$

For a particular force the constant of proportionality in Equation 2.12 is referred to as a coefficient and is modified by the name of the force, for example, the lift coefficient. Thus the lift and drag forces, L and D, can be expressed as

$$L = \tfrac{1}{2}\rho\, V^2 S\, C_L \tag{2.13a}$$

$$D = \tfrac{1}{2}\rho\, V^2 S\, C_D \tag{2.13b}$$

Note that the square of the characteristic length, l^2, has been replaced by a reference area, S. Also, a factor of 1/2 has been introduced. This can be done, since the lift and drag coefficients, C_L and C_D, are arbitrary at this point. The quantity $\rho V^2/2$ is referred to as the dynamic pressure, the significance of which will be made clear shortly.

For many applications, the coefficients C_L and C_D remain constant for a given geometric shape over a wide range of operating conditions or body size. For example, a two-dimensional airfoil at a 1° angle of attack will have a lift coefficient of approximately 0.1 for velocities from a few meters per second up to 100 m/s or more. In addition, C_L will be almost independent of the size of the airfoil. However, a more rigorous application of dimensional analysis [see Buckingham's π theorem (Ref. 2.1)] will result in the constant of proportionality in Equation 2.12 possibly being dependent on a number of dimensionless parameters. Two of the most important of these are known as the Reynolds number, R, and the Mach number, M, defined by,

$$R = \frac{Vl\rho}{\mu} \tag{2.14a}$$

$$M = \frac{V}{a} \tag{2.14b}$$

where l is a characteristic length, V is the free-stream velocity, μ is the coefficient of viscosity, and a is the velocity of sound. The velocity of sound is the speed at which a small pressure disturbance is propagated through the fluid; at this point, it requires no further explanation. The coefficient of viscosity, however, is not as well known and will be elaborated on by reference to Figure 2.5. Here, the velocity profile is pictured in the boundary layer of a laminar, viscous flow over a surface. The viscous shearing produces a shearing stress of τ_w on the wall. This force per unit area is related to the gradient of the velocity $u(y)$ at the wall by

$$\tau_w = \mu \left(\frac{du}{dy}\right)_{y=0} \tag{2.15}$$

Actually, Equation 2.15 is applicable to calculating the shear stresses between fluid elements and is not restricted simply to the wall. Generally, the viscous shearing stress in the fluid in any plane parallel to the flow and away

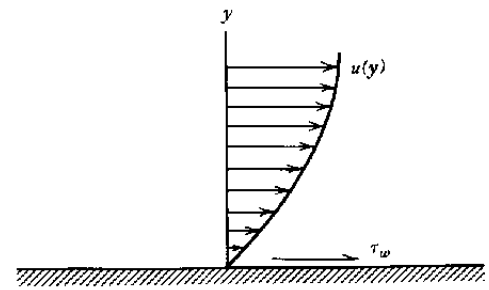

Figure 2.5 Viscous flow adjacent to a surface.

from the wall is given by the product of μ and the velocity gradient normal to the direction of flow.

The kinematic viscosity, ν, is defined as the ratio of μ to ρ.

$$\nu = \frac{\mu}{\rho}$$

ν is defined as a matter of convenience, since it is the ratio of μ to ρ that governs the Reynolds number. The kinematic viscosity for the standard atmosphere is included in Figure 2.3 as an *inverse fraction* of the standard sea level value.

A physical significance can be given to the Reynolds number by multiplying numerator and denominator by V and dividing by l.

$$R = \frac{\rho V^2}{(\mu V/l)}$$

In the following material (see Equation 2.28) the normal pressure will be shown to be proportional to ρV^2 whereas, from Equation 2.15, $\mu V/l$ is proportional to the shearing stress. Hence for a given flow the Reynolds number is proportional to the ratio of normal pressures (inertia forces) to viscous shearing stresses. Thus, relatively speaking, a flow is less viscous than another flow if its Reynolds number is higher than that of the second flow.

The Mach number determines to what extent fluid compressibility can be neglected (i.e., the variation of mass density with pressure). Current jet transports, for example, can cruise at Mach numbers up to approximately 0.8 before significant compressibility effects are encountered.

At lower Mach numbers, two flows are geometrically and dynamically similar if the Reynolds numbers are the same for both flows. Hence, for example, for a given shape, C_D for a body 10 m long at 100 m/s will be the same as C_D for a 100-m long body at 10 m/s. As another example, suppose transition occurs 2 m back from the leading edge of a flat plate aligned with a flow having a velocity of 50 m/s. Then, at 25 m/s transition would occur at a distance of 4 m from the leading edge. Obviously the effects of R and M on dimensionless aerodynamic coefficients must be considered when interpreting test results obtained with the use of small models.

For many cases of interest to aerodynamics the pressure field around a shape can be calculated assuming the air to be inviscid and incompressible. Small corrections can then be made to the resulting solutions to account for these "real fluid" effects. Corrections for viscosity or compressibility will be considered as needed in the following chapters.

Conservation of Mass

Fluid passing through an area at a velocity of V has a mass flow rate equal to ρAV. This is easily seen by reference to Figure 2.6. Here flow is

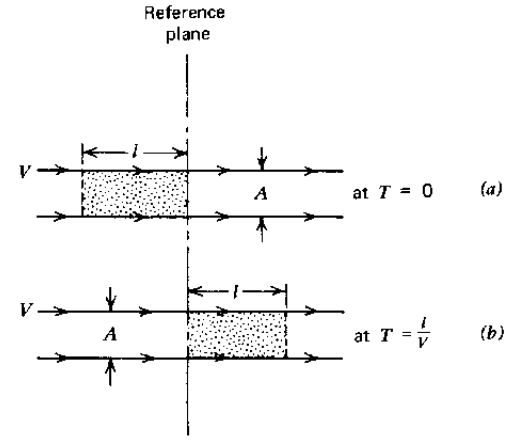

Figure 2.6 Mass flow through a surface.

pictured along a streamtube of cross-sectional area A. The fluid velocity is equal to V. At time $t = 0$, picture a small slug of fluid of length, l, about to cross a reference plane. At time l/V, this entire slug will have passed through the reference plane. The volume of the slug is Al, so that a mass of ρAl was transported across the reference plane during the time l/V. Hence the mass rate of flow, m, is given by

$$m = \frac{\rho Al}{(l/V)}$$
$$= \rho AV \tag{2.16}$$

Along a streamtube (which may be a conduit with solid walls) the quantity ρAV must be a constant if mass is not to accumulate in the system. For incompressible flow, ρ is a constant, so that the conservation of mass leads to the continuity principle

$$AV = \text{constant}$$

AV is the volume flow rate and is sometimes referred to as the flux. Similarly, ρAV is the mass flux. The mass flux through a surface multiplied by the velocity vector at the surface is defined as the momentum flux. Generally, if the velocity vector is not normal to the surface, the mass flux will be

$$\rho A\mathbf{V} \cdot \mathbf{n}$$

with the momentum flux written as

$$(\rho A\mathbf{V} \cdot \mathbf{n})\mathbf{V}$$

here $\mathbf{n}$ is the unit vector normal to the surface and in the direction in which the flux is defined to be positive. For example, if the surface encloses a volume and the net mass flux out of the volume is to be calculated, $\mathbf{n}$ would

be directed outward from the volume, and the following integral would be evaluated over the entire surface.

$$\int_S \int \rho \mathbf{V} \cdot \mathbf{n}\, dS$$

Consider the conservation of mass applied to a differential control surface. For simplicity, a two-dimensional flow will be treated. A rectangular contour is shown in Figure 2.7. The flow passing through this element has velocity components of u and v in the center of the element in the x and y directions, respectively. The corresponding components on the right face of the element are found by expanding them in a Taylor series in x and y and dropping second-order and higher terms in Δx. Hence the mass flux out through the right face will be

$$\left[\rho u + \frac{\partial(\rho u)}{\partial x}\frac{\Delta x}{2}\right]\Delta y$$

Writing similar expressions for the other three faces leads to the net mass flux out being

$$\left[\frac{\partial(\rho u)}{\partial x} + \frac{\partial(\rho v)}{\partial y}\right]\Delta x\, \Delta y$$

The net mass flux out of the differential element must equal the rate at which the mass of the fluid contained within the element is decreasing, given by

$$-\frac{\partial}{\partial t}(\rho\, \Delta x\, \Delta y)$$

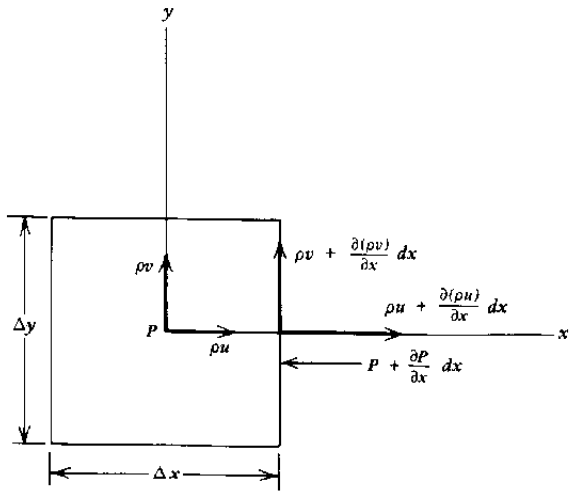

Figure 2.7 A rectangular differential control surface.

Since Δx and Δy are arbitrary, it follows that, in general,

$$\frac{\partial \rho}{\partial t} + \frac{\partial(\rho u)}{\partial x} + \frac{\partial(\rho v)}{\partial y} = 0$$

In three dimensions the preceding equation can be written in vector notation as

$$\frac{\partial \rho}{\partial t} + \nabla \cdot (\rho \mathbf{V}) = 0 \tag{2.17}$$

where ∇ is the vector operator, del, defined by

$$\nabla = \mathbf{i}\frac{\partial}{\partial x} + \mathbf{j}\frac{\partial}{\partial y} + \mathbf{k}\frac{\partial}{\partial z}$$

Any physically possible flow must satisfy Equation 2.17 at every point in the flow.

For an incompressible flow, the mass density is a constant, so Equation 2.17 reduces to

$$\nabla \cdot \mathbf{V} = 0 \tag{2.18}$$

The above is known as the divergence of the velocity vector, div **V**.

The Momentum Theorem

The momentum theorem in fluid mechanics is the counterpart of Newton's second law of motion in solid mechanics, which states that a force imposed on a system produces a rate of change in the momentum of the system. The theorem can be easily derived by treating the fluid as a collection of fluid particles and applying the second law. The details of the derivation can be found in several texts (e.g., Ref. 2.1) and will not be repeated here.

Defining a control surface as an imaginary closed surface through which a flow is passing, the momentum theorem states:

"The sum of external forces (or moments) acting on a control surface and internal forces (or moments) acting on the fluid within the control surface produces a change in the flux of momentum (or angular momentum) through the surface and an instantaneous rate of change of momentum (or angular momentum) of the fluid particles within the control surface."

Mathematically, for linear motion of an inviscid fluid, the theorem can be expressed in vector notation by

$$-\int_S \int p\mathbf{n}\, dS + \mathbf{B} = \int_S \int \rho \mathbf{V}(\mathbf{V} \cdot \mathbf{n})\, dS + \frac{\partial}{\partial t}\int\int_V \int \rho \mathbf{V}\, d\tau \tag{2.19}$$

In Equation 2.19, **n** is the unit normal directed outward from the surface,

S, enclosing the volume, V. $\mathbf{V}$ is the velocity vector, which generally depends on position and time. $\mathbf{B}$ represents the vector sum of all body forces within the control surface *acting on the fluid*. ρ is the mass density of the fluid defined as the mass per unit volume.

For the angular momentum,

$$\mathbf{Q} = \int_S \int \rho(\mathbf{V} \times \mathbf{r})(\mathbf{V} \cdot \mathbf{n})\, dS + \frac{\partial}{\partial t} \int_V \int \int \rho(\mathbf{V} \times \mathbf{r})\, d\tau \qquad (2.20)$$

Here, $\mathbf{Q}$ is the vector sum of all moments, both internal and external, acting on the control surface or the fluid within the surface. $\mathbf{r}$ is the radius vector to a fluid particle.

As an example of the use of the momentum theorem, consider the force on the burning building produced by the firehose mentioned at the beginning of this chapter. Figure 2.8 illustrates a possible flow pattern, admittedly simplified. Suppose the nozzle has a diameter of 10 cm and water is issuing from the nozzle with a velocity of 60 m/s. The mass density of water is approximately 1000 kg/m^3. The control surface is shown dotted. Equation 2.19 will now be written for this system in the x direction. Since the flow is steady, the partial derivative with respect to time of the volume integral given by the last term on the right side of the equation vanishes. Also, $\mathbf{B}$ is zero, since the control surface does not enclose any

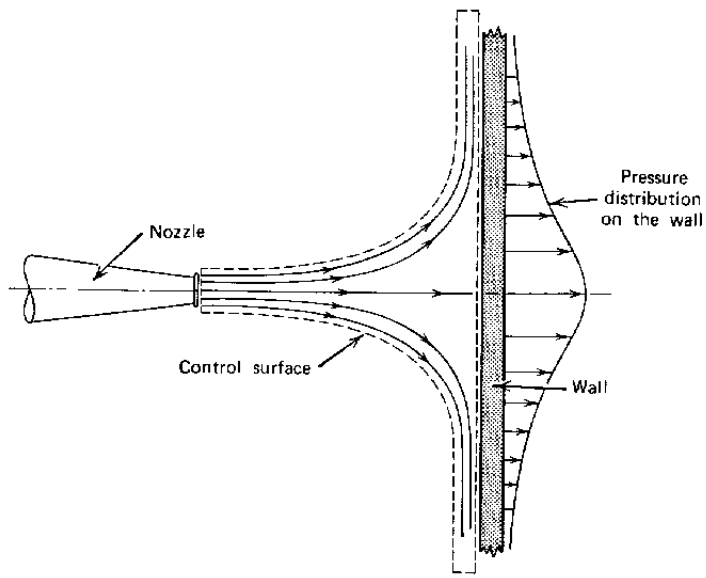

Figure 2.8 A jet of water impacting on a wall.

bodies. Thus Equation 2.19 becomes

$$-\int_S \int p\mathbf{n}\, dS = \int_S \int \rho\mathbf{V}(\mathbf{V} \cdot \mathbf{n})\, dS$$

Measuring p relative to the atmospheric static pressure, p is zero everywhere along the control surface except at the wall. Here $\mathbf{n}$ is directed to the right so that the surface integral on the left becomes the total force exerted on the fluid by the pressure on the wall. If F represents the magnitude of the total force on the wall,

$$-\mathbf{i}F = \int_S \int \rho\mathbf{V}(\mathbf{V} \cdot \mathbf{n})\, dS$$

For the fluid entering the control surface on the left,

$$\mathbf{V} = 60\mathbf{i}$$
$$\mathbf{n} = -\mathbf{i}$$

For the fluid leaving the control surface, the unit normal to this cylindrical surface has no component in the x direction. Hence,

$$-\mathbf{i}F = -\int_S \int (1000)60\mathbf{i}(-60)\, dS$$
$$= -36 \times 10^5 \mathbf{i} \int_S \int dS$$

The surface integral reduces to the nozzle area of 7.85×10^{-3} m^2. Thus, without actually determining the pressure distribution on the wall, the total force on the wall is found from the momentum theorem to equal 28.3 kN.

Euler's Equation of Motion

The principle of conservation of mass, applied to an elemental control surface, led to Equation 2.17, which must be satisfied everywhere in the flow. Similarly, the momentum theorem applied to the same element leads to another set of equations that must hold everywhere.

Referring again to Figure 2.7, if p is the static pressure at the center of the element then, on the center of the right face, the static pressure will be

$$p + \frac{\partial p}{\partial x} \frac{\Delta x}{2}$$

This pressure and a similar pressure on the left face produce a net force in the x direction equal to

$$-\frac{\partial p}{\partial x} \Delta x\, \Delta y$$

Since there are no body forces present and the fluid is assumed inviscid, the above force must equal the net momentum flux out plus the instantaneous change of fluid momentum contained within the element.

The momentum flux out of the right face in the x direction will be

$$\left[\rho u + \frac{\partial(\rho u)}{\partial x}\frac{\Delta x}{2}\right]\left(u + \frac{\partial u}{\partial x}\frac{\Delta x}{2}\right)\Delta y$$

Out of the upper face the corresponding momentum flux will be

$$\left[\rho v + \frac{\partial(\rho v)}{\partial y}\frac{\Delta y}{2}\right]\left(u + \frac{\partial u}{\partial y}\frac{\Delta y}{2}\right)\Delta x$$

Similar expressions can be written for the momentum flux in through the left and bottom faces.

The instantaneous change of the fluid momentum contained within the element in the x direction is simply

$$\frac{\partial}{\partial t}(\rho u\,\Delta x\,\Delta y)$$

Thus, equating the net forces in the x direction to the change in momentum and momentum flux and using Equation 2.17 leads to

$$\frac{\partial u}{\partial t} + u\frac{\partial u}{\partial x} + v\frac{\partial u}{\partial y} = -\frac{1}{\rho}\frac{\partial p}{\partial x} \tag{2.21}$$

Generalizing this to three dimensions results in a set of equations known as Euler's equations of motion.

$$\frac{\partial u}{\partial t} + u\frac{\partial u}{\partial x} + v\frac{\partial u}{\partial y} + w\frac{\partial u}{\partial z} = -\frac{1}{\rho}\frac{\partial p}{\partial x} \tag{2.22a}$$

$$\frac{\partial v}{\partial t} + u\frac{\partial v}{\partial x} + v\frac{\partial v}{\partial y} + w\frac{\partial v}{\partial z} = -\frac{1}{\rho}\frac{\partial p}{\partial y} \tag{2.22b}$$

$$\frac{\partial w}{\partial t} + u\frac{\partial w}{\partial x} + v\frac{\partial w}{\partial y} + w\frac{\partial w}{\partial z} = -\frac{1}{\rho}\frac{\partial p}{\partial z} \tag{2.22c}$$

Notice that if u is written as $u(x, y, z, t)$, the left side of Equation 2.22 is the total derivative of u. The operator, $\partial(\ )/\partial t$, is the local acceleration and exists only if the flow is unsteady.

In vector notation Euler's equation can be written

$$\frac{\partial \mathbf{V}}{\partial t} + (\mathbf{V}\cdot\nabla)\mathbf{V} = -\frac{1}{\rho}\nabla p \tag{2.23}$$

If the vector product of the operator ∇ is taken with each term in Equation 2.23, Equation 2.24 results.

$$\frac{\partial \boldsymbol{\omega}}{\partial t} + (\mathbf{V}\cdot\nabla)\boldsymbol{\omega} = 0 \tag{2.24}$$

$\boldsymbol{\omega}$ is the curl of the velocity vector, $\nabla \times \mathbf{V}$, and is known as the vorticity.

$$\nabla \times \mathbf{V} = \begin{vmatrix} \mathbf{i} & \mathbf{j} & \mathbf{k} \\ \dfrac{\partial}{\partial x} & \dfrac{\partial}{\partial y} & \dfrac{\partial}{\partial z} \\ u & v & w \end{vmatrix} \tag{2.25}$$

One can conclude from Equation 2.24 that, for an inviscid fluid, the vorticity is constant along a streamline. Since, far removed from a body, the flow is usually taken to be uniform, the vorticity at that location is zero; hence, it is zero everywhere.

Bernoulli's Equation

Bernoulli's equation is well known in fluid mechanics and relates the pressure to the velocity *along a streamline* in an inviscid, incompressible flow. It was first formulated by Euler in the middle 1700s. The derivation of this equation follows from Euler's equations using the fact that along a streamline the velocity vector is tangential to the streamline.

$$\frac{dx}{u} = \frac{dy}{v} = \frac{dx}{w} \tag{2.26}$$

First, multiply Equation 2.22a through by dx and then substitute Equation 2.26 for $v\,dx$ and $w\,dx$. Also, the first term of the equation will be set equal to zero; that is, at this time only steady flow will be considered.

$$u\frac{\partial u}{\partial x}dx + u\frac{\partial u}{\partial y}dy + u\frac{\partial u}{\partial z}dz = -\frac{1}{\rho}\frac{\partial p}{\partial x}dx$$

Similarly, multiply Equation 2.22b by dy, Equation 2.22c by dz, and substitute Equation 2.26 for $u\,dy$, $w\,dy$ and $u\,dz$, $v\,dz$, respectively. Adding the three equations results in perfect differentials for p and V^2, V being the magnitude of the resultant velocity along the streamline. This last term results from the fact that

$$u\frac{\partial u}{\partial x} = \frac{1}{2}\frac{\partial u^2}{\partial x}$$

and

$$V^2 = u^2 + v^2 + w^2$$

Thus, along a streamline, Euler's equations become

$$V\,dV + \frac{dp}{\rho} = 0 \tag{2.27}$$

If ρ is not a function of p (i.e., the flow is incompressible), Equation 2.27 can be integrated immediately to give

$$p + \tfrac{1}{2}\rho V^2 = \text{constant} \tag{2.28}$$

If the flow is uniform at infinity, Equation 2.28 becomes

$$p + \tfrac{1}{2}\rho V^2 = \text{constant} = p_\infty + \tfrac{1}{2}\rho V_\infty^2 \tag{2.29}$$

Here V is the magnitude of the local velocity and p is the local static pressure. V_∞ and p_∞ are the corresponding free-stream values. Equation 2.29 is known as Bernoulli's equation.

The counterpart to Equation 2.29 for compressible flow is obtained by assuming pressure and density changes to follow an isentropic process. For such a process,

$$p/\rho^\gamma = \text{constant} \tag{2.30}$$

γ is the ratio of the specific heat at constant pressure to the specific heat at constant volume and is equal approximately to 1.4 for air. Substituting Equation 2.30 into Equation 2.27 and integrating leads to an equation sometimes referred to as the compressible Bernoulli's equation.

$$\frac{V^2}{2} + \frac{\gamma}{\gamma - 1}\frac{p}{\rho} = \text{constant} \tag{2.31}$$

This equation can be written in terms of the acoustic velocity. First it is necessary to derive the acoustic velocity, which can be done by the use of the momentum theorem and continuity. Figure 2.9 assumes the possibility of a stationary disturbance in a steady flow across which the pressure, density, and velocity change by small increments. In the absence of body forces and viscosity, the momentum theorem gives

$$-dp = (\rho + d\rho)(u + du)^2 - \rho u^2$$

But, from continuity,

$$(\rho + d\rho)(u + du) = \rho u$$

or

$$u\,d\rho = -\rho u$$

Thus

$$u^2 = \frac{dp}{d\rho} \tag{2.32}$$

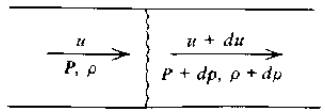

Figure 2.9 A stationary small disturbance in a steady compressible flow.

If the small disturbance is stationary in the steady flow having a velocity of u, then obviously u is the velocity of the disturbance relative to the fluid. By definition, it follows that u, given by Equation 2.32, is the acoustic velocity.

By the use of Equation 2.30, the acoustic velocity is obtained as

$$a = \left(\frac{\gamma p}{\rho}\right)^{1/2} \tag{2.33}$$

An alternate form, using the equation of state (Equation 2.1), is

$$a = (\gamma RT)^{1/2} \tag{2.34}$$

Thus Equation 2.31 can be written

$$\frac{V^2}{2} + \frac{a^2}{\gamma - 1} = \text{constant} \tag{2.35}$$

The acoustic velocity is also included in Figure 2.3 for the standard atmosphere.

Determination of Free-Stream Velocity

At low speeds (compared to the acoustic velocity) a gas flow is essentially incompressible. In this case, and for that of a liquid, Equation 2.29 applies. If the fluid is brought to rest so that the local velocity is zero then, from Equation 2.29, the local pressure, referred to in this case as the stagnation or total pressure, is equal to the sum of the free-stream static pressure, p_∞, and $\rho V_\infty^2/2$. This latter term is called the dynamic pressure and is frequently denoted by the symbol q. Thus,

$$V_\infty = \left[\frac{2(p_0 - p_\infty)}{\rho}\right]^{1/2} \tag{2.36}$$

where p_0 is the total pressure, also referred to as the stagnation or reservoir pressure. The pitot-static tube shown in Figure 2.2 measures $(p_0 - p_\infty)$ and is probably the most common means used to determine airspeed. However, notice that Equation 2.36 contains the mass density that must be determined before the airspeed can be calculated. This is most readily achieved by measuring, in addition to the difference between the stagnation pressure and the static pressure, the static pressure itself and the temperature. The density is then determined from the equation of state (Equation 2.1).

At higher speeds (and we will now examine what is high) Equation 2.29 no longer holds, so that V_∞ must be determined from Equation 2.31.

$$\frac{V^2}{2} + \frac{\gamma}{\gamma - 1}\frac{p}{\rho} = \frac{\gamma}{\gamma - 1}\frac{p_0}{\rho_0}$$

At this point the subscript ∞ has been dropped, so that p, ρ, and V without a subscript may be local or free-stream values.

Remembering that $\gamma p/\rho$ is the square of the acoustic velocity, the preceding equation becomes

$$\frac{M^2}{2}+\frac{1}{\gamma-1}=\frac{1}{\gamma-1}\frac{p_0}{p}\frac{\rho}{\rho_0}$$

Using Equation 2.3, this can be written as

$$\frac{p_0}{p}=\left[1+\frac{\gamma-1}{2}M^2\right]^{\gamma/(\gamma-1)} \tag{2.37}$$

The dynamic pressure, q, is defined as

$$q=\tfrac{1}{2}\rho V^2 \tag{2.38}$$

which can be written in terms of the Mach number as

$$q=\tfrac{1}{2}\gamma p M^2$$

Combining this with Equation 2.37 gives

$$\frac{p_0-p}{q}=\frac{2}{\gamma M^2}\left[\left(1+\frac{\gamma-1}{2}M^2\right)^{\gamma/(\gamma-1)}-1\right] \tag{2.39}$$

The square root of Equation 2.39 is presented graphically in Figure 2.10. The departure of this function from unity is a measure of the error to be incurred in calculating the airspeed from the incompressible Bernoulli equation. Below a Mach number of 0.5 the error is seen to be less than 3%.

Determination of True Airspeed

During training, a pilot soon learns that the airspeed that appears on the airspeed indicator is not the true airspeed. Instead, in order to determine the true airspeed, the pilot must also read the altimeter and outside air temperature. The pilot then resorts to a small hand calculator or, in some instances, adjusts the dial on the airspeed indicator accordingly to allow for the atmospheric properties.

The airspeed indicator is nothing more than an accurate differential pressure gage calibrated according to Equation 2.31. This equation can be put in the form

$$V^2=\frac{2a^2}{\gamma-1}\left[\left(\frac{p_0-p}{p}+1\right)^{(\gamma-1)/\gamma}-1\right]$$

The airspeed indicator measures the difference, p_0-p (sometimes called the compressible dynamic pressure), but then is calibrated to obtain V by assuming standard sea level values for the acoustic velocity and the free-

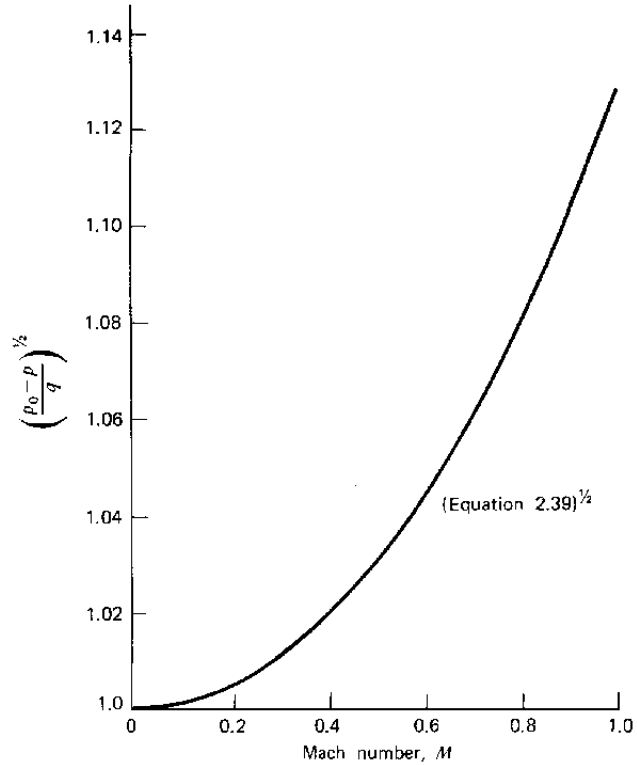

Figure 2.10 Relationship between reservoir pressure and dynamic pressure as a function of Mach number.

stream static pressure. Thus the calibrated airspeed is defined by

$$v_{cal}=\left[\frac{2a_{SL}^2}{(\gamma-1)}\left[\left(\frac{p_0-p}{p_{SL}}+1\right)^{(\gamma-1)/\gamma}-1\right]\right]^{1/2} \tag{2.40}$$

where a subscript SL is used to denote standard sea level values.

As a ratio to V_{cal}, the true airspeed can be written

$$\frac{V}{V_{cal}}=\left\{\theta\left[\frac{[f(V_{cal})/\delta+1]^{(\gamma-1)/\gamma}-1}{[f(V_{cal})+1]^{(\gamma-1)/\gamma}-1}\right]\right\}^{1/2} \tag{2.41}$$

where

$$\frac{p_0-p}{P_{SL}}=f(V_{cal})$$

and can be obtained from Equation 2.40. θ and δ are the temperature and pressure ratios, respectively.

If compressibility can be neglected, the airspeed will be given by Equa-

tion 2.36. In this case, using the standard sea level value of ρ to calibrate the airspeed indicator dial leads to the equivalent airspeed.

$$V_e = \left[\frac{2(p_0 - p)}{\rho_{SL}}\right]^{1/2}$$

or

$$\frac{V}{V_e} = \sigma^{-1/2} \tag{2.42}$$

where σ is the density ratio.

Finally, the indicated airspeed, V_i, is defined simply as the airspeed that the pilot reads from the airspeed indicator. If the indicator has no mechanical error (*instrument error*) and if the static source is located so that it samples the true free-stream static pressure (otherwise a *position* error incurs), $V_i = V_{cal}$. Furthermore, if the Mach number is not too high, $V_i = V_{cal} = V_e$.

As an example in determining true airspeed, suppose a pilot reads an indicated airspeed of 180 m/s for an OAT of 239 °K and an altimeter reading of 6000 m. This altitude, according to Equations 2.8 and 2.10, corresponds to a pressure ratio δ of 0.466. The measured temperature ratio, θ, is equal to 0.826. Hence $\sigma = 0.564$. According to Equation 3.42, the true airspeed will be 239.7 m/s. From Equation 2.41, the true airspeed is calculated to be 231.6 m/s. Thus, using the incompressible relationship to estimate the true airspeed from the indicated airspeed results in a speed a few percent higher than that obtained from the calibrated airspeed relationship.

To be precise one calculates the true airspeed from the calibrated airspeed and then determines the equivalent airspeed from its definition, Equation 2.42. In the previous example, this results in a V_e of 173.9 m/s, a value 3.4% less than the calibrated airspeed.

POTENTIAL FLOW

For a steady, inviscid, incompressible flow, Euler's equations of fluid motion reduce to two relatively simple relationships that govern the velocity vector.

$$\text{div } \mathbf{V} = \nabla \cdot \mathbf{V} = 0 \tag{2.43a}$$

$$\text{curl } \mathbf{V} = \nabla \times \mathbf{V} = 0 \tag{2.43b}$$

The first equation satisfies conservation of mass; the second one assures that the dynamics of the flow is treated correctly.

In addition to satisfying Equation 2.43 one must assure that any mathematical description of the flow field around a given body shape satisfies the boundary condition that there be no velocity normal to the body at all points

on its surface. If $\mathbf{n}$ is the unit vector normal to the surface, the following must hold.

$$\mathbf{V} \cdot \mathbf{n} = 0 \tag{2.44}$$

Velocity Potential and Stream Function

To assist in the solution of Equation 2.43, two functions are introduced. The first of these is known as the velocity potential, ϕ, and is defined such that

$$u = \frac{\partial \phi}{\partial x}$$

$$v = \frac{\partial \phi}{\partial y}$$

$$w = \frac{\partial \phi}{\partial z}$$

or, generally,

$$\mathbf{V} = \nabla \phi \tag{2.45}$$

Equation 2.43 satisfies identically Equation 2.43*b*. However, in order to satisfy Equation 2.43*a*, it follows that ϕ must be a harmonic function; that is,

$$\nabla^2 \phi = 0 \tag{2.46}$$

The operator, ∇^2, known as the Laplacian, is defined as

$$\nabla^2 = \frac{\partial^2}{\partial x^2} + \frac{\partial^2}{\partial y^2} + \frac{\partial^2}{\partial z^2}$$

A flow for which Equation 2.43 is satisfied, and hence ϕ can be defined, is known as a potential flow. The resulting fluid motion is described as being irrotational. This follows since, in the limit at a point, the curl of the velocity vector, which is zero, is equal to twice the rotational or angular velocity.

The stream function, ψ, is related to the velocity components by

$$u = \frac{\partial \psi}{\partial y}$$

$$v = -\frac{\partial \psi}{\partial x} \tag{2.47}$$

ψ can only be defined for two-dimensional, or axisymmetric, flow. To obtain a particular component, the partial derivative of ψ is taken in the direction normal to the velocity and to the left as one looks in the direction of the velocity.

A line element is pictured in Figure 2.11 with flow passing through it. This element is a segment of an arbitrary line connecting two points A and B. The

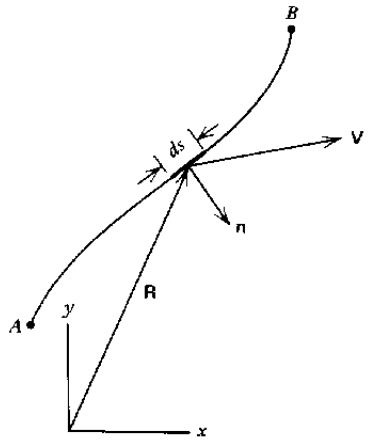

Figure 2.11 Two-dimensional flow through a line element.

differential flux through this element will be

$$dQ = \mathbf{V} \cdot \mathbf{n}\, ds$$

But

$$\mathbf{n} = (\mathbf{i}\, dy - \mathbf{j}\, dx)/ds$$
$$\mathbf{V} = \mathbf{i}\, u + \mathbf{j}\, v$$

Substituting $\mathbf{n}$ and $\mathbf{V}$ into dQ and using Equation 2.47 results in

$$dQ = \frac{\partial \psi}{\partial x}\, dx + \frac{\partial \psi}{\partial y}\, dy$$

or

$$dQ = d\psi$$

Thus

$$\psi(B) = \psi(A) = \int_A^B \mathbf{V} \cdot \mathbf{n}\, ds \tag{2.48}$$

That is, the change in the stream function between two points is equal to the flux between the points. It follows that ψ is a constant along a streamline. This can be shown by noting that along a streamline

$$\frac{v}{u} = \frac{dy}{dx}$$

and

$$d\psi = dQ = u\, dy - v\, dx$$

Combined, the two relationships give

$$d\psi = 0$$

or

$$\psi = \text{constant (along a streamline)}$$

The stream function, as a measure of the flux, satisfies identically Equation 2.43*a*. For an irrotational flow, however, in order to meet Equation 2.43*b* it follows that ψ must also be harmonic.

$$\nabla^2 \psi = 0 \tag{2.49}$$

In a manner similar to the derivation of Equation 2.48, the change in ϕ between two points can also be easily obtained. If

$$\phi = \phi(x, y)$$

then

$$d\phi = \frac{\partial \phi}{\partial x}\, dx + \frac{\partial \phi}{\partial y}\, dy$$
$$= u\, dx + v\, dy$$

or, using vector notation,

$$\phi(B) - \phi(A) = \int_A^B \mathbf{V} \cdot \mathbf{dR} \tag{2.50}$$

where $\mathbf{R}$ is the radius vector to the curve along which the integration is being performed, as shown in Figure 2.11. $\mathbf{dR}$ is then the differential vector along the curve, directed positively, with a magnitude of ds.

As an example in the use of ϕ and ψ, consider the uniform flow pictured in Figure 2.12. For this flow,

$$u = U = \text{constant}$$
$$v = 0$$

ψ will be taken to be zero along the x-axis. This choice is arbitrary, since the values of both ϕ and ψ can be changed by a constant amount without affecting the velocity field obtained from their derivatives. Equation 2.48 will be zero if the integral is performed along a line for which y is a constant.

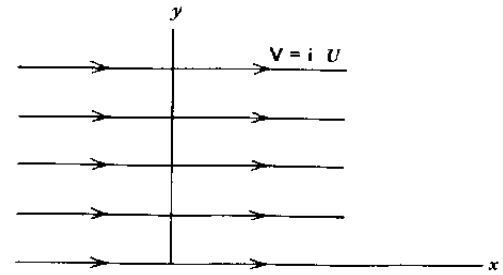

Figure 2.12 Uniform flow in the x direction.

Thus ψ changes only in the y direction. Integrating Equation 2.48 in this direction gives

$$\psi(y) - \psi(0) = \int_0^y (\mathbf{i}\, U) \cdot \mathbf{i}\, dy$$

or

$$\psi = Uy$$

If the uniform flow contains, in addition to U, a constant velocity component V in the y direction, ψ becomes

$$\psi = Uy - Vx \tag{2.51}$$

The minus sign in Equation 2.51 is in accordance with the positive direction of $\mathbf{n}$, as shown in figure 2.11. $\mathbf{n}$ is directed to the right as one looks in the direction of point B from point A. In this case the integration for the second term is in the positive x direction, so $\mathbf{n}$ equals $-\mathbf{j}$.

In a more formal manner, ϕ will be derived for this same flow using Equation 2.50.

$$\mathbf{V} = \mathbf{i}\, U + \mathbf{j}\, V$$

$$\mathbf{R} = \mathbf{i}\, x + \mathbf{j}\, y$$

Hence

$$d\mathbf{R} = \mathbf{i}\, dx + \mathbf{j}\, dy$$

so that, taking $\phi = 0$ at $x, y = 0$,

$$\phi(x, y) = \int_0^{x,y} U\, dx + V\, dy$$

$$= Ux + Vy \tag{2.52}$$

Elementary Flow Functions

If ϕ_1 and ϕ_2 are functions satisfying Equation 2.50 then, because this equation is linear, their sum will also satisfy Equation 2.50. In general, both the velocity potential and stream function can be constructed by summing less complicated functions.

$$\phi(x, y) = \sum_{i=1}^{n} \phi_i(x, y) \tag{2.53a}$$

$$\psi(x, y) = \sum_{i=1}^{n} \psi_i(x, y) \tag{2.53b}$$

Equation 2.53 represents the real benefit to be gained in describing a flow in terms of ϕ and ψ. This statement will become obvious as the developments proceed.

The simple flows from which more complicated patterns can be developed are referred to as elementary flow functions. There are three of them: uniform rectilinear flow, vortex, and source. The first of these has already been covered with ϕ and ψ given by Equations 2.52 and 2.51, respectively.

Vortex

A vortex is pictured in Figure 2.13. This flow in two dimensions is purely circular around a point with no radial velocity component. Denoting the tangential velocity component by v_θ, the problem is to find v_θ as a function of r that will satisfy the set of Equations 2.42a and 2.42b. v_θ is to be independent of θ.

In polar coordinates,

$$\nabla \times \mathbf{V} = \frac{\partial v_\theta}{\partial r} + \frac{v_\theta}{r} - \frac{1}{r}\frac{\partial v_r}{\partial \theta} \tag{2.54a}$$

$$\nabla \cdot \mathbf{V} = \frac{1}{r}\frac{\partial v_\theta}{\partial \theta} + \frac{\partial v_r}{\partial r} + \frac{v_r}{r} \tag{2.54b}$$

where r and θ are the polar coordinates, with v_r being the radial component of velocity and v_θ the tangential component.

Since v_r is zero in Figure 2.13 and v_θ is independent of θ, Equation 2.54b is satisfied identically and, from Equation 2.54a

$$\frac{dv_\theta}{dr} + \frac{v_\theta}{r} = 0$$

or, after integrating,

$$rv_\theta = \text{constant}$$

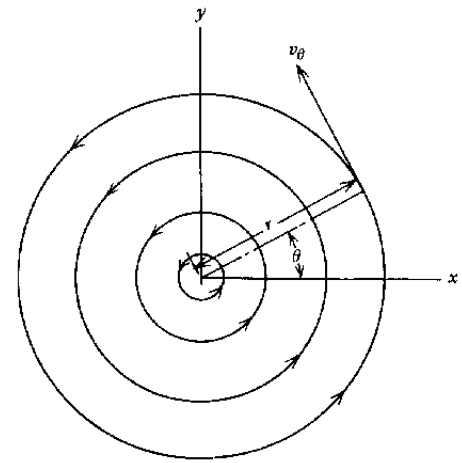

Figure 2.13 Flow field around a vortex.

Thus, for potential flow, the tangential velocity around a vortex must vary inversely with the radial distance from the center of the vortex.

The strength of a vortex, denoted by γ, is measured by integrating the tangential velocity completely around the vortex. The value of this integral is independent of the path providing it encloses the singular point at the center of the vortex.

$$\gamma = \oint \mathbf{V} \cdot d\mathbf{R} \tag{2.55}$$

This closed-line integral of the velocity is known as the *circulation*. Evaluating Equation 2.55 on a constant radius leads to the relationship between the tangential velocity around a vortex, the radius, and the vortex strength.

$$v_\theta = \frac{\gamma}{2\pi r} \tag{2.56}$$

Equation 2.55 is a well-known relationship and can be easily remembered from the definition of γ.

ϕ and ψ for a vortex follow immediately from Equations 2.50, 2.48, and 2.56.

$$\phi(B) - \phi(A) = \int_A^B \frac{\gamma}{2\pi r}(r\, d\theta)$$

$$= \frac{\gamma}{2\pi}[\theta(B) - \theta(A)]$$

If θ is measured relative to zero and $\theta(B)$ is taken to be any value of θ,

$$\phi = \frac{\gamma\theta}{2\pi} \tag{2.57}$$

The stream function for a vortex is found from

$$\psi(B) - \psi(A) = -\int_A^B \frac{\gamma}{2\pi r}\, dr$$

$$= -\frac{\gamma}{2\pi} \ln \frac{r(B)}{r(A)}$$

Letting $\psi(A)$ be zero and $r(A)$ be an arbitrary radius, a, leads to

$$\psi = -\frac{\gamma}{2\rho} \ln \frac{r}{a} \tag{2.58}$$

The minus sign results from the choice of positive coordinate directions.

Source

The source is the counterpart of a vortex. Here the flow, pictured in Figure 2.14, is again symmetrical about the center, but it is entirely radial with no tangential velocity component.

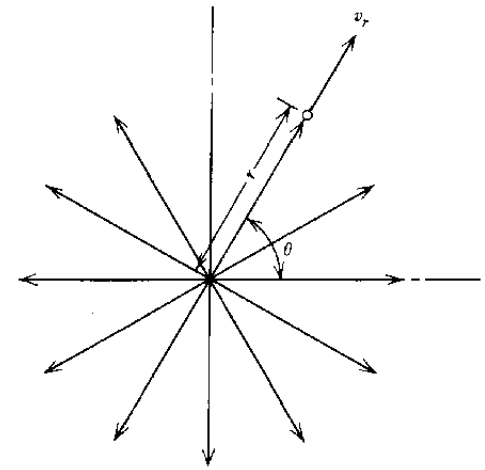

Figure 2.14 Flow from a source.

The strength of a source, q, is measured by the total flux emanating from the center. From Figure 2.14, q is obviously given by

$$q = 2\pi r v_r$$

or

$$v_r = \frac{q}{2\pi r} \tag{2.59}$$

In a manner similar to that followed for the vortex, one may verify that for the source

$$\phi = \frac{q}{2\pi} \ln r \tag{2.60}$$

$$\psi = \frac{q\theta}{2\pi} \tag{2.61}$$

Equations 2.56 and 2.59, which define the velocities around vortices and sources, can be extended to three dimensions. If Q is the strength of a three-dimensional source, this flux will equal the product of the radial velocity and the surface area through which the velocity is passing. Thus, one can write v_r immediately as

$$v_r = \frac{Q}{4\pi r^2} \tag{2.62}$$

Biot–Savart Law

The three-dimensional velocity field associated with a vortex line is considerably more complicated and is given by the Biot–Savart law. The derivation of this law is beyond the scope of this text. Figure 2.15*a* illustrates

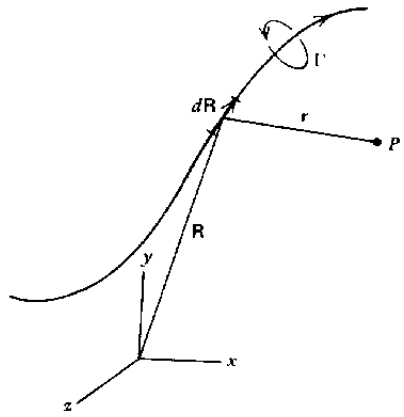

Figure 2.15a Definition of quantities used in the Biot–Savart law.

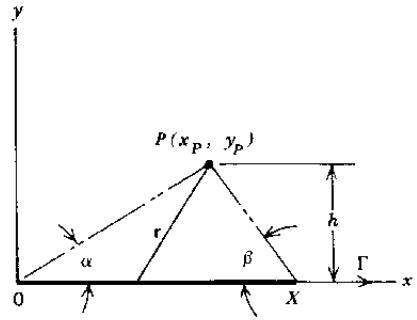

Figure 2.15b The Biot–Savart law for a straight-line vortex.

a portion of a vortex line about which at any point the circulation, Γ, is constant. If $\mathbf{v}_i$ is the velocity vector induced at any point, P, in the field by the vortex line, the Biot–Savart law states

$$d\mathbf{v}_i = \frac{\Gamma}{4\pi}\frac{\mathbf{r}\times d\mathbf{R}}{|\mathbf{r}|^3} \tag{2.63}$$

This is the most general form of the Biot–Savart law. $\mathbf{dR}$ is the derivative of the radius vector from the origin to the vortex line and is thus the directed differential distance along the line. $\mathbf{r}$ is the radius vector from the point P to the line element $\mathbf{dR}$. The positive direction of the circulatory strength, Γ, is defined according to the right-hand rule. The x, y, z orthogonal coordinate system is also right-handed.

A special form of the Biot–Savart law for a straight-line vortex segment found in many texts can be obtained by integrating Equation 2.63. Referring

to Figure 2.15*b*, for convenience the line vortex is placed on the x-axis and lies between 0 and x. The z-axis will project out of the paper according to the right-hand rule. The circulation Γ is taken to be positive in the x direction which means it will be clockwise when viewed in that direction. For this figure,

$$\mathbf{R} = \mathbf{i}\,x$$

$$\mathbf{OP} + \mathbf{r} = \mathbf{R}$$

$$\mathbf{OP} = \mathbf{i}\,x_p + \mathbf{j}\,y_p$$

Thus

$$\mathbf{r} = \mathbf{i}(x - x_P) - \mathbf{j}\,y_P$$

$$d\mathbf{R} = \mathbf{i}\,dx$$

so that

$$\mathbf{r}\times d\mathbf{R} = \begin{vmatrix} \mathbf{i} & \mathbf{j} & \mathbf{k} \\ (x-x_P) & -y_P & 0 \\ dx & 0 & 0 \end{vmatrix}$$

$$= \mathbf{k}\,y_P\,dx$$

$$|\mathbf{r}| = [(x - x_P)^2 + y_P^2]^{1/2}$$

Equation 2.63 then becomes

$$\mathbf{v}_i = \frac{k\Gamma y_P}{4\pi}\int_0^X \frac{dx}{[(x-x_P)^2 + y_P^2]^{3/2}}$$

This reduces to

$$\mathbf{v}_i = \mathbf{k}\frac{\Gamma}{4\pi h}(\cos\alpha + \cos\beta) \tag{2.64}$$

α, β, and h are defined in Figure 2.15*b*. Notice that the velocity has only a z component. As the line becomes infinite in length, the angles α and β approach zero, and Equation 2.64 reduces to the expression for the velocity around a two-dimensional point vortex given by Equation 2.56.

The Calculation of Flows for Well-Defined Body Shapes

The flow functions described thus far are basic functions. By combining these functions a multitude of more complicated flows can be described. When combining these functions, the velocities will add vectorially. This is obvious from Equation 2.53*a*, since

$$\text{grad}\,\phi = \text{grad}\,\phi_1 + \text{grad}\,\phi_2 + \cdots$$

or

$$\mathbf{V} = \mathbf{V}_1 + \mathbf{V}_2 + \cdots$$

As an example of the use of these functions, consider the classic

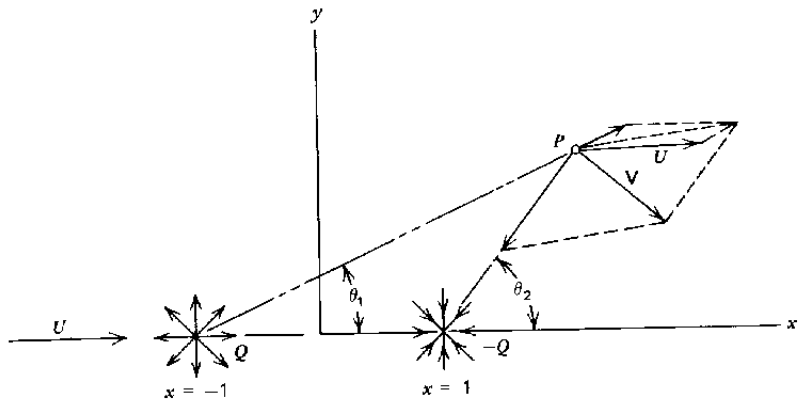

Figure 2.16 Source-sink combination in a uniform flow.

two-dimensional case illustrated in Figure 2.16. Here a source and a sink (a negative source) of equal strength are placed a unit distance from either side of the origin in a uniform flow. Three velocities from the source, sink, and uniform flow are shown added vectorially at P giving the resultant velocity, $\mathbf{V}$.

It is easily verified that the entire resulting flow is symmetrical about both the x- and y-axes. To the left of the source along the x-axis a distance of x_0 from the origin a stagnation point exists where the resultant velocity is zero. The location of this point can be found from Equation 2.59 for the velocity from a source (or sink).

$$0 = U - \frac{q}{2\pi(x_0 - 1)} + \frac{q}{2\pi(x_0 + 1)}$$

or

$$x_0^2 = 1 + \frac{q}{\pi U} \tag{2.65}$$

It will be seen that this point lies on a dividing streamline that is closed and that separates the flow leaving the source and entering the sink from the uniform flow. The resultant streamline pattern can be constructed by calculating the velocity at many points in the field and fairing streamlines tangent to these vectors. However, a more direct way is to form the stream function and then solve for $y(x)$ for constant values of ψ. Adding the ψ functions for the uniform flow, source, and sink, one obtains

$$\psi = \frac{q}{2\pi}(\theta_1 - \theta_2) + Uy \tag{2.66}$$

where θ_1 and θ_2 are shown in Figure 2.16. Because of the multivaluedness of the tangent function, one must be careful in evaluating this expression.

At the stagnation point, $\theta_1 = \theta_2$ and $y = 0$, so that $\psi = 0$. Since this point lies on the dividing streamline, a value of $\psi = 0$ will define this streamline. Hence

$$\theta_2 - \theta_1 = \frac{2\pi U y}{q} \tag{2.67}$$

Since the flow is symmetrical, we only need to calculate the streamline shapes in one quadrant, say the one for which x and y are both positive. In this quadrant,

$$\theta_1 = \tan^{-1}\frac{y}{1+x}$$

$$\theta_2 = \pi - \tan^{-1}\frac{y}{1-x}$$

Hence x and y along the dividing streamline are related by

$$\tan^{-1}\frac{2y}{1 - x^2 - y^2} = \pi\left(1 - 2\frac{U}{q}y\right) \tag{2.68}$$

This can be solved explicitly for x.

$$x^2 = 1 - y^2 - \frac{2y}{\tan\{\pi[1 - (2Uy/q)]\}} \tag{2.69}$$

Notice that as y approaches zero in Equation 2.68, x approaches the value given by Equation 2.65.

Since any streamline can be replaced by a solid boundary, the dividing streamline represents a closed body. If it is assumed that the body's fineness ratio (i.e., thickness to length) is small, then at its maximum thickness point ($x = 0$), Equation 2.68 can be written approximately as

$$2y_0 = \pi\left(1 - 2\frac{U}{q}y_0\right)$$

or

$$y_0 = \frac{\pi}{2[1 + (\pi U/q)]} \tag{2.70}$$

y_0 is the semithickness of the body corresponding to x_0, the semilength. Hence the fineness ratio of the body, t/l, is related to q/U by

$$\frac{t}{l} = \frac{q/U}{2[1 + (q/\pi U)]^{3/2}} \tag{2.71}$$

This classical body shape is referred to as the Rankine oval. The streamline pattern can be determined as a function of the streamline position far from the body. If y_∞ is the location of a particular streamline away from the body

then, for this particular streamline,

$$\psi = y_\infty U$$

Equating this to Equation 2.66, one obtains a relationship between x and y along the streamline as a function of y_∞ and q/U that can be solved explicitly for x.

$$x = \left\{1 - y^2 - \frac{2y}{\tan \pi[1 - 2(U/q)(y - y_\infty)]}\right\}^{1/2} \tag{2.72}$$

This relation was used to calculate the streamline patterns of Figure 2.17. Only the flow external to the dividing streamline is shown.

For comparison, this figure presents the streamline patterns (in one quadrant only) for 20% and 50% thick ovals. For each thickness, q/U was chosen on the basis of Equation 2.69. Because this equation assumes t/l to be small, the thickness ratio of the one shape is slightly greater than 50%.

Having defined the shape of a body and the velocity field around it, the next obvious point of interest is the pressure distribution over the body's surface. In order to remove the dependence of the predicted pressure distribution on the free-stream pressure and velocity, the pressure distribution is normally presented in coefficient form, C_p, where C_p is defined according to

$$C_p = \frac{p - p_0}{(1/2)\rho V_0^2} \tag{2.73}$$

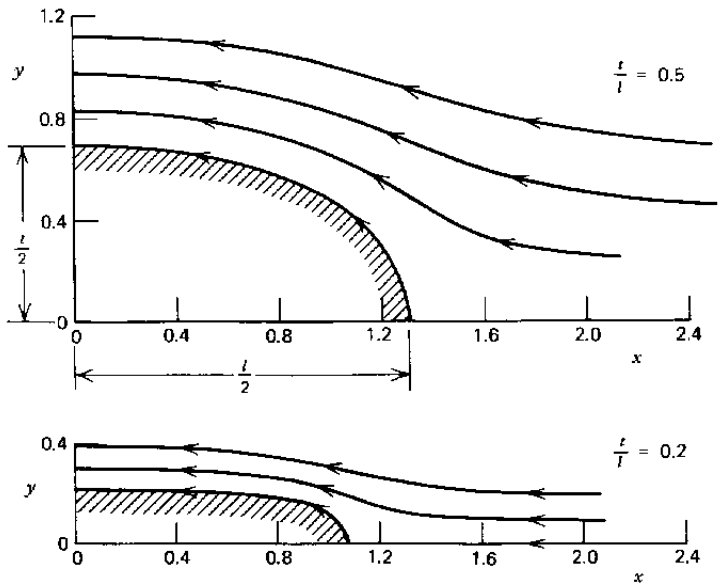

Figure 2.17 Calculated streamlines for 20 and 50% thick Rankine ovals.

From Equation 2.29, C_p is found from the ratio of local velocity to free-stream velocity.

$$C_p = 1 - \left(\frac{V}{V_0}\right)^2 \tag{2.74}$$

Returning now to the Rankine oval, note first that $C_p = 1$ at the stagnation point where V is zero. Moving away from the nose along the $\psi = 0$ streamline, the velocity increases to a maximum at some location. Depending on the fineness ratio, this point of maximum velocity may or may not be at the maximum thickness of the body; that is, $x = 0$.

Although one could work with ψ, knowing the source (and sink) strength the easiest approach is to calculate the u and v components directly by adding the components attributed to each elementary flow function. In this case it will be found that

$$\frac{u}{U_0} = 1 + \frac{q}{2\pi U_0}\left[\frac{x+1}{(x+1)^2 + y^2} - \frac{x-1}{(x-1)^2 + y^2}\right]$$

$$\frac{v}{U_0} = \frac{q}{2\pi U_0}\left[\frac{y}{(x+1)^2 + y^2} - \frac{y}{(x-1)^2 + y^2}\right]$$

The pressure coefficient is then calculated from

$$C_p = 1 - \left[\left(\frac{u}{U_0}\right)^2 + \left(\frac{v}{U_0}\right)^2\right] \tag{2.75}$$

The pressure distribution along the surfaces of 20 and 50% thick Rankine ovals have been calculated using the preceding equations, and the results are presented in Figure 2.18. It is not too surprising to find that, for the 20% oval, the minimum pressure occurs near the nose, where the curvature is the greatest. For the 50% thick oval the minimum pressure occurs approximately halfway from the center of the body to the nose, but it is nearly flat over the middle 70% of the body's length.

The Circular Cylinder

The flow field around a circular cylinder and resulting pressure distribution can be determined as a limiting case of the Rankine oval. In Figure 2.16 the source and sink were placed at $x = -1.0$ and $x = 1.0$, respectively. We will now move them instead toward the origin, but increase their strengths in inverse proportion to the distance between them. In the limit as the distance between the source and sink goes to zero, a so-called source-sink doublet is obtained.

Letting 2ϵ equal the distance between the source and sink and m the

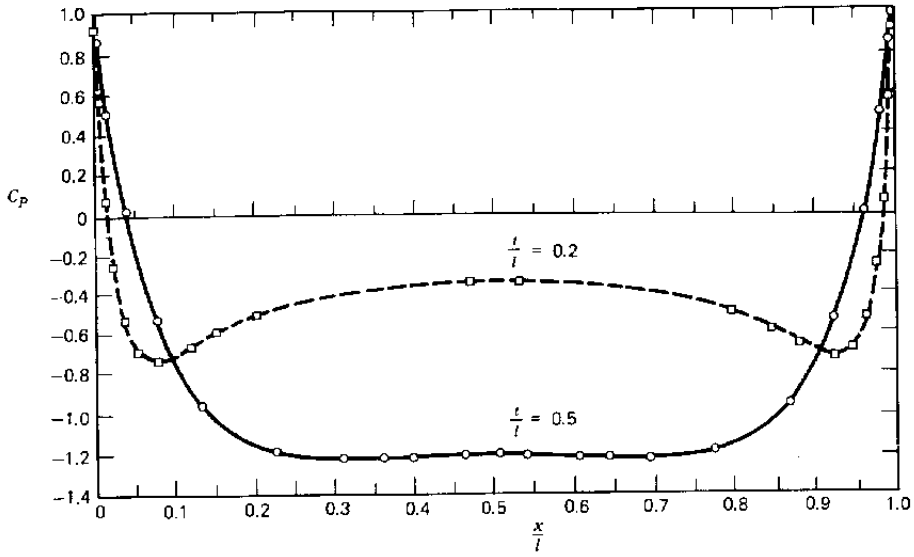

Figure 2.18 Predicted pressure distributions for 20 and 50% thick Rankine ovals.

constant doublet strength equal to $2\epsilon Q$, Equation 2.64 can be written as

$$\psi = \frac{m}{4\pi\epsilon}\left(\tan^{-1}\frac{y}{\epsilon + x} + \tan^{-1}\frac{y}{\epsilon - x} - \pi\right) U_y$$

$$\lim\ \epsilon \to 0$$

In the limit, this becomes

$$\psi = -\frac{m}{2\pi}\frac{y}{x^2 + y^2} + Uy$$

For $\psi = 0$, since y is not generally zero, it follows that

$$x^2 + y^2 = \frac{m}{2\pi U}$$

This is the equation of a circle of radius

$$R = (m/2\pi U)^{1/2}$$

Thus ψ can be written in polar coordinates as

$$\psi = Ur \sin\theta\left[1 - \left(\frac{R}{r}\right)^2\right] \tag{2.76}$$

where $r^2 = x^2 + y^2$

$$\theta = \tan^{-1}\left(\frac{y}{x}\right)$$

The tangential velocity along the surface of the cylinder is found from Equation 2.47 by differentiating ψ with respect to r and evaluating the result at $r = R$. In this way v_θ is found to be

$$v_\theta = 2U \sin\theta \tag{2.77}$$

The pressure coefficient distribution, from Equation 2.45, is thus predicted to be

$$C_p = 1 - 4\sin^2\theta \tag{2.78}$$

In Chapter Four it will be seen that Equation 2.78 agrees fairly well with experimental results over the front half of the cylinder, but departs from actual measurements over the rear portion as the result of viscosity.

A point vortex of strength γ can be placed at the origin without altering the streamline representing the surface of the cylinder. If this is done, Equation 2.77 becomes

$$v_\theta = 2U \sin\theta + \frac{\gamma}{2\pi R} \tag{2.79}$$

Relative to p_0 the pressure on the surface of the cylinder will be

$$p - p_0 = \frac{1}{2}\rho U^2 - \frac{1}{2}\rho\left|2U \sin\theta + \frac{\gamma}{2\pi R}\right|^2 \tag{2.80}$$

Referring to Figure 2.19, the net vertical force, or lift, on the cylinder resulting from the pressure distribution will be

$$L = -\int_0^\pi pR \sin\theta\, d\theta$$

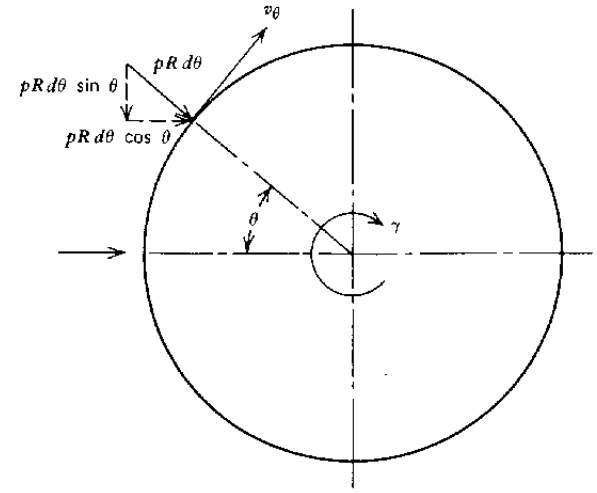

Figure 2.19 Circular cylinder with circulation.

or, from Equation 2.78, this reduces to

$$L = \rho U \gamma \tag{2.81}$$

This is referred to as the Kutta–Joukowski law. Although derived here specifically for a circular cylinder, it can be applied to other shapes where γ represents generally the circulation around the shape. This will be amplified further in Chapter Three.

The net horizontal force, or drag, on the cylinder is found from

$$D = \int_0^{2\pi} pR \cos\theta \, d\theta$$

Using Equation 2.80, the drag is found to be zero, a result that is true in general for a closed body in steady potential flow. This result is known as D'Alembert's paradox, after Jean le Rond D'Alembert, a French mathematician who first reached this conclusion around 1743.

The Numerical Calculation of Potential Flow Around Arbitrary Body Shapes

The preceding has demonstrated how particular body shapes can be generated by the superposition of elementary flow functions. This procedure can be generalized and the inverse problem can be solved where the body shape is prescribed and the elementary flow functions that will generate the body shape are found.

The concept of a point source or a point vortex can be extended to a continuous distribution of these functions. Consider first the two-dimensional source distribution shown in Figure 2.20. Here q is the source strength per unit length.

Consider the closed contour shown dashed in Figure 2.20, having a length of Δx and a vanishing small height. The total flux through this surface must equal $q\,\Delta x$. Close to the surface the u velocity components from the elemental sources will cancel so that only a v component remains. Thus

$$2v\,\Delta x = q\,\Delta x$$

or

$$v = \frac{q}{2} \tag{2.82}$$

In Reference 2.4 this relationship is used to determine the flow about arbitrary shapes. Thus, unlike the Rankine oval, the body shape is specified, and the problem is to find the distribution of singularities to satisfy the condition that the velocity everywhere normal to the body surface to be zero. This particular problem is referred to as the Neumann problem. Essentially the numerical solution of the problem proceeds by segmenting the body

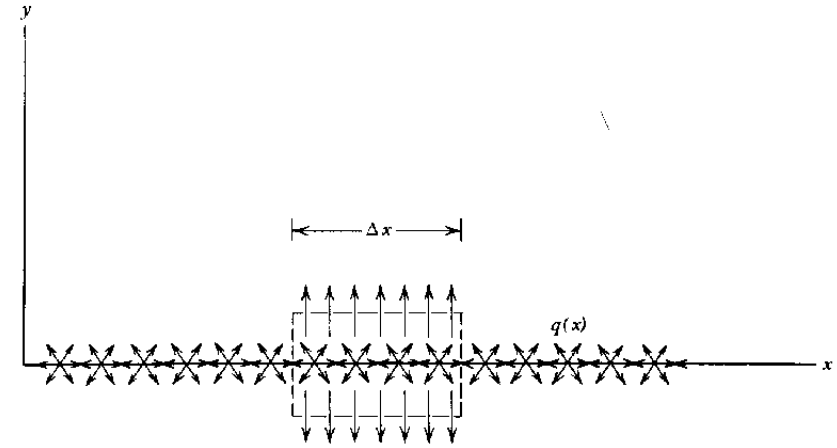

Figure 2.20 Distributed sources in two-dimensional flow.

surface and distributing a unit source strength, q_i, over the ith element. The normal velocity induced at the middle of the ith element by q_i is obtained immediately from Equation 2.82. The contribution to the velocity at the ith element from another element is calculated by assuming the total source strength at the second element to be a point source located at the middle of that element. Taking n elements and letting $i = 1, 2, 3, \ldots, n$ leads to a set of n linear simultaneous algebraic equations for the unknowns, $q_1, q_2, q_3, \ldots, q_n$.

Consider in more detail this approach for two-dimensional flow. Figure 2.21 shows two elements along the surface of a body. The ith element is the control element over which the unit source strength q_i is distributed. At the jth element a point source is located having a strength equal to $q_j\,\Delta S_j$, ΔS_j being the length of the jth element. The free-stream velocity U_0 is shown relative to the body x-axis at an angle of attack of α.

At the center of the ith element the normal velocity components from each source and the free stream must vanish. Hence

$$U_0 \sin(\theta_i - \alpha) = \frac{q_i}{2} + \sum_{j=1}^{N} q_j c_{ij} \qquad j \neq i \tag{2.83}$$

c_{ij} is an influence coefficient, which accounts for the geometry of the body shape in determining the normal velocity induced at the ith element by the source at the jth element.

If ζ_i and η_i correspond to the midpoints of the ith element then, for Figure 2.21:

$$c_{ij} = \frac{\sin(\theta_i - \phi_{ij})}{2\pi r_{ij}} \tag{2.84a}$$

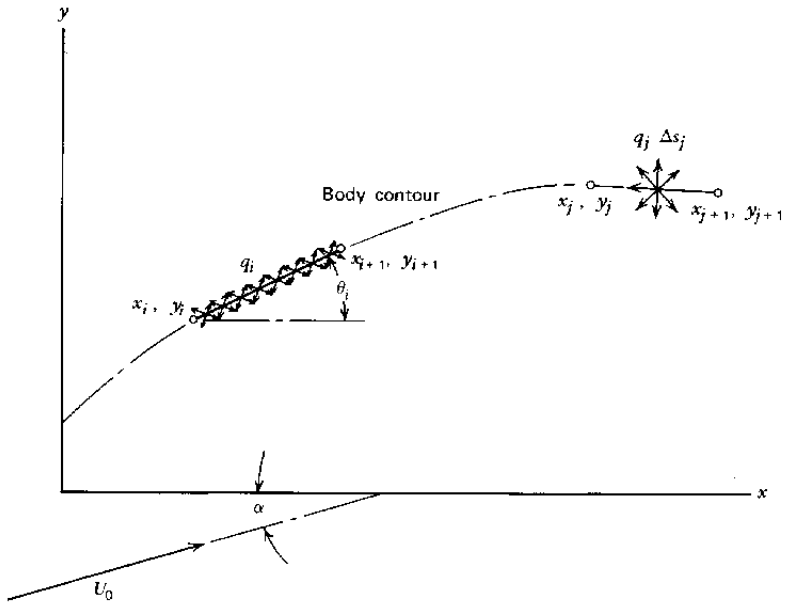

Figure 2.21 Numerical solution of the Neumann problem by a distribution of sources.

$$r_{ij} = [(\zeta_i - \zeta_j)^2 + (\eta_i - \eta_j)^2]^{1/2} \tag{2.84b}$$

$$\phi_{ij} = \tan^{-1} \frac{\eta_j - \eta_i}{\zeta_j - \zeta_i} \tag{2.84c}$$

$$\theta_i = \tan^{-1} \frac{y_{i+1} - y_i}{x_{i+1} - x_i} \tag{2.84d}$$

$$\zeta_i = \frac{1}{2}(x_i + x_{i+1}) \tag{2.84e}$$

$$\eta_i = \frac{1}{2}(y_i + y_{i+1}) \tag{2.84f}$$

Having thus determined the source strengths, q_i, the resultant velocity at any location can be determined by adding vectorially the free-stream velocity to the contributions from all of the sources. Finally, the pressure distribution can be determined from Equation 2.74.

This numerical procedure applied to a circular cylinder with a unit radius is illustrated in Figure 2.22. Here, only eight elements are shown. For this case,

$$x_i = \cos \theta_i$$
$$y_i = \sin \theta_i$$

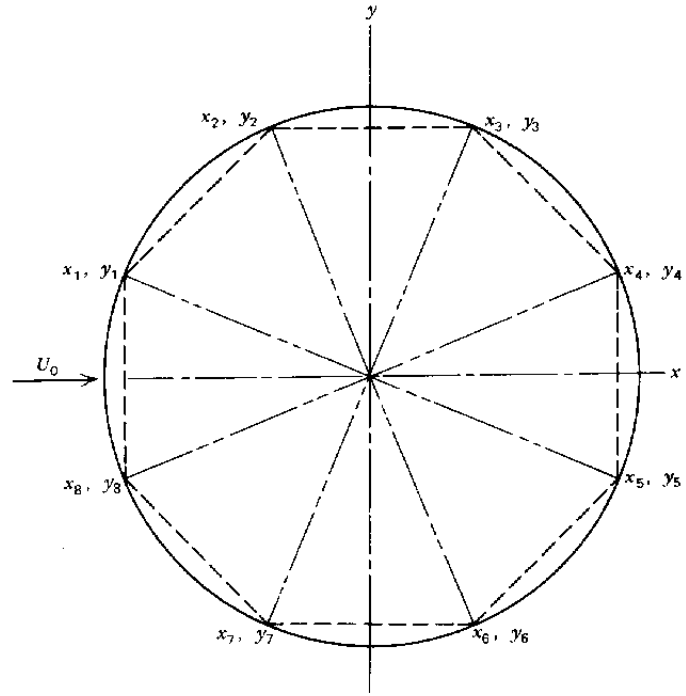

Figure 2.22 Approximation to a circular cylinder with straight-line segments.

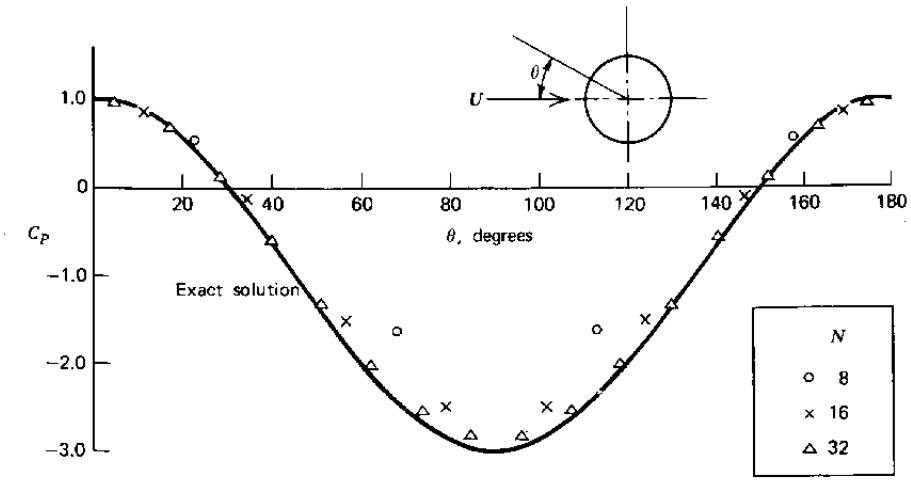

Figure 2.23 Convergence of the numerical result to the exact solution for a circular cylinder.

where

$$\theta_i = \pi - \frac{2\pi}{n}\left(i - \frac{1}{2}\right)$$

$$n = 8$$

The numerical calculation of the pressure distribution around a circular cylinder is compared in Figure 2.23 with the exact solution given by Equation 2.78. As the number of segments increases, the approximate solution is seen to approach the exact solution rapidly. In Chapter Three this numerical method will be extended to include distributed vortices in addition to sources. In this way the lift of an arbitrary airfoil can be predicted.

SUMMARY

This chapter has introduced some fundamental concepts in fluid mechanics that will be expanded on and applied to explaining the aerodynamic behavior of airplane components in succeeding chapters. Potential flow methods will be used extensively with corrections given for Reynolds and Mach numbers.

PROBLEMS

2.1 Prove that the resultant static force on the face of a dam acts at the centroid of the dam's area.

2.2 Show that the incompressible Bernoulli's equation (Equation 2.28) becomes $p + \rho g h + \frac{1}{2}\rho V^2 = \text{constant}$ for a liquid, the weight of which is significant in comparison to the static pressure forces. (h is the depth of the streamline relative to an arbitrary horizontal reference plane.)

2.3 A pilot is making an instrument approach into the University Park Airport, State College, Pennsylvania, for which the field elevation is listed at 378 m (1241 ft) above sea level. The sea level barometric pressure is 763.3 mm Hg (30.05 in. Hg), but the pilot incorrectly sets the altimeter to 758.2 mm Hg (29.85 in. Hg). Will the pilot be flying too high or too low and by how much? [*Note.* Standard sea level pressure is equal to 760 mm Hg (29.92 in. Hg)].

2.4 Set to standard sea level pressure, an altimeter reads 2500 m (8200 ft). The outside air temperature (OAT) reads −15 °C (5 °F). What is the pressure altitude? What is the density altitude?

2.5 By integrating the pressure over a body's surface, prove that the buoyant force on the body when immersed in a liquid is equal to the product of the volume of the displaced liquid, the liquid's mass density, and the acceleration due to gravity.

2.6 The hypothetical wake downstream of a two-dimensional shape is pictured below. This wake is far enough away from the body so that the static pressure through the wake is essentially constant and equal to the free-stream static pressure. Calculate the drag coefficient of the shape based on its projected frontal area.

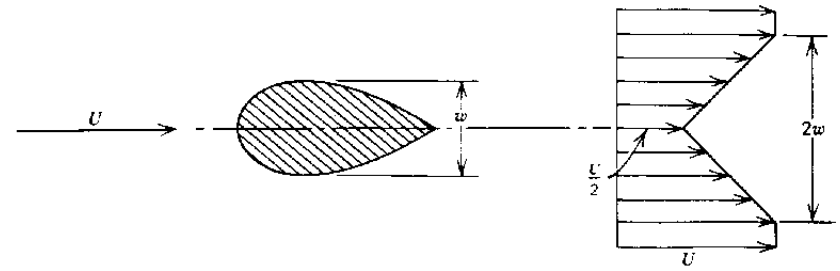

2.7 An incompressible flow has velocity components given by $u = \omega y$ and $v = \omega x$, where ω is a constant. Is such a flow physically possible? Can a velocity potential be defined? How is ω related to the vorticity? Sketch the streamlines.

2.8 Derive Bernoulli's equation directly by applying the momentum theorem to a differential control surface formed by the walls of a small streamtube and two closely spaced parallel planes perpendicular to the velocity.

2.9 A jet of air exits from a tank having an absolute pressure of 152,000 Pa (22 psi). The tank is at standard sea level (SSL) temperature. Calculate the jet velocity if it expands isentropically to SSL pressure.

2.10 A light aircraft indicates an airspeed of 266 km/hr (165.2 mph) at a pressure altitude of 2400 m (7874 ft). If the outside air temperature is −10 °C, what is the true airspeed?

2.11 Prove that the velocity induced at the center of a ring vortex (like a smoke ring) of strength Γ and radius R is normal to the plane of the ring and has a magnitude of $\Gamma/2R$.

2.12 Write a computer program to solve the Biot–Savart equations numerically. This can be done by dividing a line vortex into finite, small straight-line elements. At a desired location the velocities induced by all of the elements can then be added vectorially to give the total resultant velocity. Check your program by using it to solve Problem 2.11.

REFERENCES

2.1 Streeter, Victor L., and Wylie, E. Benjamin, *Fluid Mechanics*, 6th edition, McGraw-Hill, New York, 1975.

2.2 Roberson, John A., and Crowe, Clayton T., *Engineering Fluid Mechanics*, Houghton Mifflin, Boston, 1975.

2.3 Minzner, R. A., Champion, K. S. W., and Pond, H. L., "The ARDC Model Atmosphere," AF CRC-TR-59-267, 1959.
2.4 Smith, A. M. O., "Incompressible Flow About Bodies of Arbitrary Shape," IAS Paper No. 62–143, presented at the IAS National Sciences Meeting, Los Angeles, June 1962.

THREE
THE GENERATION OF LIFT

Lift is the component of the resultant aerodynamic forces on an airplane normal to the airplane's velocity vector. Mostly, the lift is directed vertically upward and sustains the weight of the airplane. There are exceptions however. A jet fighter with a thrust-to-weight ratio close to unity in a steep climb may be generating very little lift with its weight being opposed mainly by the engine thrust.

The component that is the major lift producer on an airplane and on which this chapter will concentrate is the wing. Depending on the airplane's geometry, other components can contribute to or significantly affect the lift, including the fuselage, engine nacelles, and horizontal tail. These latter components will be considered, but to a lesser extent than the wing.

WING GEOMETRY

The top view, or planform, of a wing is shown in Figure 3.1. The length, b, from one wing tip to the other is defined as the wingspan. The chord, c, at some spanwise station, y, is the distance from the wing's leading edge to its trailing edge measured parallel to the plane of symmetry in which the centerline chord, c_0, lies. The chord generally varies with y so that, for purposes of characterizing wing geometry, a mean chord, $\bar{c}$, is defined as the value that, when multiplied by the span, results in the planform area, S.

$$\bar{c} = \frac{S}{b} \tag{3.1}$$

The aspect ratio of a wing, A, is a measure of how long the span is with respect to the mean chord. Thus

$$A = \frac{b^2}{S} \tag{3.2}$$

For a rectangular planform where the chord is constant, this reduces to

$$A = \frac{b}{c} \tag{3.3}$$

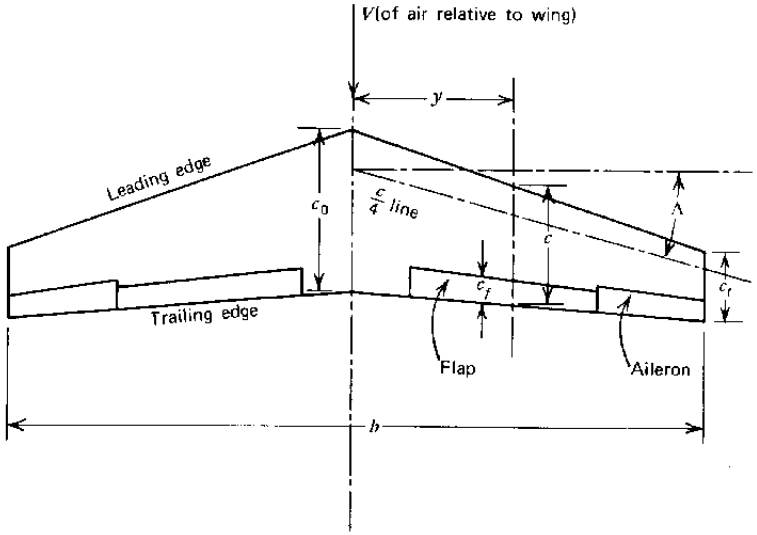

Figure 3.1 Top view of a wing (planform).

As shown in Figure 3.1, a wing planform may be tapered and swept back. The taper ratio, λ, is defined as the ratio of the tip chord, c_t, to the midspan chord, c_0.

$$\lambda = \frac{c_t}{c_0} \tag{3.4}$$

The sweep angle, Λ, is frequently measured relative to the quarter-chord line of the wing, that is, a line defined by the locus of points a quarter of the distance from the leading edge to the trailing edge. Λ, on occasion, is also measured relative to the leading edge.

Usually the center portion of a wing is enclosed by the fuselage. In such an instance the wing's aspect ratio and taper ratio are determined by ignoring the fuselage and extrapolating the planform shape into the centerline. The midspan chord in this instance is thus somewhat fictitious. The wing root is defined as the wing section at the juncture of the wing and fuselage. Occasionally, in the literature, one will find wing geometry characterized in terms of the wing root chord instead of the midspan chord.

Approximately the aft 25 to 30% of a wing's trailing edge is movable. On the outer one-third or so of the span the trailing edge on one side of the wing deflects opposite to that on the other. These oppositely moving surfaces are called ailerons; ailerons provide a rolling moment about the airplane's longitudinal axis. For example, when the aileron on the left wing moves down and the one on the right moves up, a moment is produced that tends to lift the left wing and lower the right one; this is a maneuver necessary in making a coordinated turn to the right.

The inner movable portions of the wing's trailing edge on both sides of the wing are known as the flaps. For takeoff and landing the flaps are lowered the same on both sides. There is no differential movement of the flaps on the left and right sides of the wing. The purpose of the flaps is to allow the wing to develop a higher lift coefficient than it would otherwise. Thus, for a given weight, the airplane can fly slower with the flaps down than with them up. Flaps, including leading edge flaps and the many different types of trailing edge flaps, will be discussed in more detail later.

For some applications both ailerons are lowered to serve as an extension to the flaps. In such a case they are referred to as drooped ailerons, or flaperons. When flaperons are employed, additional roll control is usually provided by spoilers. These are panels that project into the flow near the trailing edge to cause separation with an attendant loss of lift.

In order to understand and predict the aerodynamic behavior of a wing, it is expedient to consider first the behavior of two-dimensional airfoils. An airfoil can be thought of as a constant chord wing of infinite aspect ratio.

AIRFOILS

A considerable amount of experimental and analytical effort has been devoted to the development of airfoils. Much of this work was done by the National Advisory Committee for Aeronautics (NACA), the predecessor of the National Aeronautics and Space Administration (NASA). Reference 3.1 is an excellent summary of this effort prior to 1948. More recently NASA and others have shown a renewed interest in airfoil development, particularly for application to helicopter rotor blades, general aviation aircraft, and aircraft operating at transonic speeds of Mach 0.7 or higher.

The development of an unflapped airfoil shape is illustrated in Figure 3.2. First, in Figure 3.2*a*, the chord line, c, is drawn. Next in Figure 3.2*b*, the camber line is plotted up from the chord a small distance z, which is a function of the distance from the leading edge. Next, as shown in Figure 3.2*c*, the semithickness is added to either side of the camber line. Also, the nose circle is centered on a tangent to the camber line at the leading edge and passes through the leading edge. Finally, an outer contour is faired around the skeleton to form the airfoil shape. Observe that the chord line is the line joining the ends of the mean camber line.

The early NACA families of airfoils were described in this way, with the camber and thickness distributions given as algebraic functions of the chordwise position. However, for certain combinations of maximum thickness-to-chord ratios, maximum camber-to-chord ratios, and chordwise posi-

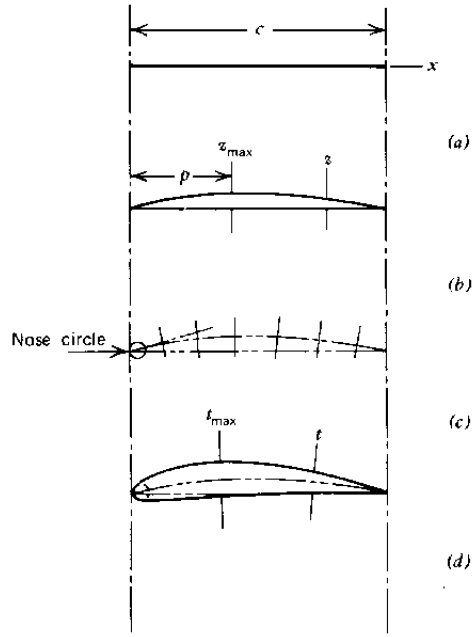

Figure 3.2 The construction of an airfoil contour.

tion of maximum camber, tabulated ordinates for the upper and lower surfaces are available (Ref. 3.1).

Before discussing the various families of airfoils in detail, we will generally consider the aerodynamic characteristics for airfoils, all of which can be influenced by airfoil geometry.

To begin, an airfoil derives its lift from the pressure being higher on the lower surface of the airfoil than on the upper surface. If a subscript l denotes lower surface and "u" denotes upper surface, then the total lift (per unit span) on the airfoil will be

$$L = \int_0^c (p_l - p_u)\, dx \tag{3.5}$$

The moment about the leading edge, defined positive nose up, will be

$$M_{LE} = -\int_0^c x(p_l - p_u)\, dx \tag{3.6}$$

In accord with Equation 2.12, the lift and moment can be expressed in terms of dimensionless coefficients.

$$C_l = \frac{L}{(1/2)\rho V^2 c} \tag{3.7}$$

$$C_{m_{LE}} = \frac{M_{LE}}{(1/2)\rho V^2 c^2} \tag{3.8}$$

Note that lowercase subscripts are used to denote coefficients for a two-dimensional airfoil, whereas uppercase subscripts are used for the three-dimensional wing.

Writing

$$\frac{p_l - p_u}{(1/2)\rho V^2} = \frac{p_l - p_0}{(1/2)\rho V^2} - \frac{p_u - p_0}{(1/2)\rho V^2}$$

and redefining x as the distance in chord lengths from the leading edge, Equations 3.5 and 3.6 become

$$C_l = \int_0^1 (C_{p_l} - C_{p_u})\, dx \tag{3.9}$$

and

$$C_{m_{LE}} = -\int_0^1 x(C_{p_l} - C_{p_u})\, dx \tag{3.10}$$

where the upper and lower pressure coefficients are defined according to Equation 2.73.

The moment calculated from Equation 3.10 can be visualized as being produced by the resultant lift acting at a particular distance back from the leading edge. As a fraction of the chord, the distance x_{cp} to this point, known as the center of pressure, can be calculated from

$$-x_{cp}C_l = C_{m_{LE}} \tag{3.11}$$

Knowing x_{cp}, the moment coefficient about any other point, x, along the airfoil can be written, referring to Figure 3.3, as

$$C_m = -(x_{cp} - x)\, C_l \tag{3.12}$$

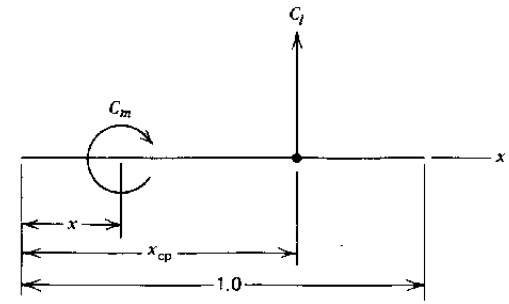

Figure 3.3 Dimensionless moment at x produced by dimensionless lift acting at x_{cp}.

It will be shown later that a point exists on an airfoil called the *aerodynamic center* about which the moment coefficient is constant and does not depend on C_l. Denoting the location of the aerodynamic center by x_{ac}, Equation 3.12 can be solved for the location of the center of pressure.

$$x_{cp} = x_{ac} - \frac{C_{m_{ac}}}{C_l} \tag{3.13}$$

Do not confuse the aerodynamic center with the center of pressure. Again, the aerodynamic center is the location about which the moment is constant, the center of pressure is the point at which the resultant lift acts.

The progressive development of an airfoil shape is illustrated by reference to Figure 3.4*a* and 3.4*b*. Historically airfoils developed approximately in this manner. Consider first the simple shape of a thin, flat plate.

Beginning with Figure 3.4*a* if the angle of attack of a thin, flat plate is suddenly increased from zero, the flow will appear for a moment as shown. Because of near-symmetry, there is practically no lift produced on the plate. However, because of viscosity, the flow at the trailing edge cannot continue to turn the sharp edge to flow upstream. Instead, it quickly adjusts to the pattern shown in Figure 3.4*b*. Here the flow leaves nearly tangent to the trailing edge. This condition is known as the *Kutta* condition after the German scientist, W. M. Kutta, who in 1902 first imposed the trailing edge condition in order to predict the lift of an airfoil theoretically. In Figure 3.4*b* observe that there is one streamline that divides the flow that passes over the plate from that below. Along this "dividing streamline," the flow comes to rest at the stagnation point, where it joins perpendicular to the lower surface of the plate near the leading edge. As the flow progresses forward along this line, it is unable to adhere to the surface around the sharp leading edge and separates from the plate. However, it is turned backward by the main flow and reattaches to the upper surface a short distance from the leading edge. The resulting nonsymmetrical flow pattern causes the fluid particles to accelerate over the upper surface and decelerate over the lower surface. Hence, from Bernoulli's equation, there is a decrease in air pressure above the plate and an increase below it. This pressure difference acting on the airfoil produces a lift.

If the angle of attack of the plate is too great, the separated flow at the leading edge will not reattach to the upper surface, as shown in Figure 3.4*c*. When this occurs, the large separated region of unordered flow on the upper surface produces an increase in pressure on that surface and hence a loss in lift. This behavior of the airfoil is known as stall. Thus the limit in C_l, that is, $C_{l_{max}}$, is the result of flow separation on the upper surface of the airfoil.

To improve this condition, one can curve the leading edge portion of the flat plate, as shown in Figure 3.4*d*, to be more nearly aligned with the flow in

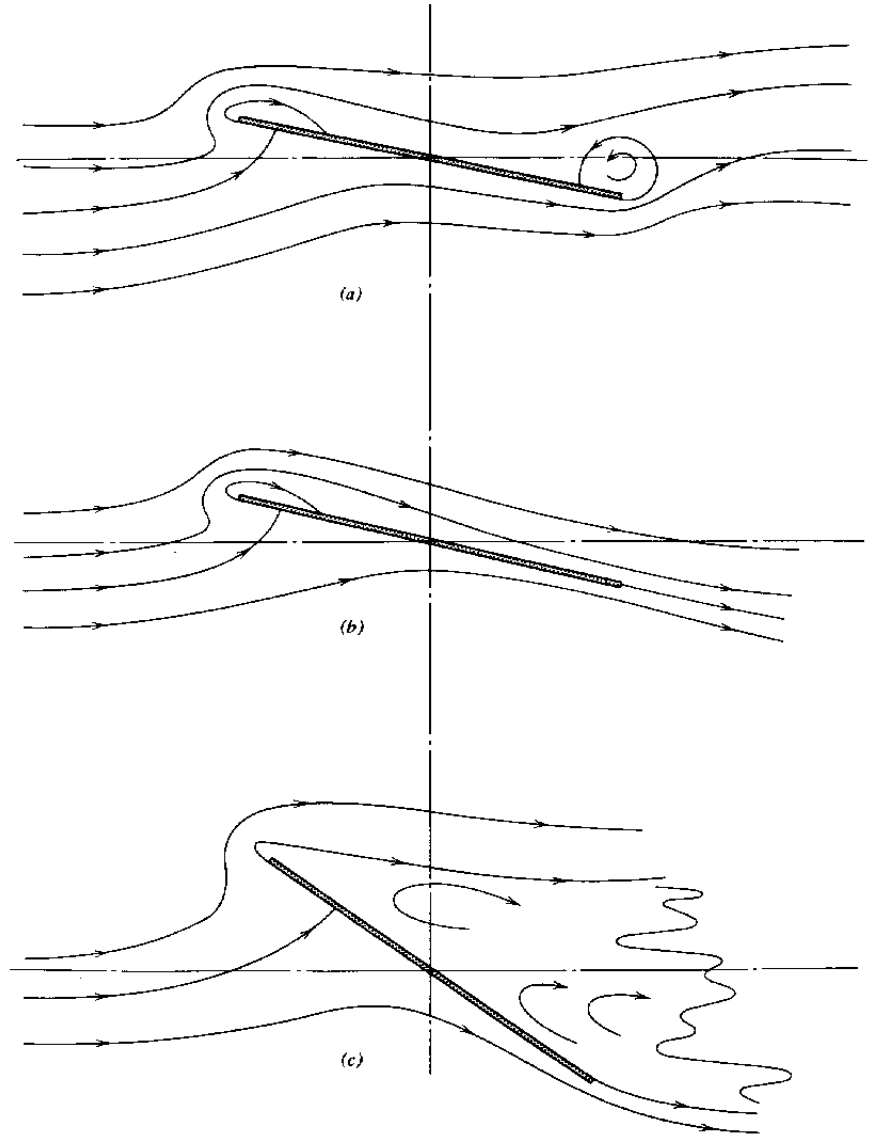

Figure 3.4 Progressive development of airfoil shapes. (*a*) Flat plate at sudden angle of attack—no lift. (*b*) Flat plate at angle of attack in steady flow and generating lift. (*c*) Flat plate experiencing leading edge separation and loss of lift (stall). (*d*) Flat plate with curved leading edge to prevent leading edge separation. (*e*) Airfoil with thickness and camber to delay stall. (*f*) Airfoil with trailing edge separation.

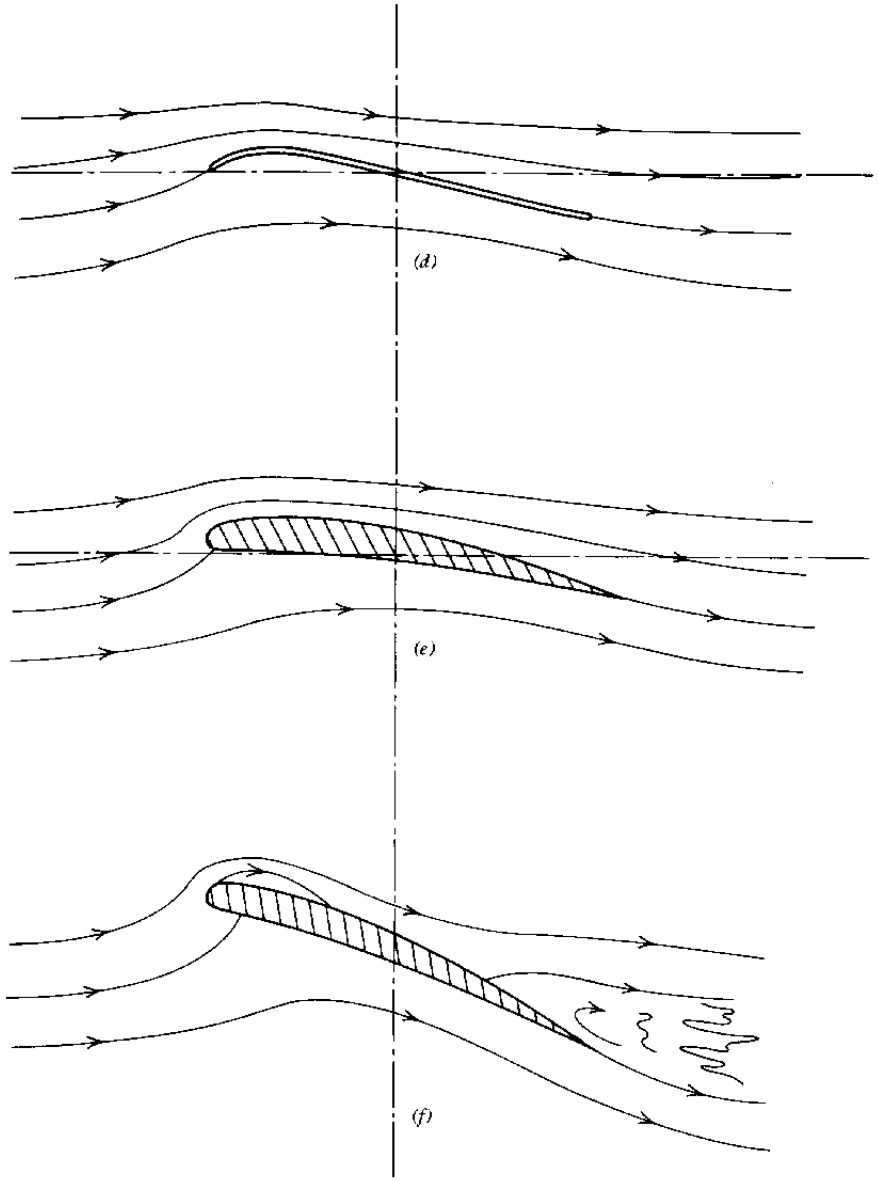

Figure 3.4 (Continued)

that region. Such a shape is similar to that used by the Wright Brothers. This solution to the separation problem, as one might expect, is sensitive to angle of attack and only holds near a particular design angle. However, by adding thickness to the thin, cambered plate and providing a rounded leading edge, the performance of the airfoil is improved over a range of angles, with the leading edge separation being avoided altogether. Thus, in a qualitative sense, we have defined a typical airfoil shape. Camber and thickness are not needed to produce lift (lift can be produced with a flat plate) but, instead, to increase the maximum lift that a given wing area can deliver.

Even a cambered airfoil of finite thickness has its limitations, as shown in Figure 3.4*f*. As the angle of attack is increased, the flow can separate initially near the trailing edge, with the *separation point* progressively moving forward as the angle of attack continues to increase.

The degree to which the flow separates from the leading or trailing edge depends on the Reynolds number and the airfoil geometry. Thicker airfoils with more rounded leading edges tend to delay leading edge separation. This separation also improves with increasing values of the Reynolds number.

Leading edge separation results in flow separation over the entire airfoil and a sudden loss in lift. On the other hand, trailing edge separation is progressive with angle of attack and results in a more gradual stalling. The situation is illustrated in Figures 3.5 and 3.6 (taken from Ref. 3.1). In Figure 3.5 note the sharp drop in C_l at an α of 12° for $R = 3 \times 10^6$, whereas for $R = 9 \times 10^6$, the lift curve is more rounded, with a gradual decrease in C_l beyond an α of 14°. In Figure 3.6, for a thicker airfoil with the same camber, the lift increases up to an angle of approximately 16° for all R values tested. At this higher angle, even for $R = 9 \times 10^6$, it appears that leading edge separation occurs because of the sharp drop in C_l for α values greater than 16°. From a flying qualities standpoint, an airfoil with a well-rounded lift curve is desirable in order to avoid a sudden loss in lift as a pilot slows down the airplane. However, other factors such as drag and Mach number effects must also be considered in selecting an airfoil. Hence, as is true with most design decisions, the aerodynamicist chooses an airfoil that represents the best compromise to conflicting requirements, including nonaerodynamic considerations such as structural efficiency.

Figures 3.5 and 3.6 illustrate other characteristics of airfoil behavior that will be considered in more detail later. Observe that the lift curve, C_l versus α, is nearly linear over a range of angles of attack. Notice also that the slope, $dC_l/d\alpha$, of the lift curve over the linear portion is unchanged by deflecting the split flap. The effect of lowering the flap or, generally, of increasing camber is to increase C_l by a constant increment for each α in the linear range. Thus the angle of attack for zero lift, α_{0l}, is negative for a cambered airfoil. In the case of the 1408 airfoil pictured in Figure 3.5, α_{0l} equals −12.5°, with the split flap deflected 60°.

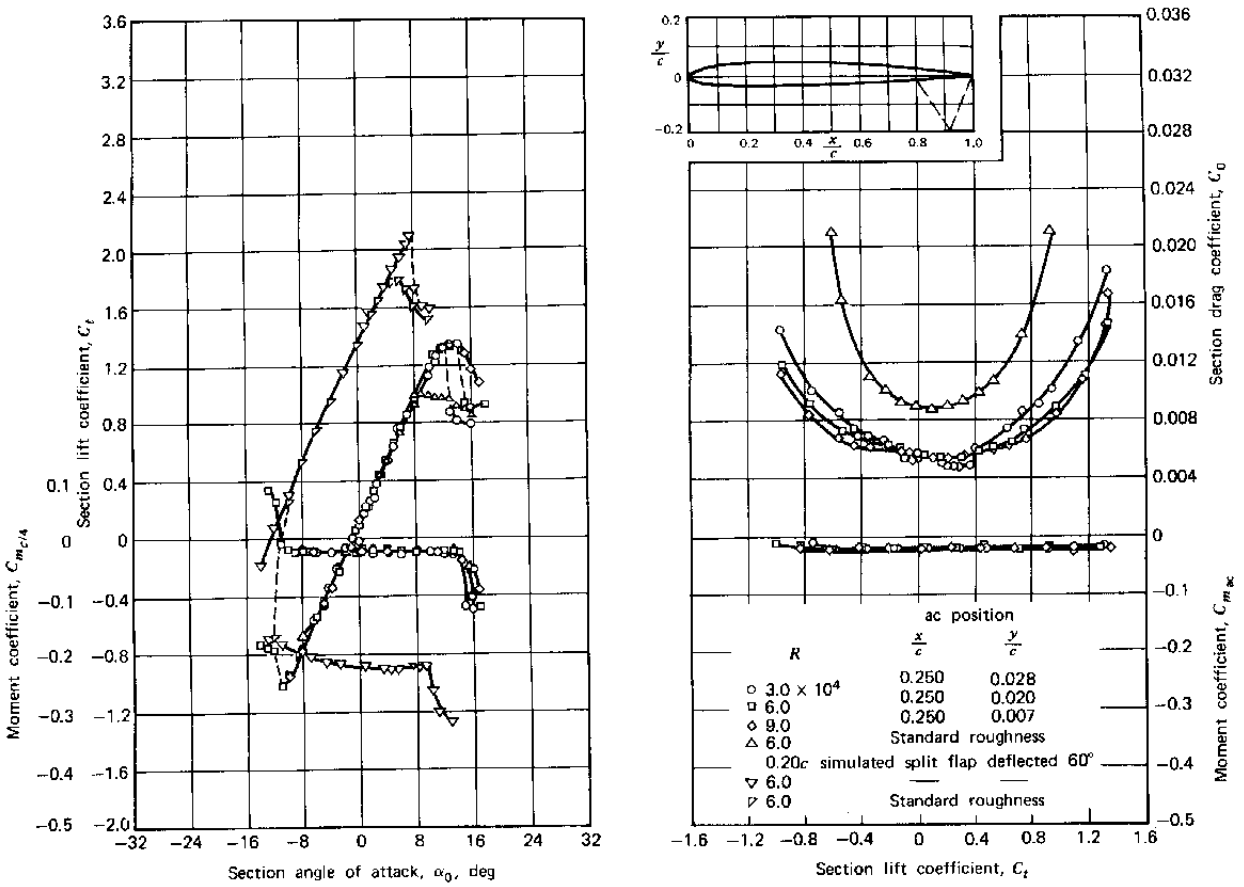

Figure 3.5 Characteristics of the NACA 1408 airfoil.

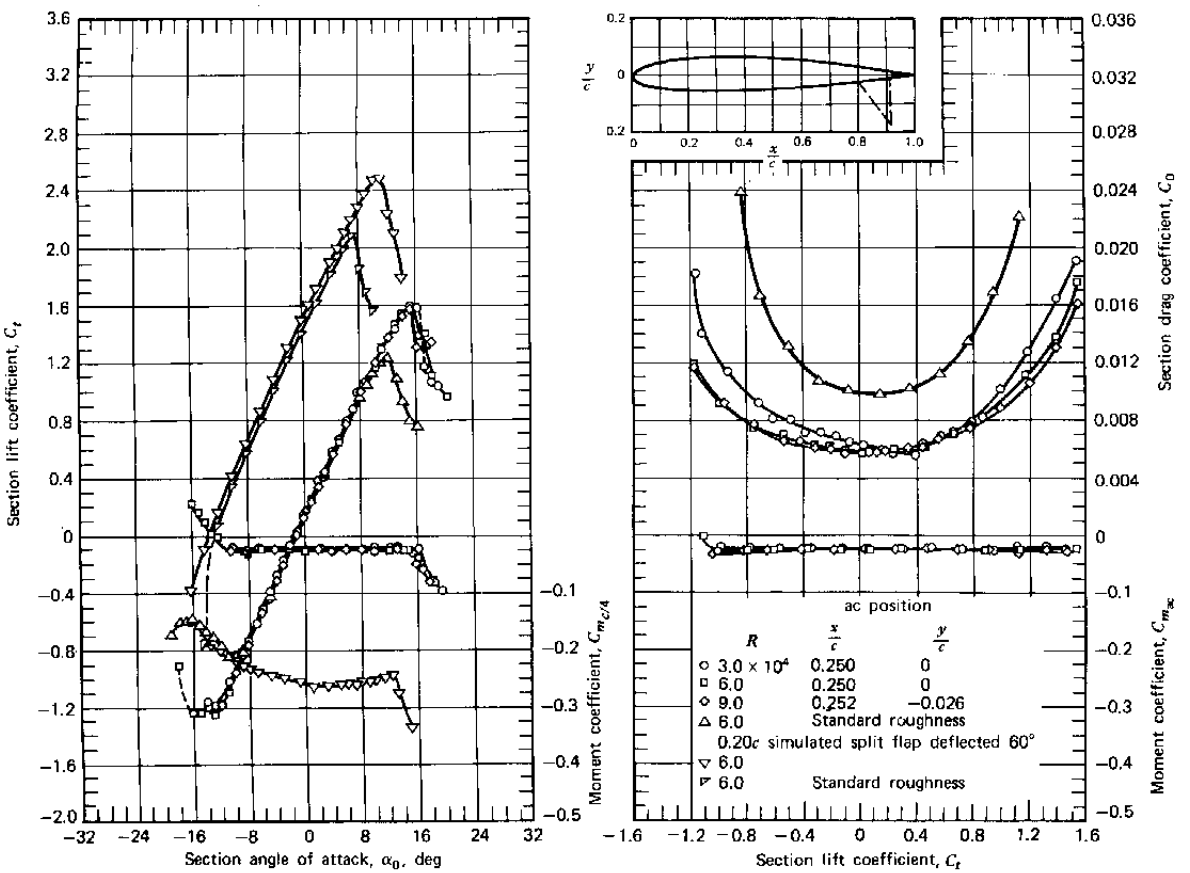

Figure 3.6 Characteristics of the NACA 1412 airfoil.

If α is increased beyond the stall C_l will again begin to increase before dropping off to zero at an α of approximately 90°. The second peak in C_l is generally not as high as that which occurs just before the airfoil stalls. S. P. Langley, in his early experiments, noted these two peaks in the C_l versus α curve but chose to fair a smooth curve through them. Later, the Wright Brothers observed the same characteristics and were troubled by Langley's smooth curve. After searching Langley's original data and finding that he, too, had a "bump" in the data, Wilbur Wright wrote to Octave Chanute on December 1, 1901.

"If he (Langley) had followed his observations, his line would probably have been nearer the truth. I have myself sometimes found it difficult to let the lines run where they will, instead of running them where I think they ought to go. My conclusion is that it is safest to follow the observations exactly and let others do their own correcting if they wish" (*Ref.* 1.1).

To paraphrase the immortal Wilbur Wright, "Do not 'fudge' your data—it may be right."

AIRFOIL FAMILIES

NACA Four-Digit Series

Around 1932, NACA tested a series of airfoil shapes known as the four-digit sections. The camber and thickness distributions for these sections are given by equations to be found in Reference 3.1. These distributions were not selected on any theoretical basis, but were formulated to approximate efficient wing sections in use at that time, such as the well-known Clark-Y section.

The four-digit airfoil geometry is defined, as the name implies, by four digits; the first gives the maximum camber in percent of chord, the second the location of the maximum camber in tenths of chord, and the last two the maximum thickness in percent of chord. For example, the 2412 airfoil is a 12% thick airfoil having a 2% camber located 0.4c from the leading edge. The 2412 airfoil is pictured in Figure 3.7 along with other airfoils yet to be described.

NACA Five-Digit Series

The NACA five-digit series developed around 1935 uses the same thickness distribution as the four-digit series. The mean camber line is defined differently, however, in order to move the position of maximum camber

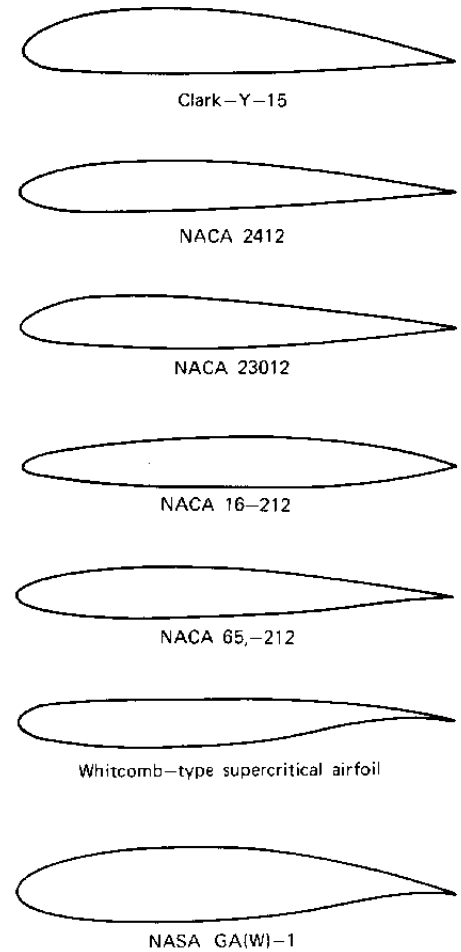

Figure 3.7 Comparison of various airfoil shapes.

forward in an effort to increase $C_{l_{max}}$. Indeed, for comparable thicknesses and cambers, the $C_{l_{max}}$ values for the five-digit series are 0.1 to 0.2 higher than those for the four-digit airfoils. The numbering system for the five-digit series is not as straightforward as for the four-digit series. The first digit multiplied by 3/2 gives the design lift coefficient of the airfoil. The next two digits are twice the position of maximum camber in percent of chord. The last two digits give the percent thickness. For example, the 23012 airfoil is a 12% thick airfoil having a design C_l of 0.3 and a maximum camber located 15% of c back from the leading edge. This airfoil is also pictured in Figure 3.7.

NACA 1-Series (Series 16)

The NACA 1-series of wing sections developed around 1939 was the first series based on theoretical considerations. The most commonly used 1-series airfoils have the minimum pressure located at the $0.6c$ point and are referred to as series-16 airfoils. The camber line for these airfoils is designed to produce a uniform chordwise pressure difference across it. In the thin airfoil theory to follow, this corresponds to a constant chordwise distribution of vorticity.

Operated at its design C_l, the series-16 airfoil produces its lift while avoiding low-pressure peaks corresponding to regions of high local velocities. Thus the airfoil has been applied extensively to both marine and aircraft propellers. In the former application, low-pressure regions are undesirable from the standpoint of cavitation (the formation of vaporous cavities in a flowing liquid). In the latter, the use of series-16 airfoils delays the onset of deleterious effects resulting from shock waves being formed locally in regions of high velocities.

Series-1 airfoils are also identified by five digits as, for example, the NACA 16–212 section. The first digit designates the series; the second digit designates the location of the minimum pressure in tenths of chord. Following the dash, the first number gives the design C_l in tenths. As for the other airfoils, the last two digits designate the maximum thickness in percent of chord. The 16–212 airfoil is shown in Figure 3.7.

NACA 6-Series

The 6-series airfoils were designed to achieve desirable drag, compressibility, and $C_{l_{max}}$ performance. These requirements are somewhat conflicting, and it appears that the motivation for these airfoils was primarily the achievement of low drag. The chordwise pressure distribution resulting from the combination of thickness and camber is conducive to maintaining extensive laminar flow over the leading portion of the airfoil over a limited range of C_l values. Outside of this range, C_d and $C_{l_{max}}$ values are not too much different from other airfoils.

The mean lines used with the 6-series airfoils have a uniform loading back to a distance of $x/c = 2$. Aft of this location the load decreases linearly. The $a = 1$ mean line corresponds to the uniform loading for the series-16 airfoils.

There are many perturbations on the numbering system for the 6-series airfoils. The later series is identified, for example, as

$$\text{NACA } 65_1\text{-}212 \qquad a = 0.6$$

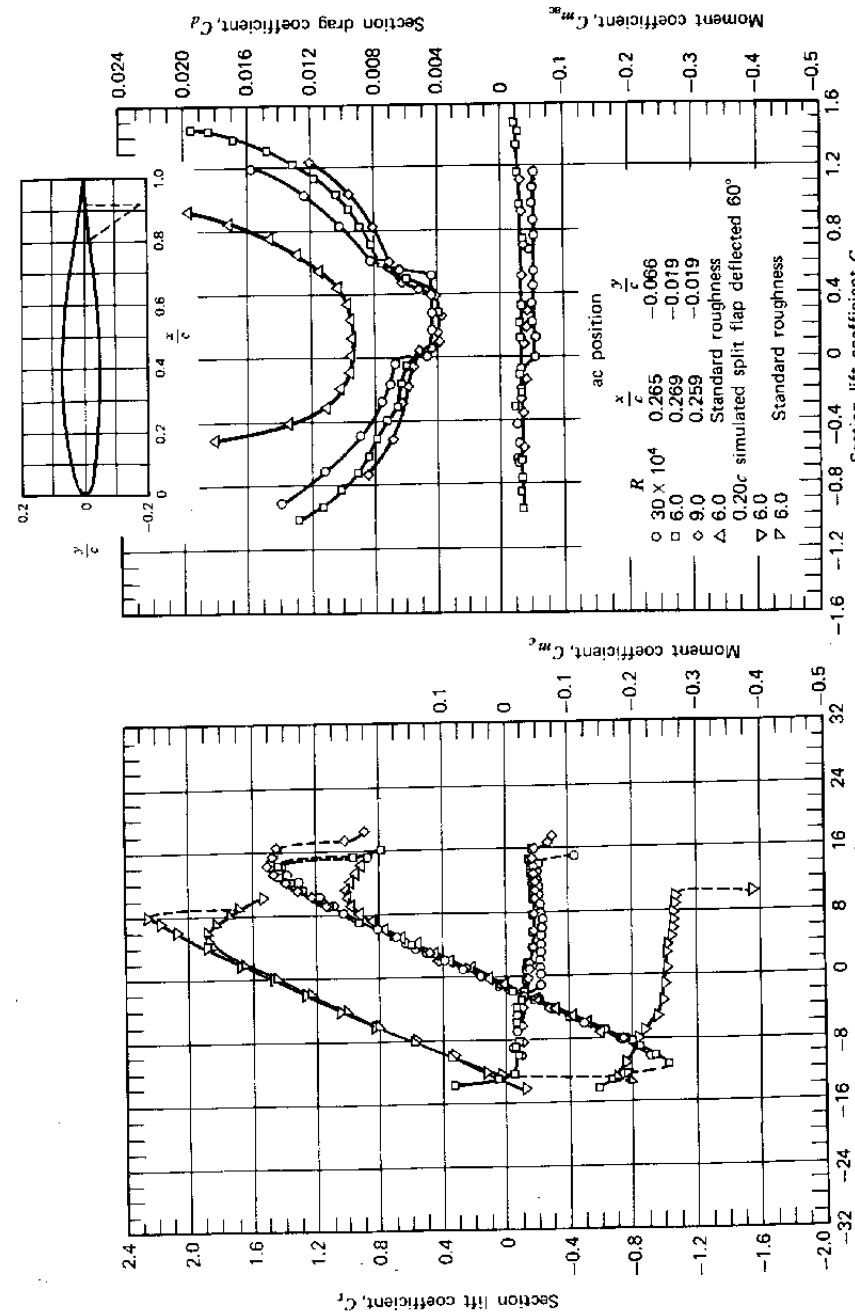

Figure 3.8 Aerodynamic characteristics of the NACA 65, −212, a = 0.6 airfoil.

Here 6 denotes the series; the numeral 5 is the location of the minimum pressure in tenths of chord for the basic thickness and distribution; and the subscript 1 indicates that low drag is maintained at C_l values of 0.1 above and below the design C_l of the 0.2, denoted by the 2 following the dash. Again, the last two digits specify the percentage thickness. If the fraction, a, is not specified, it is understood to equal unity. The 65_1-212 airfoil is shown in Figure 3.7.

Lift and drag curves for the 65_1-212 airfoil are presented in Figure 3.8. Notice the unusual shape of C_d versus C_l, where the drag is significantly lower between C_l values of approximately 0 to 0.3. In this region, for very smooth surfaces and for Reynolds numbers less than 9×10^6, extensive laminar flow is maintained over the surface of the foil with an attendent decrease in the skin friction drag. This region, for obvious reasons, is known as the "drag bucket." In practice this laminar flow, and resulting low drag, is difficult to achieve because of contamination by bugs or by structurally transmitted vibration that perturbs the laminar boundary layer, causing transition. Chapter Four will discuss the drag of these airfoils in more detail.

MODERN AIRFOIL DEVELOPMENTS

Systematic series of airfoils have given way, at least in part, to specialized airfoils designed to satisfy particular requirements. These airfoils are synthesized with the use of sophisticated computer programs such as the one described in Reference 3.5, which will be discussed in more detail later. One such special purpose airfoil is the so-called supercritical airfoil reported on in References 3.6 and 3.7. This airfoil has a well-rounded leading edge and is relatively flat on top with a drooped trailing edge. For a constant thickness of 12%, wind tunnel studies indicate a possible increase of approximately 15% in the drag-divergence Mach number for a supercritical airfoil as compared to a more conventional 6-series airfoil. In addition, the well-rounded leading edge provides an improvement in $C_{l_{max}}$ at low speeds over the 6-series, which has sharper leading edges.

A qualitative explanation for the superior performance of the supercritical airfoil is found by reference to Figure 3.9. At a free-stream Mach number as low as 0.7 or so depending on the shape and C_l, a conventional airfoil will accelerate the flow to velocities that are locally supersonic over the forward or middle portion of its upper surface. The flow then decelerates rapidly through a relatively strong shock wave to subsonic conditions. This compression wave, with its steep positive pressure gradient, causes the boundary layer to thicken and, depending on the strength of the shock, to separate. This, in turn, causes a significant increase in the drag. The minimum value of the free-stream Mach number for which the local flow becomes

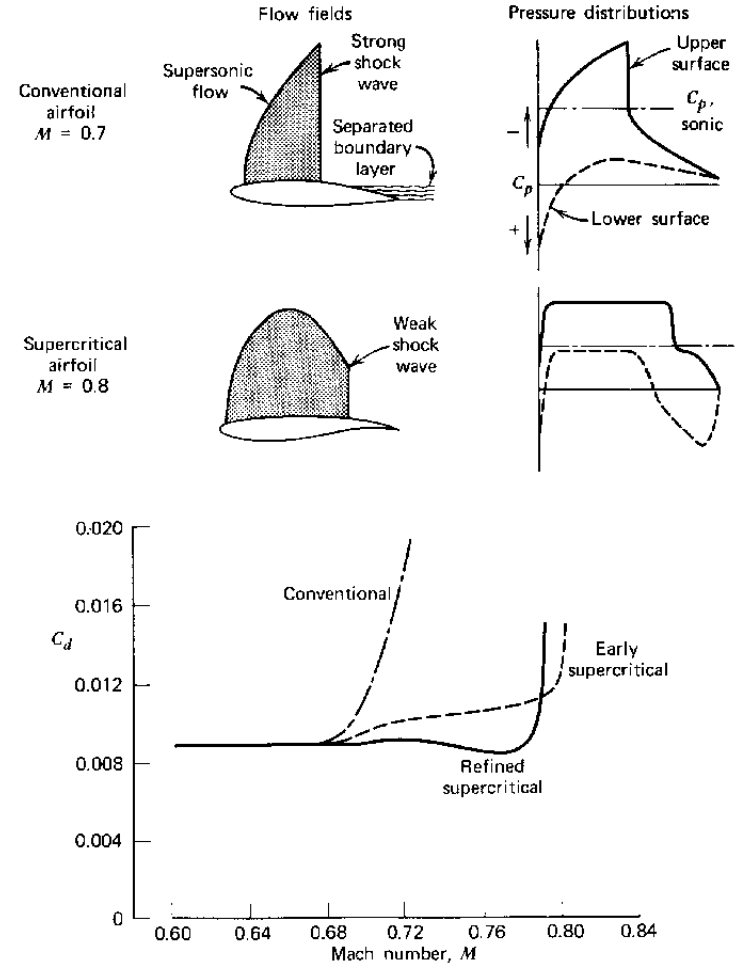

Figure 3.9 Supercritical flow phenomena.

supersonic is referred to as the critical Mach number. As this value is exceeded by a few hundredths, the shock wave strengthens sufficiently to cause the drag to rise suddenly. This free-stream Mach number is known as the drag-divergence Mach number.

The supercritical airfoil also accelerates the flow to locally supersonic conditions at free-stream Mach numbers comparable to the 1- or 6-series airfoils. However, the supercritical airfoil is shaped, so that around its design lift coefficient, the flow decelerates to subsonic conditions through a distribution of weak compression waves instead of one strong one. In this way the drag-divergence Mach number is increased substantially.

Although the possibility of such airfoils was known for some time, their successful development in modern times is attributed to R. T. Whitcomb. A Whitcomb-type supercritical airfoil is pictured in Figure 3.7.

Tested at low speeds, the supercritical airfoils were found to have good $C_{l_{max}}$ values as well as low C_d values at moderate lift coefficients. As a result, another family of airfoils evolved from the supercritical airfoils, but for low-speed applications. These are the "general aviation" airfoils, designated GA(W) for general aviation (Whitcomb). The GA(W)-1 airfoil is the last of the

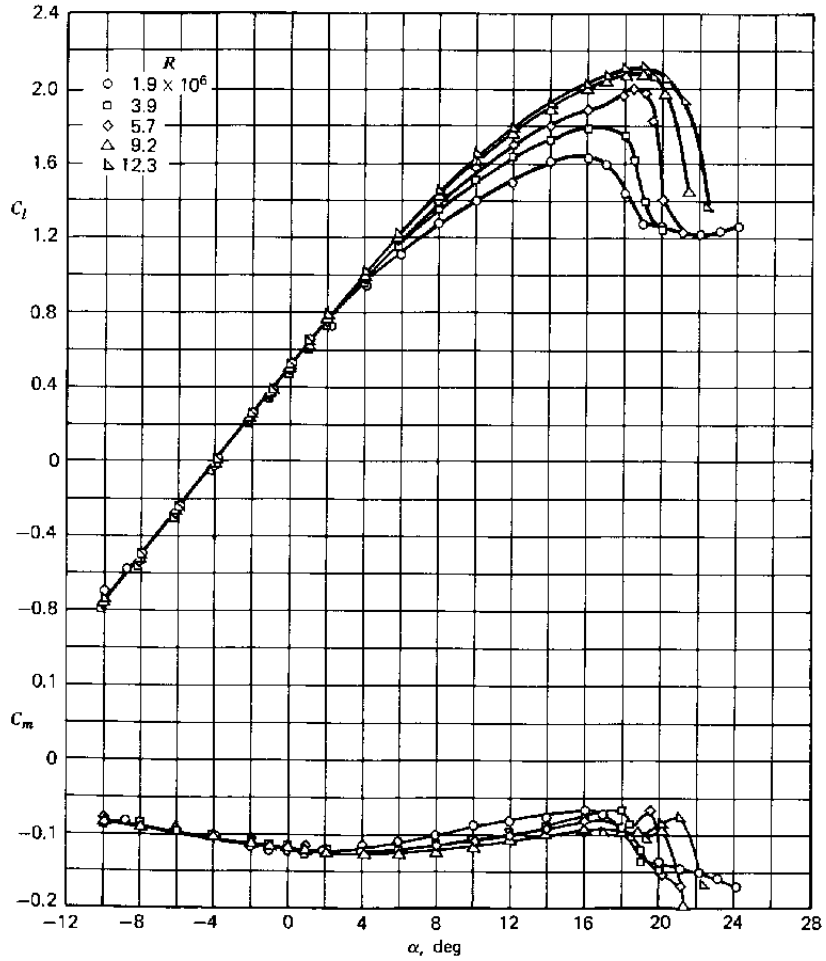

Figure 3.10a Effect of Reynolds number on section characteristics of the GA(W)-1 airfoil Model smooth, $M = 0.15$.

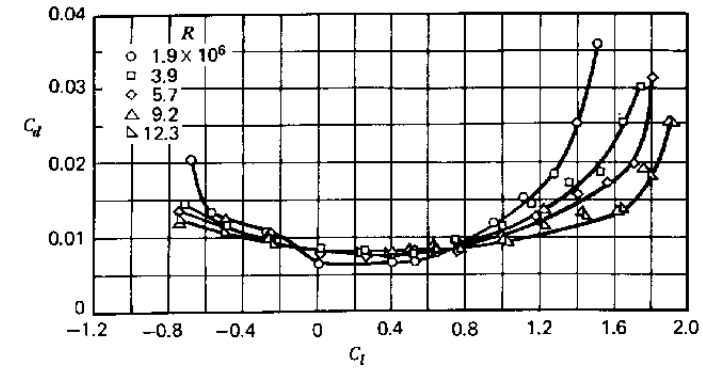

Figure 3.10b Conditions same as Figure 3.10a.

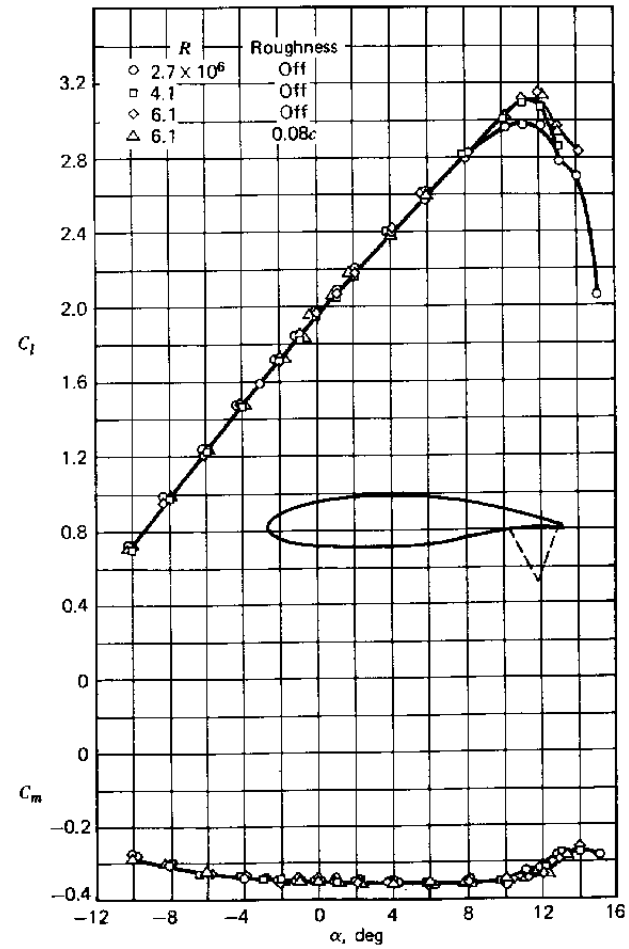

Figure 3.10c GA(W)-1 airfoil section characteristics for 0.20c simulated split flap deflected 60° ($M = 0.20$).

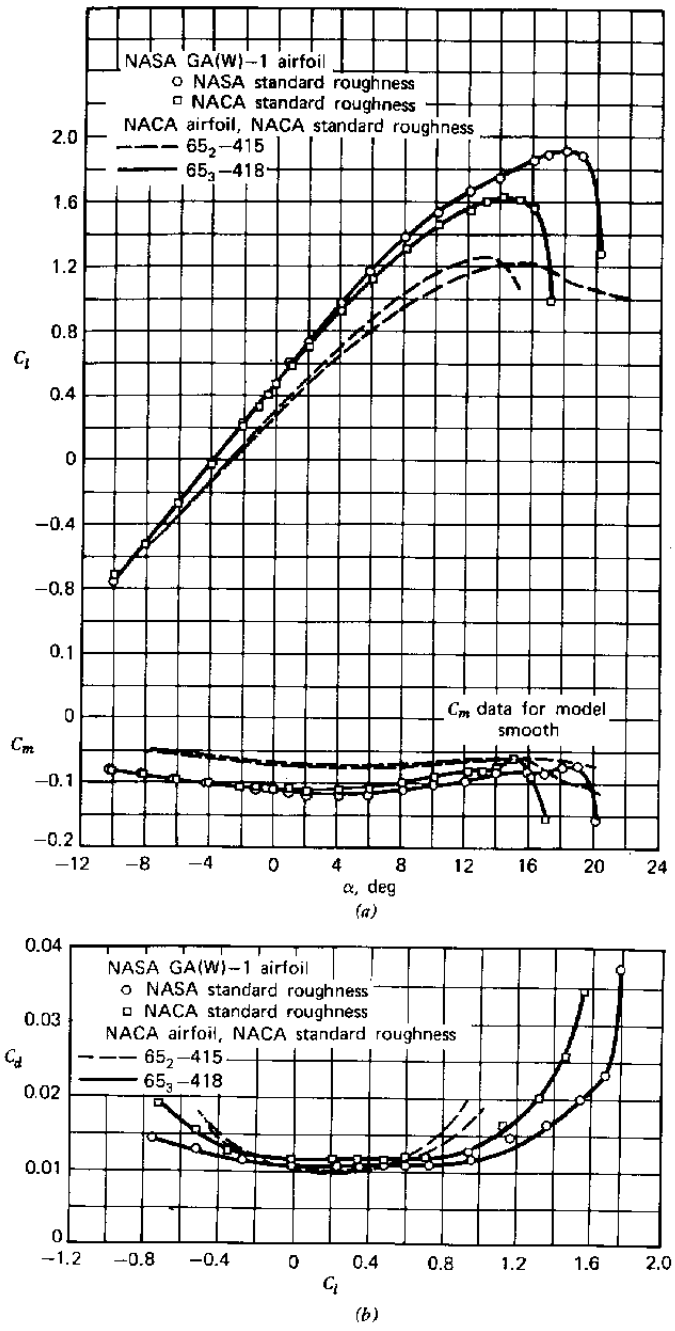

Figure 3.11 Comparison of section characteristics of NASA GA(W)-1 airfoil and NACA 65_2–415 and 65_3–418 airfoils. $M = 0.20$; $R \approx 6 \times 10^6$. (*a*) Variation of C_l and C_m with α. (*b*) Variation of C_d with C_l.

airfoils pictured in Figure 3.7. Test results for this airfoil are reported in Reference 3.8, where its $C_{l_{max}}$ values are shown to be about 30% higher than those for the older NACA 65-series airfoils. In addition, above C_l values of around 0.6, its drag is lower than the older laminar flow series with standard roughness. These data are presented in Figure 3.10 for the GA(W)-1 airfoil. Comparisons of $C_{l_{max}}$ and C_d for this airfoil with similar coefficients for other airfoils are presented in Figures 3.11 and 3.12.

Observe that the performance of the GA(W)-1 airfoil is very Reynolds number-dependent, particularly $C_{l_{max}}$, which increases rapidly with Reynolds number from 2 to 6 million. At the time of this writing, the GA(W) airfoil is beginning to be employed on production aircraft. The same is true of the supercritical airfoil. Indeed, the supercritical airfoil is being used on both the Boeing YC-14 and McDonnell-Douglas YC-15 prototypes currently being tested for the advanced medium STOL transport (AMST) competition. At the time of this writing, NASA is adopting a new nomenclature for the GA(W) airfoils. They will be designated by LS (low speed) or MS (medium speed) followed by four digits. For example, the GA(W)-1 airfoil becomes LS(1)-0417. The (1) designates a family. The 04 refers to a design lift coefficient of 0.4, and 17 is the maximum

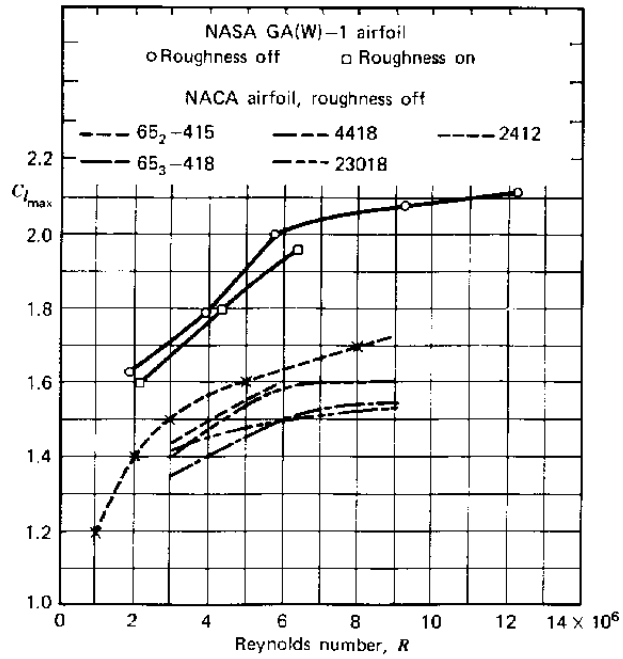

Figure 3.12 Comparison of maximum lift coefficient of the GA(W)-1 airfoil with other NACA airfoils $M = 0.15$.

thickness in percent of chord. For more information on modern airfoils, consult Reference 3.36.

PREDICTION OF AIRFOIL BEHAVIOR

In Chapter Two it was noted that the concepts of a point vortex and a point source could be extended to a continuous distribution of the elementary flow functions. In that chapter a distribution of sources in a uniform flow was found to produce a nonlifting body of finite thickness. In the case of the circular cylinder, the addition of a vortex also produced lift.

Comparable to the continuous distribution of sources pictured in Figure 2.20, consider a similar distribution of vortices as illustrated in Figure 3.13. Such a distribution is referred to as a vortex sheet. If γ is the strength per unit length of the sheet, $\gamma\,\Delta x$ will be the total strength enclosed by the dashed contour shown in the figure. The contour is taken to lie just above and below the sheet. Δx is sufficiently small so that the velocity tangent to the sheet, v, can be assumed to be constant. Because of the symmetry to the flow provided by any one segment of the sheet, the tangential velocity just below the sheet is equal in magnitude but opposite in direction to that just above the sheet. From Equation 2.55, relating circulation to the strength of a vortex, it follows that

$$\gamma\,\Delta x = 2v\,\Delta x$$

or

$$v = \frac{\gamma}{2} \tag{3.14}$$

Note the similarity of this relationship to that expressed by Equation 2.82. However, in the case of Equation 3.14, the velocity is tangent to the vortex sheet whereas, for Equation 2.82, the velocity is normal to the line on which the sources lie.

Consider now the thin airfoil pictured in Figure 3.14. If the airfoil is producing a lift, the pressure on the lower surface is greater than that on the upper. Hence, from Bernoulli's equation, the velocity on the upper surface is greater than the velocity on the lower surface. Letting this difference in

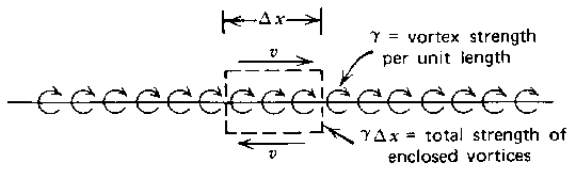

Figure 3.13 Distributed vortices in a two-dimensional flow (vortex sheet).

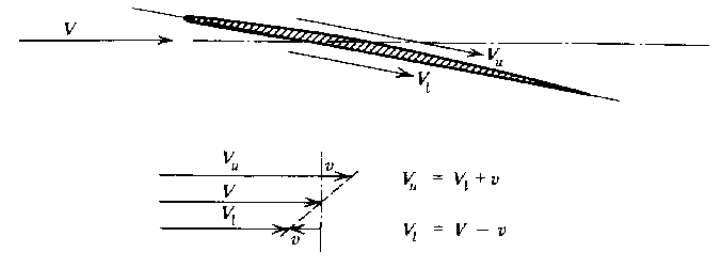

Figure 3.14 The velocity difference across a lifting thin airfoil.

velocity across the airfoil equal $2v$, the upper and lower velocities can be written as

$$V_u = V + v$$

and

$$V_l = V - v$$

Thus the flow field around the airfoil is the same as that which would be produced by placing, in a uniform flow of velocity V, a vortex sheet of unit strength 2v along the airfoil.

The contribution to the lift of a differential length of the airfoil will be

$$dl = (p_l - p_u)\,dx$$

Or, using Bernoulli's equation, this becomes,

$$dl = \rho V(2v)\,dx$$

Since $2v$ is the unit vortex strength, the Kutta–Joukowski law (Equation 2.81) is found to hold for the airfoil element.

$$dl = \rho V \gamma\,dx$$

or, integrating Equation 3.18 over the entire chord,

$$l = \rho V \Gamma \tag{3.15}$$

where Γ is the total circulation around the airfoil given by

$$\Gamma = \int_0^c \gamma\,dx \tag{3.16}$$

In order to predict the lift and moment on the airfoil, one must find the chordwise distribution of $\gamma(x)$ that will produce a resultant flow everywhere tangent to the mean camber line (thin airfoil approximation). In addition, the *Kutta* condition is applied at the trailing edge to assure that the flow *leaves* the trailing edge tangent to the mean camber line at that point. This is a

necessary condition; otherwise, the resulting flow will appear similar to Figure 3.4*a* with the lift being equal to zero.

An analytical solution to the thin airfoil will be obtained later but, first, let us consider a numerical approach to predicting the lift and moment of an airfoil.

As a gross approximation to the distributed vorticity along the airfoil, the distribution will be replaced by only one vortex of unknown strength, Γ. However, Γ will be placed at a particular point on the airfoil, at the quarter-chord point. The boundary condition and the Kutta condition will be satisfied at only one point, the three-quarter-chord point. This approximation, known as Weissinger's approximation, is illustrated in Figure 3.15 for a flat-plate airfoil.

The velocity induced at $3c/4$ *by* Γ placed at $c/4$ will be

$$v_i = \frac{\Gamma}{\pi c}$$

Assuming α to be a small angle, it follows that

$$v_i = V\alpha \tag{3.17}$$

or

$$\Gamma = \pi c V \alpha \tag{3.18}$$

From the Kutta–Joukowski relationship, $L = \rho V \Gamma$, so that

$$L = \rho \pi c V^2 \alpha \tag{3.19}$$

Expressing lift in terms of the lift coefficient and using Equation 3.19 leads to

$$C_l = 2\pi\alpha \tag{3.20}$$

where α is the angle of attack in radians.

The expression agrees identically with the theoretical solution of this problem that follows. Notice that the result predicts the slope of the lift curve, $dC_l/d\alpha$, to be 2π/rad. Experimentally this figure is usually found to be

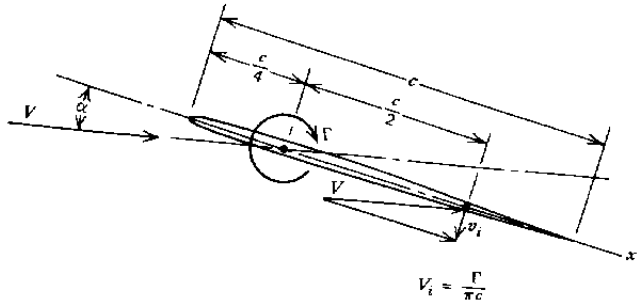

Figure 3.15 Weissinger's approximation to a thin airfoil.

somewhat less. Figures 3.5 and 3.6, for example, show a value of around 0.105/deg or 6.02/rad.

The approximation of Figure 3.15 can be improved on by dividing the airfoil chord into a number of equal segments and placing a vortex of unknown strength at the *quarter-chord point of each segment*. The unknown strengths are determined by assuring that the normal velocity vanishes at the *three-quarter-chord point of each segment*. With the last control point downstream of the last vortex singularity, the Kutta condition is assured.

To illustrate this numerical solution of the thin airfoil, consider Figure 3.16. Here, a circular arc airfoil having a unit chord length with a maximum camber ratio of z is operating at an angle of attack α.

If it is assumed that

$$z \ll 1 \tag{3.21}$$

the radius of curvature, R, of the airfoil will be related to z approximately by

$$R = \frac{1}{8z}$$

The slope of the camber line relative to the chord line (the angle ϕ in Figure 3.16) at any distance x can be determined from the geometry of the figure.

$$\phi = (4 - 8x)z \tag{3.22}$$

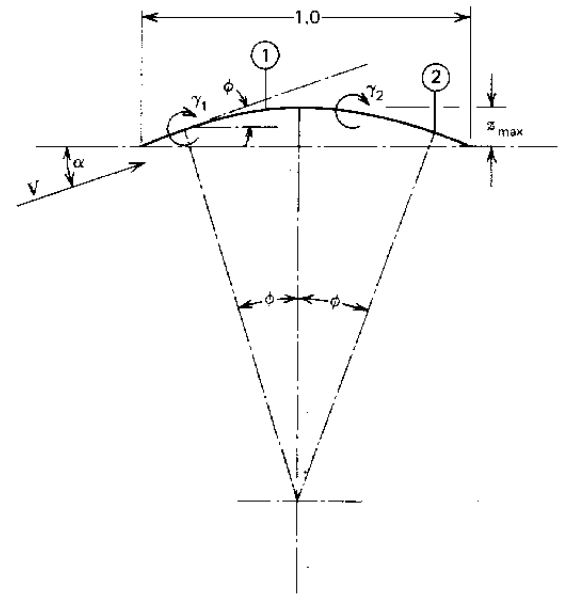

Figure 3.16 A circular arc airfoil approximated by two vortices.

The component of V normal to the mean camber line and directed upward is thus

$$v_n = V(\alpha - \phi)$$

It follows that at control points 1 and 2 located at x values of $3c/8$ and $7c/8$, respectively, the two vortices similating the airfoil must induce velocities downward given by

$$v_i = V(\alpha - z) \quad \text{at} \quad 1 \tag{3.23a}$$

$$v_i = V(\alpha + 3z) \quad \text{at} \quad 2 \tag{3.23b}$$

The problem is linearized by Equation 3.21 so that the vortices, γ_1 and γ_2, are taken to lie on the chord line. Thus, according to Equation 2.56, the total velocities induced at the two control points by the two vortices will be

$$v_i = \frac{1}{\pi}(2\gamma_1 - 2\gamma_2) \quad \text{at 1} \tag{3.24a}$$

$$v_i = \frac{1}{\pi}\left(\frac{2}{3}\gamma_1 + 2\gamma_2\right) \quad \text{at 2} \tag{3.24b}$$

Equating Equations 3.23 and 3.24 results in

$$\gamma_1 = \frac{3\pi V}{4}(\alpha + z) \tag{3.25a}$$

$$\gamma_2 = \frac{\pi V}{4}(\alpha + 5z) \tag{3.25b}$$

Applying the Kutta–Joukowski law to each vortex results not only in a predicted total lift, but also in a moment. In coefficient form the lift and moment (about the leading edge) become

$$C_l = 2\pi(\alpha + 2z) \tag{3.26a}$$

$$C_{m_{LE}} = -\pi\left(\frac{\alpha}{2} + \frac{7z}{4}\right) \tag{3.26b}$$

The moment coefficient about the leading edge can be transferred to the quarter-chord point by using

$$C_{m_{1/4}} = c_{m_{LE}} + \frac{1}{4}C_L$$

Thus,

$$C_{m_{1/4}} = -\frac{3\pi z}{4} \tag{3.27}$$

This simple, two-point model results in several important observations that are in agreement with more exact solutions. First, note that Equation 3.26*a* shows the lift coefficient to be a linear combination of α and z. Thus,

cambering an airfoil will not change the slope of the lift curve. Second, it is predicted that the moment about the quarter chord will be independent of α. Hence, this point is predicted to be the aerodynamic center.

As one divides the airfoil into a greater and greater number of elements, the resulting γ distributions will approach the theoretical pressure distribution predicted on the basis of continuous γ distributions. The strength, γ, of a vortex placed at the $c/4$ point of an element of length Δx will be related to the pressure jump, Δp, across the element by

$$\Delta p = \frac{\rho V \gamma}{\Delta x} \tag{3.28}$$

Figure 3.17 presents a comparison, for the flat-plate airfoil, between the pressure distribution obtained using the foregoing numerical procedure with that based on a continuous distribution of γ along the chord. It is seen that the numerical results rapidly converge to the continuous solution as the number of elements increases. In preparing this figure it should be noted that Δp, given by Equation 3.28, has been expressed in coefficient form and plotted at the location of each point vortex. Figure 3.18 presents a similar comparison for the circular arc airfoil. In this case α is taken to be zero, avoiding the infinitely negative C_p at the leading edge.

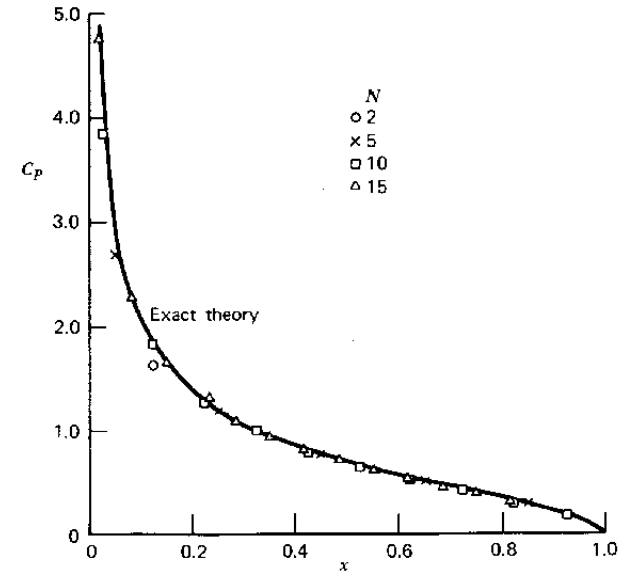

Figure 3.17 Comparison of numerical calculation of chordwise lift distribution with analytical prediction for a flat-plate airfoil at 10° angle of attack.

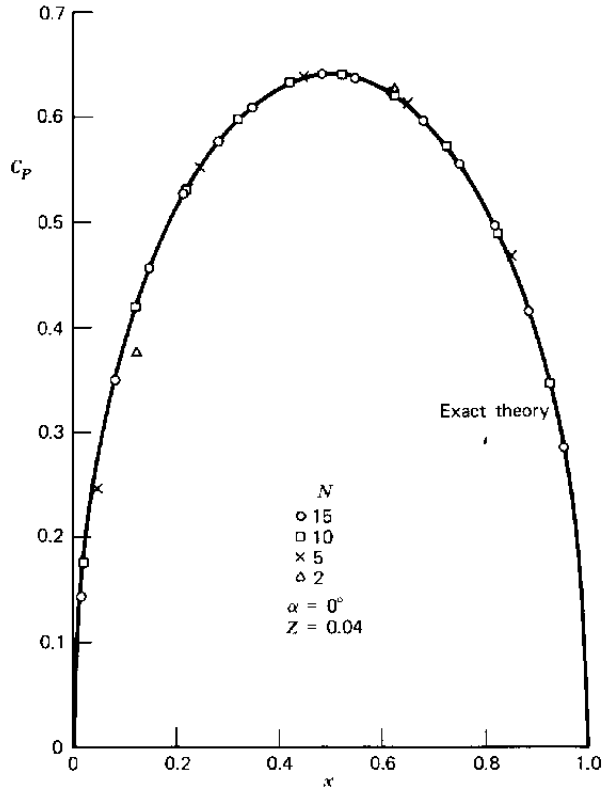

Figure 3.18 Comparison of numerical calculation of chordwise lift distribution with analytical prediction for a 4% cambered, circular arc airfoil.

The numerical model predicts the lift in exact agreement with more precise analytical models. However, the moment coefficient, given by Equation 3.27, is only three-quarters of that obtained by analytical means. Figure 3.19 shows that the exact value is approached rapidly, however, as the number of segments increases.

As indicated by Figure 3.19, the exact value of the moment coefficient about the aerodynamic center ($c/4$) for the circular arc airfoil is given by

$$C_{m_{ac}} = -\pi z \tag{3.29}$$

Using Equation 3.13, the location of the center of pressure can be found as

$$X_{cp} = \frac{1}{4} + \frac{\pi z}{C_l} \tag{3.30}$$

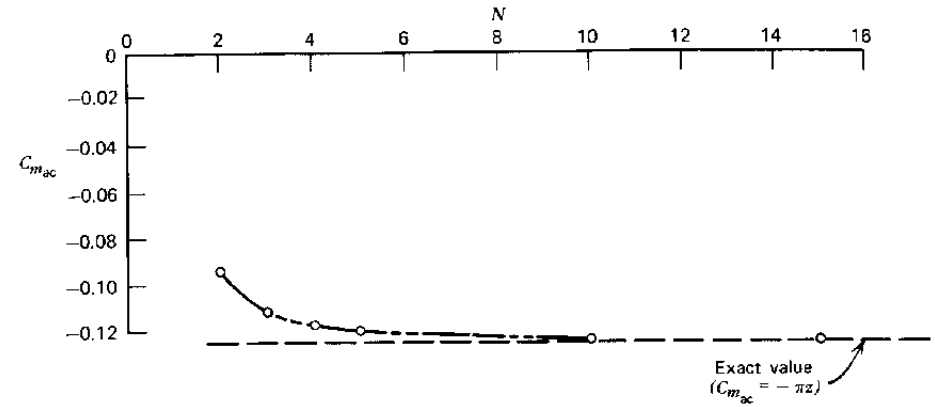

Figure 3.19 Numerical calculation of moment coefficient compared with analytical prediction for 4% cambered, circular arc airfoil.

Observe that as C_l decreases, the center of pressure moves aft, approaching infinity as C_l goes to zero. This movement of the center of pressure is opposite to what was believed to be true by the early pioneers in aviation. The Wright Brothers were probably the first to recognize the true nature of the center-of-pressure movement as a result of their meticulous wind tunnel tests.

Analytical solutions to the thin airfoil can be found in several texts (e.g., Ref. 3.2 and 3.3). Here, the airfoil is replaced by a continuous distribution of vortices instead of discrete point vortices, as used with the numerical solution.

Referring to Figure 3.20, without any loss of generality, the airfoil is taken to have a unit chord lying along the x-axis with the origin at the leading

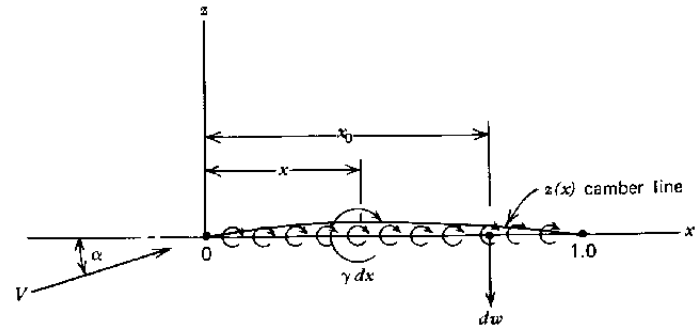

Figure 3.20 The modeling of a thin airfoil by a vortex sheet.

edge. The shape of the camber line is given by $z(x)$, and it is assumed that

$$z(x) \ll 1$$

With this assumption the problem is linearized and made tractable by replacing the airfoil with a vortex sheet of unit strength $\gamma(x)$ lying along the chord line instead of along the camber line.

At the point x_0, the downward velocity induced by an elemental vortex of strength $\gamma(x)\,dx$ located at x, according to Equation 2.56, will be given by

$$dw(x_0) = \frac{\gamma(x)\,dx}{2\pi(x_0 - x)}$$

or, integrating over the chord,

$$w(x_0) = \frac{1}{2\pi}\int_0^1 \frac{\gamma(x)\,dx}{x_0 - x} \tag{3.31}$$

In order to satisfy the boundary condition that the flow be tangent everywhere to the mean camber line, it follows that, to a small angle approximation,

$$\frac{w(x_0)}{V} = \alpha - \left(\frac{dz}{dx}\right)_{x_0} \tag{3.32}$$

Thus, given α and $z(x)$, the following integral equation must be solved for $\gamma(x)$.

$$\frac{1}{2\pi V}\int_0^1 \frac{\gamma(x)\,dx}{x_0 - x} = \alpha - \left(\frac{dz}{dx}\right)_{x_0} \tag{3.33}$$

In addition, $\gamma(x)$ must vanish at the trailing edge in order to satisfy the Kutta condition. Otherwise, the induced velocity will be infinite just downstream of this point.

Equation 3.33 is solved by first transforming to polar coordinates.

Letting

$$x = \frac{1}{2}(1 - \cos\theta) \tag{3.34}$$

Equation 3.33 becomes

$$\frac{1}{2\pi V}\int_0^\pi \frac{\gamma(\theta)\,d\theta}{\cos\theta - \cos\theta} = \alpha - \left(\frac{dz}{dx_{x_0}}\right) \tag{3.35}$$

On the basis of the more sophisticated method of conformal mapping (e.g., see Ref. 3.4), it is known that $\gamma(x)$ is generally singular at the leading edge approaching infinity as $1/x$. Thus we will assume a priori that Equation 3.35 can be satisfied by a $\gamma(\theta)$ distribution of the form

$$\gamma = 2V\left[A_0\frac{(1+\cos\theta)}{\sin\theta} + \sum_{n=1}^{\infty} A_n \sin n\theta\right] \tag{3.36}$$

Using the relationships

$$\frac{1}{2}\Big[\cos(n-1)\theta - \cos(n+1)\theta\Big] = \sin n\theta \sin\theta$$

and

$$\int_0^\pi \frac{\cos n\theta\,d\theta}{\cos\theta - \cos\theta_0} = \pi\frac{\sin n\theta_0}{\sin\theta_0} \tag{3.37}$$

Equation 3.35 becomes

$$A_0 - \sum_{n=1}^{\infty} A_n \cos n\theta = \alpha - \frac{dz}{dx}$$

Multiplying both sides of the preceding equation by $\cos m\theta$ ($m = 0, 1, 2, \ldots, n, \ldots$) and integrating from 0 to π leads to

$$A_0 = \alpha - \frac{1}{\pi}\int_0^\pi \frac{dz}{dx}\,d\theta \tag{3.38a}$$

$$A_n = \frac{2}{\pi}\int_0^\pi \frac{dz}{dx}\cos n\theta\,d\theta \tag{3.38b}$$

Thus, knowing the shape of the mean camber line, the coefficients A_0, A_1, $A_2, \ldots$ can be determined either in closed form or by graphical or numerical means (see Ref. 3.1). Having these coefficients, C_l and C_m can then be easily determined from the Kutta–Joukowski relationship.

The lift and moment about the leading edge are given by

$$L = \int_0^1 \rho V\gamma(x)\,dx$$

$$M_{LE} = \int_0^1 \rho V\gamma(x)\times dx$$

From these and using Equation 3.36,

$$C_l = 2\pi A_0 + \pi A_1 \tag{3.39}$$

$$C_{m_{LE}} = -\frac{\pi}{2}\left(A_0 + A_1 - \frac{A_2}{2}\right) \tag{3.40}$$

It follows that C_m about the quarter-chord point is independent of α, so that this point is the aerodynamic center, with the moment coefficient being given by

$$C_{m_{ac}} = -\frac{\pi}{4}(A_1 - A_2) \tag{3.41}$$

Since α is contained only in the A_0 coefficient, it can be concluded immediately without considering the actual form of $z(x)$ that C_l is given by a

linear combination of α and a function of z. Thus, camber changes can be expected to affect the angle of zero lift but not the slope of the lift curve.

Reference to airfoil data, such as that presented in Figures 3.5 and 3.6, will show that the predictions of thin airfoil theory are essentially correct. There is a range of angles of attack over which the lift coefficient varies linearly with α. The slope of this lift curve is usually not as high as the theory predicts, being approximately 4 to 8% less than the theoretical value. For many purposes an assumed value of 0.1 C_l/deg is sufficiently accurate and is a useful number to remember. Experimental data also show the aerodynamic center to be close to the quarter-chord point. The effects of camber on C_l, $dC_l/d\alpha$, and $C_{m_{ac}}$ are also predicted well.

Recently large numerical programs have been developed to predict the performance of airfoils that incorporate Reynolds number and Mach number effects. These are typified by Reference 3.5, which will be described briefly. This program begins by calculating the potential flow around the airfoil. In order to allow for both finite thickness and circulation, the airfoil contour is approximated by a closed polygon, as shown in Figure 3.21. A continuous distribution of vortices is then placed on each side of the polygon, with the vortex strength per unit length, γ, varying linearly from one corner to the next and continuous across the corner. Figure 3.22 illustrates this model for two sides connecting corners 3, 4, and 5. Control points are chosen midway between the corners. The values of the vortex unit strengths at the corners are then found that will induce velocities at each control point tangent to the polygon side at that point. Note, however, that if there are n corners and hence $n+1$ unknown γ values at the corners, the n control points provide one less equation than unknowns. This situation is remedied by applying the Kutta condition at the trailing edge. This requires that $\gamma_{n+1} = -\gamma_1$, assuring that the velocities induced at the trailing edge are finite.

Having determined the vortex strengths, the velocity field and, hence, the

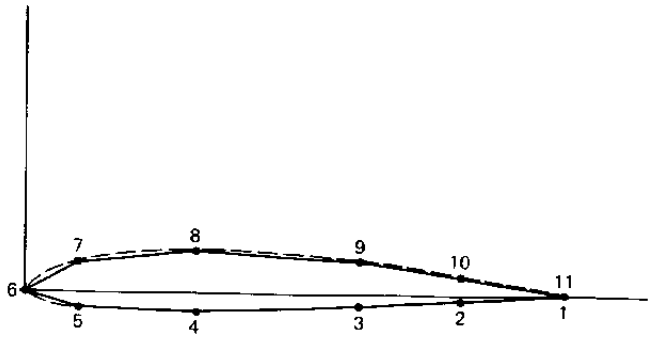

Figure 3.21 Approximation of airfoil contour by closed polygon.

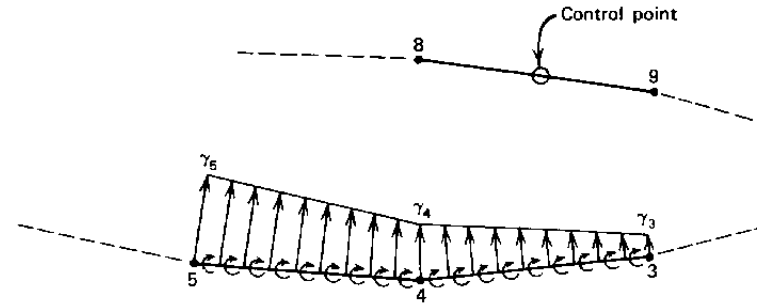

Figure 3.22 Vortex distributions representing airfoil contour.

pressure distribution around the airfoil can be calculated. This result is then used to calculate the boundary layer development over the airfoil, including the growth of the laminar layer, transition, the growth of the turbulent layer, and possible boundary layer separation. The airfoil shape is then enlarged slightly to allow for the boundary layer thickness and the potential flow solutions are repeated. The details of this iterative procedure are beyond the scope of this text.

MAXIMUM LIFT

Airfoil theory based on potential flow methods predicts the lift of an airfoil in its linear range but does not provide any information concerning maximum lift capability. As discussed previously, $C_{l_{max}}$, is determined by flow separation, which is a "real fluid" effect. Separation is difficult to predict analytically, so the following material on $C_{l_{max}}$ is mainly empirical.

Typically, conventional airfoils without any special high-lift devices will deliver $C_{l_{max}}$ values of approximately 1.3 to 1.7, depending on Reynolds number, camber, and thickness distribution. The appreciable dependence of $C_{l_{max}}$ on R shown in Figure 3.12 for the GA(W)-1 airfoil is typical of other airfoils. Figure 3.23 presents $C_{l_{max}}$ as a function of R and thickness ratio for NACA four-digit airfoils having a maximum camber of 2%, located 40% of the chord back from the leading edge. At intermediate thickness ratios of around 0.12, the variation of $C_{l_{max}}$ with R parallels that of the 17% thick GA(W)-1 airfoil. Note, at least for this camber function, that a thickness ratio of 12% is about optimum. This figure is taken from Reference 3.14. This same reference presents the following empirical formula for $C_{l_{max}}$ for NACA four-digit airfoils at an R of 8×10^6.

$$C_{l_{max}} = 1.67 + 7.8\,pz - 2.6\,\frac{(0.123 + 0.022 - 0.5z - t)^2}{t^{3/2}} \qquad (3.42)$$

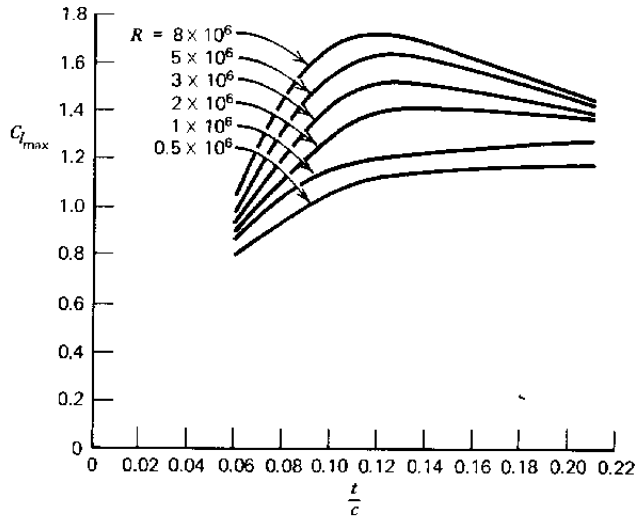

Figure 3.23 Variation of $C_{l_{max}}$ with thickness ratio of NACA 24xx airfoils for various Reynolds numbers. (B. W. McCormick, *Aerodynamics of V/STOL Flight*, Academic Press, Inc, 1967. Reprinted by permission of Academic Press, Inc.)

t, z, and p are thickness, maximum camber, and position of maximum camber, respectively, expressed as a fraction of the chord. For example, for a 2415 airfoil,

$$t = 0.15$$
$$z = 0.02$$
$$p = 0.40$$

so that according to Equation 3.42,

$$C_{l_{max}} = 1.70$$

For a plain wing (unflapped), there is little effect of aspect ratio or taper ratio on $C_{L_{max}}$. Even the presence of a fuselage does not seem to have much effect. As the angle of attack of a wing increases, $C_{L_{max}}$ is reached and any further increase in α will result in a loss of lift. Beyond $C_{L_{max}}$ the wing is said to be stalled. Although taper ratio does not significantly affect the overall wing $C_{L_{max}}$, it (and wing twist) significantly affect what portion of the wing stalls first. As the taper ratio is decreased, the spanwise position of initial stall moves progressively outboard. This tendency is undesirable and can be compensated for by "washing out" (negative twist) the tips. One usually wants a wing to stall inboard initially for two reasons. First, with inboard stall, the turbulence shed from the stalled region can shake the tail, providing a built-in stall warning device. Second, the outboard region being unstalled will still provide

aileron roll control even though the wing has begun to stall. The lift characteristics of three-dimensional wings will be treated in more detail later.

Flaps

An examination of all of the airfoil data presented in Reference 3.1 discloses that the greatest value of $C_{l_{max}}$ one can expect at a high Reynolds number from an ordinary airfoil is around 1.8. This maximum value is achieved by the NACA 23012 airfoil. Another 12% thick airfoil, the 2412, delivers the second highest value, 1.7.

In order to achieve higher $C_{l_{max}}$ values for takeoff and landing without unduly penalizing an airplane's cruising performance, one resorts to the use of mechanical devices to alter temporarily the geometry of the airfoil. These devices, known as flaps, exist in many different configurations, the most common of which are illustrated in Figure 3.24. In addition to the purely mechanical flaps, this figure depicts flaps that can be formed by sheets of air exiting at the trailing edge. These "jet flaps" can produce $C_{l_{max}}$ values in excess of those from mechanical flaps, provided sufficient energy and momentum are contained in the jet. Frequently one uses the terms "powered" and "unpowered" to distinguish between jet and mechanical flaps.

The effect of a mechanical flap can be seen by referring once again to Figure 3.6. Deflecting the flap, in this case a split flap, is seen to shift the lift curve upward without changing the slope. This is as one might expect from Equation 3.26, since deflecting the flap is comparable to adding camber to the airfoil.

Some flap configurations appear to be significantly better than others simply because, when deflected, they extend the original chord on which the lift coefficient is based. One can determine if the flap is extensible, such as the Fowler or Zap flaps in Figure 3.24, by noting whether or not the slope of the lift curve is increased with the flap deflected. Consider a flap that, when deflected, extends the original chord by the fraction x. The physical lift curve would have a slope given by

$$\frac{dL}{d\alpha} = \frac{1}{2}\rho V^2(1+x)cC_{l_\alpha} \tag{3.43}$$

since $(1+x)c$ is the actual chord. C_{l_α} does not depend significantly on thickness or camber; hence, the lift curve slope of the flapped airfoil based on the unflapped chord, c, would be

$$C_{l_\alpha}\text{ (flapped)} = (1+x)C_{l_\alpha}\text{ (unflapped)}$$

Now the maximum lift, expressed in terms of the extended chord and $C_{l_{max_e}}$

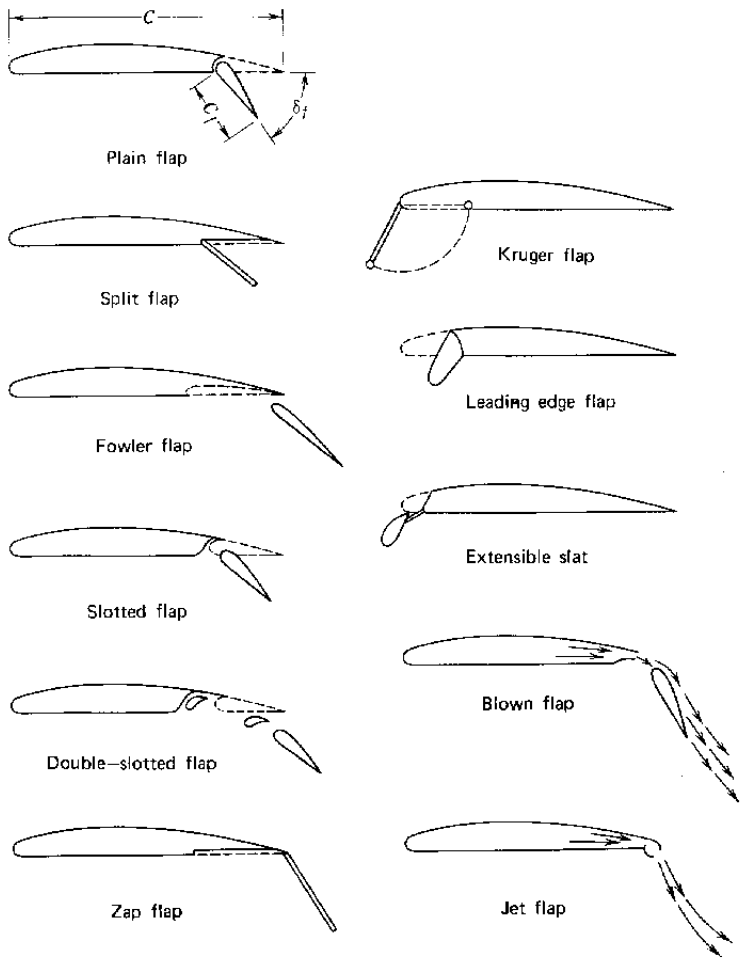

Figure 3.24 Flap configurations.

(based on that chord) would be,

$$L_{\max} = \frac{1}{2}\rho V^2(1+x)cC_{l_{\max_e}}$$

Thus $C_{l_{\max}}$ based on the original chord becomes

$$C_{l_{\max}} = (1+x)C_{l_{\max_e}}$$

or

$$C_{L_{\max_e}} = C_{l_{\max}}/(1+x)$$

$$= C_{l_{\max}} \frac{C_{l_\alpha}\ \text{(unflapped)}}{C_{l_\alpha}\ \text{(flapped)}} \qquad (3.44)$$

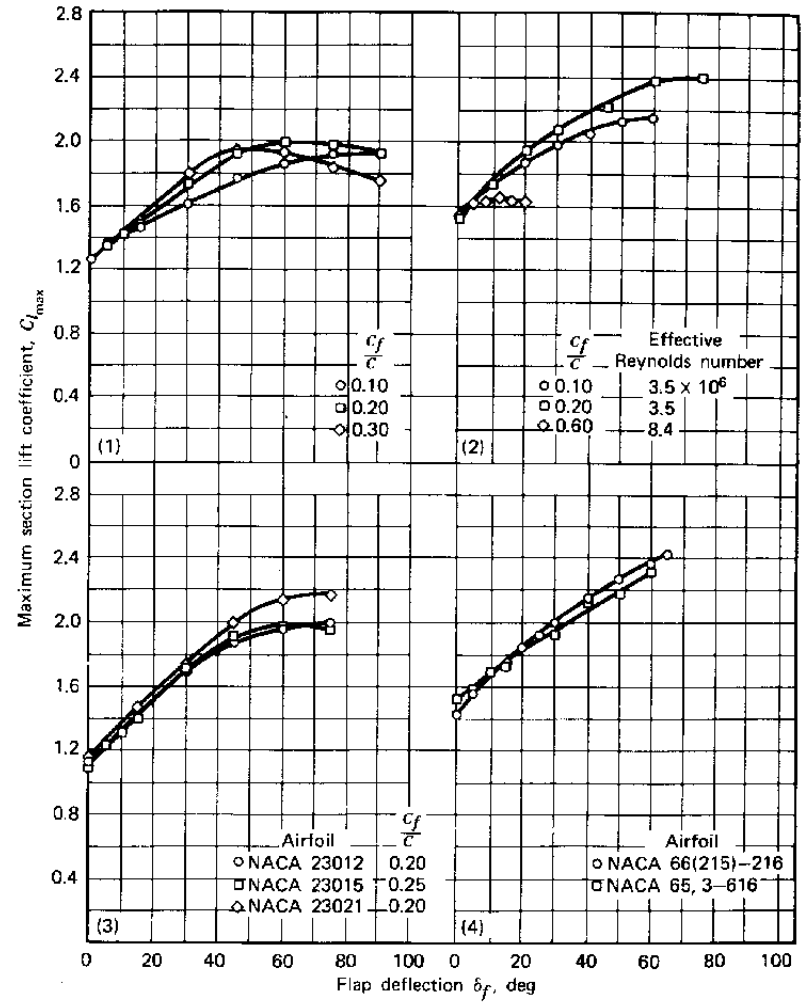

(1) Clark–Y airfoil; $R = 0.609 \times 10^6$.

(2) NACA 230–series airfoils; $R = 0.609 \times 10^6$.

(3) NACA 23012 airfoil.

(4) NACA 6–series airfoils; $R = 6.0 \times 10^6$, $\frac{c_f}{c} = 0.20$.

(a)

Figure 3.25 Performance of plain flaps. (*a*) Variation of maximum section lift coefficient with flap deflection for several airfoil sections equipped with plain flaps. (*b*) Variation of optimum increment of maximum section lift coefficient with flap chord ratio for several airfoil sections equipped with plain flaps. (*c*) Effect of gap seal on maximum lift coefficient of a rectangular Clark-Y wing equipped with a full-span 0.20*c* plain flap. $A = 6$, $R = 0.6 \times 10^4$.

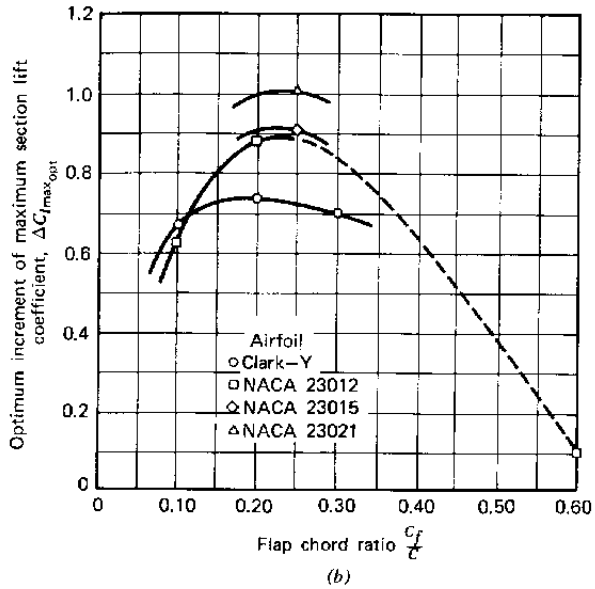

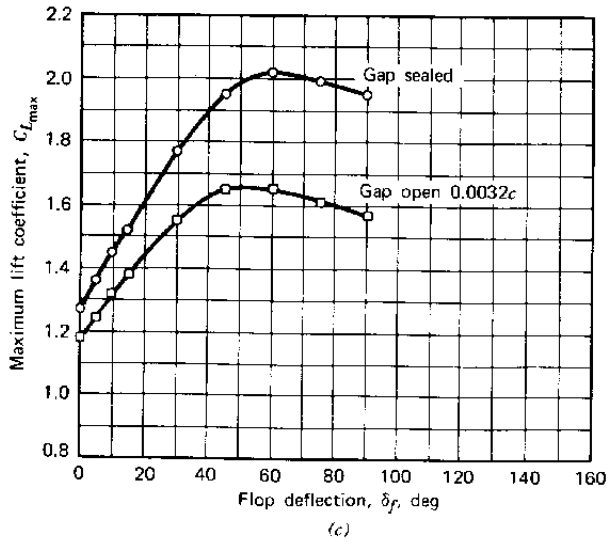

Figure 3.25 (Continued)

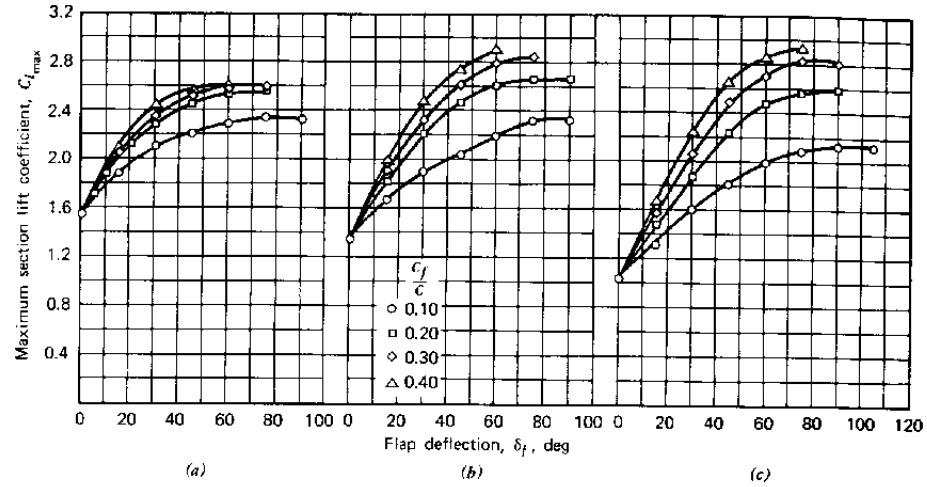

Figure 3.26 Variation of maximum section lift coefficient with flap deflection for three NACA 230-series airfoils equipped with split flaps of various sizes. $R = 3.5 \times 10^6$. (*a*) NACA 23012 airfoil section. (*b*) NACA 23021 airfoil section. (*c*) NACA 23030 airfoil section.

Figures 3.25 to 3.30 and Tables 3.1 and 3.2 present section data on plain, split, and slotted flaps as reported in Reference 3.15. With these data one should be able to estimate reasonably accurately the characteristics of an airfoil section equipped with flaps.

A study of this data suggests the following:

Plain Flaps

1. The optimum flap chord ratio is approximately 0.25.
2. The optimum flap angle is approximately 60°.
3. Leakage through gap at flap nose can decrease $C_{l_{max}}$ by approximately 0.4.
4. The maximum achievable increment in $C_{l_{max}}$ is approximately 0.9.

Split Flaps

1. The optimum flap chord ratio is approximately 0.3 for 12% thick airfoils, increasing to 0.4 or higher for thicker airfoils.
2. The optimum flap angle is approximately 70°.
3. The maximum achievable increment in $C_{l_{max}}$ is approximately 0.9.
4. $C_{l_{max}}$ increases nearly linearly with log R for $0.7 \times 10^6 < R < 6 \times 10^6$.
5. The optimum thickness ratio is approximately 18%.

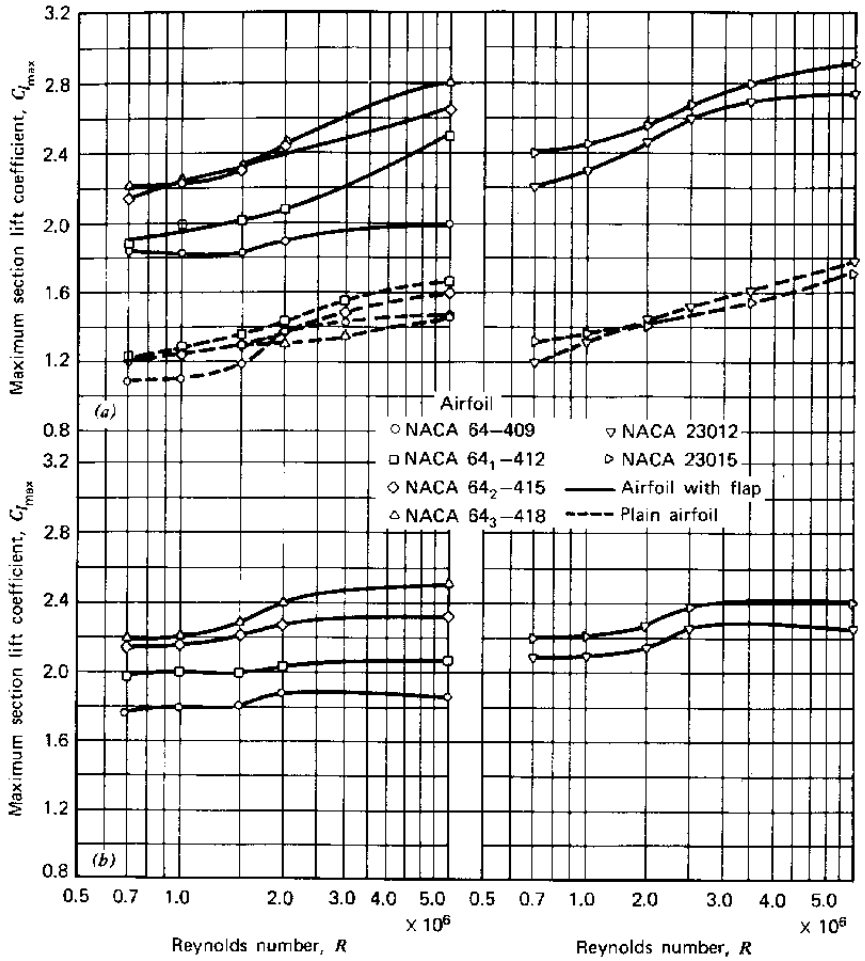

Figure 3.27 Variation of maximum section lift coefficient with Reynolds number for several NACA airfoil sections with and without 0.20c split flaps deflected 60°. (*a*) Smooth airfoil. (*b*) Airfoil with leading edge roughness.

Slotted Flaps

1. The optimum flap chord ratio is approximately 0.3.
2. The optimum flap angle is approximately 40° for single slots and 70° for double-slotted flaps.
3. The optimum thickness ratio is approximately 16%.
4. $C_{l_{max}}$ is sensitive to flap (and vane) position.
5. The maximum achievable increment in $C_{l_{max}}$ is approximately 1.5 for single slots and 1.9 for double slotted flaps.

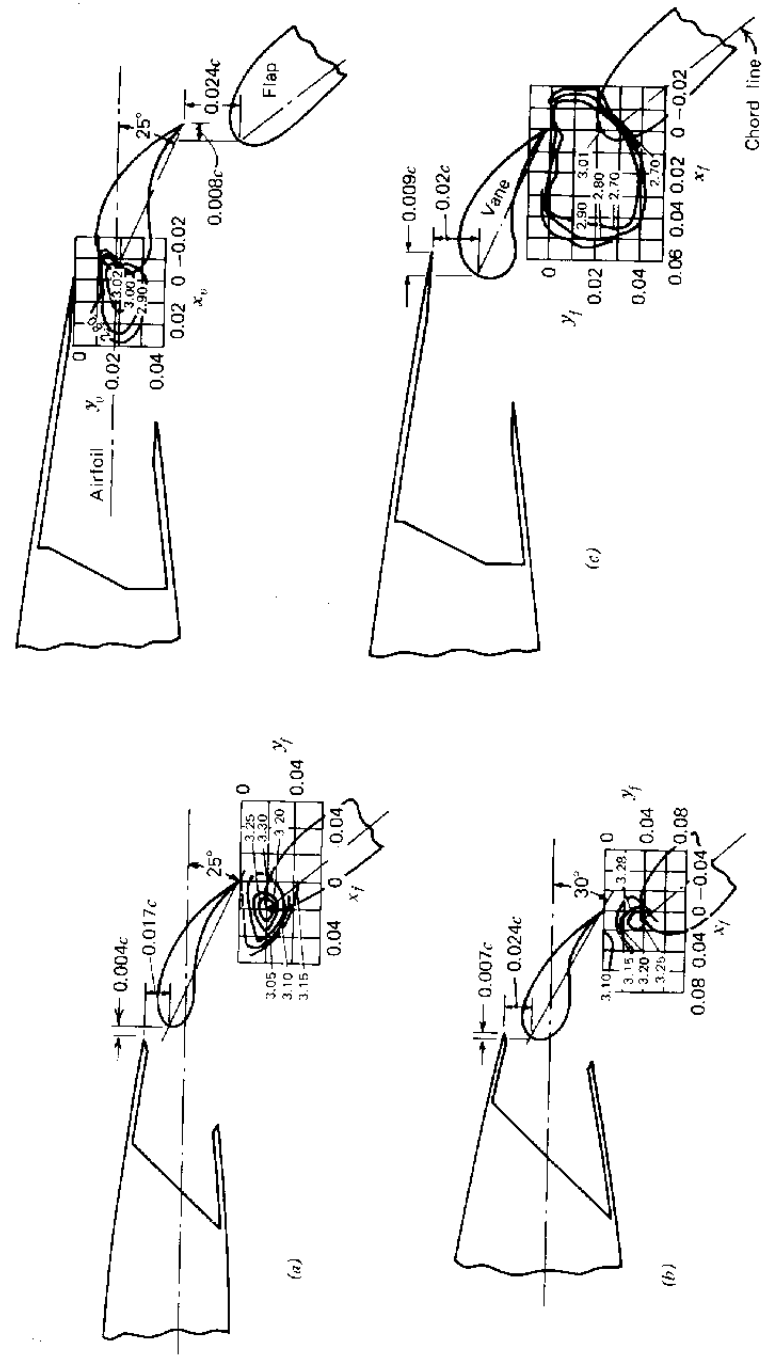

Figure 3.28 Contours of flap and vane positions for maximum section lift coefficient for several airfoil sections equipped with double-slotted flaps. (*a*) NACA 23012 airfoil section; $\delta_f = 60°$. (*b*) NACA 23021 airfoil section; $\delta_f = 60°$. (*c*) NACA 61$_1$–212 airfoil section.

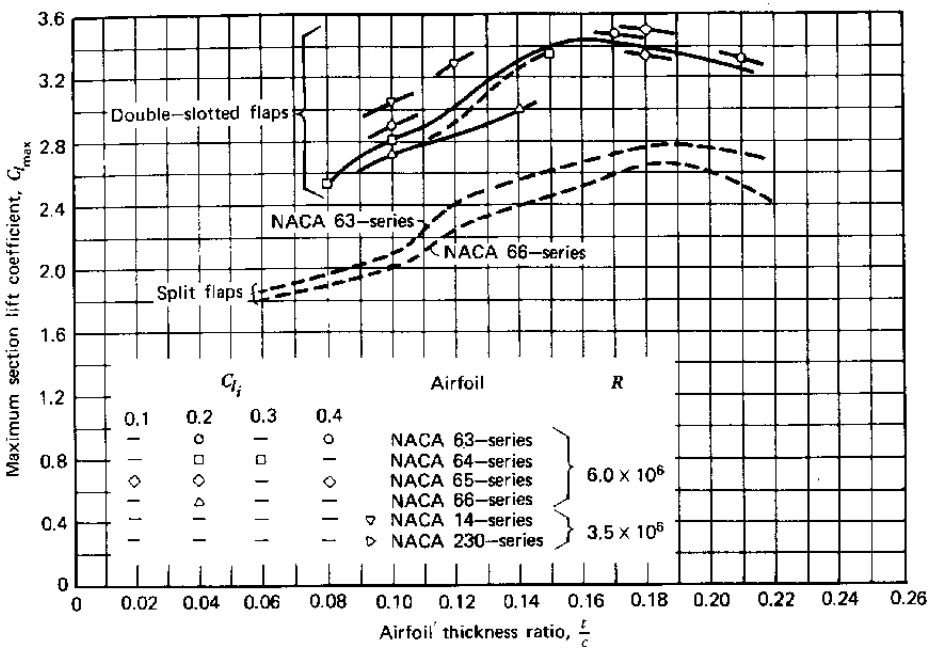

Figure 3.29 Maximum section lift coefficients for several NACA airfoil sections with double-slotted and split flaps.

Referring to Equation 3.44 and Figure 3.30, it is obvious that some of the superior performance of the double-slotted flap results from the extension of the chord. From the figure, C_{l_α} (flapped) is equal to 0.12 C_l/deg as compared to the expected unflapped value of approximately 0.1. Hence, based on the actual chord, the increment in $C_{L_{max}}$ for the double-slotted flap is only 1.6. However, this is still almost twice that afforded by plain or split flaps and points to the beneficial effect of the slot in delaying separation.

Figure 3.31 (taken from Ref. 3.15) presents pitching moment data for flapped airfoil sections. The lift and moment are taken to act at the aerodynamic center of the airfoil, located approximately 25% of the chord back from the leading edge. The moment is positive if it tends to increase the angle of attack.

From Figure 3.31, the lowering of a flap results in an incremental pitching moment. In order to trim the airplane a download must be produced on the horizontal tail. The wing must now support this download in addition to the aircraft's weight. Hence the effective increment in lift due to the flap is less than that which the wing-flap combination produces alone. This correction can typically reduce $\Delta C_{L_{max}}$ by 0.1 to 0.3.

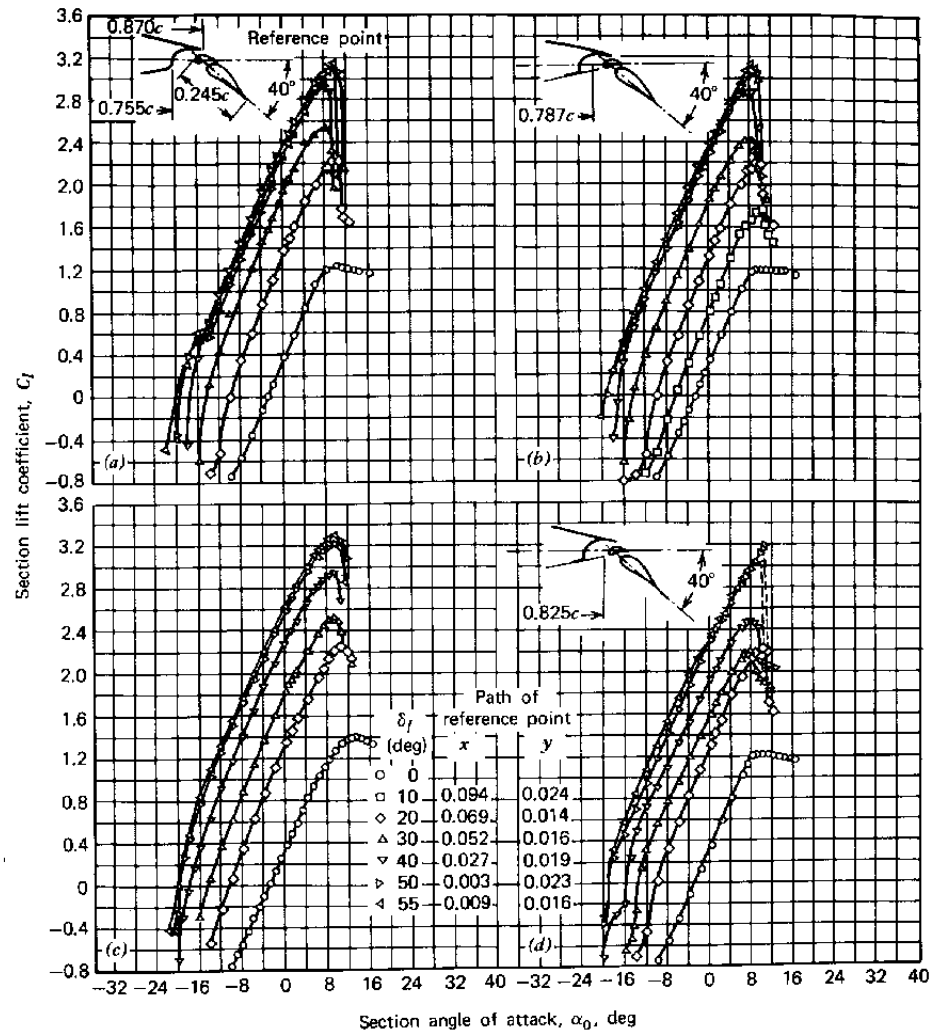

Figure 3.30 Section lift characteristics of an NACA 63, 4-421 (approximately) airfoil equipped with a double-slotted flap and several slot-entry-skirt extensions. (*a*) No skirt extension; $R = 2.4 \times 10^4$. (*b*) Partial skirt extension; $R = 2.4 \times 10^6$. (*c*) Partial skirt extension; $R = 6.0 \times 10^6$. (*d*) Full skirt extension; $R = 2.4 \times 10^6$.

Table 3.1 Maximum Lift Coefficients of Airfoil Sections Equipped with Single-Slotted Flaps

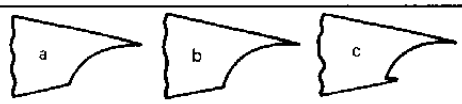

Slot–entry configuration

Flap nose shapes

Airfoil Section	c_f/c	c_a	Slot-Entry configuration	Flap Nose Shape	$C_{l_{max}}$	δf (deg)	x_f	y_f	Optimum Position	R
Clark Y	0.20	1.00	b	A	2.44	30	0	−0.025	Yes	0.61 × 10
Clark Y	0.30	1.00	b	A	2.83	40	0	−0.025	Yes	0.61
Clark Y	0.40	1.00	b	A	3.10	40	0	−0.025	Yes	0.61
23012	0.10	0.93	a	A	2.25	50	0.004	0.005	Yes	3.5
23012	0.15	1.00	b	A	2.68	30	0	0.015	Yes	3.5
23012	0.25	1.00	b	A	3.22	40	0	0.015	Yes	3.5
23012	0.256	0.800	a	B	2.76	50	0.005	0.018	Yes	3.5
23012	0.257	0.83	a	A	2.81	50	0.005	0.016	Yes	3.5
23012	0.257	0.83	a	A	2.83	40	0.013	0.024	Yes	3.5
23012	0.267	1.00	b	A	2.90	30	0	0.025	No	3.5
23012	0.30	0.90	c	A	2.92	50	0.002	0.010	No	3.5
23012	0.30	0.90	c	A	2.92	40	0.002	0.020	No	3.5
23012	0.30	0.90	c	A	2.93	30	0.002	0.030	No	3.5
23012	0.30	0.90	b	A	2.88	40	0.002	0.020	No	3.5
23012	0.30	1.00	b	A	3.29	40	0	0.015	No	3.5
23012	0.40	0.715	b	A	2.87	50	0.015	0.015	Yes	3.5
23012	0.40	0.715	a	A	2.90	50	0.015	0.015	Yes	3.5
23012	0.15	1.00	b	A	2.59	60	0	0.015	No	3.5
23021	0.15	1.00	b	A	2.66	60	0.050	0.030	Yes	3.5
23021	0.25	1.00	b	A	3.17	40	0.025	0.015	Yes	3.5
23021	0.257	0.827	b	B	2.69	60	0	0.015	Yes	3.5
23021	0.257	0.827	a	B	2.74	60	0	0.015	Yes	3.5
23021	0.257	0.827	b	A	2.71	60	0.005	0.020	Yes	3.5
23021	0.257	0.827	a	A	2.82	50	0	0.025	Yes	3.5
23021	0.40	0.715	b	A	2.79	50	0.015	0.025	Yes	3.5
23021	0.40	0.715	a	A	2.88	50	0.015	0.045	Yes	3.5
23030	0.257	0.860	b	B	2.59	60	0.025	0.040	Yes	3.5
23030	0.257	0.860	a	B	2.68	60	−0.005	0.040	Yes	3.5
23030	0.40	0.775	b	B	2.82	50	0.025	0.060	Yes	3.5
23030	0.40	0.775	a	B	2.90	50	0.025	0.060	Yes	3.5
63,4–420	0.25	0.88	b	B	3.00	35	0.018	0.045	No	6.0
3,4–421 (approximately)	0.243	0.835	a	A	3.21	40	0	0.027	Yes	9.0
65–210	0.25	0.84	c	A	2.47	45	0.009	0.010	Yes	6.0
65–210	0.25	0.90	c	A	2.48	41.3	0.014	0.009	Yes	6.0
65–210	0.25	0.975	c	A	2.45	35	0.004	0.020	Yes	6.0
$5_{(112)}$A111 (approximately)	0.35	0.839	c	A	2.69	35	−0.020	0.032	Yes	9.0
5_1-213 (approximately)	0.336	0.889	c	A	2.63	40	0.019	0.046	No	9.0
$5_{(215)}$-114	0.259	0.915	c	A	2.80	40	0.019	0.038	No	9.0
5,2–221 (approximately)	0.263	0.832	a	B	2.83	30	0.025	0.046	Yes	9.95
6(215)-116, $a = 0.6$	0.25	0.824	c	B	2.70	55	0	0.028	No	6.0
6,2–116, $a = 0.6$	0.25	0.827	a	A	2.69	45	0.017	0.038	No	6.0
6,2–216, $a = 0.6$	0.30	0.90	c	A	2.92	37	0	0.016	No	6.0
6,2–216, $a = 0.6$	0.25	0.824	a	A	2.89	40	0.023	0.040	Yes	5.1
6,2–216, $a = 0.6$	0.25	0.834	c	A	2.88	45	0.011	0.031	Yes	5.1
6,2–118	0.25	0.90			2.68	32.5	--------	--------	No	6.0

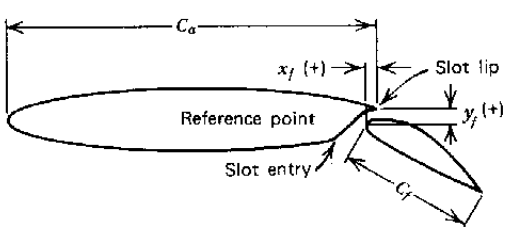

Typical single–slotted flap configuration.
(All dimensions are given in fractions of airfoil chord.)

Table 3.2 Maximum Lift Coefficients of Airfoil Sections Equipped with Double-Slotted Flaps

Airfoil Section	c_f/c	c_v/c	C_a	$C_{l_{max}}$	δ_f deg	δ_s deg	x_f	y_f	x_v	y_v	Optimum Position	R
23012	0.10	0.189	0.83	2.99	70	40	0.009	0.009	0.014	0.024	Yes	3.5×10^6
23012	0.257	0.227	0.715	3.47	70	30	0.014	0.012	0.015	0.035	No	3.5
23021	0.257	0.227	0.715	3.56	60	30	0.019	0.024	0.025	0.065	No	3.5
23030	0.257	0.260	0.715	3.71	80	40	0.049	0.050	0.045	0.040	No	3.5
23012	0.257	0.117	0.826	3.30	60	25	−0.016	0.010	−0.004	0.017	Yes	3.5
23021	0.257	0.147	0.827	3.32	70	30	0.017	0.027	0.007	0.024	Yes	3.5
63–210	0.25	0.075	0.84	2.91	50	25	0.022	0.024	0.024	0.018	Yes	6.0
63,4–421 (approximately)	0.195	0.083	0.87	3.30	55	14	0.038	0.012	0.009	0.016	No	6.0
64–208	0.25	0.075	0.84	2.51	45	30	0.015	0.015	0.015	0.019	Yes	6.0
64–208	0.25	0.056	0.84	2.40	50	25	0.018	0.014	0.015	0.024	Yes	6.0
64–210	0.25	0.075	0.84	2.82	55	30	0.023	0.006	0.012	0.018	Yes	6.0
64_1–212	0.25	0.075	0.84	3.03	50	30	0.021	0.020	0.010	0.019	Yes	6.0
64_1A212	0.229	0.083	0.833	2.83	55	26	0.044	0.005	0.004	0.014	Yes	6.0
65–210	0.25	0.075	0.84	2.72	50	25	0.025	0.011	0.009	0.024	Yes	6.0
65(216)–215, $a = 0.8$	0.248	0.096	0.82	3.38	70	12	0.024	0.010	0.025	0.032	No	6.3
65_3–118	0.244	0.10	0.864	3.35	65	23	0.038	0.007	0.009	0.025	Yes	6.0
65_3–418	0.236	0.106	0.851	3.50	65	21	0.027	0.007	0.012	0.028	Yes	6.0
65_4–421	0.236	0.109	0.85	3.08	51	20	0.029	0.017	0.012	0.024	Yes	2.2
66–210	0.25	0.075	0.84	2.64	55	25	0.029	0.023	0.012	0.022	Yes	6.0
66–210	0.25	0.100	0.84	2.72	60	25	0.027	0.039	0.024	0.021	Yes	6.0
66_2–214 (approximately)	0.227	0.085	0.854	3.00	55	20	0.044	0.009	0.004	0.025	Yes	9.0
1410	0.25	0.075	0.84	3.06	50	25	0.026	0.016	0.012	0.019	Yes	6.0

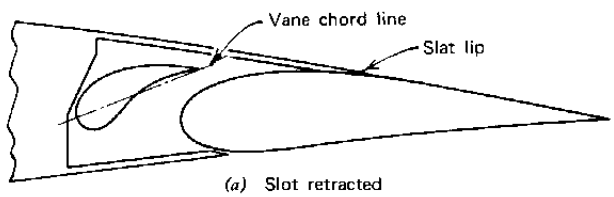

(a) Slot retracted

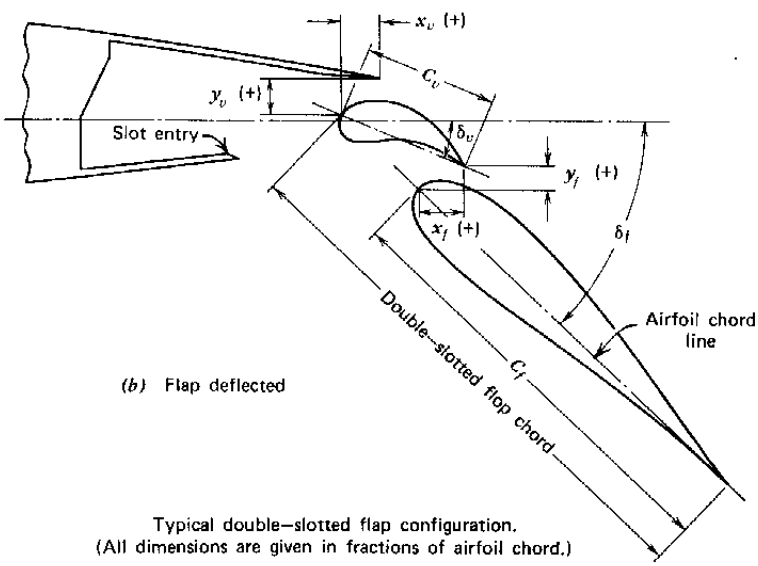

(b) Flap deflected

Typical double–slotted flap configuration.
(All dimensions are given in fractions of airfoil chord.)

Definition of Flap Geometry given in Table 3.2

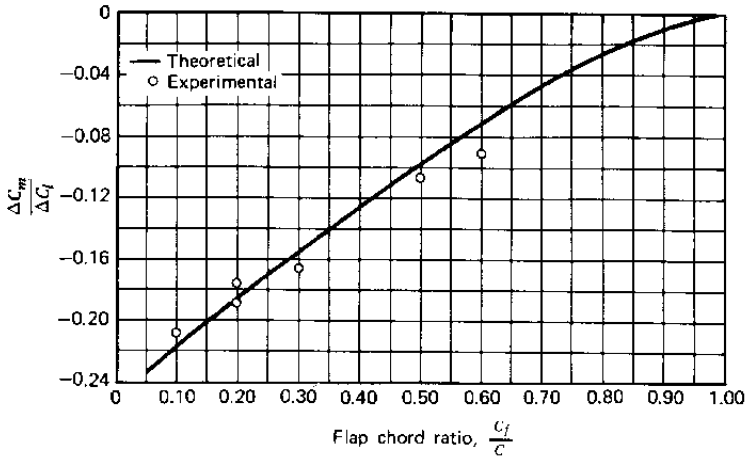

(a)

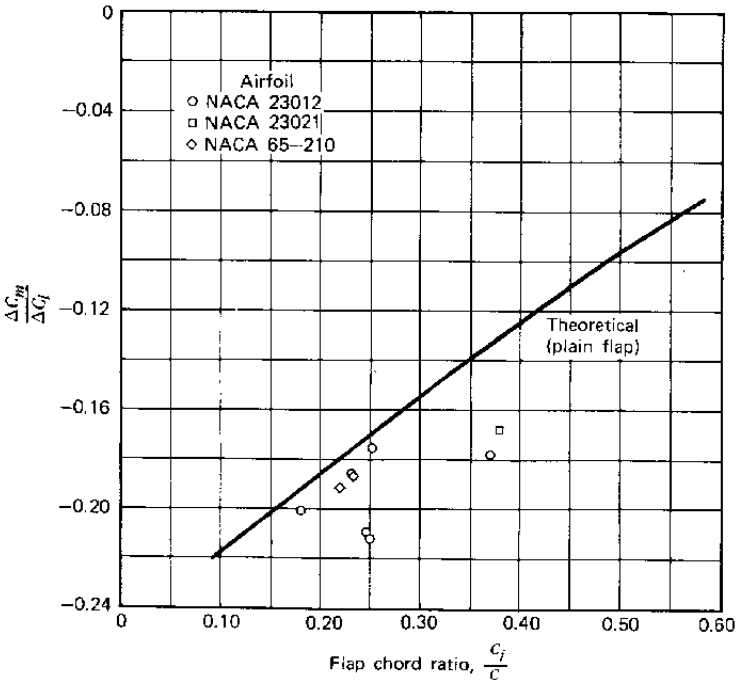

(b)

Figure 3.31 Influence of flap configuration on pitching moment coefficient. (a) Plain flaps. (b) Split flaps. (c) Slotted flaps.

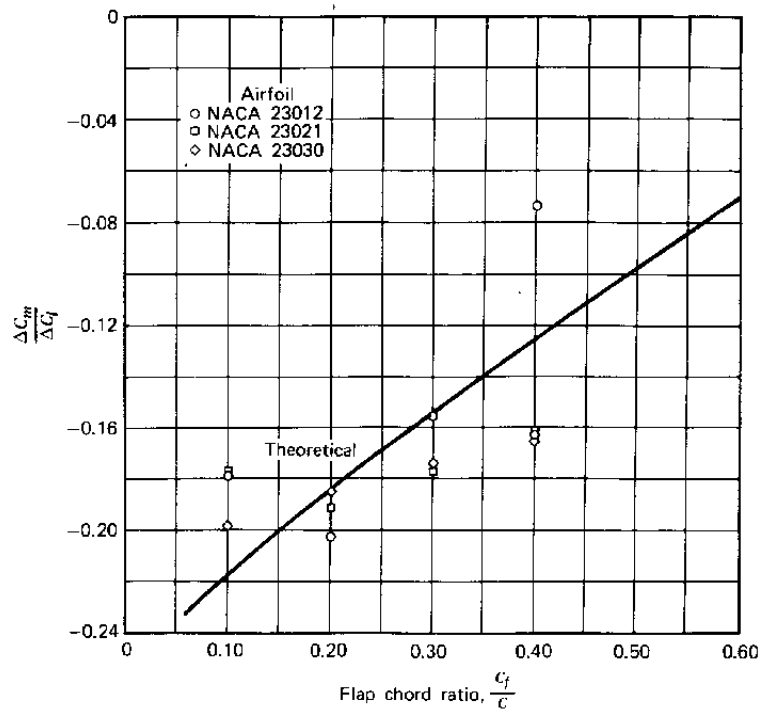

(c)

Figure 3.31 (Continued)

In a high-wing airplane, lowering the flaps can cause the nose to pitch up. This is due to the moment produced about the center of gravity from the increase in wing drag because of the flaps. Based on the wing area, the increment in wing drag coefficient, ΔC_D, due to the flaps is given approximately by,

$$\Delta C_D = 1.7(c_f/c)^{1.38}(S_f/S)\sin^2\delta_f \qquad \text{(plain and split)} \qquad (3.45)$$

$$= 0.9(c_f/c)^{1.38}(S_f/S)\sin^2\delta_f \qquad \text{(slotted)} \qquad (3.46)$$

If the wing is located a height of h above the center of gravity, a balancing upload is required on the tail. The effect of trim on $C_{L_{max}}$ for a complete airplane will be discussed in more detail later.

Flap Effectiveness in the Linear Range

Frequently one needs to estimate the increment in C_l below stall, ΔC_l, produced by a flap deflection. Not only is this needed in connection with the

wing lift, but ΔC_l is required also in analyzing the effectiveness of movable control surfaces, which frequently resemble plain flaps.

If an airfoil section has a lift curve slope of C_{l_α} and lowering its flap produces an increment of ΔC_l, the angle of zero lift, α_{0l}, is decreased by

$$\Delta\alpha_{0l} = \frac{\Delta C_l}{C_{l_\alpha}} \tag{3.47}$$

The rate of decrease of α_{0l} per unit increase in the flap angle δ_f is referred to as the flap effectiveness factor, τ. Thus, for a flapped airfoil, the lift coefficient can be written as

$$c_l = c_{l_\alpha}(\alpha + \tau\,\delta_f) \tag{3.48}$$

where α is the angle of attack of the airfoil's zero lift line with the flap undeflected.

Theoretically τ is a constant for a given flap geometry but, unfortunately, flap behavior with δ_f is rather nonlinear and hence τ must be empirically corrected by a factor η to account for the effects of viscosity. Including η, Equation 3.48 becomes,

$$c_l = c_{l_\alpha}(\alpha + \tau\eta\,\delta_f) \tag{3.49}$$

The functions τ and η can be obtained from Figures 3.32 and 3.33. Figure 3.33 is empirical and is based on data from References 3.15, 3.17, 3.19, and 3.20. Although there is some scatter in the data, as faired, the comparisons between the various types of flaps are consistent. The double-slotted flap delays separation on the upper surface, so that the decrease in flap effectiveness occurs at higher flap angles than for the other flap types. The same can be said of the slotted flap relative to the plain and split flaps. The plain flap is fairly good out to about 20° and then apparently the flow separates from the upper surface and the effectiveness drops rapidly, approaching the curve for split flaps at the higher flap angles. In a sense the flow is always separated on the upper surface of a split flap. Thus, even for small flap angles, the effective angular movement of the mean camber line at the trailing edge of an airfoil with a split flap would only be about half of the flap displacement.

In the case of the double-slotted flap it should be emphasized that this curve in Figure 3.33 is for an optimum flap geometry. The trailing segment of the flap is referred to as the main flap and the leading segment is called the vane. In applying Equation 3.49 and Figures 3.32 and 3.33 to the double-slotted flap, the total flap chord should be used together with the flap angle of the main flap. Usually, the deflection angle of the vane is less than that for the main flap for maximum lift performance.

Figure 3.32 is based on the thin airfoil theory represented by Equation 3.39. As an exercise, derive the expression for τ given on the figure. τ can also be obtained using the numerical methods that led to Figures 3.17 and

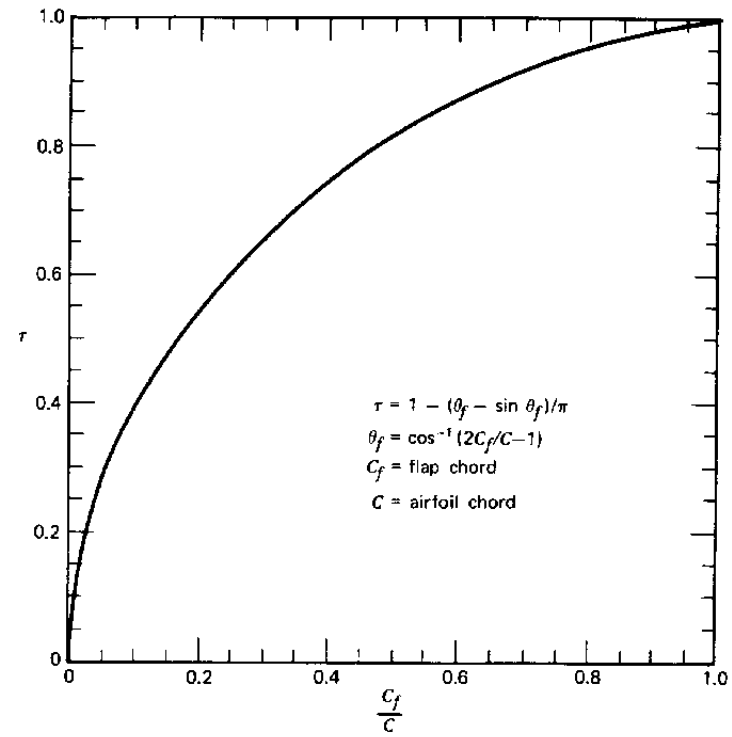

Figure 3.32 Flap effectiveness factor.

3.18. As another exercise, apply Weissinger's approximation to the flapped airfoil using only two point vortices to represent the airfoil. Placing one vortex on the quarter chord of the flap and the other on the quarter chord of the remainder of the airfoil leads to

$$\tau = \frac{3(3-2c_f)c_f}{4(1-c_f)c_f+3} \tag{3.50}$$

where c_f is the fraction of chord that is flapped. Equation 3.50 is approximately 10% lower than Figure 3.32 for c_f/c values of around 0.25.

The angle of attack at which the flapped airfoil stalls is generally less than that for the plain airfoil. Hence, the increment in $C_{l_{max}}$ because of the flap is not as great as the increment in C_l at an angle below the stall. Denoting these increments by $\Delta C_{l_{max}}$ and ΔC_l, respectively, it is obvious that the ratio $\Delta C_{l_{max}}/\Delta C_l$ must depend on c_f/c. If c_f/c, for example, is equal to 1.0, in a sense the entire airfoil is the flap and $\Delta C_{l_{max}}$ must be zero. Systematic data on $\Delta C_{l_{max}}/\Delta C_l$ are sparse. Figure 3.34 has been drawn based on a limited number of data points and should be used with discretion.

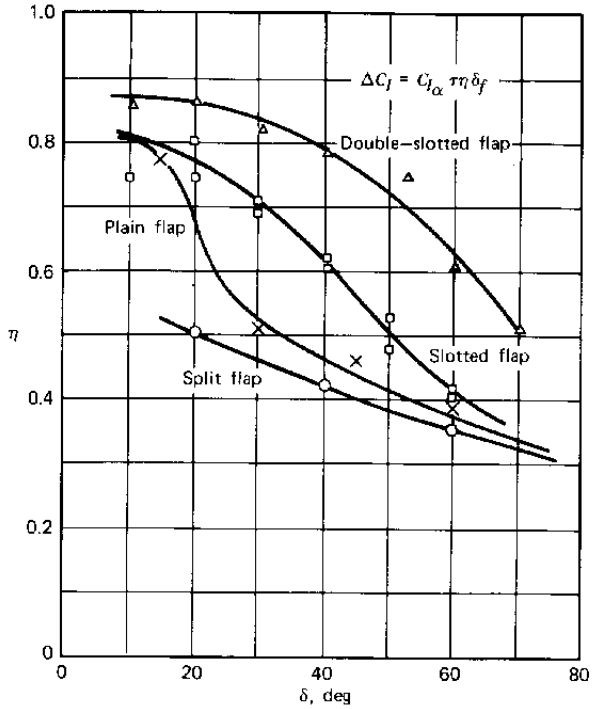

Figure 3.33 Correction factor to flap effectiveness factor τ. Note that curves apply for thickness ratios of approximately 12% and flap chord fractions of 40% or less.

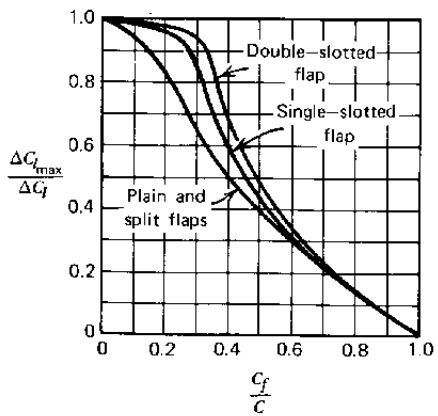

Figure 3.34 $C_{l_{max}}$ increment ratio as a function of flap chord ratio.

As an example, in using Figures 3.32, 3.33, and 3.34, consider the prediction of $C_{l_{max}}$ for a 23012 airfoil equipped with a 30% chord split flap deflected 60° and operating at a Reynold's number of 3.5×10^6. From Figure 3.32, $\tau = 0.66$ for $c_f/c = 0.3$ and from Figure 3.33, $\eta = 0.35$ for a split flap deflected 60°. Hence from Equation 3.49, ΔC_l is equal to

$$\begin{aligned} \Delta C_l &= C_{l_\alpha} \tau \eta \, \delta \\ &= (0.105)(0.66)(0.35)(60) \\ &= 1.46 \end{aligned} \tag{3.51}$$

In Equation 3.51, C_{l_α} of 0.015 is obtained from Reference 3.1. Using Figure 3.34, the ratio of $\Delta C_{l_{max}}$ to ΔC_l is obtained as 0.66. Hence,

$$\Delta C_{l_{max}} = 0.96$$

According to Figure 3.27, $C_{l_{max}}$ for a plain 23012 airfoil equals 1.65 at $R = 3.5 \times 10^6$. Thus, for the flapped airfoil, $C_{l_{max}}$ is predicted to be 1.65 + 0.96, or 2.61. This result compares closely with Figure 3.26*a*. If the procedure is repeated for other flap angles, close agreement is also obtained with the figure. However for a flap chord ratio of 0.1, the predicted values of $C_{l_{max}}$ based on Figures 3.32 to 3.34 are higher than those shown in Figure 3.26*a*.

Leading Edge Devices

In order to avoid leading edge separation, particularly at low Reynolds numbers or for airfoils with relatively sharp leading edges, special high-lift devices can also be incorporated into the leading edge to supplement the benefits of trailing edge flaps. These are illustrated in Figure 3.35. The fixed slot and extensible slat have been in use for some time, whereas the Kruger-type nose flap was first employed on the turbojet transport.

As the name implies, the fixed slot is just that—a narrow channel through which the air can flow from the lower surface to the upper surface. This channeling of the flow allows the airfoil to operate at higher angles of attack before the upper surface of the leading edge separates than otherwise would be the case. Increments in $C_{l_{max}}$ of approximately 0.1 or 0.2 are achieved by the fixed slot. It is a moot question as to why this delay in the separation occurs. As in the case of slots with trailing edge flaps, the explanation has been offered in the past that the flow through the slot feeds energy into the slower moving boundary layer, thereby decreasing its tendency to separate. More recently, however, in a Wright Brothers' Lecture (Ref. 3.16) Smith, in examining numerical results on multielement airfoils, concluded that improved stall performance from slots is most likely the result of more favorable pressure gradients being produced on one airfoil element by the other.

The extensible slat is similar in its performance to the slot, but it is

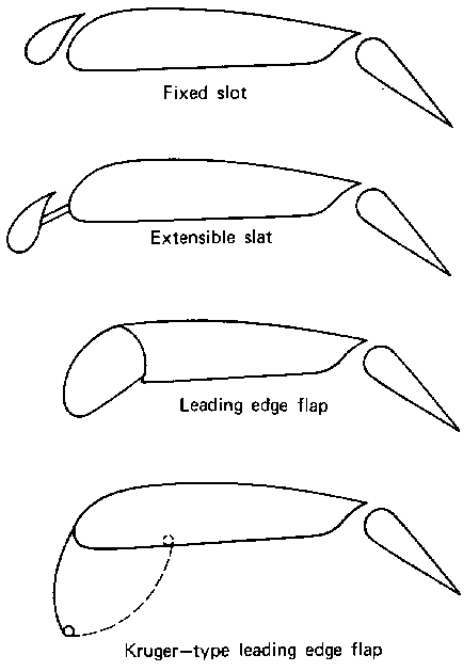

Figure 3.35 Various methods for delaying leading edge separation.

considerably more efficient because it can be positioned to optimize its contribution to $C_{l_{max}}$. The mechanically extended slat is finding increased application, particularly with the use of thinner airfoil sections for high-speed applications. Figure 3.36 presents some data on slats taken from Reference 3.17. Here a NACA 64A010 airfoil was tested using a slat in combination with split and double-slotted trailing edge flaps. The slat is seen to improve $C_{l_{max}}$ significantly, producing increments in $C_{l_{max}}$ of approximately 0.9, 0.8, and 0.6 for the no-flap, split-flap, and double-slotted flap configurations, respectively. Unlike the trailing edge flap, the primary effect of the slat is seen to be an extension of the lift curve without the slat; that is, opening the slat does not change C_l by a large increment at a fixed angle of attack. The same is true of leading edge flaps and is not unexpected in view of Figure 3.32.

The performance of a leading edge flap is presented in Figure 3.37 for the same airfoil as for Figure 3.36. Comparing the two figures, it is obvious that the two leading edge devices are nearly comparable in performance.

Figure 3.38 shows a section of a sophisticated Kruger-type flap. As this flap swings down and forward, it assumes the curved shape that is shown. With this optimum shaping, its performance probably exceeds to some extent

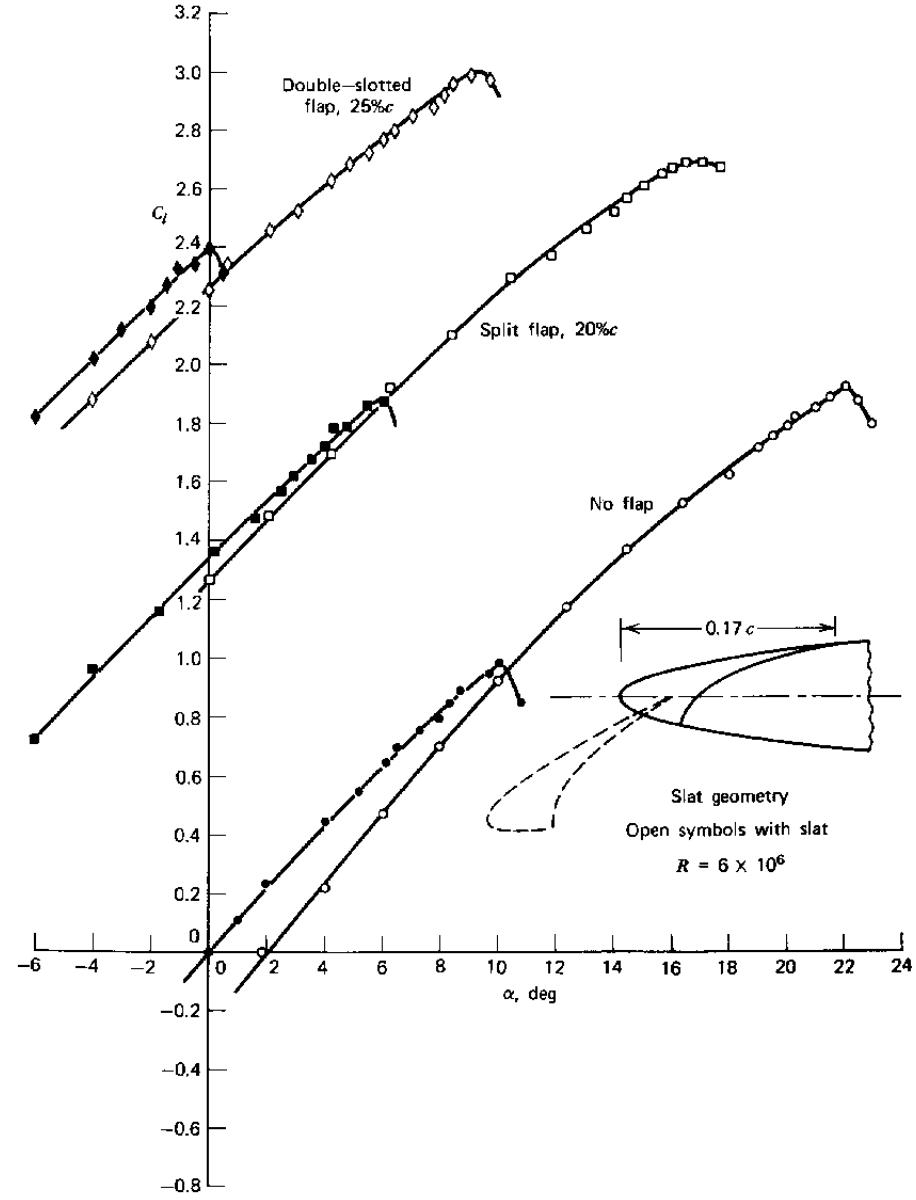

Figure 3.36 Effect of leading edge slat on NACA 64A010 airfoil with and without flaps.

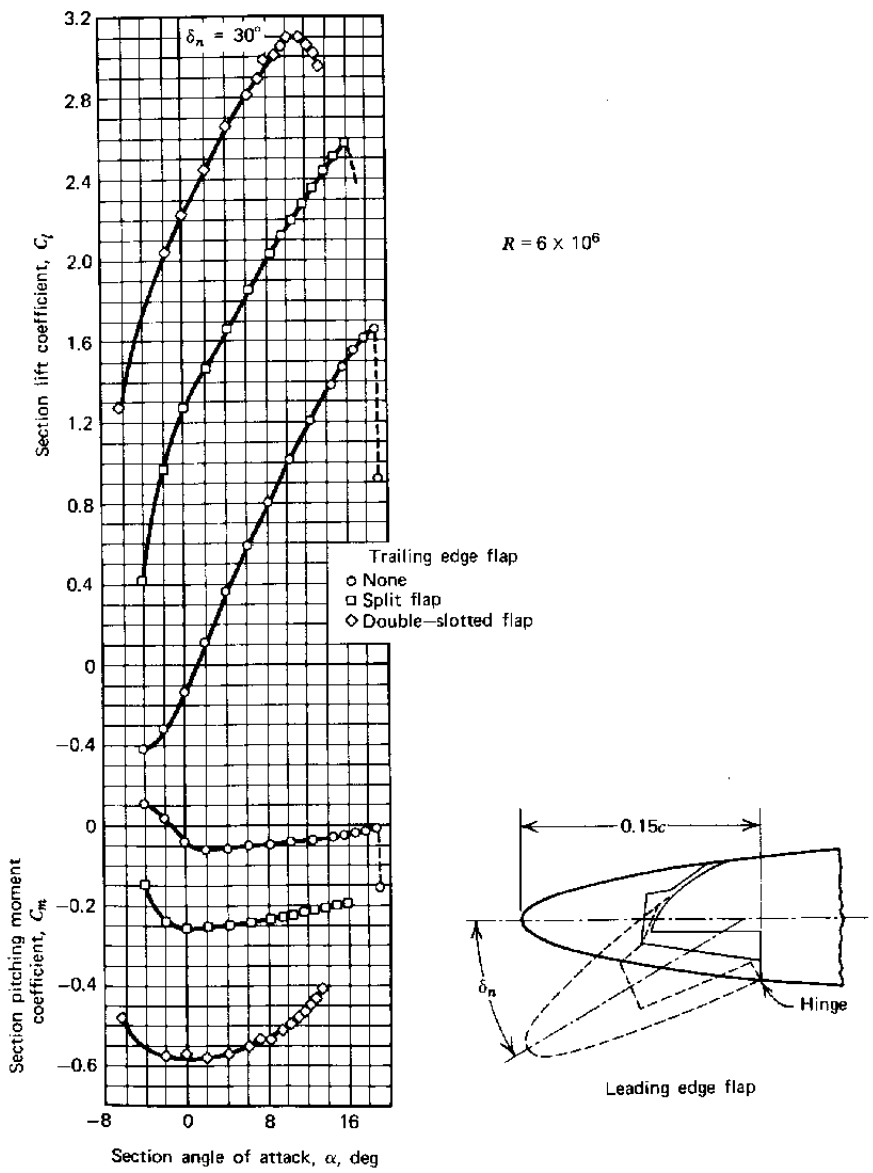

Figure 3.37 Effect of leading edge flap on NACA 64A010 airfoil with and without flaps.

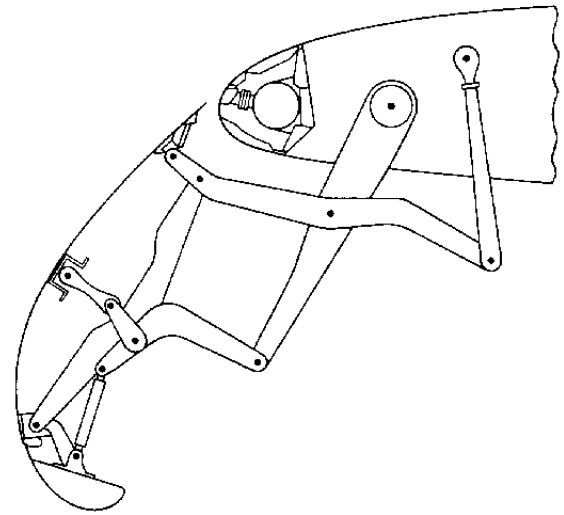

Figure 3.38 Flexible fiberglass leading edge flap used on the Boeing 747 and YC-14 airplanes.

the data presented in Figures 3.39 and 3.40. Figure 3.39 (taken from Ref. 3.18) shows that without a trailing edge flap the Kruger flap gives an increment in $C_{l_{max}}$ to the 64-012 airfoil of only 0.4. However, the plain airfoil has a higher $C_{l_{max}}$ to begin with than that of Figures 3.36 and 3.37. Hence, the total $C_{l_{max}}$ for the Kruger-flapped airfoil without a trailing edge flap is about the same as for the other two leading edge devices. However, with the split flap, the Kruger flap produces a combined $C_{l_{max}}$ equal to 3.0, which is 0.3 to 0.4 higher than the corresponding data of Figures 3.36 and 3.37.

The data of Figure 3.40 (taken from Ref. 3.21) are based on Kruger's original work.

The Optimum Airfoil for High Lift

Stratford, in References 3.23 and 3.24, examined both theoretically and experimentally the possibility of diffusing a turbulent boundary layer in such a way as to produce zero wall shear. Known as "imminent separation pressure recovery," Stratford found that it is indeed possible, with the proper pressure gradient, to maintain a velocity profile along a diffuser such that $\partial u(y)/\partial y$ is equal to zero at the wall. $u(y)$ is the velocity in the boundary layer parallel to the wall and is a function of the distance, y, from the wall. With the velocity gradient at the wall equal to zero, the boundary layer is just on the verge of separating, since a negative value of this gradient will result in reverse flow, as illustrated in Figure 3.41.

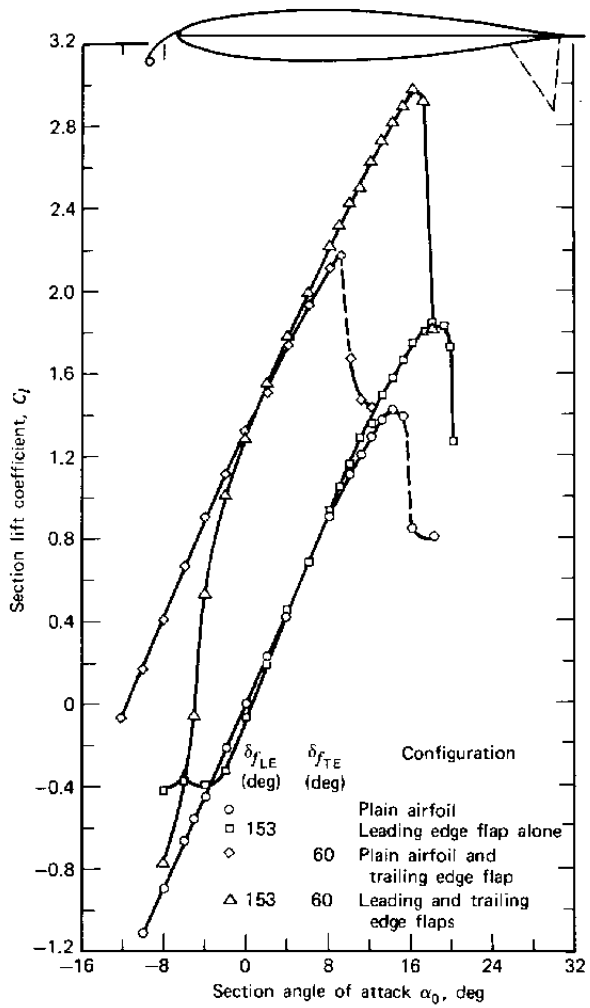

Figure 3.39 Section lift characteristics for the NACA 64_1–012 airfoil section equipped with a 0.10c upper-surface leading edge flap alone, and in combination with a 0.20c trailing edge split flap. $R = 6.0 \times 10^6$.

In the abstract to Reference 3.24, Stratford states:

"*No fundamental difficulty was encountered in establishing the flow and it had, moreover, a good margin of stability. The dynamic head in the zero skin friction boundary layer was found to be linear at the wall (i.e., $u \propto y^{1/2}$), as predicted theoretically in the previous paper. (Author's note, Stratford is referring to Ref.* 3.23.)

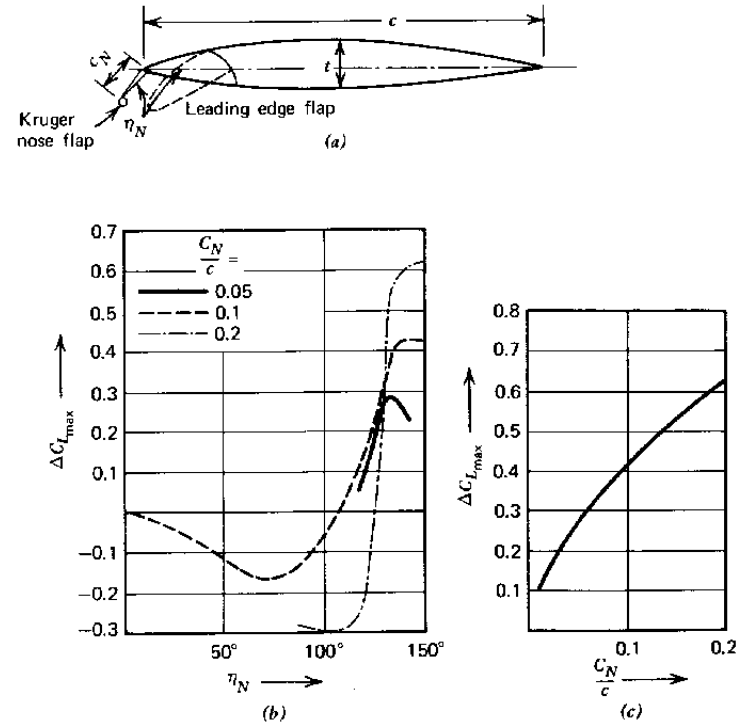

Figure 3.40 Characteristics of Kruger flaps. (*a*) Illustration of Kruger's type of nose flap and simple, hinged, leading edge flap. (*b*) Effect of flap angle on maximum lift coefficient. (c) Effect of flap chord on maximum lift coefficient.

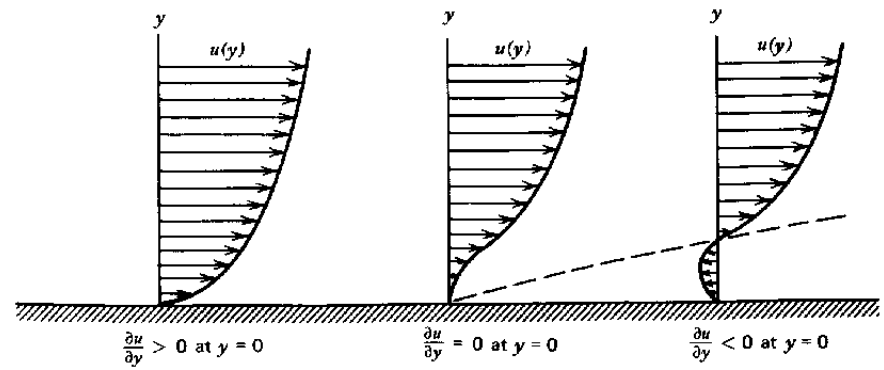

Figure 3.41 Relationship of velocity gradient at the wall to flow separation.

The flow appears to achieve any specified pressure rise in the shortest possible distance and with probably the least possible dissipation of energy for a given initial boundary layer. Thus, an airfoil which could utilize it immediately after transition from laminar flow would be expected to have a very low drag."

The Stratford imminent separation pressure recovery was adopted for airfoils by Liebeck and Ormsbee (Ref. 3.25) and was extended later by Liebeck (Ref. 3.22). Using variational calculus, optimum chordwise pressure distributions for the upper and lower surfaces are prescribed that are modified slightly by additional constraints not present in the optimization process. Specifically, the optimum C_p distributions are modified in order to (1) close the airfoil contour at the trailing edge, (2) round the leading edge to allow operation over an angle-of-attack range, and (3) satisfy the Kutta condition at the trailing edge.

The resulting modified form of the optimum pressure distribution is compared with the optimum distribution in Figure 3.42. Beginning at the stagnation point, the flow is accelerated up to a so-called rooftop region over which the velocity, and hence the pressure, is constant. Following the rooftop region, the Stratford pressure recovery distribution is employed to reduce the velocity over the upper surface to its value at the trailing edge.

One such airfoil design is presented in Figure 3.43 (taken from Ref. 3.22). Included on the figure is the pressure distribution to which the airfoil was designed. Test data on this airfoil obtained at a Reynolds number of 3×10^6 are presented in Figure 3.44*a* and 3.44*b*. Although this configuration is referred to by the reference as a "turbulent rooftop" case, transition does not occur until the start of the Stratford pressure recovery. In this case the performance of the airfoil is seen to be good from the standpoint of $C_{l_{max}}$ and C_d. The drag coefficient remains below the value of 0.01 over a wide range of C_l values from 0.6 to 1.6.

Artificially producing transition near the leading edge severely compromises $C_{l_{max}}$ and C_d, as shown in Figure 3.44*b*. Still, by comparison with the standard NACA airfoils, the Liebeck airfoil appears to offer superior performance at low speeds and, in the future, may find application to general aviation aircraft. One possible drawback in this regard is the sharp drop in its lift curve at stall.

Powered-Lift Systems

Figure 3.45 (taken from Ref. 3.26) presents the growth of $C_{L_{max}}$ over the years since the Wright Brothers' success. The two points labeled K and L are somewhat misleading, since these two aircraft were experimental in nature and used distributed suction over the wing to delay separation. From this figure and the preceding information on flapped and plain airfoils, $C_{L_{max}}$ of

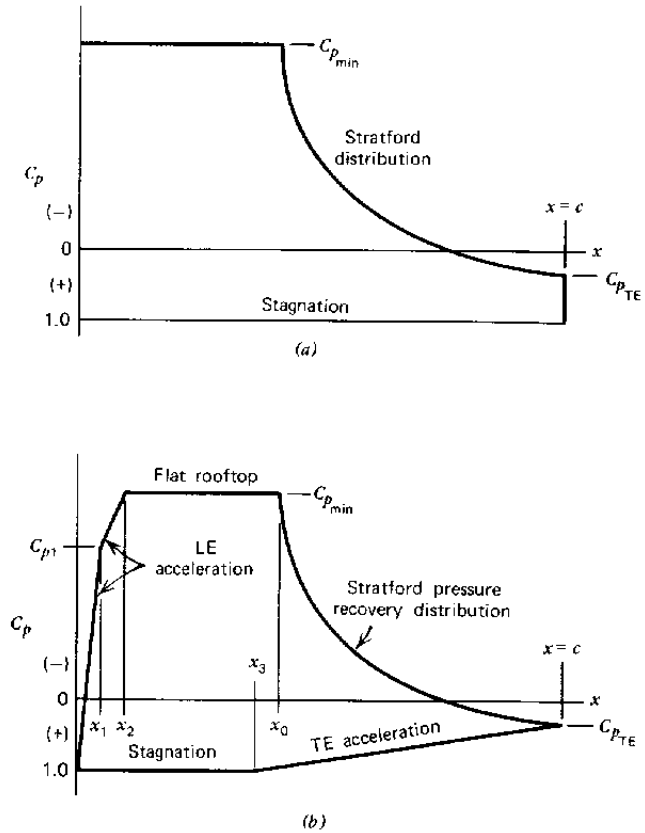

Figure 3.42 Pressure distributions for Liebeck airfoils. (*a*) Optimum airfoil pressure distribution according to variational analysis. (*b*) Modified form of optimum pressure distribution for airfoil upper and lower surfaces (not to scale). (R. H. Liebeck and A. I. Ormsbee, "Optimization of Airfoils for Maximum Lift", AIAA *Journal of Aircraft*, 1970. Reprinted from the *Journal of Aircraft* by permission of the American Institute of Aeronautics and Astronautics.)

slightly over 3 is probably the best that can be achieved without the addition of power. Although two-dimensional airfoils with double-slotted flaps can do better than this, as will be seen later, their full potential cannot be achieved when applied to an airplane. Generally, the flaps cannot be applied over the entire span of the wing. In addition to this loss in $C_{L_{max}}$, an added penalty results from the fuselage and tail download required for trim.

$C_{L_{max}}$ values considerably above those achievable with flap systems discussed so far are possible by the expenditure of power. Most of the powered-flap systems presently under consideration bear a resemblance, or can be

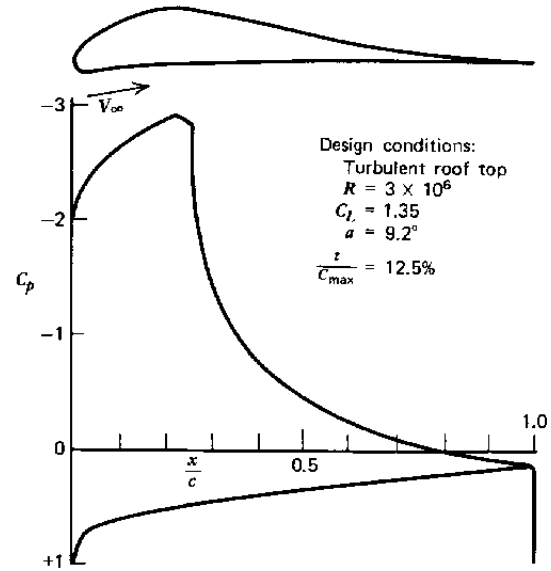

Figure 3.43 Liebeck airfoil with its pressure distribution. (R. H. Liebeck, "Class of Airfoils Designed for High Lift", AIAA *Journal of Aircraft*, 1973. Reprinted from the *Journal of Aircraft* by permission of the American Institute of Aeronautics and Astronautics.)

related in their performance, to the jet flap. Thus, in order to understand better the performance of systems such as upper surface blowing (USB), externally blown flaps (EBF), augmentor wing, and circulation control, we will begin with the jet flap shown in Figure 3.46. A thin sheet of air exits the trailing edge at a downward angle of δ relative to the airfoil zero lift line. This line is shown at an angle of attack α. If Γ_c is the total circulation around the airfoil then, assuming α and δ to be small, the total lift on the airfoil will be

$$L = \rho V \Gamma_c + m_j v_j (\alpha + \delta) \tag{3.52}$$

where m_j is the mass flux in the jet and v_j is the jet velocity.

As the jet leaves the airfoil, it gets turned in the direction of the free-stream velocity. In order to redirect the flux of jet momentum, it follows that a pressure difference must exist across the jet. This pressure difference, Δp, can be related to $m_j v_j$ and the radius of curvature R by the use of Figure 3.46*b*. Applying the momentum theorem in the direction of curvature,

$$\Delta p R \theta = m_j v_j \theta$$

or

$$\Delta p = \frac{m_j v_j}{R} \tag{3.53}$$

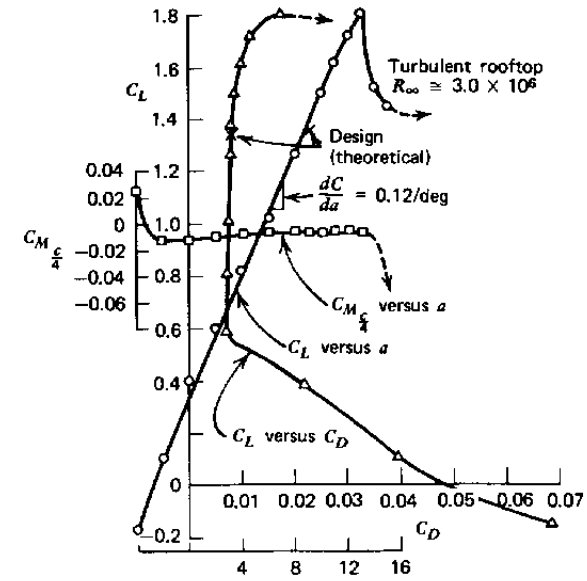

Figure 3.44a Experimental lift curve and drag polar for airfoil of Figure 3.43. (R. H. Liebeck, "Class of Airfoils Designed for High Lift", AIAA *Journal of Aircraft*, 1973. Reprinted from the *Journal of Aircraft* by permission of the American Institute of Aeronautics and Astronautics.)

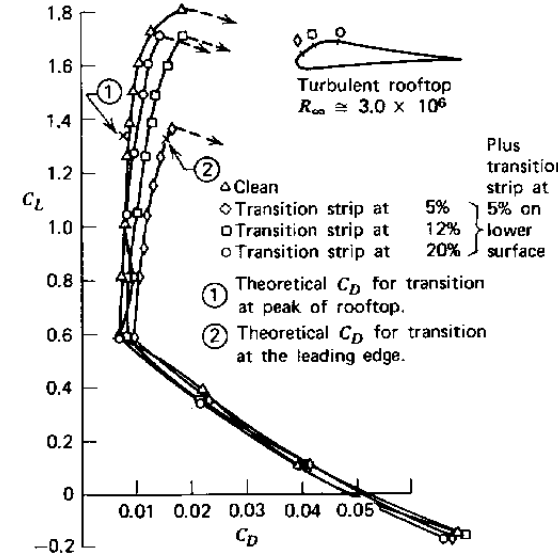

Figure 3.44b Effect of transition location on the lift and drag of a Liebeck airfoil. (R. H. Liebeck, "Class of Airfoils Designed for High Lift", AIAA *Journal of Aircraft*, 1973. Reprinted from the *Journal of Aircraft* by permission of the American Institute of Aeronautics and Astronautics.)

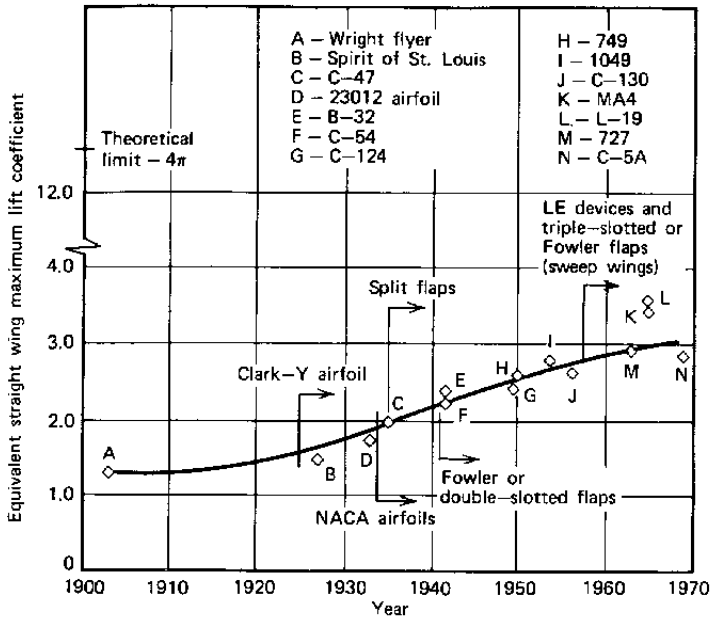

Figure 3.45 History of maximum lift coefficients for mechanical lift systems. (F. A. Cleveland, "Size Effects in Conventional Aircraft", AIAA *Journal of Aircraft*, 1970 Reprinted from the *Journal of Aircraft* by permission of the American Institute of Aeronautics and Astronautics.)

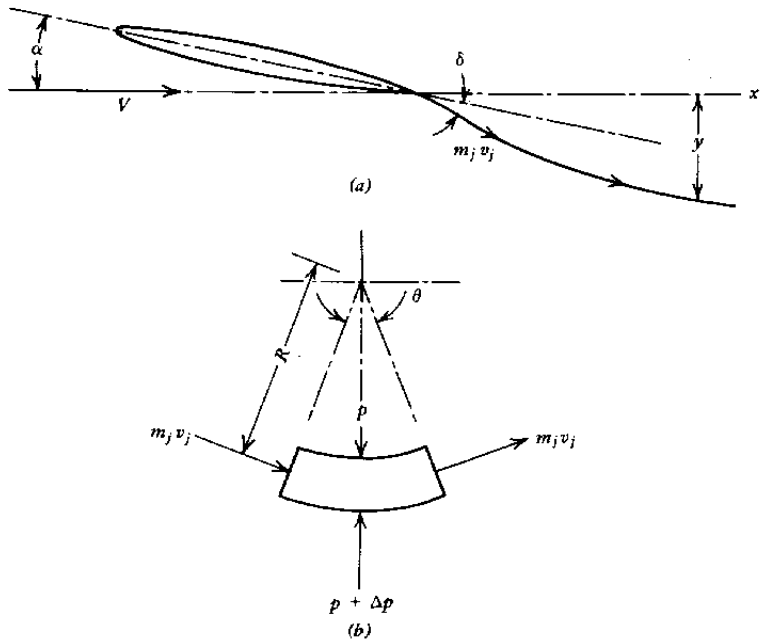

Figure 3.46 The jet flap.

Since the jet exerts a force on the fluid, it can be replaced by an equivalent continuous vortex sheet that exerts the same force. Letting γ_j be the strength per unit length of the sheet,

$$\Delta p R\theta = \rho V \gamma R\theta$$

or

$$\gamma_j = \frac{\Delta p}{\rho V} \tag{3.54}$$

Measuring the position of the jet, y, positively downward, the radius of curvature and y for a nearly horizontal jet are related by

$$\frac{1}{R} = -\frac{d^2y}{dx^2} \tag{3.55}$$

Combining Equations 3.53, 3.54, and 3.55 gives

$$\gamma_j = \frac{-m_j v_j}{\rho V}\frac{d^2y}{dx^2} \tag{3.56}$$

Equation 3.56 relates the jet vortex strength to the shape of the sheet and the jet momentum flux.

The total circulation of the jet vortex sheet can be obtained by integrating Equation 3.56 from $x = 0$ to ∞.

$$\begin{aligned}\Gamma_j &= \int_0^\infty \gamma_j \, d_x \\ &= -\frac{m_j v_j}{\rho V}\frac{dy}{dx}\int_0^\infty \\ &= \frac{m_j v_j}{\rho V}(\alpha + \delta)\end{aligned} \tag{3.57}$$

Combining Equations 3.52 and 3.57 shows that the Kutta–Joukowski relationship holds for the jet-flapped airfoil if the circulation is taken around both the airfoil and the jet.

$$L = \rho V(\Gamma_c + \Gamma_j) \tag{3.58}$$

The boundary value problem is then posed where the airfoil and jet sheet are each replaced by an unknown vortex distribution. Distributions must then be found that will induce a velocity at each point on the airfoil and combining with the free-stream velocity to give a resultant velocity tangent to the airfoil. Along the sheet the following must hold.

$$\frac{w(x)}{V} = \frac{dy}{dx}$$

The details of the solution are beyond the scope of this text and can be found in Reference 3.19.

Although the solution of Reference 3.19 is not in closed form, the results

can be expressed in a relatively simple way. As with a physical flap, the increment in C_l because of a change in angle of attack and flap angle can be expressed as a linear combination of the two angles.

$$C_l = C_{l_\alpha}\alpha + C_{l_\delta}\delta \tag{3.59}$$

where

$$C_{l_\alpha} = \frac{dC_l}{d\alpha}$$

$$C_{l_\delta} = \frac{dC_l}{d\,\delta}$$

The derivatives C_{l_α} and C_{l_δ} are a function of the ratio of the jet momentum flux to the product of the free-stream dynamic pressure and a reference area. This ratio, known as the momentum coefficient, C_μ, is defined for a two-dimensional airfoil by

$$C_\mu = \frac{m_j v_j}{qc} \tag{3.60}$$

If, in addition, the jet exits ahead of the trailing edge and blows over and is deflected by a physical flap having a chord of c_f (see the blown flap of Figure 3.24), then C_{l_δ} is also a function of c_f/c. For a pure jet flap ($C_f/C = 0$), C_{l_α} and C_{l_δ} are given by

$$C_{l_\delta} = [4\pi C_\mu(1 + 0.151C_\mu^{1/2} + 0.139C_\mu)]^{1/2} \tag{3.61}$$

$$C_{l_\alpha} = 2\pi(1 + 0.151C_\mu^{1/2} + 0.219C_\mu) \tag{3.62}$$

For c_f/c values other than zero, C_{l_δ} is given in Figure 3.47. The curve labeled $c_f/c = 1.0$ in this figure corresponds to Equation 3.62 since, for this case, $C_{l_\delta} = C_{l_\alpha}$.

Data concerning $C_{l_{max}}$ for jet-flapped airfoils is sparse. Generally, the jet flap follows the predictions of Figure 3.41 fairly closely, since the jet fixes the Kutta condition and provides some control over the boundary layer to prevent separation. As a preliminary estimate for $C_{l_{max}}$, Reference 3.3 recommends the use of the relationship presented in Figure 3.48. Here the difference in the angle of attack for stall, with and without blowing, is presented as a function of C_μ.

The negative pitching moment of the jet flaps is higher than the moment for conventional flaps for two reasons. First, the jet reaction acts at the trailing edge; second, the jet-flapped airfoil maintains lift all the way back to the trailing edge. As with the lift, C_M can be written as a linear combination of α and δ.

$$C_M = C_{M_\alpha}\alpha + C_{M_\delta}\delta$$

or

$$C_M = \left(\frac{\partial C_M}{\partial C_l}\right)_{\delta=\text{const}} C_{l_\alpha}\alpha + \left(\frac{\partial C_M}{\partial C_l}\right)_{\alpha=\text{const}} Cl_\delta\delta \tag{3.63}$$

In this equation $\partial C_M/\partial C_l$ can be obtained from Figure 3.49.

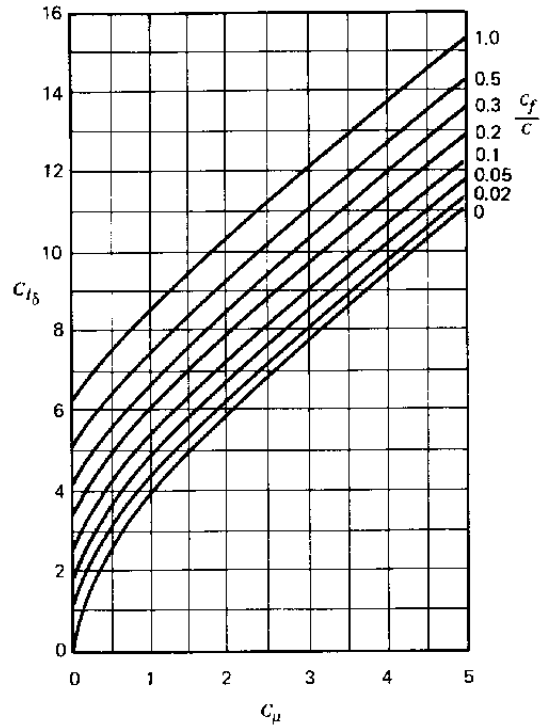

Figure 3.47 Blown flap effectiveness. (B. W. McCormick, *Aerodynamics of V/STOL Flight*, Academic Press, Inc. 1967. Reprinted by permission of Academic Press, Inc.

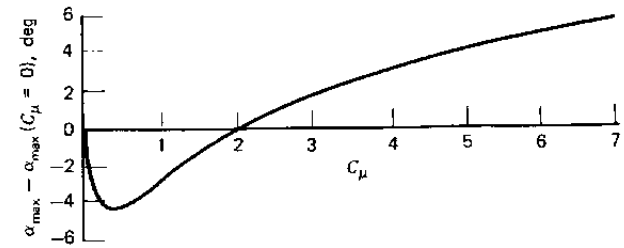

Figure 3.48 Effect of C_μ on α for $C_{l_{max}}$. (B. W. McCormick, *Aerodynamics of V/STOL Flight*, Academic Press, Inc. 1967. Reprinted by permission of Academic Press, Inc.)

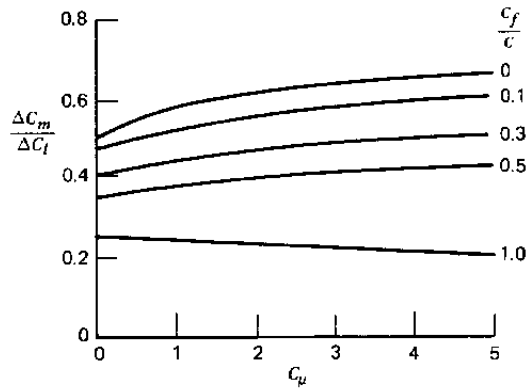

Figure 3.49 Effect of C_μ on pitching moments for blown flaps. (B. W. McCormick, *Aerodynamics of V/STOL Flight*, Academic Press, Inc. 1967. Reprinted by permission of Academic Press, Inc.)

To illustrate the use of the foregoing relationship for the jet-flapped airfoil, consider the prediction of $C_{l_{max}}$ for the NACA 63,4-421 airfoil (Figure 3.30) equipped with a 25% blown flap deflected 50°. The jet expands isentropically from a reservoir pressure of 25 psia and a temperature of 70 °F. The airfoil is operating at 50 mph at SSL conditions. It has a chord of 5 ft and the jet thickness is 0.2 in.

We begin by calculating the jet velocity from the compressible Bernoulli equation (Equation 2.31).

$$v_j^2 = \frac{2\gamma}{\gamma - 1}\left(\frac{p_0}{\rho_0} - \frac{p}{\rho}\right)$$

or, with the use of Equation 2.30,

$$v_j = \left\{\frac{2\gamma p_0}{(\gamma - 1)\rho_0}\left[1 - \left(\frac{p}{p_0}\right)^{(\gamma-1)/\gamma}\right]\right\}^{1/2}$$

From the equation of state (Equation 2.1),

$$p_0/\rho_0 = RT_0$$

Thus,

$$v_j = \left\{\frac{2(1.4)(1716)(529.7)}{0.4}\left[1 - \left(\frac{14.7}{25}\right)^{0.286}\right]\right\}^{1/2}$$
$$= 946.9 \text{ fps}$$

The mass density of the expanded jet will be

$$\rho_j = \rho_0\left(\frac{p}{p_0}\right)^{1/\gamma}$$

ρ_0 is calculated from the equation of state.

$$\rho_0 = \frac{25(144)}{1716(529.7)}$$
$$= 0.00396 \text{ slugs/ft}^3$$

Thus

$$\rho_j = 0.00271 \text{ slugs/ft}^3$$

The jet mass flux will be equal to

$$m_j = \rho_j A_j v_j$$
$$= 0.00271(0.2/12)(946.9)$$
$$= 0.0428 \text{ slugs/s}$$

The free-stream dynamic pressure is

$$q = \tfrac{1}{2}\rho V^2$$
$$= 0.0023378(50 \times 1.467)^2/2$$
$$= 6.397 \text{ psf}$$

Thus,

$$C_\mu = \frac{(0.0428)(946.9)}{6.397(5)}$$
$$= 1.27$$

From Figures 3.47 and 3.48,

$$C_{l_\alpha} = 9.09/\text{rad}$$
$$C_{l_\delta} = 6.5/\text{rad}$$

$$\alpha_{max} - \alpha_{max}(C_\mu = 0) = -2°$$

From Figure 3.30, $C_{l_{max}}$ for the unblown airfoil without a flap is equal approximately to 1.4. Using Figures 3.33 and 3.34, ΔC_l due to the plain flap ($C_\mu = 0$) is estimated as

$$\Delta C_l = 2\pi(0.6)(0.035)\left(\frac{50}{57.3}\right) = 1.15$$

so that

$$\Delta C_{l_{max}} \simeq \frac{2(1.15)}{3} = 0.77$$

Thus, for $C_\mu = 0$ with the flap deflected, $C_{l_{max}}$ is estimated to be 2.17. At $\alpha = 0$, C_l is estimated to be 1.5. Thus, with $C_{l_\alpha} = 0.109$ (from Figure 3.30),

$$\alpha_{max} = \frac{2.17 - 1.5}{0.109}$$
$$= 6.1°$$

or, relative to the zero lift line, flaps up,

$$\alpha_{max} = 9.1°$$

For the operating C_μ, the angle of attack for the zero lift line at stall is estimated to equal 7.1°.
Thus,

$$C_{l_{max}} = C_{l_\alpha}\alpha_{max} + C_{l_\delta}\delta$$

or

$$C_{l_{max}} = 9.09\frac{7.1}{57.3} + 6.5\frac{50}{57.3}$$
$$= 6.8$$

The preceding answer must, of course, be further corrected, using Figure 3.43 and Equation 3.46, to account for trimming tail loads. Also, it should be emphasized that the preceding is, at best, an estimate for preliminary design purposes or relative parametric design studies. In the final analysis, model and prototype component testing of the blowing system must be performed.

Credit for the practical application of the jet flap must be given to John Attinello. Prior to 1951, all blown systems utilized pressure ratios less than critical in order to avoid supersonic flow in the jet. Such systems required large and heavy ducting. For his honors thesis at Lafayette College, Attinello demonstrated with "homemade" equipment that a supersonic jet would adhere to a deflected flap. This was contrary to the thinking of the day that not only would a supersonic jet separate from a blown flap, but the losses associated with the shock wave system downstream of the nozzle would be prohibitive. Later, more sophisticated testing performed by the David Taylor Model Basin confirmed Attinello's predictions (Ref. 3.38) of high lift coefficients for supersonic jet flaps. This led to the development of compact, lightweight systems using bleed air from the turbojet engine compressor section. The Attinello flap system was flight tested on an F9F-4 and produced a significant decrease in the stalling speed for an added weight of only 50 lb. Following this success, the Attinello flap went into production on the F-109, F-4, F8K, A5, and other aircraft, including several foreign models.

THE LIFTING CHARACTERISTICS OF A FINITE WING

A two-dimensional airfoil with its zero lift line at an angle of attack of 10° will deliver a lift coefficient, C_l, of approximately 1.0. When incorporated into a wing of finite aspect ratio, however, this same airfoil at the same angle of attack will produce a wing lift coefficient, C_L, significantly less than 1.0. The effect of aspect ratio is to decrease the slope of the lift curve C_{L_α} as the aspect ratio decreases. Figure 3.50 illustrates the principal differences in the

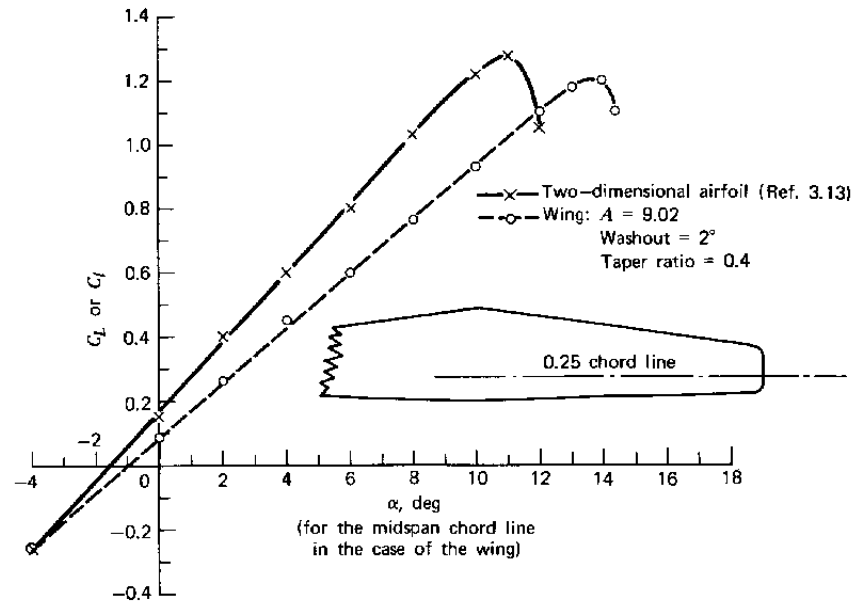

Figure 3.50 Comparison of NACA 65–210 airfoil lift curve with that of a wing using the same airfoil.

lift behavior of a wing and an airfoil. First, because the wing is twisted so that the tip is at a lower angle of attack than the root (washout), the angle for zero lift, measured at the root, is higher for the wing by approximately 0.6°. Next, the slope of the wing's lift curve, C_{L_α}, is approximately 0.79 of the slope for the airfoil. Finally, $C_{L_{max}}$ is only slightly less than $C_{l_{max}}$, in the ratio of approximately 0.94. These three differences are almost exactly what one would expect on the basis of wing theory, which will now be developed.

The Vortex System for a Wing

A wing's lift is the result of a generally higher pressure acting on its lower surface compared with the pressure on the upper surface. This pressure difference causes a spanwise flow of air outward toward the tips on the lower surface, around the tips, and inward toward the center of the wing. Combined with the free-stream velocity, this spanwise flow produces a swirling motion of the air trailing downstream of the wing, as illustrated in Figure 3.51. This motion, first perceived by Lanchester, is referred to as the wing's trailing vortex system.

Immediately behind the wing the vortex system is shed in the form of a vortex sheet, which rolls up rapidly within a few chord lengths to form a pair

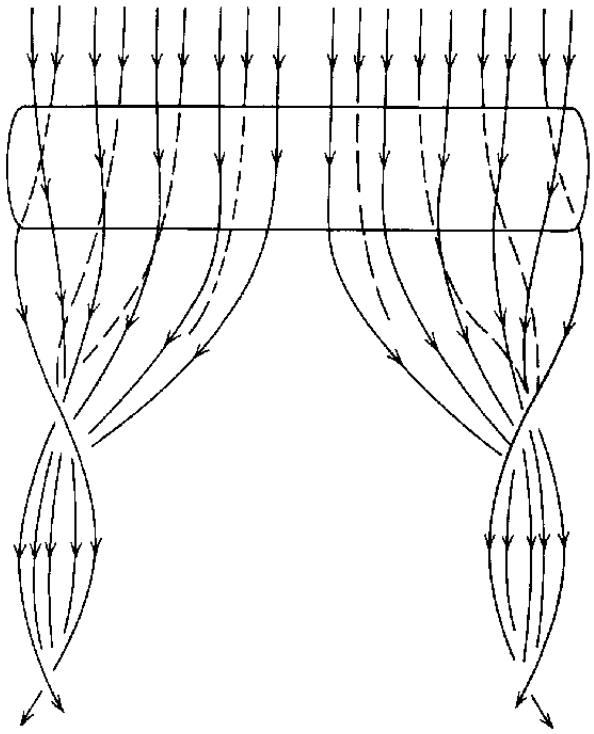

Figure 3.51 Generation of vortex system by finite aspect ratio wing.

of oppositely rotating line vortices. Looking in the direction of flight, the vortex from the left wing tip rotates in a clockwise direction; the right tip vortex rotates in the opposite direction.

The trailing vortex system, not present with a two-dimensional airfoil, induces an additional velocity field at the wing that must be considered in calculating the behavior of each section of the wing.

If the aspect ratio of the wing is large, approximately 5 or higher, the principal effect of the trailing vortex system is to reduce the angle of attack of each section by a small decrement known as the induced angle of attack, α_i. In this case Prandtl's classical lifting line theory (Ref. 3.28) applies fairly well. As shown in Figure 3.52, the wing is replaced by a single equivalent vortex line, known as the "bound vortex," since it is in a sense bound to the wing. The strength of this vortex, $\Gamma(y)$, is related to the lift distribution along the wing by the Kutta–Joukowski relationship.

$$\frac{dL(y)}{dy} = \rho V \Gamma(y) \tag{3.64}$$

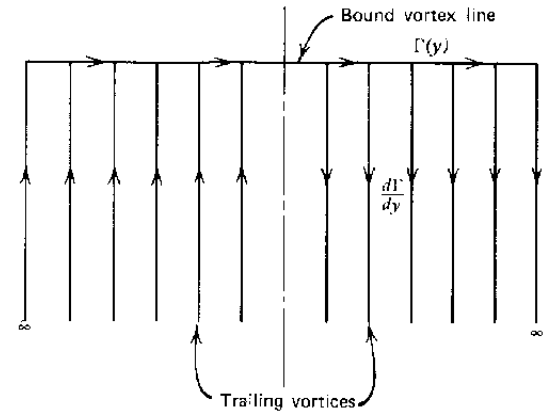

Figure 3.52 Lifting line model of a wing and trailing vortex system.

Expressing the lift per unit length of span in terms of the section chord length, $c(y)$, and section lift coefficient, $C_l(y)$, leads to

$$\Gamma(y) = \tfrac{1}{2} c(y) C_l(y) V \tag{3.65}$$

With no physical surface outboard of the wing tips to sustain a pressure difference, the lift, and hence Γ, must vanish at the tips.

According to the Helmholtz theorem regarding vortex continuity (Ref. 1.3, p. 120), a vortex line or filament can neither begin nor end in a fluid; hence it appears as a closed loop, ends on a boundary, or extends to infinity. Thus, it follows that if in going from y to $y + dy$ the bound circulation around the wing increases from Γ to $\Gamma + d\Gamma$, a free vortex filament of strength $d\Gamma$, lying in the direction of the free-stream velocity, must be feeding into Γ in order to satisfy vortex continuity. This statement may be clarified by reference to Figure 3.53.

The entire vortex system shown in Figure 3.52 can be visualized as being closed infinitely far downstream by a "starting" vortex. This vortex, opposite

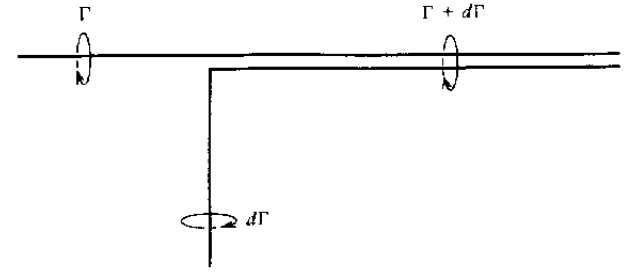

Figure 3.53 Illustration of vortex continuity.

in direction to the bound vortex, would be shed from the trailing edge of the wing as its angle of attack is increased from zero.

The trailing vortex system of strength $d\Gamma$ induces a downwash, $w(y)$, at the lifting line, as mentioned earlier. As pictured in Figure 3.54, this reduces the angle of attack by the small angle α_i. Thus the section lift coefficient will be given by

$$C_l = C_{l_\alpha}(\alpha - \alpha_i) \tag{3.66}$$

α being measured relative to the section zero lift line.

To a small angle approximation, the induced angle of attack, α_i, is given by w/V. The downwash, w, can be determined by integrating the contributions of the elemental trailing vortices of strength $d\Gamma$. If the vortex strength $d\Gamma$ trails from the wing at a location of y, its contribution to the downwash at another location y_0 can be found by Equation 2.64 to be

$$dw(y_0) = \frac{d\Gamma(y)}{4\pi(y_0 - y)} \tag{3.67}$$

Thus, α_i becomes

$$\alpha_i(y_0) = \frac{1}{4\pi V}\int_{-b/2}^{b/2} \frac{d\Gamma(y)}{y_0 - y} \tag{3.68}$$

Equations 3.65, 3.66, and 3.68 together relate $\Gamma(y)$ to $c(y)$ and $\alpha(y)$ so that, given the wing geometry and angle of attack, one should theoretically be able to solve for Γ and hence the wing lift. In order to accomplish the solution, it is expedient to make the coordinate transformation pictured in Figure 3.55.

$$y = \frac{b}{2}\cos\theta$$

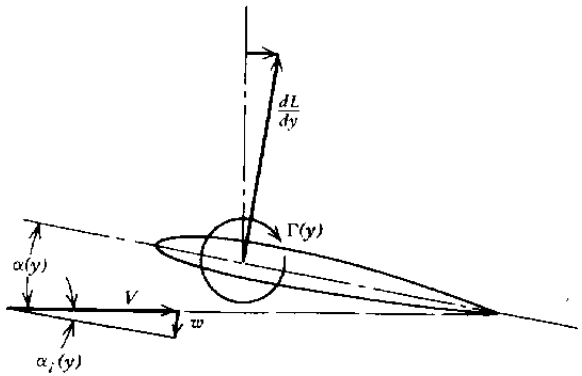

Figure 3.54 A wing section under the influence of the free-stream velocity and the downwash.

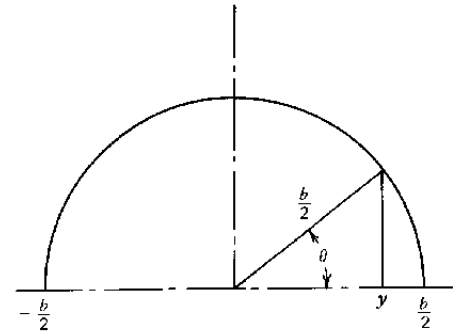

Figure 3.55 Coordinate transformation used in the reduction of the lifting line equations.

Hence, Equation 3.67 becomes

$$\alpha_i(\theta_0) = \frac{1}{2\pi bV}\int_0^\pi \frac{d\Gamma(\theta)}{\cos\theta - \cos\theta_0} \tag{3.69}$$

Since more elaborate and comprehensive treatments of wing theory can be found in texts devoted specifically to the subject (e.g., see Ref. 3.29), only the classical solution for the eliptic Γ distribution will be covered here. This particular case is easily handled and results in the essence of the general problem.

Assume that Γ is of the form

$$\Gamma = \Gamma_0\sqrt{1 - \left(\frac{2y}{b}\right)^2} \tag{3.70}$$

Using Equation 3.68 this transforms to

$$\Gamma = \Gamma_0 \sin\theta$$

Here, Γ_0 is obviously the midspan value of the bound circulation. Thus Equation 3.69 becomes

$$\alpha_i(\theta_0) = \frac{\Gamma_0}{2\pi bV}\int_0^\pi \frac{\cos\theta\, d\theta}{\cos\theta - \cos\theta_0}$$

The preceding integral was encountered previously in thin airfoil theory and has a value of π. Thus, for an elliptic Γ distribution, α_i and hence the downwash is found to be a constant independent of y.

$$\alpha_i = \frac{\Gamma_0}{2bV} \tag{3.71}$$

If the wing is untwisted so that α is also not a function of y then, from

Equation 3.66, it follows that the section C_l is constant along the span. Thus,

$$L = \int_{-b/2}^{b/2} \frac{1}{2}\rho V^2 c C_l \, dy$$

$$= \frac{1}{2}\rho V^2 C_l \int_{-b/2}^{b/2} c \, dy$$

$$= \frac{1}{2}\rho V^2 C_l S$$

But

$$C_l = \frac{L}{qS}$$

Hence,

$$C_l = C_L$$

Equation 3.65 then gives

$$\Gamma(y) = \frac{1}{2} c(y) C_L V$$

or,

$$c(y) = \frac{2\Gamma_0}{C_L V}\sqrt{1-\left(\frac{2y}{b}\right)^2}$$

$$= c_0\sqrt{1-\left(\frac{2y}{b}\right)^2}$$

Thus it is found that, according to lifting line theory, an untwisted wing with an elliptical planform will produce an elliptic Γ distribution. Such a wing will have a constant downwash and section C_l.

Since C_l is constant and equal to C_L, Equations 3.65, 3.66, and 3.71 can be applied at the midspan position in order to determine the slope of the wing lift curve. First, from Equations 3.72 and 3.65,

$$\alpha_i = \frac{c_0 C_L}{4b}$$

But, for the planform given by Equation 3.66, c_0 and b are related to the aspect ratio by

$$A = \frac{4b}{\pi c_0}$$

Thus, α_i becomes

$$\alpha_i = \frac{C_L}{\pi A} \tag{3.72}$$

Inserted into Equation 3.66, the preceding results in

$$C_L = C_{l_\alpha}\left(\alpha - \frac{C_L}{\pi A}\right)$$

or,

$$C_L = C_{l_\alpha}\left[\frac{1}{(1 + C_{l_\alpha})/\pi A}\right]\alpha$$

Using the theoretical value of 2π C_l/rad derived earlier, the preceding becomes

$$C_L = C_{l_\alpha}\left(\frac{A}{A+2}\right)\alpha \tag{3.73}$$

Equations 3.72 and 3.73 are important results. The induced angle of attack is seen to increase with decreasing aspect ratio which, in turn, reduces the slope of the lift curve, C_{L_α}. A wing having a low aspect ratio will require a higher angle of attack than a wing with a greater aspect ratio in order to produce the same C_L.

It was stated previously that the comparative performance between the wing and airfoil shown in Figure 3.50 could be explained theoretically. In this case, $A = 9.02$ so that, on the basis of Equation 3.73,

$$C_{L_\alpha} = 0.819\, C_{l_\alpha}$$

This result is within about 2% of the experimental results presented in Figure 3.50.

As the aspect ratio decreases, the lifting line becomes progressively less accurate. For example, for an aspect ratio of 4.0, Equation 3.73 is approximately 11% higher than that predicted by more exact methods.

As described in Reference 3.3, a more accurate estimate of C_{L_α} is obtained from

$$C_{L_\alpha} = C_{l_\alpha}\frac{A}{A + [2(A+4)/(A+2)]} \tag{3.74a}$$

An alternate to Equation 3.74*a* is offered by Reference 3.35 and is referred to as the Helmbold equation, after the original source noted in the reference. The Helmbold equation reads

$$C_{L_\alpha} = C_{l_\alpha}\frac{A}{(C_{l_\alpha}/\pi) + \sqrt{(C_{l_\alpha}/\pi)^2 + A^2}}$$

Replacing C_{l_α} by 2π in the denominator,

$$C_{L_\alpha} = C_{l_\alpha}\frac{A}{2 + \sqrt{4 + A^2}} \tag{3.74b}$$

Equation 3.74*a* and 3.74*b* agree within a couple of percent over the range of practical aspect ratios and approach each other in the limits of $A = 0$ or $A = \infty$. This holds for high or low aspect ratios and is based on an approximate lifting surface theory, which accounts for the chordwise distribution of bound circulation as well as the spanwise distribution.

The Maximum Lift of a Finite Wing

The maximum lift coefficient of a finite wing is influenced by several factors. Obviously, $C_{L_{max}}$ is strongly dependent on $C_{l_{max}}$; that is, the wing's performance depends on it's airfoil performance. Second, the spanwise extent to which the wing is flapped has a significant influence on $C_{L_{max}}$. Also in estimating $C_{L_{max}}$, one must account for the presence of the fuselage, the tail download required to trim the aerodynamic pitching moment, and the spanwise distribution of loading over the wing.

The effect of aspect ratio on $C_{L_{max}}$ is slight, as one might expect from the preceding considerations on the elliptic wing. The wing lift coefficient and section lift coefficients are nearly equal.

The detailed estimation of a wing's $C_{L_{max}}$ begins with a calculation of its spanwise load distribution. There are several methods to be found in the literature for doing this. Many of these fall into a class known as vortex lattice methods. One of the first of these can be found in Reference 3.30.

The vortex lattice method is similar to lifting line theory except that discrete vortex lines are also distributed in the chordwise direction. As illustrated in Figure 3.56, the wing is covered with a mesh of spanwise and

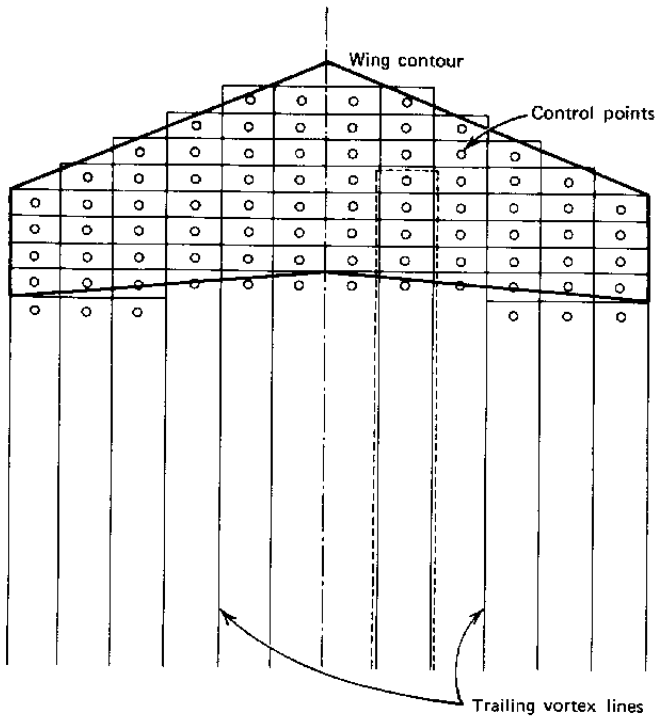

Figure 3.56 Vortex lattice model for a wing.

chordwise bound vortex lines with free vortex lines shed downstream from the trailing edge. At every juncture of the vortex lines, Helmholtz's law of vortex continuity must hold. In addition, control points are chosen over the wing equal in number to the number of unknown vortex line strengths. The unknown vortex strengths are then adjusted to assure that the resultant flow at each control point is tangent to the mean surface of the wing.

The lattice model shown in Figure 3.56, in the manner of Reference 3.30, is formed by the superposition of horseshoe-shaped line vortices. One such vortex is shown dashed for illustrative purposes. Note that the downstream control points are aft of the last bound vortex lines; some points are even slightly off of the wing's surface. Stipulating that the flow at these points parallels the camber surface at the trailing edge will satisfy approximately the Kutta condition.

Trends in the behavior of $C_{L_{max}}$ as related to wing geometry can be seen by the application of an approximate method for determining spanwise load distribution known as Schrenk's approximation (Ref. 3.31).

This method deals with two distributions: a basic lift distribution, and an additional lift distribution. The basic distribution is that which exists along the span when the total lift is equal to zero. Approximately, this lift distribution is taken as the average of a constant "zero" distribution and one obtained by neglecting any induced velocities. Thus,

$$\tfrac{1}{2}\rho V^2 c C_l = \tfrac{1}{2}[\tfrac{1}{2}\rho V^2 c C_{l_\alpha}(\alpha_{w_0} + \epsilon) + 0]$$

or the basic section lift coefficient, C_{l_b}, will be

$$C_{l_b} = \frac{C_{l_\alpha}}{2}(\alpha_{w_0} + \epsilon) \tag{3.78}$$

The additional lift distribution results from an angle of attack different from α_{w_0} and is assumed to be the average of an elliptic distribution and one proportional to the planform, both having the same total lift. For the latter,

$$\begin{aligned} cC_l &\propto c \\ &= kc \end{aligned}$$

But

$$\begin{aligned} L &= \int_{-b/2}^{b/2} qcC_l\, dy \\ &= qk \int_{b/2}^{b/2} c\, dy \\ &= qks \end{aligned}$$

Thus, $k = C_L$.

For the elliptic distribution,

$$cC_L = K\sqrt{1 - \left(\frac{2y}{b}\right)^2}$$

so that

$$L = \int_{-b/2}^{b/2} qK\sqrt{1-\left(\frac{2y}{b}\right)^2}\,dy$$

The constant of proportionality, K, in this case becomes

$$K = \frac{4S}{\pi b}C_L$$

The additional section lift coefficient then becomes

$$C_{l_a} = \frac{C_L}{2}\left[1+\frac{4S}{\pi bc}\sqrt{1-\left(\frac{2y}{b}\right)^2}\right] \tag{3.79}$$

Usually C_{l_a} is defined as the value of Equation 3.79 for a C_L of unity; thus,

$$C_l = C_{l_b} + C_{l_a}C_L \tag{3.80}$$

The manner in which this equation is used to estimate $C_{L_{max}}$ is best explained by an example. Consider the wing of Figure 3.50. This particular wing has a taper ratio of 0.4 and a washout of 2°. Using Equations 3.78 and 3.79, the basic and additional section lift coefficient distributions given in Figure 3.57 were calculated. Also graphed on this figure is $C_{l_{max}}$ as a function of spanwise location. In this instance, $C_{l_{max}}$ is taken from Figure 3.50 to be a constant. In many cases, $C_{l_{max}}$ decreases toward the tip as the airfoil becomes relatively thinner or as the chord lengths become smaller.

Combining C_{l_b} and C_{l_a} in the form of Equation 3.80, Figure 3.57 shows that a wing C_L of 1.22 results in a section C_l halfway out along the span, which is just equal to the section $C_{l_{max}}$ at that location. Any attempt to increase C_L above this value will therefore cause the wing to stall at this location. Since the C_l curve is rather flat in this location, the stalling would be expected to spread to either side of $2y/b$ equal to 0.5. Thus, to estimate the $C_{L_{max}}$ of a wing, one finds the wing C_L that results in a section C_l somewhere along the span, which is just equal to the section $C_{l_{max}}$. In this instance, the $C_{L_{max}}$ value of 1.22 compares favorably with the experimental results. Generally, however, the $C_{L_{max}}$ predicted by this method will be somewhat conservative, since the total wing C_L may still increase somewhat, even though a section of it begins to stall.

As a further and more extreme example of the method, consider the wing of Figure 3.50 equipped with 60% span, 20% chord split flaps deflected 60°. From Equation 3.43, ΔC_l is estimated to be

$$\begin{aligned}\Delta C_l &= C_{l_\alpha}\tau\eta\,\delta \\ &= 0.108\ (0.545)(0.35)(60) \\ &= 1.236\end{aligned}$$

$\Delta C_{l_{max}}$, empirically, is approximately 0.83 of the preceding equation (Figure 3.34) or 1.026. Thus, Figure 3.57 is revised as shown in Figure 3.58 to increase the section $C_{l_{max}}$ to 2.30 over the inner 60% of the span.

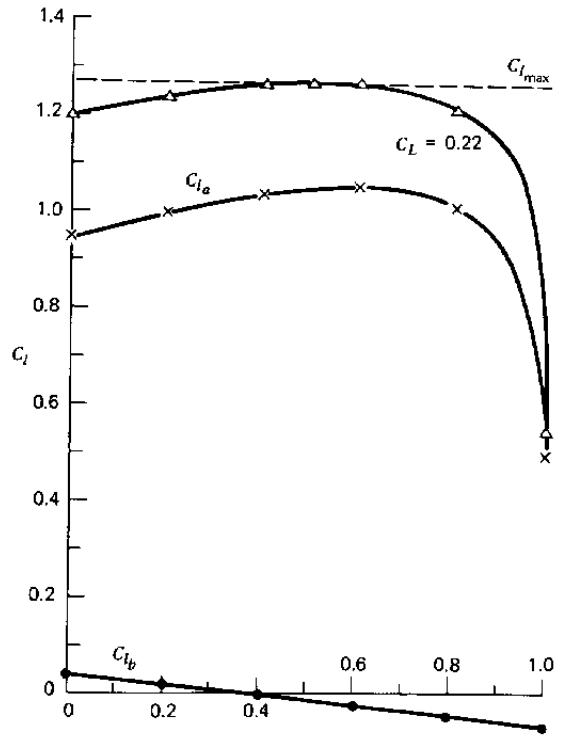

Figure 3.57 Predicted lift coefficient distributions for wing of Figure 3.50.

Aerodynamically the twist of the wing is changed by lowering the flaps. Relative to the midspan chord, the zero lift lines of the sections outboard of the flaps are reduced in angle of attack by $\Delta C_l/C_{l_\alpha}$, or 11.4°. Thus, for this flapped wing, ϵ, in degrees, becomes

$$\epsilon = -2\left|\frac{2y}{b}\right| \qquad 0 \le \left|\frac{2y}{b}\right| \le 0.6$$

$$\epsilon = -2\left|\frac{2y}{b}\right| - 11.4 \qquad \left|\frac{2y}{b}\right| > 0.6$$

For this twist distribution and a taper ratio of 0.4, the angle of attack of the midspan zero lift line, α_{w_0}, for zero lift becomes 4.24°. Thus

$$C_{l_b} = 0.054(4.24 + \epsilon)$$

The additional lift distribution remains the same, since the planform is

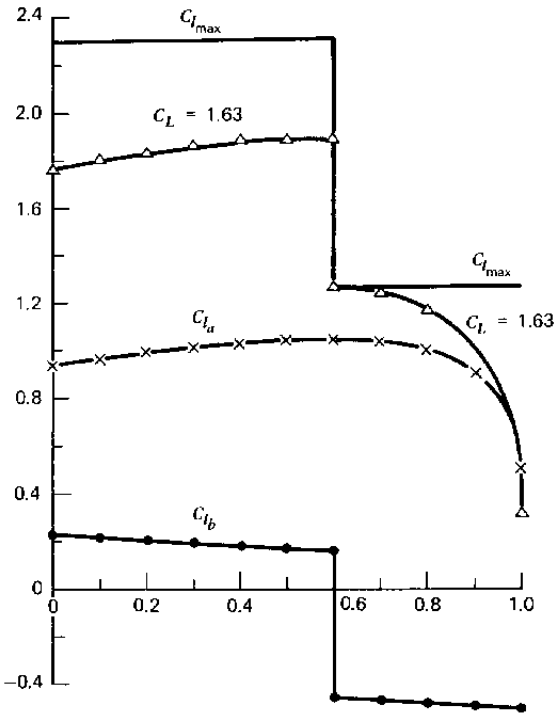

Figure 3.58 Predicted lift coefficient distributions for wing of Figure 3.50 with 60% span, 20% chord split flaps deflected 60°.

unchanged. The predicted C_l distributions with the partial span split flaps are presented in Figure 3.58.

Figure 3.58 predicts that the wing will begin to stall just outboard of the flaps at a wing C_L of 1.63. This result agrees exactly with Reference 3.27 with regard to both $C_{L_{max}}$ and the location of the initial stall. This agreement is somewhat fortuitous in view of Shrenk's approximation, which is obviously inexact, since it allows a finite loading at the tip and other discontinuities in the cC_l distribution. Nevertheless, for preliminary design studies, or in lieu of more exact lifting surface methods, Shrenk's approximation is a useful tool.

Effect of Fuselage on $C_{L_{max}}$

In working with a wing-fuselage combination, one normally defines the wing planform area to include the portion submerged within the fuselage. When a lift coefficient is quoted for the combination, it is based on this total wing planform area obtained by extrapolating the leading and trailing edges into the fuselage centerline. Generally, the fuselage will effect a decrease in

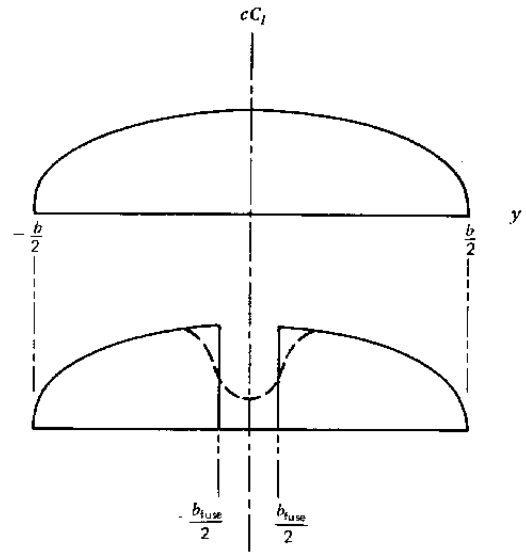

Figure 3.59 Effect of fuselage on spanwise lift distribution.

the lift per unit span over the portion of the wing covered by the fuselage. This is illustrated in Figure 3.59. The upper distribution is without the fuselage. The dashed line on the lower figure is the qualitative drop in cC_l due to the fuselage. As an approximation, let us assume that the fuselage effects a constant drop in cC_l over its width proportional to the midspan value of cC_l. Thus, the lift decrement resulting from the fuselage will be

$$\Delta L = -kqC_{l_0}S_{\text{fuse}}$$

S_{fuse} is the wing planform area submerged in the fuselage, and C_{l_0} is the nearly constant section C_l near the center of the wing. k is the constant of proportionality. Thus the total C_L with the fuselage, $C_{L_{\text{fuse}}}$, can be written in terms of C_L before the fuselage is added as

$$C_{L_{\text{fuse}}} = C_L\left(1 - k\frac{C_{l_0}}{C_L}\frac{S_{\text{fuse}}}{S}\right) \tag{3.81}$$

In Reference 3.27, two wings equipped with partial and full-span, split, single-slotted, and double-slotted flaps were tested with and without a fuselage. The fuselage was circular in cross-section and the wing was mounted slightly above the middle of the fuselage. The ratio S_{fuse}/S was equal to 0.083. The results of these tests are plotted in Figure 3.60 and compared with Equation 3.79 using $kC_{l_0}/C_L = 1.0$. Also plotted on Figure 3.60 are test results from References 3.32 and 3.33. The ratio S_{fuse}/S was nearly the same for these

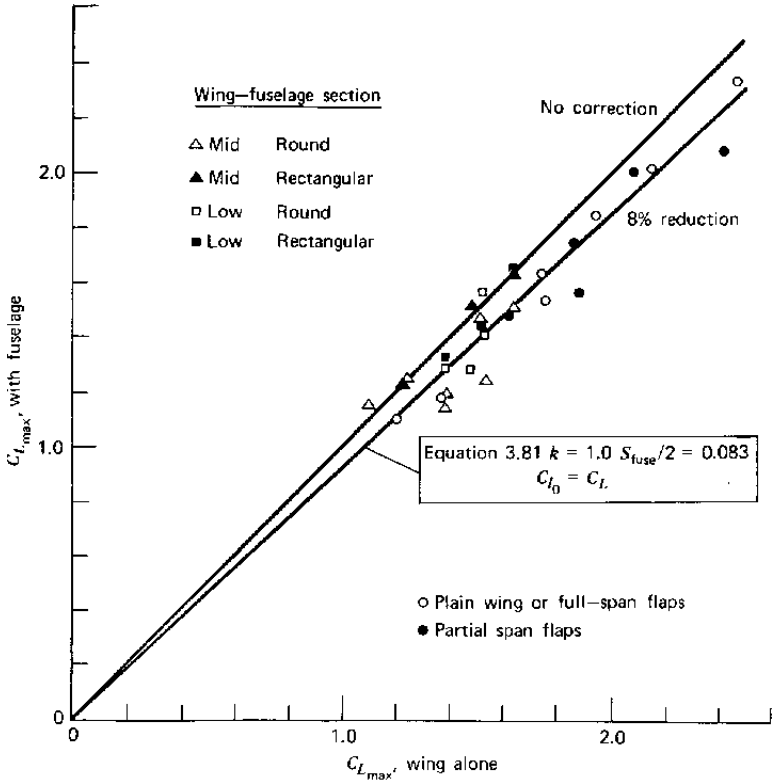

Figure 3.60 Effect of fuselage on $C_{L_{max}}$.

two references as for Reference 3.27. These data support the form of Equation 3.81, at least to the extent that the correction to $C_{L_{max}}$ for the fuselage appears to increase linearly with $C_{L_{max}}$ of the wing alone. The correction depends on the cross-sectional shape of the fuselage and seems to vanish or even be slightly favorable for a rectangularly shaped section. Reference 3.34 also shows the correction to be slight for elliptical shapes where the height is greater than the width.

The decrement in $C_{L_{max}}$ also depends on wing position and appears to be a maximum for the midwing configuration.

Effect of Trim on $C_{L_{max}}$

In order to calculate the stalling speed of an airplane in steady flight, one must consider that, in addition to the weight, the wing's lift must support any download on the horizontal tail required to trim the airplane around its pitching axis. In order to determine this additional trim load, refer to Figure

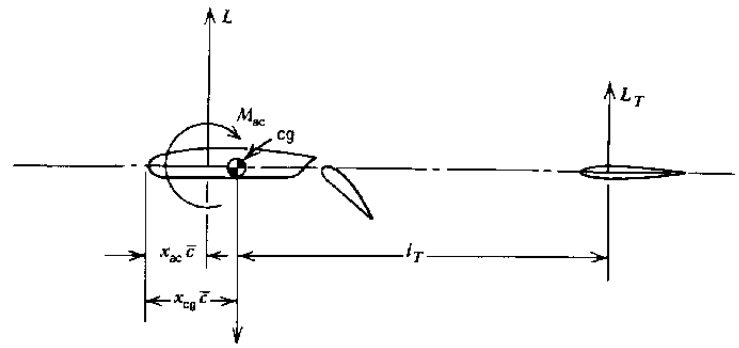

Figure 3.61 Longitudinal trim of an airplane.

3.61. Here, the wing lift L, the tail lift, L_T, the pitching moment about the wing's aerodynamic center, M_{ac}, and the weight are all shown in a positive sense. With the aerodynamic center of the tail located a distance of l_T behind the center of gravity and the wing's aerodynamic center a distance of $(x_{cg} - x_{ac})\bar{c}$ ahead, the tail lift to trim is given by

$$L_T = \frac{M_{ac}}{l_T} + L\frac{\bar{c}}{l_T}(x_{cg} - x_{ac})$$

In addition, static equilibrium in the vertical direction requires that

$$L + L_T = W$$

Therefore, it follows that

$$W = L\left[1 + \frac{\bar{c}}{l_T}(x_{cg} - x_{ac})\right] + \frac{M_{ac}}{l_T}$$

In coefficient form this becomes

$$C_L = C_{L_W}\left[1 + \frac{\bar{c}}{l_T}(x_{cg} - x_{ac})\right] + C_{M_{ac}}\frac{\bar{c}}{l_T} \tag{3.82}$$

Here, C_L is taken to mean the trim C_L.

$$C_L = \frac{W}{qS}$$

C_{L_W} refers to the untrimmed wing lift coefficient corrected for the fuselage.

It was mentioned earlier that the added drag caused by flaps must sometimes be considered in the trim of an airplane. If ΔC_D denotes this increment in the drag coefficient and if the flaps are located a distance of h above the center of gravity, Equation 3.82 modified to account for the flap

drag becomes

$$C_L = C_{L_W}\left[1 + \frac{\bar{c}}{l_T}(x_{cg} - x_{ac})\right] + C_{M_{ac}}\frac{\bar{c}}{l_T} + \Delta C_D \frac{h}{\bar{c}} \qquad (3.83)$$

ΔC_D can be obtained experimentally or estimated on the basis of Equations 3.45 and 3.46.

$C_{M_{ac}}$ is normally negative and greater in magnitude than the moments resulting from C_{L_W} and ΔC_D. Thus C_L is normally less than C_{L_W}. Since Equation 3.83 holds for maximum lift conditions, it follows that the trim $C_{L_{max}}$ is normally less than the wing $C_{L_{max}}$.

In calculating $C_{M_{ac}}$ for use in Equation 3.83, the section aerodynamic moment determined from $C_{M_{ac}}$, including the increment because of the flaps, is integrated over the wing excluding the part submerged in the fuselage.

Estimation of $C_{L_{max}}$ for a Complete Airplane Configuration

A Piper Cherokee PA-28 is pictured in Figure 3.62. Pertinent dimensions, areas, weights, and other data are tabulated on the figure. Extrapolating the

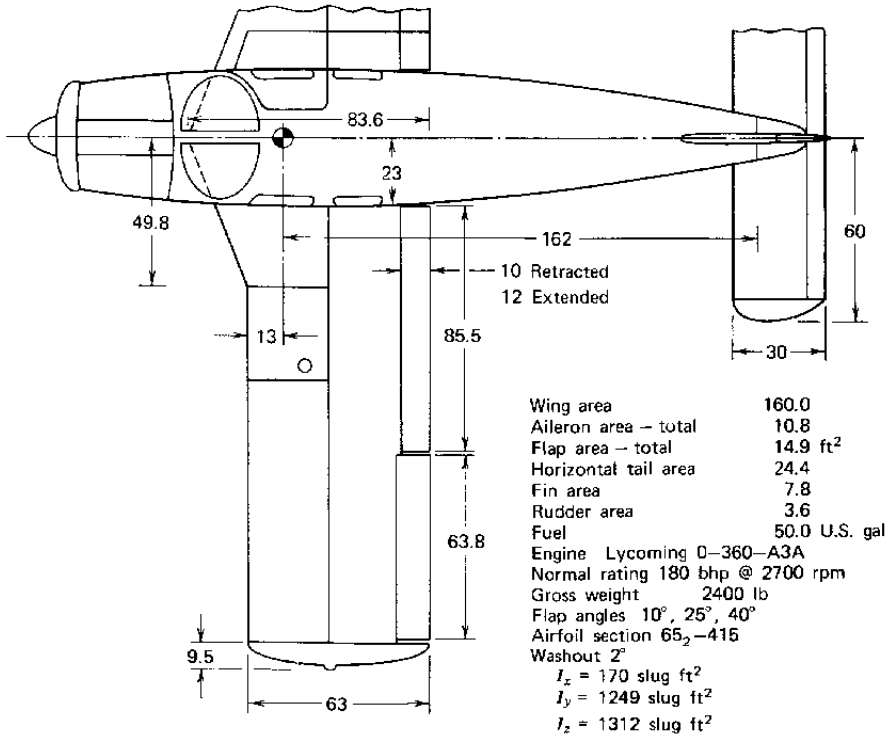

Figure 3.62 Piper Cherokee PA-28-180.

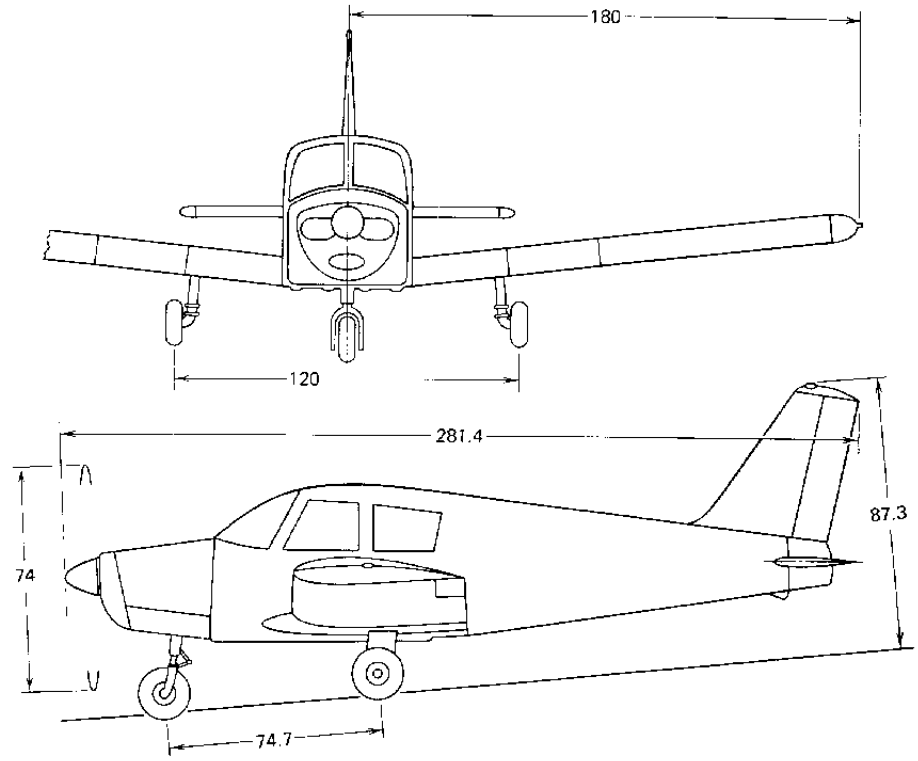

Figure 3.62 (Continued)

swept leading edge near the root into the fuselage centerline and accounting for the elliptically shaped tips gives a total wing area when the flaps are extended of 165.1 ft². The area of the wing within the fuselage is 25.3 ft². Assuming beforehand, or by iteration, a reasonable value for the "stalling speed" of 60 mph leads to a Reynold's number of approximately 3×10^6 for a wing section. For this Reynold's number, Reference 3.1 shows a value for $C_{l_{max}}$ of 1.45 for the plain 65_2-415 airfoil with a lift curve slope of 0.106 C_l/deg.

Using an 18.5% chord, single-slotted flap deflected 40°, Figures 3.32, 3.33, and 3.34 predict a ΔC_l of 1.37 corresponding to an increase of 12.9° in the angle of attack of the zero lift line. $\Delta C_{l_{max}}$ is estimated at 1.33 giving a $C_{l_{max}}$ of 2.78 for the flapped wing sections. The derivative dC_m/dC_l is estimated from Figure 3.31 to equal −0.20. Since $C_{M_{ac}} \simeq -0.07$ for the plain airfoil (Ref. 3.1), $C_{M_{ac}} \simeq -0.34$ for the flapped airfoil.

Accounting for the 2° of washout and the increment of α_{0l} caused by flaps leads to an α_{w_0} value of 6.0° from Equation 3.76. This is the angle of attack of the zero lift line at midspan for a zero wing C_L. C_{l_α} and C_{l_b} can then be calculated for the wing alone and are given in Table 3.3. The section $C_{l_{max}}$

Table 3.3 Calculated Additional and Basic Lift Coefficients for the PA-28 Wing with Flaps Down 40°

$\frac{2y}{b}$	$C_{l_a}(C_L = 1.0)$	C_{l_b}	$C_{l_{max}}$
0.1	1.04	0.62	2.78
0.2	1.09	0.59	2.78
0.3	1.12	0.57	2.78
0.4	1.09	0.55	2.78
0.5	1.06	0.53	2.78
0.6	1.02	0.51	2.78
0.7	0.98	−0.88	1.45
0.8	0.90	−0.90	1.45
0.9	0.79	−0.92	1.45
1.0	0.50	−0.94	1.45

values are also included in the table. A small amount of trial and error will show that the wing stalls initially at $2y/b$ of around 0.3 at a wing C_L of 1.97. This estimated wing $C_{L_{max}}$ must next be corrected for the effect of the fuselage.

However, since the cross section of the Cherokee's fuselage is essentially rectangular, and with the low-wing configuration, the correction to $C_{L_{max}}$ for the fuselage is taken to be zero.

The aerodynamic moment of the wing is determined by integrating the section pitching moments from the wing-fuselage juncture to the wing tip.

$$M = 2\int_{\text{y fuse}}^{b/2} qc^2 C_m \, dy$$

Expressed as a moment coefficient,

$$C_M = \frac{M}{qS\bar{c}} = \frac{b\bar{c}}{S}\left[\int_{0.128}^{0.603}\left(\frac{c}{\bar{c}}\right)(-0.34)\,dx + \int_{0.603}^{1}\left(\frac{c}{\bar{c}}\right)(-0.07)\,dx\right]$$

In this case $b\bar{c} = S$ and $\bar{c} = 66$ in., and C_M becomes

$$C_M = -0.198$$

Assuming the increment in drag from the flaps to have a negligible effect on the trim, Equation 3.82 becomes

$$C_{L_{max}} = 1.97\left[1 + \frac{5.5}{13.5}(0.214 - 0.25)\right] - 0.198\,\frac{5.5}{13.5}$$
$$= 1.86$$

In a similar manner, trim $C_{L_{max}}$ values were calculated for flap angles of 0, 10, and 25°. The resulting $C_{L_{max}}$ values were found to be 1.33, 1.42, and 1.70, respectively. These results are presented in Figure 3.63 together with experimental values. The points labeled "flight tests" were obtained by aerospace engineering students at The Pennsylvania State University as one of the experiments in a course on techniques of flight testing. The other two points were calculated from the stalling speeds quoted by the manufacturer in the airplane's flight manual.

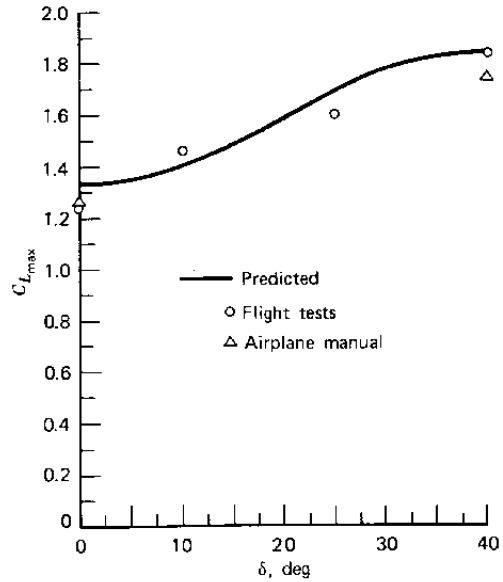

Figure 3.63 Maximum trim lift coefficient of a Piper Cherokee 180 versus flap angle.

AIRFOIL CHARACTERISTICS AT LOW REYNOLDS NUMBERS

Occasionally one has the need for airfoil characteristics at Reynolds number values much lower than those used by the NACA and others to obtain the majority of the readily available airfoil data. Most of these data

were obtained at R values of 3×10^6 and higher. For remote-piloted vehicles (RPV), model airplanes, and the like, Reynolds numbers as low as 5×10^4 can be encountered. A search of the literature will show little airfoil data available in this Reynolds number range. The most reliable low-Reynolds number airfoil data appear to be those given in Reference 3.35, where tests of five different airfoil shapes are reported for R values as low as 42,000. These tests were conducted in a low-turbulence tunnel.

The five airfoil shapes that were tested in Reference 3.37 are shown in Figure 3.64. These are seen to comprise a thin, flat plate, a thin, cambered plate, two 12% thick airfoils with 3 and 4% camber, and one 20% thick airfoil with 6% camber. The airfoil shapes are similar in appearance to the NACA four-digit series.

The lift curves for these airfoils are presented in Figure 3.65 for four different Reynolds numbers. As one might expect, the flat-plate results are nearly independent of R since the separation point at the leading edge is well defined. To a slightly lesser degree, the same can be said for the cambered plate. The form of the lift curves for the three airfoils is seen to change substantially, however, over the R range from 4.2×10^5 down to 0.42×10^5. Particularly at the very lowest Reynolds number, the C_l versus α curve is no longer linear. The flow apparently separates at all positive angles just downstream of the minimum pressure point, near the maximum thickness location.

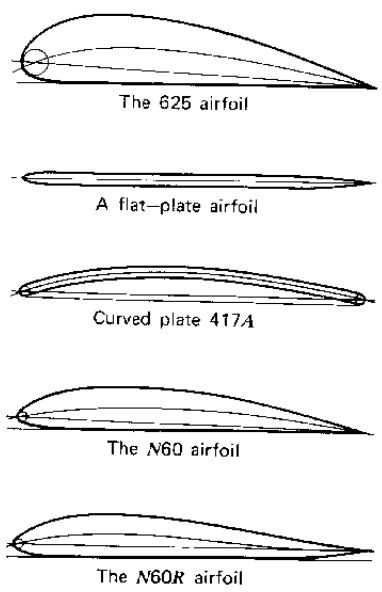

Figure 3.64 Airfoil shapes tested at low Reynolds numbers.

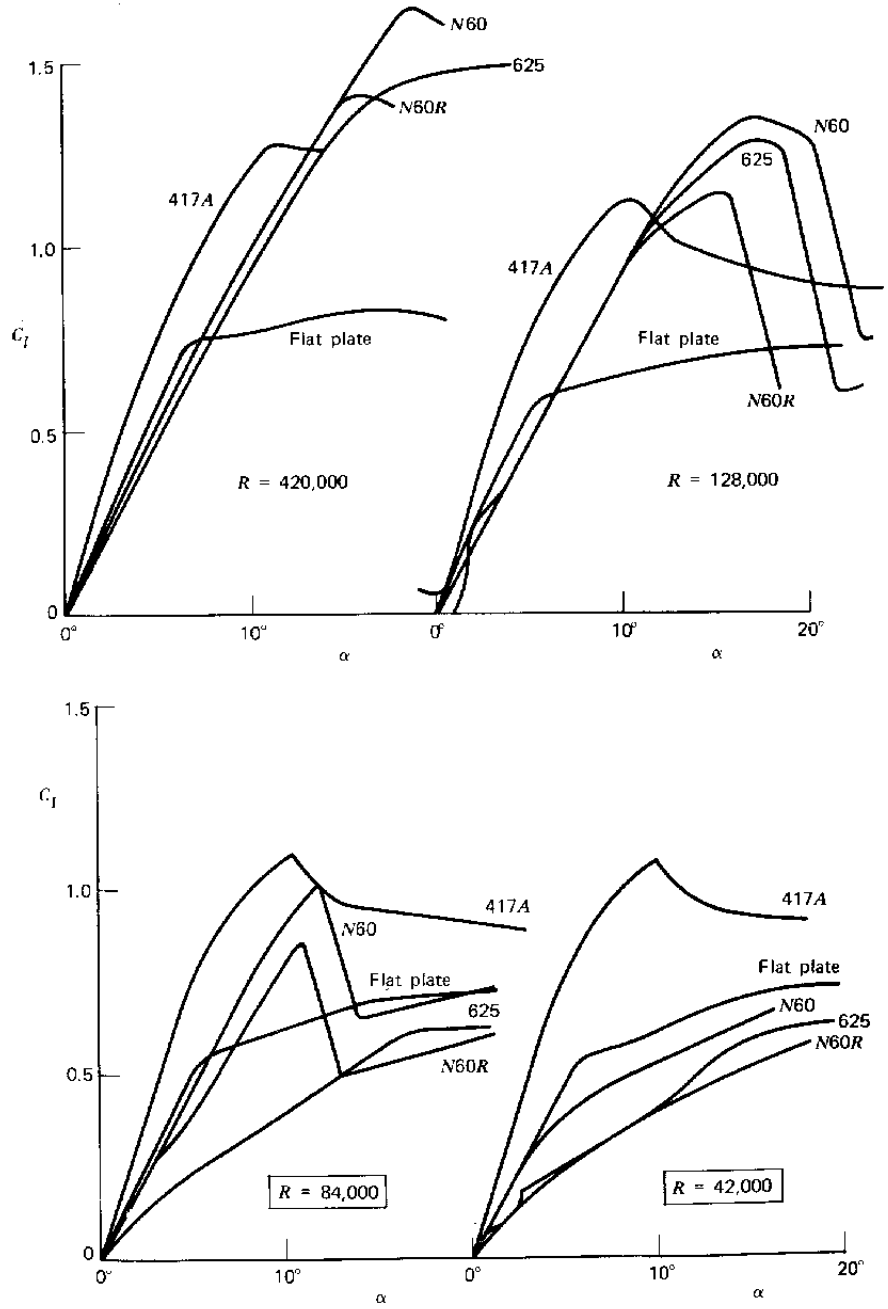

Figure 3.65 Effect of Reynolds number on airfoil lift coefficients.

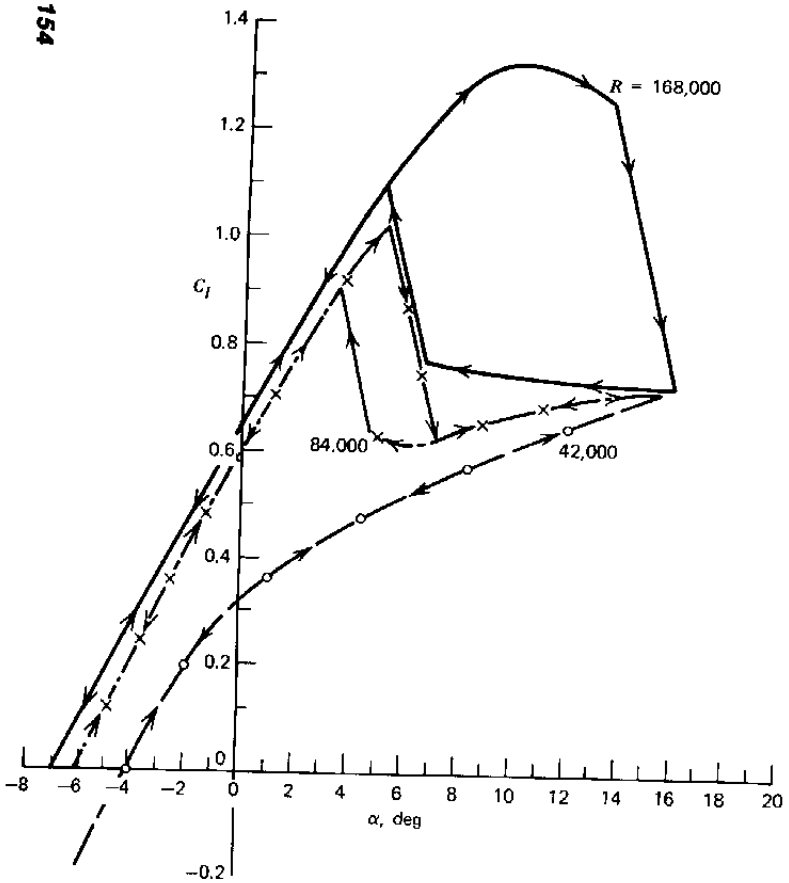

Figure 3.66 Lift curve for the N60 airfoil.

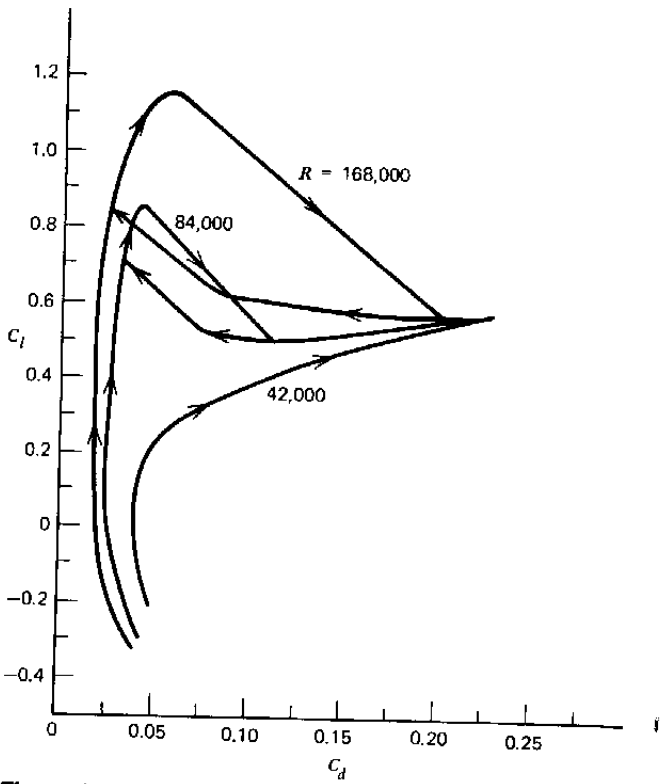

Figure 3.67 Drag polar for N60R airfoil at low Reynolds numbers.

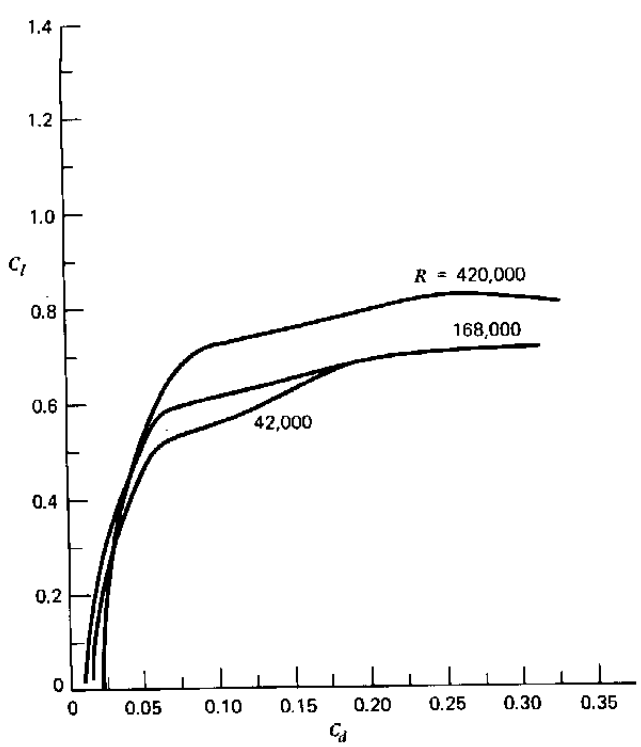

Figure 3.68 Drag polar for the flat-plate airfoil at low Reynolds numbers.

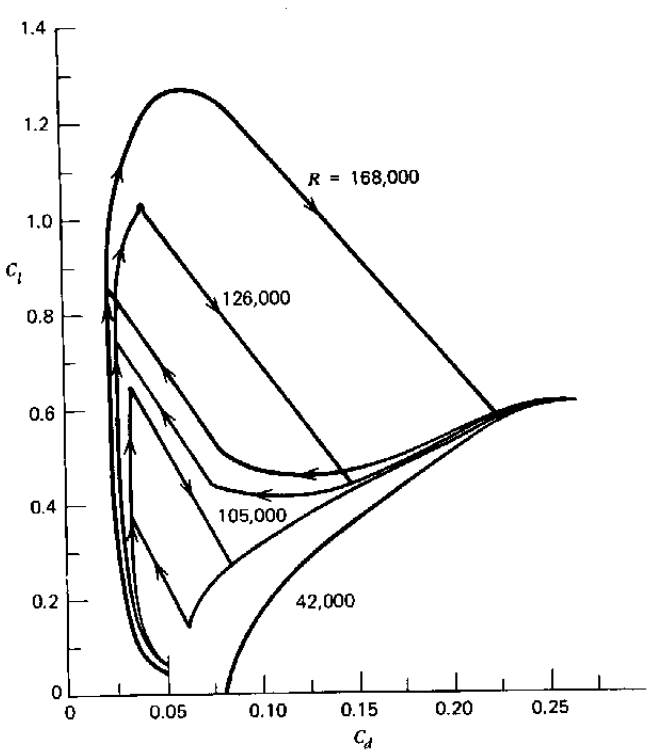

Figure 3.69 Drag polar for the 625 airfoil at low Reynolds numbers.

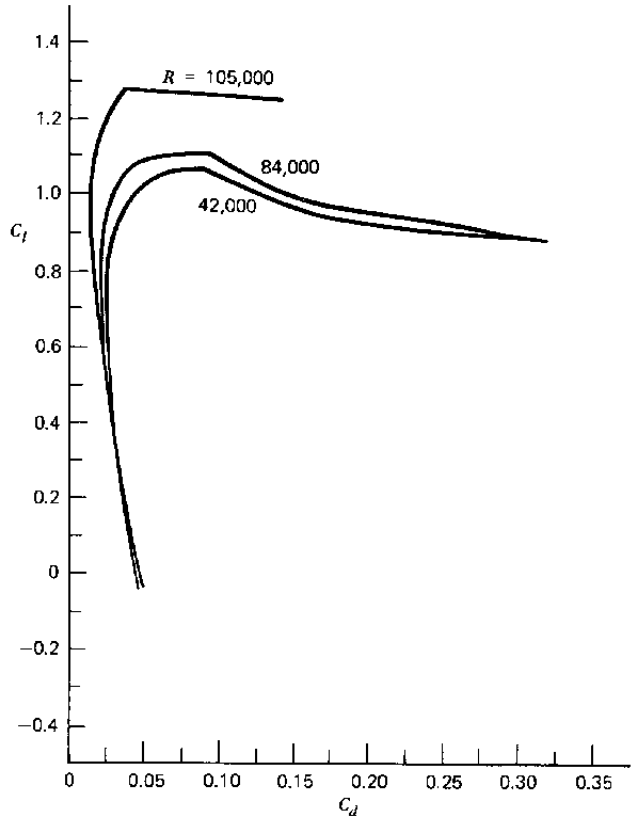

Figure 3.70 Drag polar for the 417a airfoil at low Reynolds numbers.

This explanation is substantiated by Figure 3.66. Here C_l versus α is given for the N60 airfoil. As α is first increased up to a value well beyond the stall and then decreased, a large hysteresis is seen to exist in the curves for the higher Reynolds numbers. Typically, as α is increased, complete separation on the upper surface occurs at around 12°. The angle of attack must then be decreased to around 5° before the flow will again reattach. At the lowest Reynolds number, the lift curve tends to follow the portion of the curves at the higher Reynolds numbers after stall has occurred and α is decreasing. Thus, above an α of approximately 0°, it would appear that the flow is entirely separated from the upper surface for the lower R values of 21,000 and 42,000.

Aerodynamic drag is considered in more detail in the following chapter. Nevertheless, the drag characteristics for these low-Reynolds number tests are presented now in Figures 3.67 to 3.71.

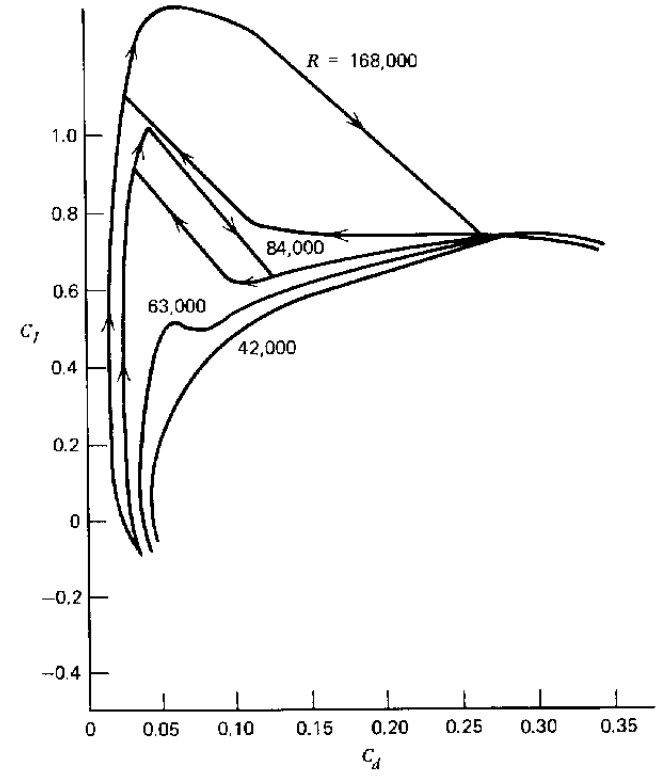

Figure 3.71 Drag polar for the N60 airfoil at low Reynolds numbers.

PROBLEMS

3.1 A wing has a taper ratio of 1/3, an area of 20 m^2, and a tip chord of 1.5 m. What is its aspect ratio?

3.2 A thin, cambered airfoil is approximated by two straight-line segments, as illustrated. Calculate C_l and $C_{m_{ac}}$ for this airfoil according to Equations 3.39 and 3.41.

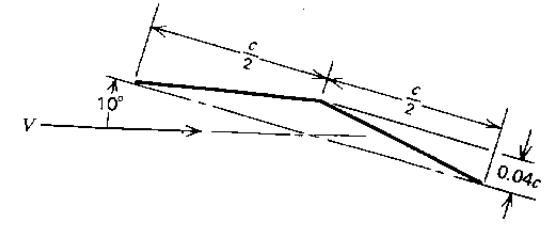

3.3 The airfoil of Problem 3.2 can be thought of as a flat-plate airfoil at an angle of attack with a 50% chord flap deflected through a given angle. What are these two equivalent angles? For this α and zero flap angle, what would C_l be? Comparing this C_l to the value from Problem 3.2, calculate the flap effectiveness factor τ and compare it with Figure 3.32.

3.4 Taking a cue from Problems 3.2 and 3.3, derive the equation for τ given in Figure 3.32.

3.5 A 23015 airfoil is equipped with a 25% fully extensible, double-slotted flap deflected at an optimum angle. It has a 6 ft chord and is operating at 100 mph at SSL conditions. Estimate $C_{l_{max}}$ from: (*a*) the summary observations listed at the beginning of the section on flaps, (*b*) the numerous tables and graphs of data, and (*c*) Figures 3.32, 3.33, and 3.34.

3.6 Estimate C_l for a thin flat-plate airfoil at a 5° angle of attack having a 33% c plain flap deflected 15°. Divide the chord into three equal segments and model the airfoil with three suitably placed point vortices.

3.7 The GA(W)-1 airfoil of Figure 3.10*a* is equipped with a pure jet flap. The jet expands isentropically from a reservoir pressure of 170 kPa absolute and a temperature of 290 °K. The airfoil is operating at SSL conditions at 15 m/s. The chord is 3 m long and the jet thickness equals 2.5 mm. Calculate C_l for an α of 2° and a jet flap angle of 30°.

3.8 A finite wing is simulated by an approximate lifting line model consisting of a bound vortex and two vortices trailing from each side, one from the tip and the other one halfway out along the span. Using the midspan and three-quarter-span stations as control points, calculate the section lift coefficients at these stations for a flat, untwisted rectangular wing with an aspect ratio of 6 at an angle of attack of 10°.

3.9 Use Schrenk's approximation instead of the approximate lifting line model to answer Problem 3.8.

3.10 The wing of Problem 3.1 has a washout of 4° and plain .3c flaps over the inboard 60% of the span. Assuming $R \simeq 9 \times 10^6$ and a smooth airfoil with the characteristics given by Figure 3.6, calculate $C_{L_{max}}$ for a flap angle of 40°. Do this by comparing section C_l and $C_{l_{max}}$ values along the span.

3.11 Write a computer program to solve the lifting line model illustrated in Figure 3.52. This is not as difficult and laborious as it may sound. Place symmetrically disposed trailing vortices of strength γ_i at a distance of $y_i(1,2,3,\ldots,n)$ from the centerline line. Choose control points of 0, $(y_1+y_2)/2$, $(y_2+y_3)/2$, $\ldots$, $(y_{n-1}+y_n)/2$. At each control point, the bound circulation equals the sum of the vortices shed outboard of the point. Also, it is easy to show that $C_l = 2\Gamma/cV$. But C_l is given by Equation 3.66, where $\alpha_i = w/V$. The downwash w can be expressed as a sum of contributions from each trailing vortex. Hence these relationships lead to a system of n simultaneous equations for the unknown vortex strengths $\gamma_1, \gamma_2, \ldots, \gamma_n$ Once these are found, Γ and C_l can be calculated.

Check your program by calculating the C_l distribution for an elliptic wing. You should find that C_l is nearly constant except near the tips, where the accuracy of the numerical model deteriorates. An n of 20 should suffice for this example.

3.12 A cambered airfoil has an angle of attack for zero lift of −4°. If this airfoil is incorporated into an untwisted wing having an elliptical planform, what will the wing lift coefficient be for an angle of attack of 8°? The wing aspect ratio is equal to 5.0.

REFERENCES

3.1 Abbot, Ira H., and Von Doenhoff, Albert E., *Theory of Wing Sections (including a summary of airfoil data)* Dover Publications, New York, 1958.

3.2 Kuethe, A. M., and Schetzer, J. D., *Foundations of Aerodynamics*, John Wiley, New York, 1959.

3.3 McCormick, B. W., *Aerodynamics of V/STOL Flight*, Academic Press, New York, London, 1967.

3.4 Rauscher, Manfred, *Introduction to Aeronautical Dynamics*, John Wiley, New York, 1953.

3.5 Stevens, W. A., Goradia, S. H., and Braden, J. A., *Mathematical Model for Two-Dimensional Multi-Component Airfoils in Viscous Flow*, NASA CR-1843, 1971.

3.6 Whitcomb, R. T., and Clark, L. R., *An Airfoil Shape for Efficient Flight at Supercritical Mach Numbers*, NASA TM X-1109, NASA Langley Research Center, July 1965.

3.7 Ayers, T. G., "Supercritical Aerodynamics Worthwhile over a Range of Speeds," *Astronautics and Aeronautics, 10* (8), August 1972.

3.8 McGhee, R. J., and Beasley, W. D., *Low-Speed Aerodynamic Characteristics of a 17-Percent Thick Airfoil Section Designed for General Aviation Applications*, NASA TN D-7428, December 1973.

3.9 Carlson, F. A., "Transonic Airfoil Analysis and Design Using Cartesian Coordinates," *AIAA J. of Aircraft, 13* (5), May 1976 (also NASA CR-2578, 1976).

3.10 Hurley, F. X., Spaid, F. W., Roos, F. W., Stivers, L. S., and Bandettini, A., "Supercritical Airfoil Flowfield Measurements," *AIAA J. of Aircraft, 12* (9), September 1975.

3.11 Lindsey, W. F., Stevenson, D. B., and Daley B. N., *Aerodynamic Characteristics of 24 NACA 16-Series Airfoils at Mach Numbers between 0.3 and 0.8*, NACA TN 1546, September 1948.

3.12 Anonymous, *Aerodynamic Characteristics of Airfoils-V (Continuation of Reports Nos. 93, 124, 182 and 244)*, NACAR 285, April 1928.

3.13 Abbott, I. H., von Doenhoff, A. E., and Stivers, Louis S., *Summary of Airfoil Data*, NACAR 824, 1945.
3.14 Anonymous, "Airfoil Information for Propeller Design," Ordnance Research Laboratory, The Pennsylvania State University, Report No. NOrd 7958–71, November 1947.
3.15 Cahill, J. F., *Summary of Section Data on Trailing-Edge High-Lift Devices*, NACAR 938, 1949.
3.16 Smith, A. M. O., "High-Lift Aerodynamics," *J. of Aircraft, 12*, (6), June 1975.
3.17 Kelly, J. A., and Hayter, N. F., *Lift and Pitching Moment at Low Speeds of the NACA 64A010 Airfoil Section Equipped with Various Combinations of a Leading-Edge Slat, Leading-Edge Flap, Split Flap, and Double-Slotted Flap*, NACA TN 3007, September 1953.
3.18 Fullmer, F. F., *Two-Dimensional Wind Tunnel Investigation of the NACA 64_1-012 Airfoil Equipped with Two Types of Leading-Edge Flap*, NACA TN 1277, May 1947.
3.19 Harris, T. A, and Recant, I. G., *Wind Tunnel Investigation of NACA 23012, 23021, and 23030 Airfoils Equipped with 40-Percent Chord Double Slotted Flaps*, NACAR 723, 1941.
3.20 Wenzinger, C. J., and Rogallo, F. M., *Résumé of Air-Load Data on Slats and Flaps*, NACA TN 690, March 1939.
3.21 Young, A. D., "The Aerodynamic Characteristics of Flaps," ARC R&M 2622, 1953.
3.22 Liebeck, R. H., "A Class of Airfoils Designed for High Lift in Incompressible Flow," *J. of Aircraft, 10* (10), October 1973.
3.23 Stratford, B. S., "The Prediction of the Separation of the Turbulent Boundary Layer," *J. of Fluid Mechanics, 5*, 1959.
3.24 Stratford, B. S., "An Experimental Flow with Zero Skin Friction Throughout its Region of Pressure Rise," *J. of Fluid Mechanics, 5*, 1959.
3.25 Liebeck, R. H., and Ormsbee, A. I., "Optimization of Airfoils for Maximum Lift," *J. of Aircraft, 7* (5), September–October 1970.
3.26 Cleveland, F. A., "Size Effects in Conventional Aircraft Design," *J. of Aircraft, 7* (6), November–December 1970.
3.27 Sivells, J. C., and Spooner, S. H., *Investigation in the Langley 19-Foot Pressure Tunnel of Two Wings of NACA 65-210 and 64-210 Airfoil Sections with Various Type Flaps*, NACA 941, 1949.
3.28 Prandtl, L., and Betz, A., "Vier Abhandlungen Zur Hydrodynamik und Aerodynamic," Göttingen, 1927 (reprint Edward Bros., 1943, Ann Arbor, Mich.).
3.29 Ashley, H., and Landahl, M., *Aerodynamics of Wings and Bodies*, Addison–Wesley, Reading, Mass., 1965.
3.30 Faulkner, V. M., "The Calculation of Aerodynamic Loading on Surfaces of Any Shape," ARC R&M 1910, 1943.

3.31 Schrenk, O., *A Simple Approximation Method for Obtaining the Spanwise Lift Distribution*, NACA TM 1910, 1940.
3.32 Jacobs, Eastman N., and Ward, Kenneth E., *Interference of Wing and Fuselage from Tests of 209 Combinations in the NACA Variable-Density Tunnel*, NACAR 540, 1936.
3.33 Sherman, Albert, *Interference of Wing and Fuselage from Tests of 28 Combinations in the NACA Variable-Density Tunnel*, NACA R 575, 1936.
3.34 Sherman, Albert, *Interference of Wing and Fuselage from Tests of 30 Combinations with Triangular and Elliptical Fuselages in the NACA Variable-Density Tunnel*, NACA TN 1272, 1947.
3.35 Lowry, J. G., and Polhamas, E. C., *A Method for Predicting Lift Increments Due to Flap Deflection at Low Angles of Attack in Incompressible Flow*, NACA TN 3911, January 1957.
3.36 Advanced Technology Airfoil Research Conference, NASA Langley Research Center, March 7–9, 1978.
3.37 Schmitz, F. W., *Aerodynamics of Model Aircraft Wing Measurements I*, R. T. P. Translation No. 2460, Issued by Ministry of Aircraft Production.
3.38 Attinello, J. S., An Interim Attack Airplane from a Navy Fighter, BuAir Report DR 1417, July 1952.

FOUR
DRAG

As a child, it was fun to stick your hand out of the car window and feel the force of the moving, invisible air. To the aeronautical engineer, however, there is nothing very funny about aerodynamic drag. A continuing struggle for the practicing aerodynamicist is that of minimizing drag, whether it is for an airplane, missile, or ground-based vehicle such as an automobile or train. It takes power to move a vehicle through the air. This power is required to overcome the aerodynamic force on the vehicle opposite to its velocity vector. Any reduction of this force, known as the drag, represents either a direct saving in fuel or an increase in performance.

The estimation of the drag of a complete airplane is a difficult and challenging task, even for the simplest configurations. A list of the definitions of various types of drag partly reveals why this is so.

Induced Drag The drag that results from the generation of a trailing vortex system downstream of a lifting surface of finite aspect ratio.

Parasite Drag The total drag of an airplane minus the induced drag. Thus, it is the drag not directly associated with the production of lift. The parasite drag is composed of many drag components, the definitions of which follow.

Skin Friction Drag The drag on a body resulting from viscous shearing stresses over its wetted surface (see Equation 2.15).

Form Drag (Sometimes Called Pressure Drag) The drag on a body resulting from the integrated effect of the static pressure acting normal to its surface resolved in the drag direction.

Interference Drag The increment in drag resulting from bringing two bodies in proximity to each other. For example, the total drag of a wing-fuselage combination will usually be greater than the sum of the wing drag and fuselage drag independent of each other.

Trim Drag The increment in drag resulting from the aerodynamic forces required to trim the airplane about its center of gravity. Usually this takes the form of added induced and form drag on the horizontal tail.

Profile Drag Usually taken to mean the total of the skin friction drag and form drag for a two-dimensional airfoil section.

Cooling Drag The drag resulting from the momentum lost by the air that passes through the power plant installation for purposes of cooling the engine, oil, and accessories.

Base Drag The specific contribution to the pressure drag attributed to the blunt after-end of a body.

Wave Drag Limited to supersonic flow, this drag is a pressure drag resulting from noncanceling static pressure components to either side of a shock wave acting on the surface of the body from which the wave is emanating.

With the exception of wave drag, the material to follow will consider these various types of drag in detail and will present methods of reasonably estimating their magnitudes. Wave drag will be discussed in Chapter 6.

SKIN FRICTION DRAG

Figure 4.1 depicts a thin, flat plate aligned with the free-stream velocity. Frequently the drag of a very streamlined shape such as this is expressed in terms of a skin friction drag coefficient, C_f, defined by,

$$C_f = \frac{D}{qS_w} \tag{4.1}$$

where S_w is the wetted surface area that is exposed to the flow. This coefficient is presented in Figure 4.1 as a function of Reynolds number for the two cases where the flow in the boundary layer is entirely laminar or entirely turbulent over the plate. Here the Reynolds number is based on the total length of the plate in the direction of the velocity. In a usual application, the boundary layer is normally laminar near the leading edge of the plate undergoing transition to a turbulent layer at some distance back along the surface, as described in Chapter Two. The situation is pictured in Figure 4.1, where the velocity profile through the layer is shown. In order to illustrate it, the thickness of the layer is shown much greater than it actually is.

As shown in this figure, a laminar boundary layer begins to develop at the leading edge and grows in thickness downstream. At some distance from the leading edge, the laminar boundary becomes unstable and is unable to suppress disturbances imposed on it by surface roughness or fluctuations in the free stream. In a short distance the boundary layer undergoes transition to a turbulent boundary layer. Here the layer suddenly increases in thickness and is characterized by a mean velocity profile on which a random fluctuating velocity component is superimposed. The distance, x, from the leading edge

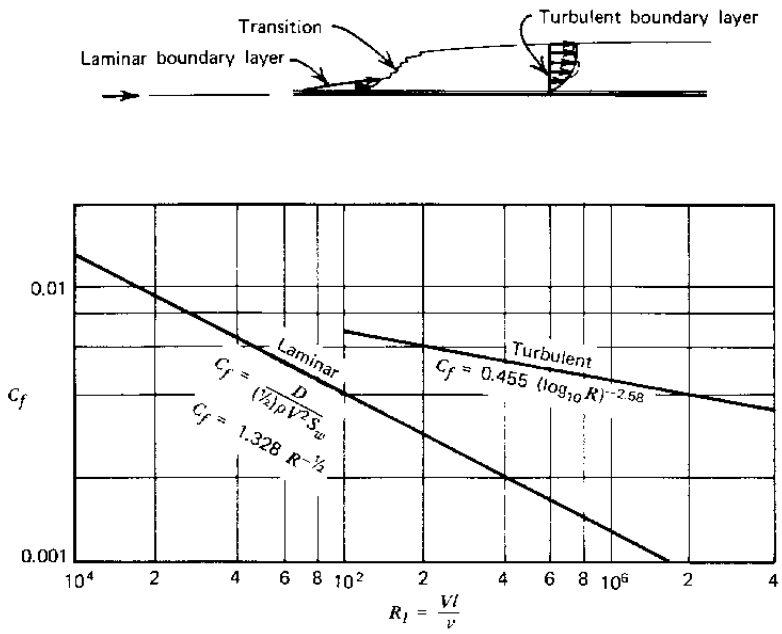

Figure 4.1 Drag of a thin flat plate.

of the plate to the transition point can be calculated from the transition Reynolds number, R_x. R_x is typically, for a flat plate, of the order of 3×10^5, R_x being defined by

$$R_x = \frac{\rho V x}{\mu} \tag{4.2}$$

For very smooth plates in a flow having a low level of ambient turbulence, R_x can exceed 1×10^6.

Since the velocity profile through the boundary layer approaches the velocity outside the layer asymptotically, the thickness of the layer is vague. To be more definitive, a displacement thickness, δ^*, is frequently used to measure the thickness of the layer. δ^* is illustrated in Figure 4.2 and is defined mathematically by

$$\delta^* = \int_0^\infty \left(1 - \frac{u}{V}\right) dy \tag{4.3}$$

where y is the normal distance from the plate at any location such that, without any boundary layer, the total flow past that location would equal the flow for the original plate with a boundary layer. To clarify this further, let δ be the boundary layer thickness where, for all intents and purposes, $u = V$.

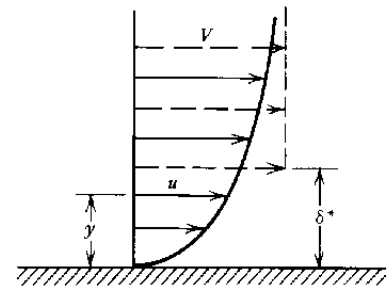

Figure 4.2 Displacement thickness.

Then

$$V(\delta - \delta^*) = \int_0^\infty u\, dy \tag{4.4}$$

Allowing δ to become infinite leads to Equation 4.3.

If we arbitrarily define δ as the value of y at which $u = 0.99V$ then, for a laminar layer,

$$\delta \simeq 5.2\left(\frac{\nu x}{V}\right)^{1/2} = 5.2x\left(\frac{Vx}{\nu}\right)^{-1/2} \tag{4.5}$$

$$\delta^* = \frac{\delta}{3} \tag{4.6}$$

For a turbulent layer,

$$\delta \simeq 0.37x\left(\frac{Vx}{\nu}\right)^{-1/5} \tag{4.7}$$

$$\delta^* = \frac{\delta}{8} \tag{4.8}$$

Observe that relatively speaking, the turbulent boundary layer is more uniform, with δ^* being only one-eighth of δ as compared to one-third for the laminar layer.

In order to clarify the use of Figure 4.1 and Equations 4.5 to 4.8, let us consider the horizontal tail of the Cherokee pictured in Figure 3.62 at a velocity of 60.4 m/s (135 mph) at a 1524 m (5000 ft) standard altitude. We will assume that the tail can be approximately treated as a flat plate at zero angle of attack.

From Figure 3.62, the length of the plate is 30 in or 0.762 m. The total wetted area, taking both sides and neglecting the fuselage, is 4.65 m^2 (50 ft^2). From Figure 2.3, at an altitude of 1.52 km, $\rho = 0.1054$ kg/m^3 and $\nu = 1.639 \times 10^{-5}$ m^2/s. We will assume that the transition Reynolds number is equal to 3×10^5.

The distance from the leading edge to the transition point is found from Equation 4.2.

$$x = \frac{\nu R_x}{V}$$

$$= 1.639 \times 10^{-5} \times 3 \times \frac{10^5}{60.4}$$

$$= 0.0814 \text{ m } (3.2 \text{ in.})$$

The Reynolds number based on the total length will be equal to

$$R_l = \frac{Vl}{\nu}$$

$$= \frac{60.4\ (0.762)}{1.639 \times 10^{-5}}$$

$$= 2.81 \times 10^6$$

If the flow over the tail were entirely turbulent then, from Figure 4.1,

$$C_f = 0.455\ (\log_{10} R_l)^{-2.58} \tag{4.9}$$

$$= 0.00371$$

The dynamic pressure q for this case is

$$q = \rho V^2/2$$

$$= \frac{0.1054\ (60.4)^2}{2}$$

$$= 1923 \text{ N/m}^2$$

Hence the total skin friction drag would be

$$D = qS_w C_f$$

$$= 1923\ (4.65)(0.00371)$$

$$= 33.17 \text{ N}$$

However, the leading portion of the plate is laminar. The wetted area of this portion is equal to 0.497 m^2. For laminar flow over this portion,

$$C_f = 1.328 R^{-1/2} \tag{4.10}$$

$$= 1.328\ (3 \times 10^5)^{-1/2}$$

$$= 0.00242$$

Hence the drag of this portion of the plate is equal to

$$D = qC_f S_w$$

$$= 1923(0.00242)(0.497)$$

$$= 2.31 \text{ N}$$

If the flow were turbulent over the leading portion of the plate, its C_f would be

$$C_f = 0.455\ (\log_{10} R)^{-2.58}$$

$$= 0.455\ (\log_{10} 3 \times 10^5)^{-2.58}$$

$$= 0.00566$$

Thus its drag for a turbulent boundary layer would be

$$D = qC_f S_w$$

$$= (1923)(0.00566)(0.497)$$

$$= 5.35 \text{ N}$$

The above is 5.35 − 2.31, or 3.04 N higher than the actual drag for laminar flow. Hence this difference must be subtracted from the total drag of 33.17 N previously calculated assuming the boundary layer to be turbulent over the entire plate. Hence the final drag of the total horizontal tail is estimated to be

$$D = 33.17 - 3.04$$

$$= 30.13 \text{ N}$$

$$= 6.77 \text{ lb.}$$

The thickness, δ, of the laminar boundary layer at the beginning of transition can be calculated from Equation 4.5.

$$\delta = 5.2\ (0.0814)(3 \times 10^5)^{-1/2}$$

$$= 7.728 \times 10^{-4} \text{ m}$$

$$= 0.0304 \text{ in.}$$

The thickness of the turbulent layer right after transition is found from Equation 4.7 assuming the layer to have started at the leading edge.

$$\delta = 0.37(0.0814)(3 \times 10^5)^{-1/5}$$

$$= 2.418 \times 10^{-3} \text{ m}$$

$$= 0.0952 \text{ in.}$$

At the trailing edge, the thickness of the turbulent layer will be

$$\delta = 0.37(0.762)(2.81 \times 10^6)^{-1/5}$$

$$= 0.0145 \text{ m}$$

$$= 0.5696 \text{ in.}$$

The displacement thickness at the trailing edge is thus only 0.0018 m (0.071 in.).

Before leaving the topic of skin friction drag, the importance of surface roughness should be discussed. Surface roughness can have either a beneficial or adverse effect on drag. If it causes premature transition, it can result in a

reduced form drag by delaying separation. This is explained more fully in the next section. Adversely, surface roughness increases the skin friction coefficient. First, by causing premature transition, the resulting turbulent C_f is higher than C_f for laminar flow, in accordance with Figure 4.1. Second, for a given type of flow laminar or turbulent, C_f increases as the surface is roughened.

It is difficult to quantify the increment in C_f as a function of roughness, since roughness comes in many forms. For some information on this, refer to the outstanding collection of drag data noted previously (e.g., Ref. 4.4). Generally, if a roughness lies well within the boundary layer thickness, say of the order of the displacement thickness, then its effect on C_f will be minimal. Thus, for the preceding example of the horizontal tail for the Cherokee, the use of flush riveting near the trailing edge is probably not justified.

An approximate estimate of the effect of roughness, at least on streamlined bodies, can be obtained by examining the airfoil data of Reference 3.1. Results are presented for airfoils having both smooth and rough surfaces. The NACA "standard" roughness for 0.61-m (2-ft) chords consisted of 0.028-cm (0.011-in.) carborundum grains applied to the model surface starting at the leading edge and extending 8% of the chord back on both the upper and lower surfaces. The grains were spread thinly to cover 5 to 10% of the area.

An examination of the drag data with and without the standard roughness discloses a 50 to 60% increase in airfoil drag resulting from the roughness. It is difficult to say how applicable these results are to production aircraft. Probably the NACA standard roughness is too severe for high-speed aircraft employing extensive flush riveting with particular attention to the surface finish. In the case of a production light aircraft for general aviation usage, the standard roughness could be quite appropriate.

FORM DRAG

In addition to skin friction drag, a body generally experiences some form drag. Unlike the skin friction drag that results from viscous shearing forces tangential to a body's surface, form drag results from the distribution of pressure normal to the body's surface. The extreme case of a flat plate normal to the flow is pictured in Figure 4.3. Here the drag is totally the result of an unbalance in the normal pressure distribution. There is no skin friction drag present in this case.

Generally, form drag is difficult to predict. For that matter, so is skin friction drag except for the simplest cases. Thus, in general cases, such as that pictured in Figure 4.4, where the total drag results from both normal and tangential stresses (or pressures) one must usually resort to experimental data to estimate the drag.

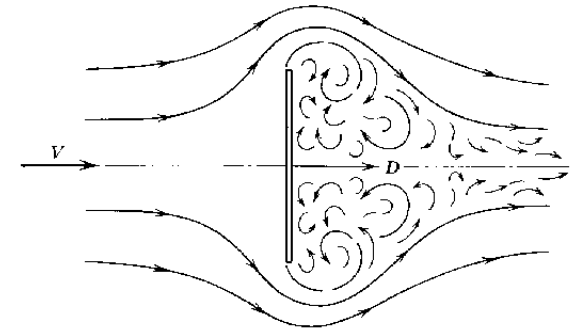

Figure 4.3 Flat plate normal to flow.

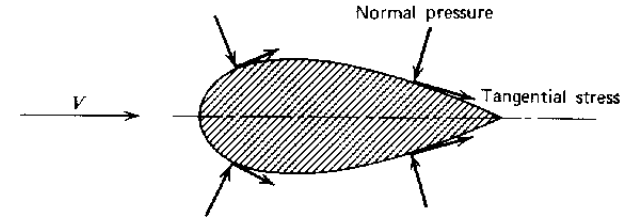

Figure 4.4 Body having both skin friction and form drag.

As with skin friction drag, form drag is generally dependent on Reynolds number. To see why, consider the flow around the circular cylinder pictured in Figure 4.5. In Figure 4.5*a* flow is pictured at a low Reynolds number. Here, beginning at the stagnation point, a laminar boundary layer develops. On the surface of the cylinder, the static pressure (normal) is highest at the stagnation point and decreases to a minimum at the top and bottom. Moving around toward the rear, beyond these points, the static pressure increases, tending toward the stagnation pressure at the very rear. In the absence of viscosity the normal pressure distribution would be symmetrical (Equation 2.78) and there would be no drag. This is a clear example of D'Alembert's paradox, which states that a body in a inviscid fluid will experience no drag. As the slower moving fluid in the laminar boundary layer moves beyond the minimum pressure point on the cylinder, its momentum is insufficient to move against the positive pressure gradient, referred to as an adverse gradient, and thus the flow separates just past the top and bottom locations on the cylinder. In the separated region over most of the rear portion of the cylinder the static pressure is constant and equal to the low pressure at the top and bottom. Thus the high pressure acting over the front and the low pressure over the rear result in a high form drag.

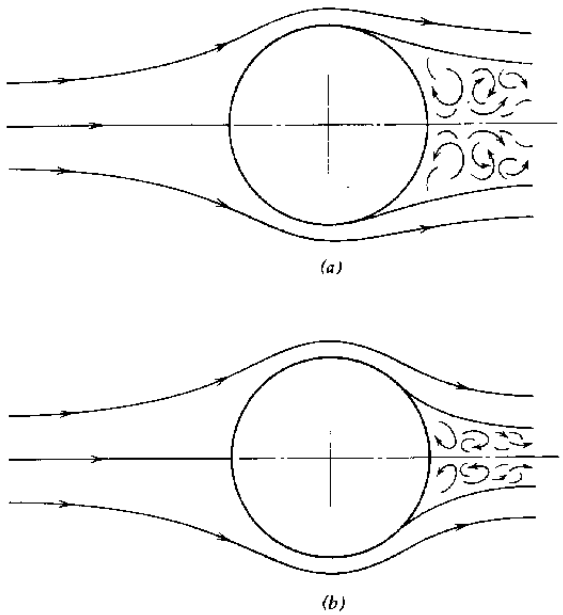

Figure 4.5 Flow over a circular cylinder. (*a*) Low Reynolds number. Separation occurs before transition. Large wake. (*b*) High Reynolds number. Transition occurs before separation. Small wake.

The high-Reynolds number case is shown in Figure 4.5*b*. Here the laminar boundary layer undergoes transition to a turbulent boundary layer before separating. The subsequent turbulent mixing increases the momentum and energy of the boundary layer so that it remains attached toward the rear of the cylinder, well beyond the separation point of the laminar layer. Thus, in this case, the separation region is much smaller and the static pressure is higher on the rear of the cylinder than for the laminar case. Therefore, because of reduced form drag, the drag coefficient of a cylinder is lower at higher Reynolds numbers.

C_d as a function of Reynolds number is presented in Figure 4.6 for both spheres and two-dimensional circular cylinders. Here, C_d is based on the projected frontal area. Note the rapid drop in C_d above an R value of approximately 2×10^6. This is the so-called critical Reynolds number, where the transition point is nearly coincident with the separation point. "Subcritical" refers to flow at Reynolds numbers that are less than critical; "supercritical" denotes R values that are higher than critical. A body shape having a well-defined separation point will not exhibit a critical Reynolds number; neither will streamlined shapes.

Although not concerned with drag per se, Figure 4.6*a* also includes the

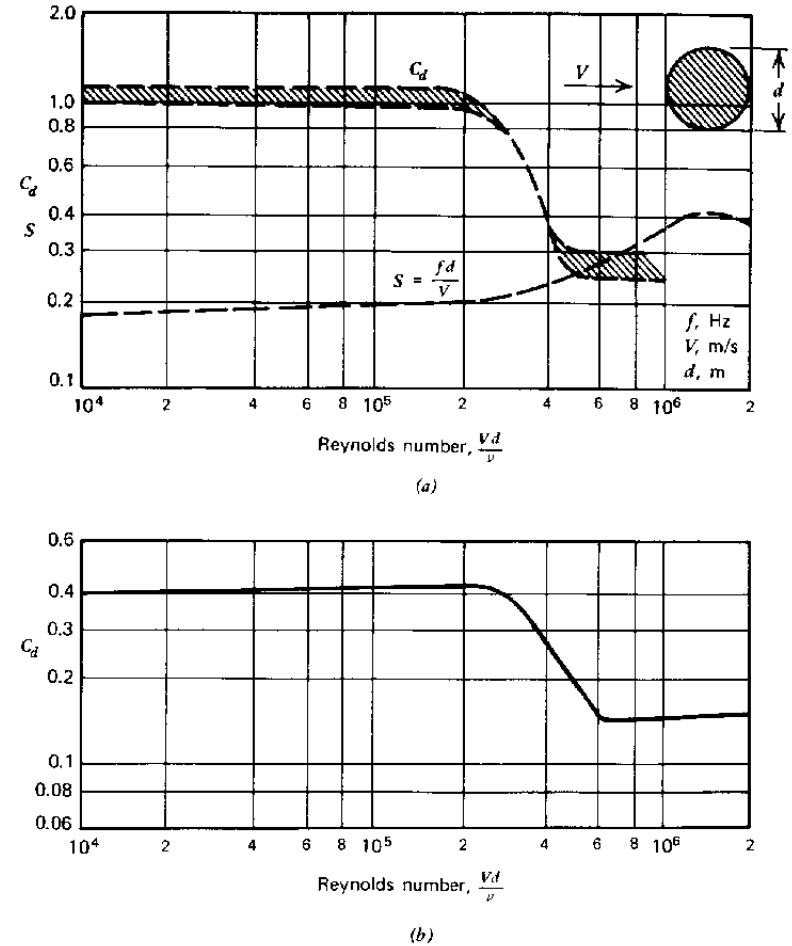

Figure 4.6 Drag coefficients of cylinders and spheres versus Reynolds number. (*a*) Two-dimensional circular cylinders. (*b*) Spheres.

quantity fD/V, known as the Strouhal number, S. S characterizes an interesting behavior of bluff bodies with rounded trailing edges. As such a body first begins to move through a fluid, the vorticity in the boundary layer is shed symmetrically from the upper and lower surfaces to form two vortices of opposite rotation. However, the symmetrical placement of the vortex pair is unstable, so that succeeding vortices are then shed alternately from the upper and lower surfaces. The resulting flow pattern of periodically spaced vortices downstream of the body is known as a Karman vortex street.

In the definition of Strouhal number, f is the frequency at which the

vortices are shed. As a vortex is shed from one surface of the cylinder, it produces a momentary circulation around the cylinder opposite in direction to the vortex. From the Kutta-Joukowski law, a force on the cylinder normal to V results. As the next vortex is shed, the force reverses its direction, resulting in an alternating force on the cylinder. This particular phenomenon is the cause for the "singing" of telephone wires in the wind.

As an example of the use of Figure 4.6*a*, consider a wire 2 cm in diameter in a wind blowing at a speed of 8 m/s. Assuming standard sea level conditions,

$$R = \frac{Vd}{\nu}$$
$$= \frac{8(0.02)}{1.456 \times 10^{-5}}$$
$$= 1.099 \times 10^{4}$$

From Figure 4.6*a*, for this Reynolds number,

$$C_d = 1.1$$
$$S = 0.18$$

Thus the drag per unit length on the wire will be

$$D = qC_d d$$
$$= \frac{1}{2}(1.226)(8)^2(1.1)(0.02)$$
$$= 0.863 \text{ N/m}$$

The frequency of the alternating lift force on the wire will be,

$$f = \frac{VS}{d}$$
$$= \frac{8(0.18)}{0.02}$$
$$= 72 \text{ Hz}$$

Let us now consider the extreme case of form drag illustrated in Figure 4.3, where the point of flow separation is well defined and not dependent on Reynolds number. It is not too surprising to find that drag coefficients for such shapes are nearly constant over a wide range of Reynolds number values. A number of such shapes are pictured in Figure 4.7*a*.

This figure presents values for both two-dimensional and three-dimensional shapes. Three-dimensional shapes are all bodies of revolution. Observe that for the same profile shape,

$$\frac{C_d(2\text{-D})}{C_d(3\text{-}D)} \simeq 1.8$$

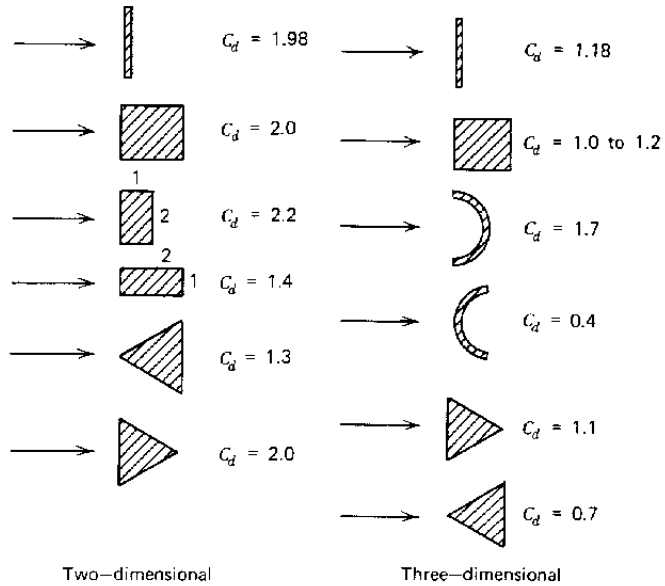

Figure 4.7a Examples of shapes having C_d values nearly independent of Reynolds number.

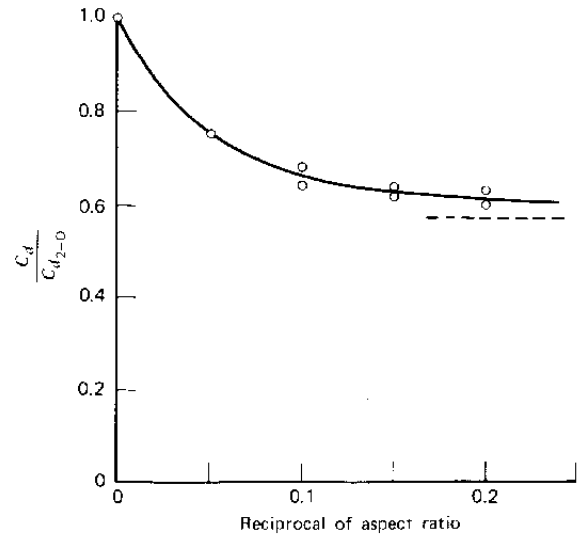

Figure 4.7b Transition from three-dimensional to two-dimensional drag for cylinders at supercritical Reynolds numbers.

If the ratio of the span to the height (or diameter) of a flat plate (or cylinder) normal to the flow is approximately 5 or less, C_d is nearly constant and equal to the 3-D value. For aspect ratios greater than 5, C_d varies approximately in the manner given by the normalized curve of Figure 4.7*b*. This curve is based on data from several sources, including Reference 4.4.

A qualitative evaluation of the drag coefficient for a given shape can be made using some "educated intuition." Referring to Figure 4.8, the drag

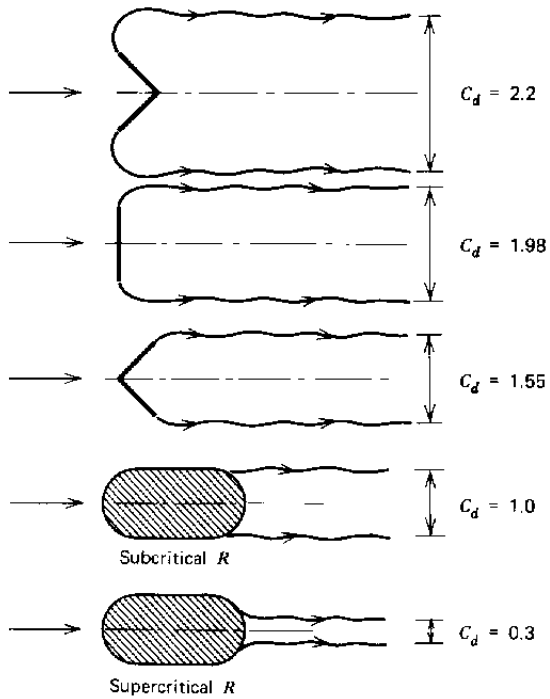

Figure 4.8 Qualitative estimate of drag for two-dimensional shapes.

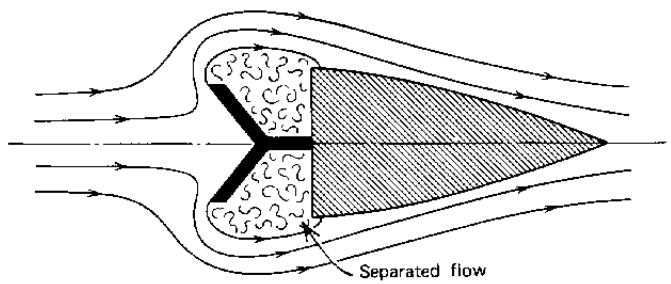

Figure 4.9 Drag reduction of a high drag shape.

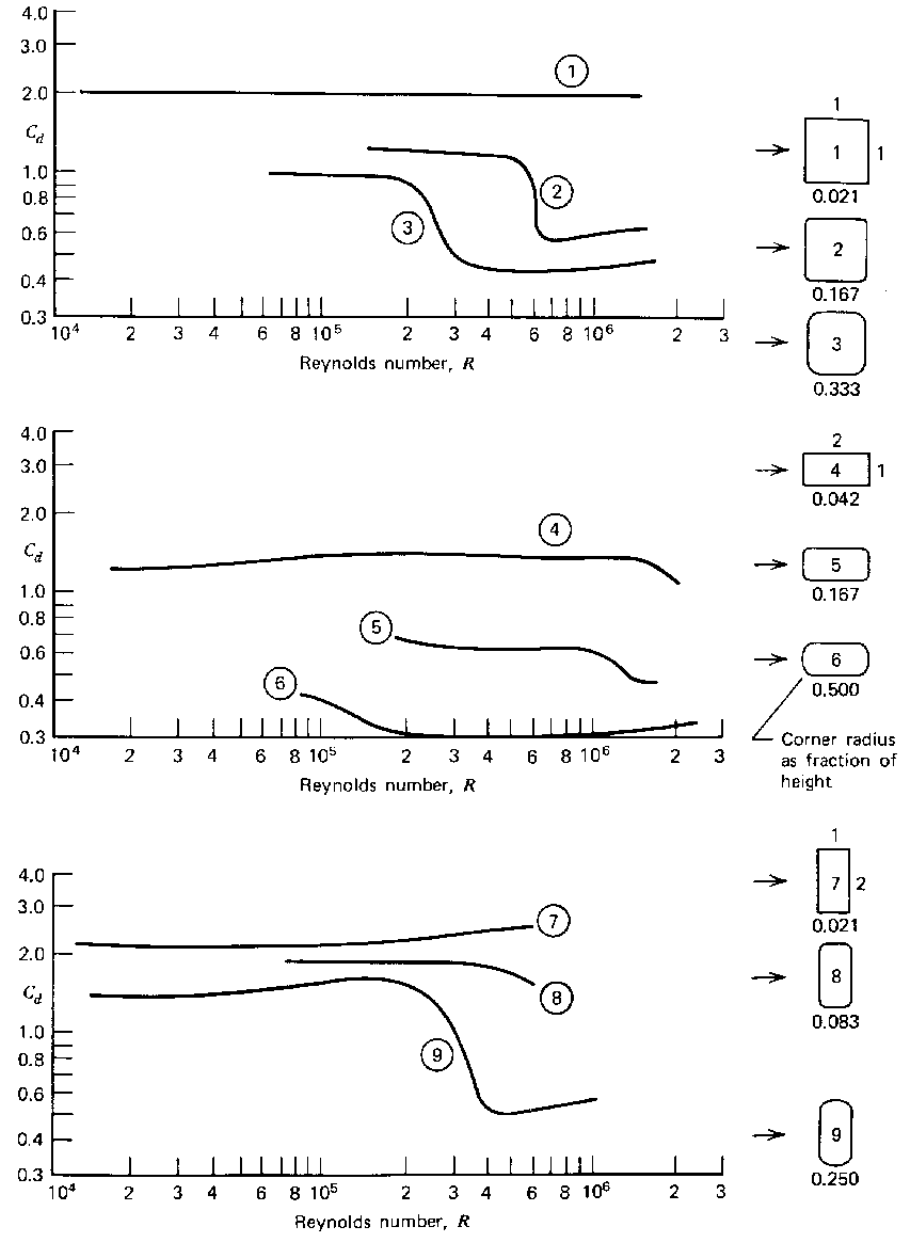

Figure 4.10 Drag coefficients for various cylindrical shapes as a function of Reynolds number.

coefficient of a bluff shape depends on the width of the wake behind the body (before viscosity dissipates it). Beginning with the top figure and working downward, one would expect, for the same projected frontal area, that the widths of the wakes would diminish progressively. Intuitively, such a progression is visualized by picturing the flow as separating tangent to the surface and then being turned gradually in the direction of the main flow.

With regard to drag, the trailing edge shape of a body is usually more important than the leading edge shape. For example, the drag of the top shape in Figure 4.8 can be reduced significantly by providing a body behind it to which the flow can reattach. This is illustrated in Figure 4.9. As opposed to Figure 4.8, in this case, the low pressure in the separated region between the front and the afterbody reacts on both parts, contributing little or nothing to the drag.

In order to provide an additional basis for estimating the drag of two-dimensional sections, the data in Figure 4.10 are provided (Ref. 4.5). This figure shows that for a shape with sharp corners, a rounding of the corners will reduce the drag coefficient as well as the critical Reynolds number.

DRAG OF STREAMLINED SHAPES

The drag of shapes such as airfoils, fuselages, nacelles, torpedoes, submarines, and airships is composed of both form drag and skin friction drag. As the fineness ratio (length/maximum thickness) of a streamlined shape increases, more and more of its drag is attributable to skin friction. Conversely, at low fineness ratios, the drag is principally form drag.

Data on the drag of two-dimensional and three-dimensional streamlined shapes are presented in Figures 4.11, 4.12, and 4.13. Based on the projected frontal area, C_d is given as a function of fineness ratio in Figure 4.11 at a high Reynolds number. In this figure, a fineness ratio of 1.0 corresponds to a circular cylinder and sphere for two-dimensional and three-dimensional shapes, respectively. Notice that the minimum drag occurs at a fineness ratio of approximately 2 for a three-dimensional shape, and at a value of approximately 3 for a two-dimensional shape. However, in view of the sharp rise in both curves at the lower fineness ratios, it might be well in either case to use fineness ratios higher than these, say around 4, if one wishes to fair a blunt shape of a given frontal area.

The crossover of the two curves in Figure 4.11 is to be expected. At low values of fineness ratio, C_d for the two-dimensional shapes is higher than that for the three-dimensional bodies, based on the data of Figures 4.6 and 4.7. At the other extreme, as the fineness ratio becomes large, the skin friction drag predominates. If C_f is assumed to be the same for either the two-dimensional or three-dimensional shapes, the ratio of the C_d values, based on the pro-

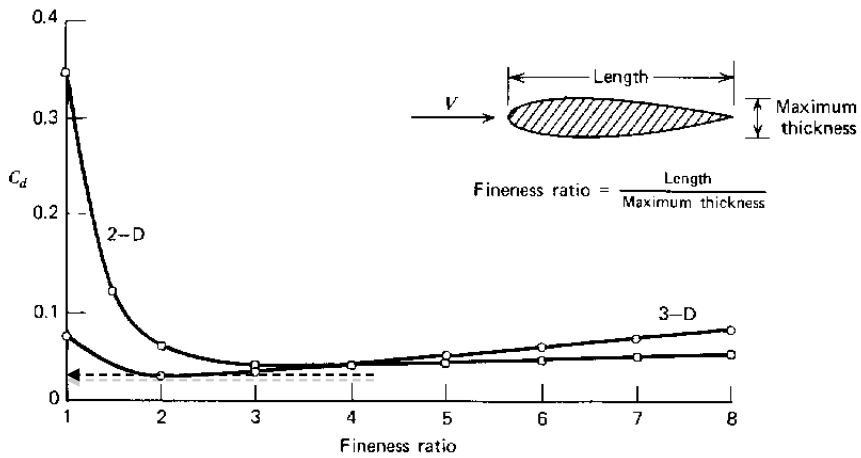

Figure 4.11 Drag coefficients for streamlined shapes as a function of fineness ratio. C_d based on frontal area; R–10^7 based on length.

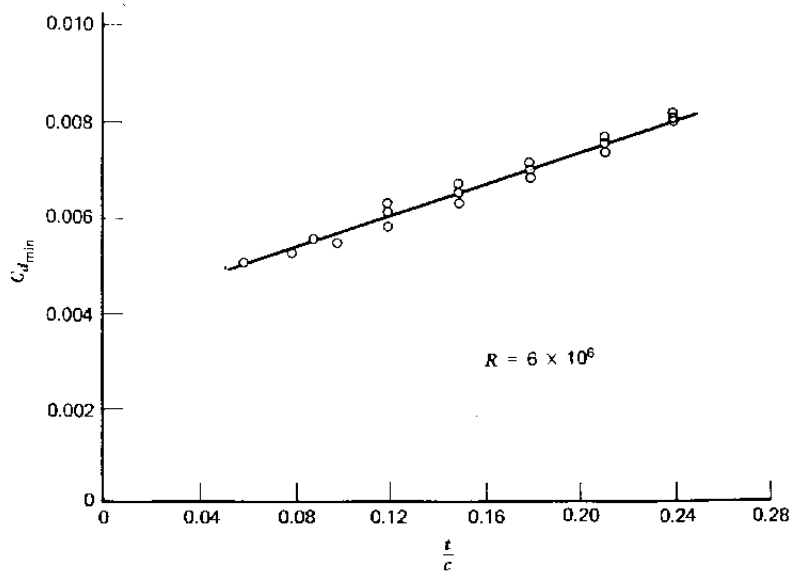

Figure 4.12 Minimum C_d for four and five-digit airfoils of varying camber ratios as a function of thickness ratio. C_d based on chord; smooth surface.

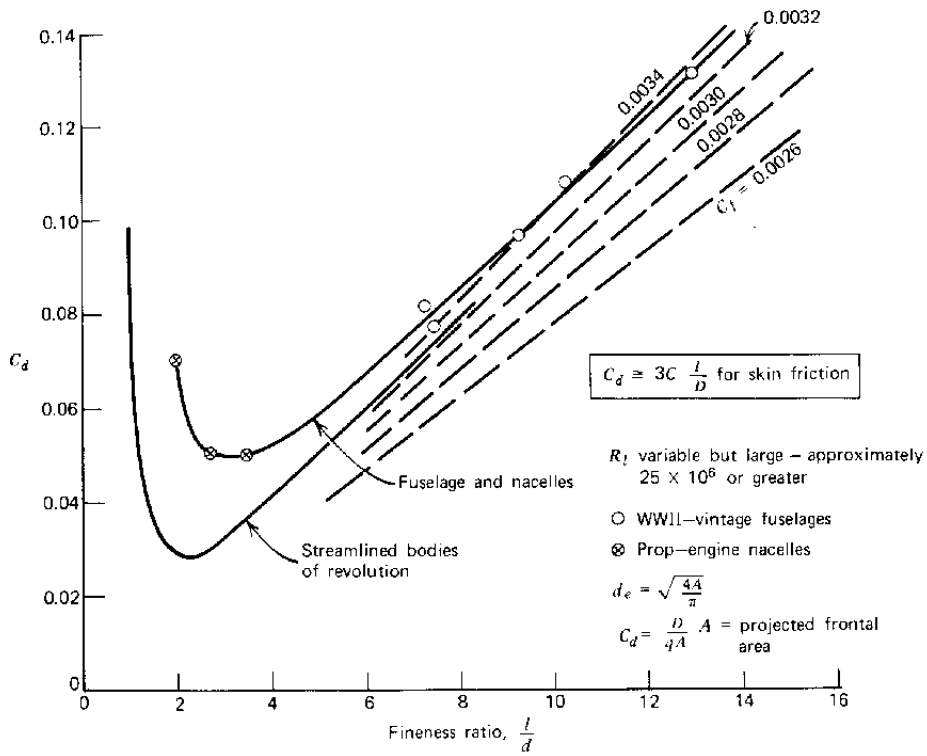

Figure 4.13 Drag of fuselages and similar shapes.

jected frontal areas becomes

$$\frac{C_d(3\text{-D})}{C_d(2\text{-D})} = \frac{S_w(3\text{-D})}{S_w(2\text{-D})}\frac{4}{\pi D}$$

where D is the maximum three-dimensional body diameter or the maximum thickness of the two-dimensional shape. For an elliptical two-dimensional shape compared to an ellipsoid, this becomes

$$\frac{C_d(3\text{-D})}{C_d(2\text{-D})} = \frac{\pi}{2} \tag{4.11}$$

This is close to the ratio from Figure 4.11 for a finess ratio of 8 and only slightly lower than the corresponding ratio given earlier for the form drag.

Minimum profile drag coefficients for NACA four- and five-digit airfoils are presented in Figure 4.12 as a function of thickness ratio at a Reynolds number of 6×10^6. Here, as is usual for airfoils, C_d is based on the chord length. The several data points at each thickness ratio result from airfoils of different camber ratios. Note that $C_{d_{\min}}$ does not vary significantly with

camber. $C_{d_{\min}}$ appears to vary almost linearly with t/c and extrapolates to a value of 0.004 for a t/c of zero. This corresponds to a C_f value of 0.002. According to Figure 4.1, this would require laminar flow over these sections more extensive than one would expect. Probably, transition is delayed until approximately the 25% chord point, the location of maximum thickness. One would then expect a $C_{d_{\min}}$ value of about 0.005.

Figure 4.13 presents three-dimensional drag data directly comparable to Figure 4.11, but with more detail. Data representing practical fuselage and nacelle construction are included in Figure 4.13 together with C_d results from torpedo-shaped bodies. Assuming a reasonable relationship between the frontal and wetted areas of such bodies, expected C_d values for various values of C_f are also included on the figure. For a given C_f value, the experimental results should approach one of these lines as the fineness ratio gets large.

For fully turbulent flow at an R of 25×10^6, C_f for a flat plate would be 0.0026, whereas the data appears to be approaching a C_f of 0.0032 to 0.0034. The higher skin friction drag on the bodies is probably the result of surface roughness.

It is interesting to examine the data of Figure 4.13 in terms of minimum drag for a given body volume. This is particularly important for airship and underwater applications. It is also of interest to the design of tip tanks, where minimum drag for a given volume of fuel is desirable. Denoting the volume by V_m, we will define another drag coefficient.

$$C_{d_V} = \frac{D}{qV_m^{2/3}} \tag{4.12}$$

C_{d_V} is related to C_d in Figure 4.13 by

$$C_{d_V} = \frac{A}{V_m^{2/3}} C_d$$

Obviously, the ratio of the frontal area, A, to the 2/3 power of the volume depends on the particular body shape. We will assume the body to be composed approximately of a hemispherical nose, a cylindrical midbody extending to the middle of the body, and a tail cone. For this particular shape,

$$\frac{A}{V_m^{2/3}} = \left[\frac{9\pi}{\left(4\frac{l}{d} - 1\right)^2}\right]^{1/3} \tag{4.13}$$

Using this relationship and Figure 4.13, the graphs presented in Figure 4.14 were obtained. From this figure it can be seen that to enclose a given volume with a minimum drag body, its fineness ratio should be higher than the optimum values from Figure 4.13. Indeed, for fuselages, the drag for a given volume is nearly constant for l/d values from 4 to 10.